Universiteit Antwerpen

Faculteit Wetenschappen
Departement Wiskunde-Informatica

Parameterization and Correspondence for Improved Modeling, Analysis, and Visualization of Tubular Surfaces

---

Parameteriseren en Corresponderen voor Verbeterde Modelering, Analyse en Visualisatie van Buisvormige Oppervlakken

Proefschrift voorgelegd tot het behalen van de graad van

Doctor in de Wetenschappen

aan de Universiteit Antwerpen te verdedigen door

Toon HUYSMANS

Promotor:
Prof. Dr. Jan Sijbers

Antwerpen, 24 maart 2010

Doctoral committee

Chairman
Prof. Dr. Annie Cuyt

Members
Prof. Dr. Jan Sijbers
Prof. Dr. Ekaterina Vladislavleva

External members
Prof. Dr. Tim Cootes
Prof. Dr. Wiro Niessen

Contact information

✉ Toon Huysmans
Vision Lab, Dept. of Physics
University of Antwerp (CDE)
Universiteitsplein 1, Building N1.19
B-2610 Wilrijk – Antwerpen, Belgium

☎ +32 (0) 3 265 24 72

+32 (0) 498 100 256

+32 (0) 3 265 22 45

toon.huysmans@ua.ac.be

http://webhost.ua.ac.be/visielab/tohu

Cover illustration
A cylindrically parameterized tubular bell. The mapping from the cylinder to the tubular bell is visualized by means of a texture: the iso-parametric lines of the cylindrical domain appear as red and blue lines on the surface. The tubular bell was modeled after the cover of Mike Oldfield's album 'Tubular Bells'.

The Wordles that appear in this manuscript were generated using `http://www.wordle.net/`.

Opgedragen aan Muisje.

Dankwoord

U: “En? Is ’t al af?”
Ik: “Euh, mwa bijna wel. Nog efkes, he.”

Wat was u toch nieuwsgierig het afgelopen anderhalf jaar. En zo ongeduldig. Foei! Maar nu dus excellent nieuws: ’t is af! Echt. Sla maar alvast een lading leesbrilletjes in bij het Kruidvat. Zet de pantoffels al te warmen bij de haard en trek je gezelligste pyjama aan want met “De avonturen van Pluisje in Buisvormigland” bij de hand staan er onvergetelijk knusse winteravonden voor de deur! Uren leesplezier, gegarandeerd! En daarna kom ik u natuurlijk persoonlijk overhoren. Mondeling, zonder schriftelijke voorbereiding. Jeej!
Ik: “En? Is ’t al uit?”
U: “Euh, mwa bijna wel. Nog efkes, he.”

Nu maar even ernstig. Dit boek is het product van een lang en erg interessant traject. Een doctoraat is veel meer dan een boekje, het is één lang leerproces, zeg maar. Aan het begin was ik een groentje dat wat kon programmeren, ondertussen ben ik een zelfstandig wetenschappelijk onderzoeker. Zoiets gebeurt niet vanzelf. Het vereist een grote en aanhoudende inspanning, niet alleen van mijzelf maar ook van de mensen rondom mij. Met vallen en opstaan. U hielp mij telkens weer opstaan. Een doctoraat doe je niet alleen. Zes jaar lang heb ik kunnen investeren in mezelf, mezelf kunnen vervolledigen. Ik heb het gevoel dat het een geslaagde reis was en hopelijk voelt u dat ook. Omdat u mij gedurende al die tijd onvoorwaardelijk gesteund heeft volgt hier een korte dankbetuiging. Mogelijks komt u onterecht niet in het volgende lijstje voor, dan zet ik alvast mijn joker in en trakteer ik u alsnog met plezier een pint om het goed te maken!

De persoon die het meeste lof verdient is zonder twijfel mijn promotor Jan Sijbers. Hij was er vanaf het begin bij en heeft mij over het hele traject onvoorwaardelijk gesteund. Van hem heb ik geleerd hoe je aan onderzoek doet en wat belangrijk is binnen een doctoraat. Jan zit altijd vol goeie ideeën. Ook was hij steeds direct mee als ik met iets nieuws op de proppen kwam. Onze discussies vormden de fundamenten van mijn onderzoek. Dat we nog vele ideeën samen mogen uitwerken!

In de eerste helft van mijn doctoraat werd ik naast Jan ook begeleid door Brigitte Verdonk. Zij was altijd even enthousiast als ik mijn vorderingen met haar besprak, dat deed deugd en voorzag mij telkens van nieuwe werklust.

Dit doctoraat zou niet hetzelfde zijn zonder de inbreng van collega Amit Bernat. Zijn onaflatende zoektocht naar de Heilige Graal onder de sleutelbeenplaatjes zorgde voor een nieuwe wind in mijn doctoraat. Ik heb nog niet dikwijls iemand ontmoet die zo gedreven is. Al wat hij voor ons project deed, en dat is heel wat, deed hij in zijn vrije tijd naast zijn studies. Onze samenwerking verliep niet zonder horten of stoten (de discussies konden soms hoog oplopen) maar op het resultaat zijn wij beiden bijzonder fier.

Zonder het Universitair Ziekenhuis Antwerpen zou ik nooit in de mogelijkheid geweest zijn om mijn technieken te toetsen aan de werkelijkheid. Paul Parizel en Jan Gielen voorzagen vele uren scantijd die telkens weer netjes verzorgd werden door Michel Geldof. Maarten Spinhoven, Marc Van Outryve en Katrien De Jongh maakten mij moeiteloos wegwijs in de echte én virtuele wereld van de dikke darm. Het sleutelbeenproject zou er nooit geweest zijn zonder Francis Van Glabbeek. Hij was mee de drijvende kracht in de zoektocht naar een beter fixatieplaatje. Het enthousiasme waarmee Francis telkens de recentste vorderingen in het sleutelbeenproject onthaalde werkte erg inspirerend.

De mensen van de Interfacedienst van de Universiteit Antwerpen, met name Philip Hendrickx en Jan Van Havenbergh, en de mensen van het BiiP (Business-integrated intellectual Property), met name Krista De Clerck, zijn van onschatbare waarde geweest in het valorisatieluik van dit doctoraat. Het is dankzij hun inspanningen dat de technieken uit dit doctoraat in de toekomst mogelijks ingezet worden in de medische sector.

Ik dank ook het IWT (Instituut voor de Aanmoediging van Innovatie door Wetenschap en Technologie in Vlaanderen) en het IBBT (Interdisciplinair Instituut voor Breedband Technologie) voor de verleende financiële steun.

Ik heb het geluk gehad om mijn doctoraat uit te kunnen voeren temidden een geweldige groep collega's waarvan er vele ondertussen vrienden geworden zijn. Alain, Wouter, Jef en Gert, mijn beste bureaumaatjes, het klikte onmiddellijk tussen ons. De ontstane vriendschap, een beetje zoals die bij strijdmakkers, is me zeer waardevol. Onze ellenlange discussies over van alles en nog wat, het één al wat relevanter dan het ander, zullen mij nog lang bijblijven. De talloze lunchbezoekjes aan de plaatselijke kastelen en hoeves maakten van mijn doctoraat in feite één lange gastronomische uitstap. Laat ons dit nog lang voortzetten!

In feite zijn alle huidige en voormalige collega's op het visielab verantwoordelijk voor de toffe en ongedwongen sfeer waarin ik mijn onderzoek kon uitvoeren. X-factor Sander, Romulo, Zhenhua, Paul, Joost, Willem-Jan, de drie Wimmen, Yifan, Wolfgang, Ruben, Hoshiang, Arno, Ben, Jaber, de twee Dirken, Jeny, Jenny, Guy, Rob, Tom, Jelle, Steve, Rudi, Alexander, Jos, Greg, Elke, Gert, Geert, Jochen, Joachim, Zahid, Valerie, Karen, Nico, Wouter, Stijn en Edwin: thanks!

Zo tussen de geneugten (programmeren, papers schrijven, etc.) van het doctoreren door vond ik gelukkig hier en daar nog wat tijd om door te brengen met familie en vrienden. Na de vrijdagavond- en zaterdagochtendlessen Statistiek in het Leuvense werd ik steevast professioneel opvangen en van geestrijke nazorg voorzien door mijn beste Ivo. De weinige tijd dat ik me niet met wetenschap diende bezig te houden spendeerde ik regelmatig aan de protowetenschap en dat samen met Meester Nick: hopelijk gaat onze raket ooit toch nog tot aan de maan en kunnen we met onze duikklok de diepste regionen van de oceaan verkennen! Na al die inspanningen mocht de ziel ook wel eens ontspannen: de weekends uit, de avonden in de Stanny en de nachtjes in de Capital samen met de lieve vriendjes May, Werner, Dirk, Hannah, Dirk, Bart, Greetje, Frank, Matthias, Gert, Griet, Pieter, Sophie, Vincent en Lotte deden mij bijzonder goed. Dat we nog veel nachtjes vol mogen zeveren en dansen!

Velen onder u hebben mij jaren gesteund maar er zijn er enkelen die dat al mijn hele leven doen: Koen, Carolien, Lisa en Roger, bedankt voor al de kansen die jullie mij gegeven hebben en om altijd in mij te blijven geloven.

Meestal eindigt zo een dankwoord bij één bijzonder persoon. Maar in dit geval zijn het er drie: mijn drie poezen Loja, Miniman en Mieke. De eerste twee zijn van het pluizige type dat zich graag laat bedienen onder het bevel “Miauw!” en huppelden op ongelofelijk schattige wijze achter de derde aan toen ik deze op een ochtend van de dansvloer plukte en de mijne maakte. Mieke, sinds ik jou ken sta ik stevig in mijn schoenen en is alles aangenamer. Jij brengt mij wijsheid die echt telt. Zonder jou zou ik niet de persoon zijn die ik nu ben en daarvoor ben ik je ongelooflijk dankbaar!

Groetjes,

Toon.

Contents

List of Figures

List of Tables

PART I

INTRODUCTION

CHAPTER 1

INTRODUCTION

1.1 Visualization, Analysis, and Modeling of Tubular Surfaces

The nature of an object is reflected in its many properties such as its shape, texture, color and weight. In each of these properties lies a wealth of information possibly valuable to the observer. The work in this manuscript is concerned with the geometric shape of objects. Most objects have a complex volumetric shape that consists out of many substructures. Here, the shape of an object will be represented by its boundary surface. However, object substructures that can be represented by a surface can also be the subject of investigation.

The boundary surfaces considered in this manuscript are represented by a sufficiently fine patchwork of triangles, i.e., a triangle mesh. These surfaces are derived from the digital representation of the studied object which can originate from a range of sources such as CT, MRI or laser scans. Note that the surface representation of the object is generally the result of many complex preprocessing operations applied to the digital representation such as smoothing, segmentation, and surface extraction. This preprocessing stage is considered to be out of the scope of this manuscript. In this manuscript, the terms object, boundary surface, and shape all refer to the same concept of “the shape of an object represented by its boundary surface” and they will be used interchangeably.

The investigation of the shape of a single object or a population of objects has many uses in many different fields. Especially in the biomedical field, a strong increase in interest is observed recently. It should not be surprising that knowledge of the average shape and the possible variations of an organ or bone can be employed by many applications, including segmentation, reconstruction, and diagnosis. This manuscript focuses on biomedical objects and applications. The enabling methodology proposed in this manuscript can, however, also be applied to other classes of objects. Applications that benefit from the methodology can be divided into the following three categories: (1) *visualization* of the shape of a surface or of the shape present in a population of surfaces, (2) *analysis* of shape differences between subgroups in a population of surfaces, and (3) *modeling* of a single surface or of the shape of a population of surfaces. The main ingredient needed for these applications is a technique to establish a correspondence between surfaces. For some applications a correspondence between the surface and a simple domain is needed which is called a surface parameterization. In other cases, a correspondence is needed for a whole population of surfaces. In any case, a correspondence between two surfaces is a one-to-one map that maps points from one surface to equivalent points on the other surface.

The construction of a parameterization or a correspondence is a challenging task. Most research was focused on parameterizations and correspondences for surfaces of disc-like and spherical topology. Many biomedical objects are covered with these two topologies and excellent results can be obtained. (In Figure 1.2 four parameterized surfaces of different topology are shown.) For more complex topologies, some techniques have been proposed but they generally require extensive user interaction. This manuscript aims to extend the excellent results of the spherical and disc-like topologies to the surfaces of cylindrical topology. There are many examples of biomedical objects that have the topology of a cylinder. See Figure 1.1.

It should be noted that the techniques that are developed in this manuscript are also applicable to elongated spherical surfaces. By creating two small holes in a spherical surface, its topology is modified to that of a cylinder. In Figure 1.3, an example surface is shown that is topologically modified and subsequently parameterized on the cylinder. More examples of elongated spherical surfaces can be found in Figure 1.1.

1.2 Methodology Overview

In this manuscript, two methods are proposed to parameterize surfaces of cylindrical topology onto the cylinder. A short overview of these methods is given in Section 1.2.1. These parameterization methods are then combined with an optimization framework in order to establish correspondences for populations of surfaces of cylindrical topology. A short overview of that technique is provided in Section 1.2.2.

The applications developed in this manuscript rely heavily on the proposed parameterization and correspondence techniques. The parameterization techniques are employed for virtual inspection of tubular organs. More specifically, for unfolding of the colon. The correspondence technique is applied to a pop-

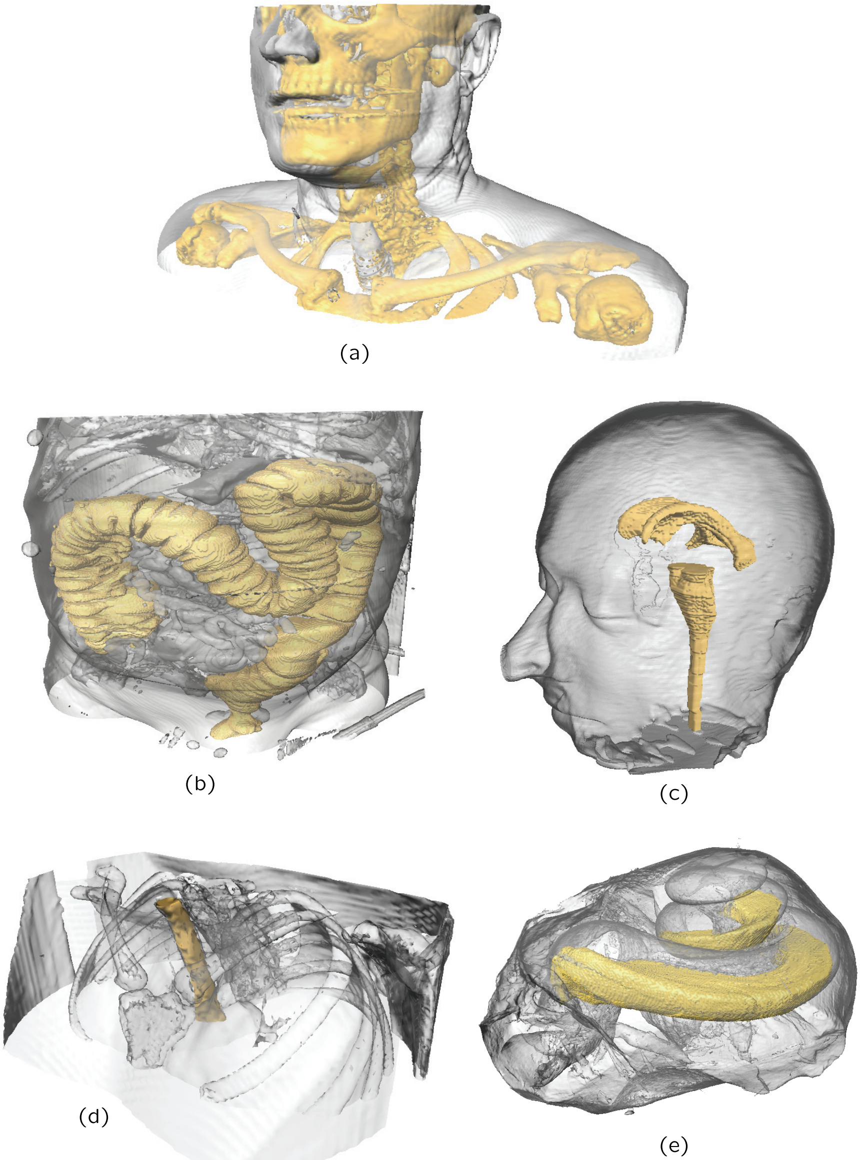

Figure 1.1: There are many examples of tubular or elongated structures in the human body, e.g, elongated bones like (a) the mandible and the clavicles, tubular intestines like (b) the colon and (d) the trachea, brain structures like (c) the ventricles and the brainstem, and cochlear canals like (e) the scala tympani. All these surfaces can be parameterized onto the cylinder.

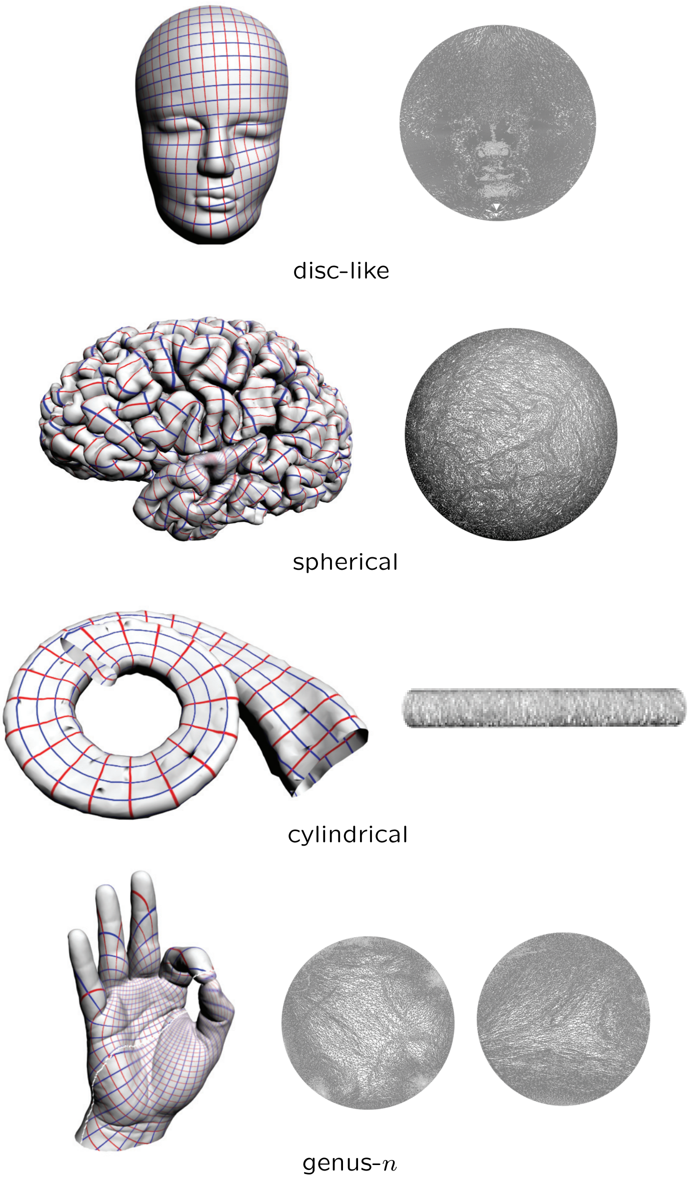

Figure 1.2: Examples of parameterized surfaces of different topologies. From top to bottom: a disc-like mask parameterized onto a planar disc, a cortical hemisphere of spherical topology parameterized onto the sphere, a tubular cochlear scala parameterized onto the cylinder, and a hand model of more complex topology that was divided in two charts and parameterized onto planar discs.

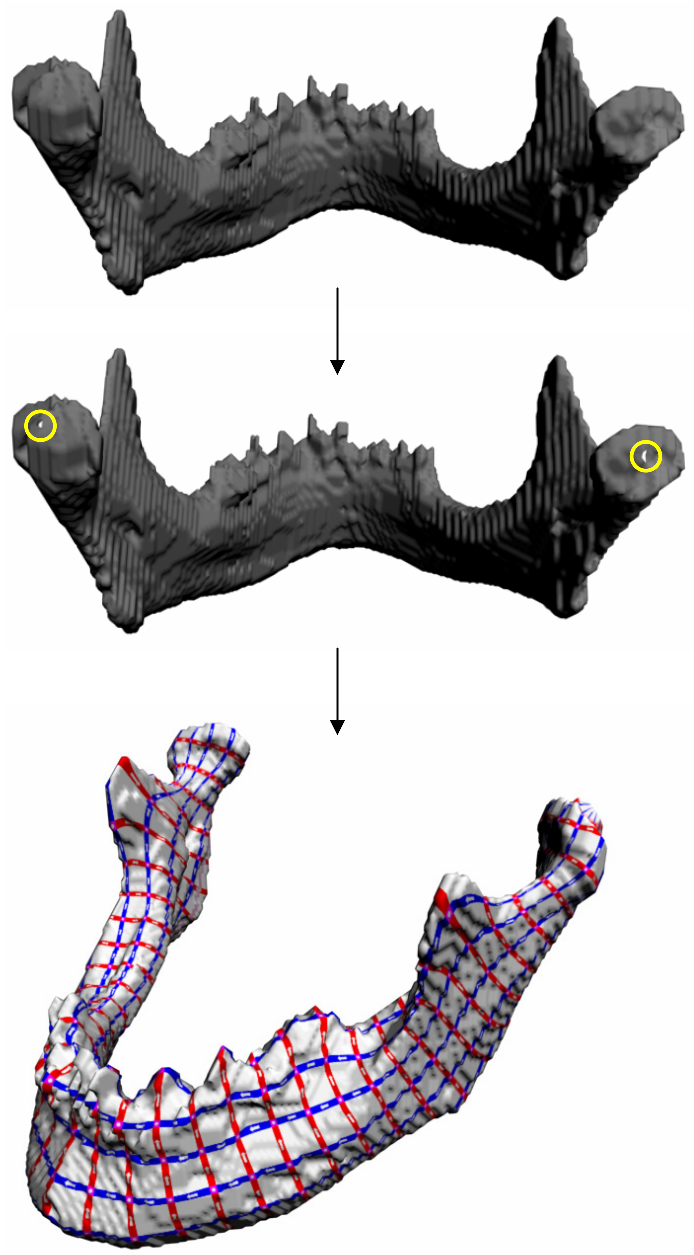

Figure 1.3: A human mandible is shown. This is an elongated surface of spherical topology. The topology can be converted to that of a cylinder by punching two small holes (encircled in yellow) through the surface. In this way, the methodology presented in this manuscript can be applied.

ulation of clavicles. The obtained correspondence is then employed to explore the shape of the population and to derive a set of clavicular fracture fixation plates. An overview of these applications can be found in Section 1.2.3.

1.2.1 Cylindrical Parameterization

Parameterization of a surface is the task of defining a map between the surface and some simple parameter domain. The obtained map should be one-to-one, continuous, and it should have a continuous inverse. Therefore, the parameter domain should have the same topology as the surface. Many surfaces have a spherical or disc-like topology. Therefore, most parameterization techniques are designed for surfaces of spherical or disc-like topology. A surface that has a more complex topology can always be modified by cutting it into one or more surfaces of disc-like topology. Topological modification, however, introduces prior constraints that may affect the quality of the parameterization.

A surface parameterization can be obtained by embedding the triangle mesh of the surface into the parameter domain. In that way, a direct map is obtained between vertices of the original surface and vertices of the embedded surface. This map is then extended to the triangles by interpolation. Of the infinitely many embeddings that are possible for a given surface, usually the one that minimizes a certain measure of distortion is chosen: each triangle of the surface has a corresponding triangle in the embedding and the triangle in the embedding generally has a different shape and area. The introduced distortion can be measured for each triangle and integrated over the whole surface by summation in order to quantify the total distortion that a parameterization exhibits.

In this manuscript, two methods are proposed to parameterize a surface of cylindrical topology onto the cylinder and this without topological modifications. In addition, these methods also determine the optimal length of the cylinder onto which the surface is parameterized. Both methods produce a parameterization by embedding the triangle surface into the cylindrical domain. See Figure 1.5 for the visualization of a section of a human colon and its embedding into the cylindrical domain. The proposed methods differ in the distortion measure they optimize: one method minimizes deformation in angles while the other balances angle and area deformations.

The method that minimizes angle deformations produces maps in which the angles are preserved as much as possible. Exact preservation is generally not possible for discrete surfaces. The obtained maps are called quasi-conformal maps or discrete conformal maps and in this manuscript they will be referred to as conformal maps. The method proposed in this manuscript obtains such a conformal map by defining two harmonic functions on the surface (i.e., minimizers of the Dirichlet integral) and by explicitly enforcing the conformality property at the boundaries of the domain. As will be seen, this can done by solving a single linear system. This method is, therefore, very efficient.

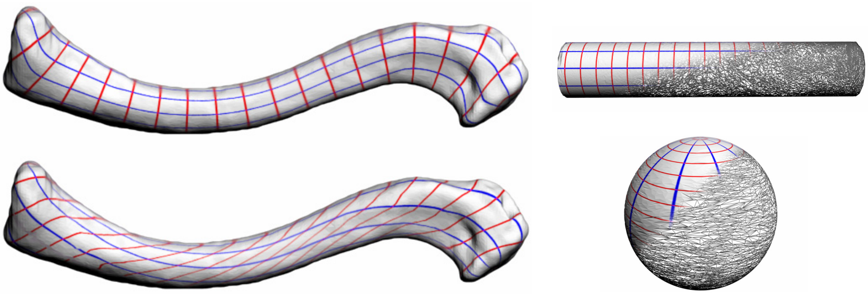

Figure 1.4: A comparison of the spherical parameterization of a clavicle (bottom) with the cylindrical parameterization of the topologically modified clavicle (top). The cylindrical parameterization exhibits less distortion and provides an intuitive axial-angular structure for the clavicle.

For cylindrical surfaces that exhibit large variations in cross-sectional diameter, the linear method has the disadvantage that large distortions in area may occur. For such surfaces, it is advised to use the second parameterization method proposed in this manuscript. The second method produces parameterizations with balanced angle and area distortions. The optimization problem, however, becomes nonlinear with such a distortion measure. In order to efficiently and robustly optimize the nonlinear distortion measure, a hierarchical approach is taken that utilizes the progressive mesh of the surface. The method starts by parameterizing the base mesh of the progressive mesh which has a simple form and, therefore, can be parameterized easily. The next levels in the progressive mesh are parameterized by inserting the removed vertices one at a time and optimizing their positions. When all vertices are inserted, the parameterization of the original surface is obtained. This nonlinear method generates parameterizations with low angle and area distortions, even for surfaces with large variation in diameter, but this comes at the cost of an increased computation time.

The parameterization methods proposed in this manuscript are the basic building blocks for the construction of a correspondence for surfaces of cylindrical topology. However, there are also many direct applications such as surface approximation and surface unfolding. See Figure 1.5 for an unfolding and an approximation of the parameterized colon section.

Note that the cylindrical parameterization methods can also be applied to spherical surfaces after topological modification. Although this constrains the parameterization at two points, it turns out to be useful for elongated surfaces with clearly identifiable endpoints such as the human clavicle. See Figure 1.4 for a comparison between spherical and cylindrical parameterization for a clavicle.

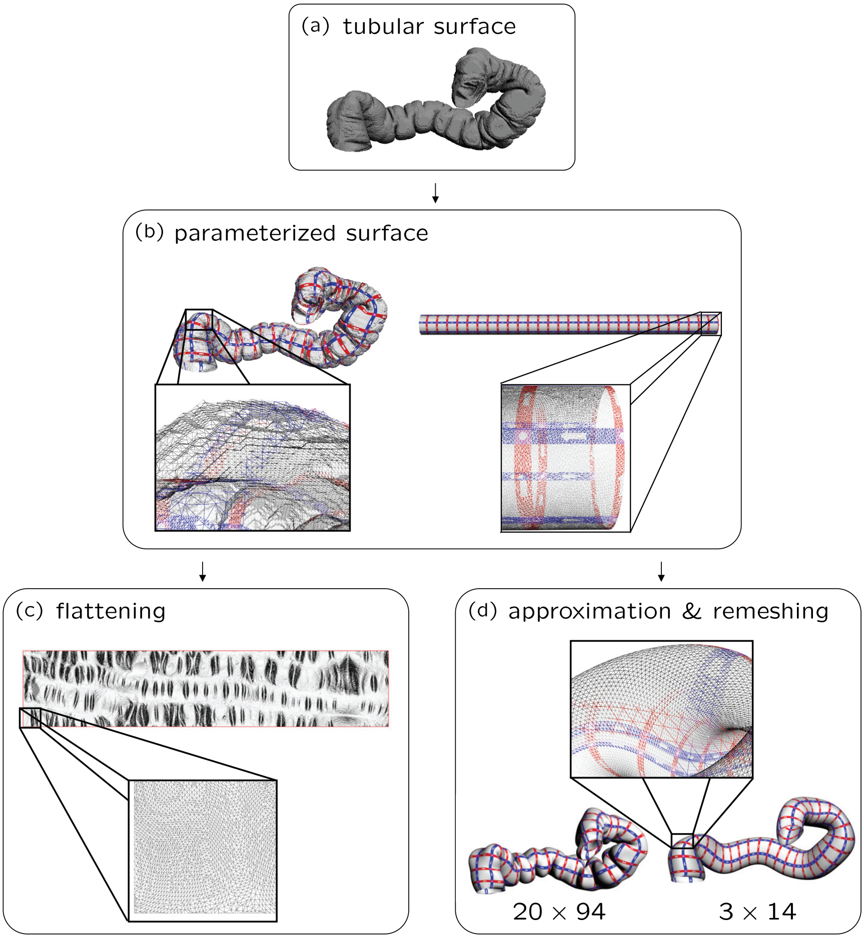

Figure 1.5: An overview of the parameterization of a tubular surface and some of its applications. (a) A section of a colon serves as an example tubular surface. (b) The parameterized colon section. The parameterization is represented by the deformation of the colon section into the cylinder. (c) Unfolding the parameterized colon onto a planar rectangle. By using appropriate lighting, a virtual dissection view is obtained which can be used for virtual inspection of the colon. (d) The parameterization can also be used for remeshing and surface approximation. An approximation using B-splines is shown for a control point grid size of 20×94 and 3×14. The magnification shows the regular structure of the remesh.

1.2.2 Correspondence for Tubular Surfaces

This manuscript proposes a method to construct a correspondence for a population of surfaces of cylindrical topology. The method can also be applied to a population of elongated spherical surfaces after topological modification. A population correspondence should provide a mapping between equivalent points on the surfaces of the population and it should also provide a spatial alignment of the surfaces. In this manuscript, the correspondence is represented by a set of cylindrical parameterizations: one parameterization for each surface in the population. The mapping between the surfaces in the population is then obtained from the parameterizations by function composition.

Any set of cylindrical parameterizations provides a population correspondence. However, the quality of the correspondence is determined by how well it matches equivalent points. In this manuscript, the approach of Davies et al. [2002b] will be followed when measuring the quality of a correspondence. Thereby, the quality is determined by the complexity of the derived point distribution model: a correspondence that gives rise to a simpler model, that is a model with less variance or less modes, is considered to be of better quality. The quality measure can then be used in an optimization process to improve the correspondence.

The method of this manuscript constructs a correspondence in a number of steps. First, all surfaces are parameterized with one of the cylindrical parameterization methods proposed in this manuscript. Then, the parameterization domains are scaled to the average length. This is followed by an optimization procedure that finds the optimal alignment of the surfaces in the spatial and parameterization domain with respect to the correspondence quality measure. As a result, an initial correspondence is obtained. The final correspondence is obtained after a second optimization process that improves the correspondence by applying non-rigid deformations to the parameterizations. The obtained correspondence and the derived point distribution model have many applications such as shape guided image segmentation, statistical shape analysis, and fracture fixation plate design. See Figure 1.6 for an overview of the correspondence construction and some of its applications.

1.2.3 Applications

The parameterization techniques and the correspondence technique proposed in this manuscript have a wide range of possible applications. See Figures 1.5 and 1.6 for a few examples.

The cylindrical parameterization methods proposed in this manuscript will be employed for virtual inspection of the human colon. Note that the presented approach can be used for inspection of any organ of cylindrical topology. Fly-through navigation is an established technique to inspect tubular organs. For organs with a convoluted shape, however, such an approach often fails in pro-

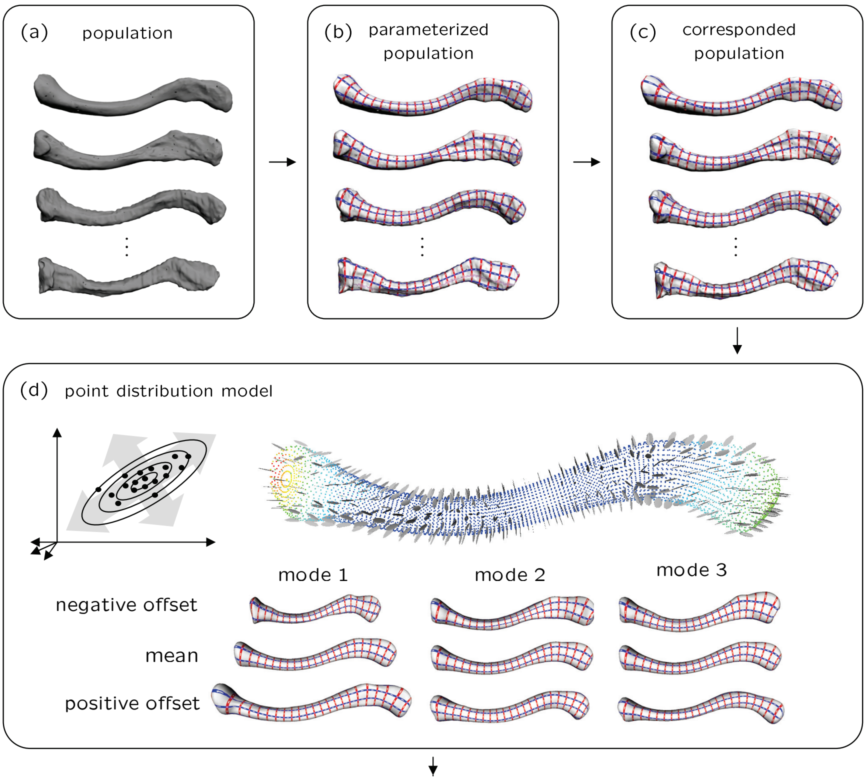

Figure 1.6: The construction of a correspondence, the derived point distribution model, and some of its possible applications. (a) A population of human clavicles. (b) Each of the clavicles is equipped with a cylindrical parameterization. (c) Starting from the parameterized clavicles, an optimization procedure established a correspondence for the population. (d) From the obtained correspondence a point distribution model (PDM) is derived comprising a mean shape and a set of modes of variation. The following applications make use of the obtained PDM: (e) generation of fracture fixation plate shapes, (f) comparison of the shape of subpopulations through statistical testing, and (g) image segmentation guided by the obtained model of shape.

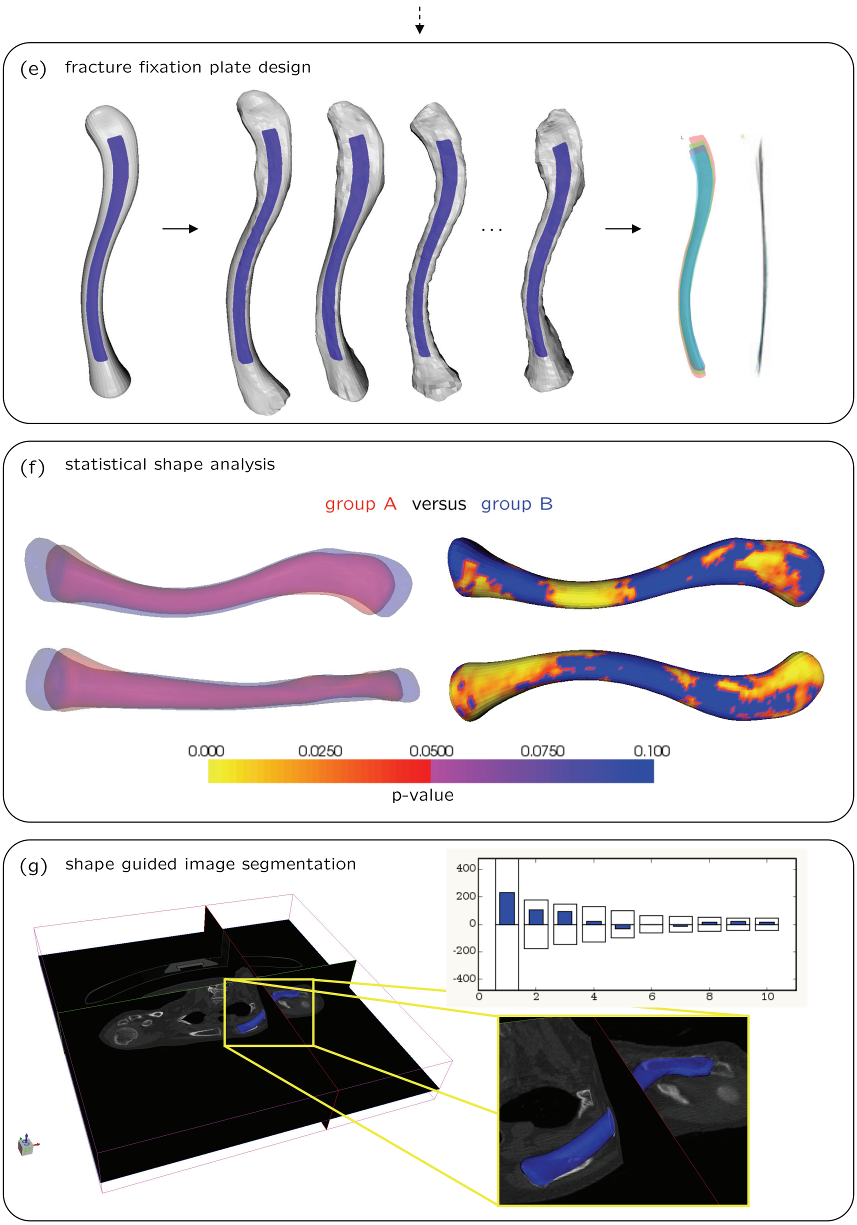

Figure 1.6: Continued.

viding full inspection coverage of the organ surface. In this manuscript, a well known approach is followed in which the virtual inspection is facilitated by unfolding the organ surface onto the plane and, thereby, generating a virtual dissection view of the organ. In the process of unfolding, care must be taken not to miss or repeat parts of the surface. Here, a parameterization approach is followed which guarantees full coverage of the organ surface. The unfolding is achieved by cylindrical parameterization of the organ surface, followed by cutting and unfolding of the cylindrical embedding into a planar rectangle. In the unfolding process, however, all shape information of the organ surface is lost. This information is reintroduced by equipping the obtained planar representation with appropriate normals. In this way, a planar representation of the organ surface is obtained in which the lighting reveals the original shape of the organ surface. Furthermore, a comparison between the two parameterization methods will be provided. It is shown that the conformal parameterization method tends to scale down large protrusions of the organ surface. As a result, protrusions might be missed during the inspection. The parameterization method that balances angle and area distortions, on the other hand, does not suffer from such severe downscaling.

In Chapter 5, the correspondence method proposed in this manuscript is used to establish a correspondence for a large population of human clavicles. The obtained correspondence is then employed to investigate shape differences between different subgroups of the populations. Clavicles of males are compared with those of females, old clavicles are compared with more recent ones, and the asymmetry between left and right clavicles is analysed. The shape comparison is done in a local sense: at each point of the surface, a statistical test is performed that decides whether or not the average position of that surface point is different for the subgroups. In that way, differences in shape can be located on the clavicle surface.

The correspondence of the clavicle population is also used to design a set of clavicle fracture fixation plates. The correspondence is used to construct an average clavicle. On this average, the desired plate shape is indicated by an orthopedic expert. The obtained region is then mapped, by the correspondence, to all the clavicles in the population. In this way, each individual clavicle is equipped with its own plate shape. A clustering technique is then applied to these plate shapes in order to extract a small number of plate shapes that provide a tight fit to the population. Several plating approaches are compared by this approach. It should be noted that the developed techniques can also be used for the development of other osteosynthesis hardware and that it is not restricted to the clavicle.

1.3 Related Work

This manuscript covers several subjects: surface parameterization, surface correspondence construction, virtual organ inspection, statistical shape modeling, etc. A considerable amount of research has been done in each of these areas. In the following sections, an overview is given of the most important related work.

1.3.1 Related Work on Parameterization

For excellent and extensive reviews of parameterization methods and their applications, the interested reader is referred to Floater and Hormann [2002], Floater et al. [2005], Sheffer et al. [2006].

Different parameterization domains are possible, such as a sphere, a rectangular disc, a cylinder or a torus. The choice of the domain is dictated by the surface that is parameterized: the parameterization domain and the surface should be topologically equivalent. Many results are available for parameterization of surfaces of disc-like [Floater, 1997, Levy et al., 2002, Sander et al., 2001] or spherical topology [Brechbühler et al., 1995, Hurdal et al., 1999, Praun and Hoppe, 2003, Gotsman et al., 2003, Gu et al., 2004]. Surfaces of other topologies are usually handled by dividing the surface in charts of disc-like topology and subsequently parameterizing these charts to the plane [Eck et al., 1995, Sander et al., 2001, Levy et al., 2002, Lamecker et al., 2002, Grimm, 2004, Lamecker et al., 2004]. A notable exception is the work of Jin et al. [2008] in which Ricci flow is used to construct a seamless periodic tiling of a genus-n surface in the plane, sphere, or hyperbolic space and it is known as the universal covering space. The obtained map is angle preserving and can be used to construct harmonic maps between surfaces of the same topology [Li et al., 2008].

A comparison between cylindrical and spherical parameterization for elongated surfaces is provided in [Huysmans et al., 2006]. There has been little research in parameterization of surfaces of cylindrical topology. Haker et al. [2000a] obtain a parameterization by solving two boundary value problems. Zöckler et al. [2000] map a dissected version of the surface to the planar rectangle and then iteratively relaxes the parameterization on the cylinder. Antiga and Steinman [2004] combine harmonic parameterization with a heuristic method for the parameterization of star shaped tubular surfaces. Grimm [2004] also uses surface chartification combined with subsequent relaxation on the cylinder. Hong et al. [2006] provide a conformal cylindrical using holomorphic one-forms. In comparison with these methods, the cylindrical parameterization methods of this manuscript have the following advantages: (1) the nonlinear method allows direct optimization of a balanced distortion measure, (2) both methods take the periodicity of the domain directly into account and also provide the optimal length of the parameterization domain, and (3) the linear parameterization method requires only a single linear system to be solved and allows seamless integration of extra constraints.

Linear parameterization methods, such as proposed by Eck et al. [1995], Haker et al. [2000b], Pinkall and Polthier [1993], Desbrun et al. [2002], Levy et al. [2002], Gu and Yau [2003], are popular since they are very fast. Usually, the parameterization is obtained by solving the Laplace equation on the surface for both parameter coordinates while enforcing certain boundary constraints. Several discretisations of the Laplace operator are possible [Pinkall and Polthier, 1993, Floater, 2003]. Often, the boundary mapping of the parameterization is defined beforehand but free boundary parameterizations are also possible [Levy et al., 2002, Desbrun et al., 2002, Kami et al., 2005]. The length optimization of the linear method proposed in this manuscript is closely related to the free boundary problem. A notable difference of cylindrical parameterization with the above-mentioned linear planar parameterization techniques, is the periodicity of the angular parameter. As first noted by Brechbühler et al. [1995] in their work on spherical parameterization, the periodic part of a parameter can be factored out of the linear system. This technique was later used for toric parameterization [Steiner and Fischer, 2004] and to globally align the parameterizations of different charts on a surface [Tong et al., 2006]. The linear method of this work also adopts this approach for the angular parameter.

Many parameterization methods directly minimize some measure of deformation in order to keep the metric distortion under control [Degener et al., 2003, Hormann and Greiner, 2000, Sander et al., 2001, Sheffer and de Sturler, 2001, Sorkine et al., 2002, Zhang et al., 2005, Yoshizawa et al., 2004]. The resulting optimization problem is usually nonlinear. Therefore, considerable effort has been dedicated to the development efficient hierarchical solution methods, e.g, Hormann et al. [1999], Praun and Hoppe [2003]. The nonlinear parameterization technique of this manuscript is closely related to the method of Praun and Hoppe [2003] since a progressive mesh is used to construct a hierarchy and the parameterization distortion is measured using the stretch measure.

1.3.2 Related Work on Correspondence Construction

For 2D shapes, a correspondence between the boundary curves of the individual shapes is often defined by manual landmarking [Bookstein, 1991]. Although this approach is feasible, it turns out to be a time consuming and error prone task. In principle, the approach can be extended to 3D but it becomes highly impractical due to the large amount of landmarks that need to be located and the increased level of difficulty in pin-pointing them.

A relatively simple but effective approach is to establish the correspondence by means of surface parameterization [Eck et al., 1995, Brechbühler et al., 1995, Zöckler et al., 2000, Lamecker et al., 2002, 2004, Huysmans et al., 2006]. A one-to-one map is constructed between each surface of the set and some common parameter domain. The surface-to-surface correspondence is defined by the assigned parameter values i.e., points between the surfaces correspond when they share the same parameters.

Although the parameterization approach produces valid correspondences, there is still room for improvement. The parameterization of each shape in the training set is done independently of the other shapes, thus correlations between the shapes are not taken into account. An approach taking this extra information into account can lead to better correspondences. Kotcheff and Taylor [1998] used the determinant of the landmark covariance matrix as an optimization objective. Based on their ideas, Davies et al. [2002b] developed a minimum description length (MDL) formulation for the assessment of correspondence quality for 2D curves, which was later simplified by Thodberg [2003]. The method for building MDL correspondences has been extended to surfaces of spherical topology [Davies et al., 2002a], which was later improved in Heimann et al. [2005] in terms of computational efficiency. Horkeaw and Yang applied the MDL principle to surfaces of disc-like topology [Horkaew and Yang, 2004] and an extension to more complex topologies was obtained by cutting surfaces into topological discs prior to optimization [Horkaew and Yang, 2003a]. This of course constrains the optimization along the cuts. In the recent work of Li et al. [2008], a globally optimal map, in terms of harmonic energy, is obtained between two surfaces sharing arbitrary complex topology. An extension of their method to populations of surfaces and to other correspondence metrics, e.g. MDL, is, however, not addressed. Recently introduced point-based correspondence techniques can also handle arbitrary topology. In Ferrarini et al. [2007], self organising maps were used to obtain a pairwise correspondence between each population member and a template. In Cates et al. [2007], particle systems were used to optimize geometry sampling and groupwise correspondence with respect to an information theoretic measure comparable to MDL. Point-based correspondence techniques are promising but problems occurring with highly convoluted surfaces still need to be addressed.

Specifically for shape modeling of cylindrical surfaces, little work has been done. In de Bruijne et al. [2003], an improved modeling scheme for tubular objects was proposed. They used a manually determined correspondence. Some of the previously discussed techniques could be employed to build a correspondence for a set of cylindrical shapes. For example, the spherical MDL framework can be applied when the holes of the cylindrical shapes are closed but this can result in an invalid correspondence at the boundaries and this approach will not perform well for elongated surfaces [Huysmans et al., 2006]. The correspondence methods that rely on chartification [Horkaew and Yang, 2003a, Lamecker et al., 2002] could also be applied to cylindrical surfaces but obviously the performance of the chartification heuristic will influence the final quality. The method proposed in this manuscript does not suffer from these drawbacks since, here, the description length minimization method is designed specifically to treat sets of surfaces of cylindrical topology.

1.3.3 Related Applications

Parameterization has a wide range of applications. It is used in computer graphics for detail mapping [Levy et al., 2002, Sander et al., 2001], remeshing and level of detail construction [Eck et al., 1995, Praun and Hoppe, 2003, Alliez et al., 2002, 2007], rendering acceleration [Gu et al., 2002], and also morphing and detail transfer between surfaces [Alexa, 2002, Zöckler et al., 2000]. A parameterization is also very useful for describing surfaces using basis functions which has applications in surface fitting [Brechbühler et al., 1995, Floater, 1997, He et al., 2005], description, and compression [Sijbers and Van Dyck, 2002]. In medical imaging, parameterizations are useful for easing the visualization of complex structures [Haker et al., 2000b, Gu et al., 2004, Wang et al., 2007]. Applications of specific interest for cylindrical parameterization are mapping [Antiga and Steinman, 2004, Zhu et al., 2005] and centerline calculation [Zhu et al., 2005] of possibly bifurcating blood vessels. Cylindrical parameterization can also be used for virtual flattening of the colon in virtual colonoscopy [Haker et al., 2000a, Hong et al., 2006, Mai et al., 2007, Wang et al., 2008]. Alternatives to parameterization based flattening have been proposed [Wang et al., 1998, Bartrolí et al., 2001, Balogh et al., 2002, Shin et al., 2009]. However, these approaches can introduce large shape distortions.

Shape correspondences and the derived statistical shape models have a wide range of applications in medical image computing [Cootes et al., 1995, Dryden and Mardia, 1998]. They have been used to analyze shape differences between different classes of objects [Wang et al., 2007, Ferrarini et al., 2008], for example, the lateral ventricles of schizophrenics versus a healthy group. They have also been employed to gain more knowledge about the anatomical variability of certain organs or bones as for example the human ear canal [Paulsen et al., 2002]. Such knowledge can in turn be used to reconstruct malformed, missing, or fractured bone structures [Zachow et al., 2005]. A widespread application of statistical shape models is their use as prior knowledge in automatic image segmentation [Cootes et al., 1994, Kelemen et al., 1999, de Bruijne et al., 2004, Lamecker et al., 2004, Kainmüller et al., 2007]. The probability density function of the shape is estimated from a set of manual segmentations. This knowledge is then used to guide the segmentation process of an unseen instance and to restrict the segmentation result to the class of plausible shapes. Applications of specific interest for cylindrical parameterization are segmentation and analysis of tubular structures, e.g. automatic shape guided segmentation of human trachea [Pinho et al., 2007] and non-invasive stent shape prediction for surgical intervention in tracheal stenosis [Pinho et al., 2008].

1.4 Contributions

The main contributions of this manuscript can be summarized as follows:

- A new parameterization method is introduced that produces a one-to-one map from a given tubular surface to a cylinder. The mapping problem is formulated as a nonlinear optimization problem and an objective is used that balances angle and area distortions. As a result, maps are obtained that exhibit low distortions in both angles and areas, even when the mapping requires large deformations. In contrast to previous methods, no unwanted distortions are introduced by prior surface cutting because the periodicity of the cylindrical domain is taken directly into account. Furthermore, the parameterization method automatically finds the length of the cylindrical parameterization domain that results in the least mapping distortion.

- A new method to construct an angle preserving one-to-one map from a given tubular surface to a cylinder is introduced. As with the nonlinear parameterization method, the optimal length of the cylindrical domain is automatically obtained. In contrast with previous angle preserving techniques, this new method has a simple formulation, leading to a single linear system, and it allows additional constraints to be incorporated directly.

- A new method is introduced that is specifically designed to establish correspondences for populations of tubular surfaces. The method uses the cylindrical parameterizations of the tubular surfaces as an initial correspondence and gradually improves the correspondence by a sequence of optimizations. In contrast with previous methods, no constraining surface chartifications are required. The method uses the celebrated correspondence quality measure introduced by Davies et al. [2002b]. Furthermore, the optimization of the correspondence with respect to this quality measure uses gradient information and is carried out in a multi-scale fashion, resulting in a robust and efficient technique.

- It is demonstrated that the cylindrical parameterization methods introduced in this manuscript can be used to generate dissection views for virtual inspection of tubular organs. In contrast with angle preserving methods, the nonlinear method generates dissection views with balanced area and angle distortions and, as a result, it ensures full coverage of the organ.

- It is shown that the correspondence methodology introduced in this manuscript can also be applied to populations of elongated spherical surfaces with minimal effort from the user. For spherical surfaces that exhibit an axial structure, the proposed methodology provides an intuitive correspondence. Detailed results are shown for a population of human clavicles.

- An automated fracture fixation plate precontouring technique is presented. The technique generates a set of plate shapes from a population of elongated bones. The obtained shapes can be used to model fracture fixation plates that will provide a good fit to the given population of bones.

1.5 Manuscript Organisation

The remainder of this manuscript is organized as follows:

Part II details the methods for the construction of parameterizations and correspondences for tubular surfaces:

Chapter 2 explains the concept of cylindrical parameterization and presents two methods, one linear and one nonlinear, to obtain such a parameterization for a tubular surface. A comparison of the two methods is also provided in that chapter.

Chapter 3 details the concept of cylindrical correspondence and introduces a methodology to obtain such a correspondence for a population of tubular surfaces using a multi-resolution approach. For six surface populations, a number of experiments are conducted in order to demonstrate the quality of the correspondence obtained with the proposed method.

Part III presents the results of applying the methods of Part II in specific applications:

Chapter 4 describes how the cylindrical parameterization methods of this work can be utilized in the virtual inspection of tubular organs. Both the linear and the nonlinear methods are used to generate a flattened representation of a human colon data set. A comparison of the obtained results is made.

Chapter 5 demonstrates how the correspondence methodology of this work can be used to obtain a correspondence for a population of human clavicles. The obtained correspondence is used to investigate the shape of the clavicles in the population. It is also shown how the shape of the clavicle in different subgroups of the population can be compared by means of statistical testing. Finally, a technique is provided to extract a set of plate shapes that can be used in the design of fixation plates for midclavicular fractures.

Part IV concludes this manuscript:

Chapter 6 provides a summary of the work, draws conclusions, and presents ideas for future improvements and possible extensions.

Note that the main body of this manuscript, Parts II and III, is the result of the composition of four articles. One of these articles has been accepted for publication, two other articles are under review and one article was used in a patent application.

Part II

Parameterization and Correspondence for Tubular Surfaces

CHAPTER 2

MAPPING TUBULAR SURFACES TO THE CYLINDER

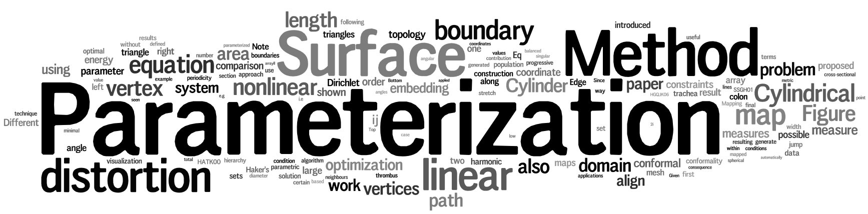

The work in this chapter has been submitted to Elsevier Medical Image Analysis as:

Toon Huysmans and Jan Sijbers, "Mapping Tubular Surfaces to the Cylinder", 2009.

It has also been included in the following patent application:

T. Huysmans and J. Sijbers, "Method for Mapping Tubular Surfaces to a Cylinder", European patent application number EP09162289.4, submitted June 9, 2009.

Abstract

Surface parameterization is a widely used technique with numerous applications. A parameterization defines a one-to-one map between the surface and some mathematically simple parameter domain. Most research has focused on planar and spherical parameterization because many real world surfaces are either of disc-like or spherical topology. A class of surfaces that is much less covered but also commonly encountered are surfaces of cylindrical topology. This work is concerned with cylindrical parameterization of such of surfaces.

Cylindrical parameterization constructs a map from a surface of cylindrical topology to the cylinder. The few methods that already exist to construct such maps, usually alter the topology of the surface prior to parameterization and often fail in keeping distortions within acceptable bounds. This work provides two complementary methods that do not rely on such prior cutting: a fast, linear method for surfaces with small cross-sectional diameter variance and a computationally more complex, nonlinear method that can be used for arbitrarily complex surfaces. Moreover, in contrast to previously proposed methods, both methods presented here automatically determine the optimal length of the cylindrical parameter domain. The performance of the presented methods, in terms of execution time and various distortion measures, is demonstrated for a large number of data sets of varying complexity.

2.1 Introduction

Parameterization of a surface is the task of defining a map between the surface and a specific parameter domain. Such a map equips each point of the surface with a coordinate in the space of the parameter domain. In this work, surfaces are represented with a triangle mesh. In such a case, the map is usually only defined explicitly for the vertices. Barycentric interpolation extends these coordinates to the rest of the surface, i.e. the triangles. Intuitively, a parameterization can be seen as the result of a continuous deformation of the surface into the parameter domain. As one can imagine, infinitely many such maps are possible for a certain surface. A useful parameterization should, however, have several properties: it should be a continuous one-to-one map and it should keep the introduced deformation to a minimum. The deformation, or metric distortion, can be measured in terms of local changes in area and angles. For the applications targeted in this work, a balanced trade-off between angle and area distortions is pursued. Parameterizations with minimal stretch distortion [Sander et al., 2001] are considered optimal.

With all its applications, it is clear that surface parameterization is a very useful technique. It is used in computer graphics for detail mapping [Levy et al., 2002, Sander et al., 2001], remeshing and level of detail construction [Eck et al., 1995, Praun and Hoppe, 2003, Alliez et al., 2002, 2007], rendering acceleration [Gu et al., 2002], and also morphing and detail transfer between surfaces [Alexa, 2002, Zöckler et al., 2000]. A parameterization is also very useful for describing surfaces using basis functions which has applications in surface fitting [Brechbühler et al., 1995, Floater, 1997, He et al., 2005], description, and compression

[Sijbers and Van Dyck, 2002]. In medical imaging, parameterization is useful for easing the visualization of complex structures [Haker et al., 2000b, Gu et al., 2004, Wang et al., 2007] and it also allows the construction of a surface correspondence which makes statistical shape analyses [Styner, 2001, Wang et al., 2007, Huysmans et al., 2009] and model based image segmentation [Kelemen et al., 1999, Lamecker et al., 2004, Kainmüller et al., 2007] possible. Applications of specific interest for cylindrical parameterization are segmentation and analysis of tubular structures, e.g. automatic shape guided segmentation of human trachea [Pinho et al., 2007] and non-invasive stent shape prediction for surgical intervention in tracheal stenosis [Pinho et al., 2008]. It has also been employed for mapping [Antiga and Steinman, 2004, Zhu et al., 2005], segmentation [Bruijne et al., 2003] and centerline calculation [Zhu et al., 2005] of possibly bifurcating blood vessels. Furthermore, cylindrical parameterization can be used for virtual flattening of the colon in virtual colonoscopy [Haker et al., 2000a, Bartrolí et al., 2001, Hong et al., 2006, Mai et al., 2007] and prone-supine scan colon registration is also envisioned.

Different parameterization domains are possible, such as a sphere, a rectangular disc, a cylinder or a torus. The choice of the domain is imposed by the topology of the surface that needs parameterization. Since the parameterization should be a continuous map, the parameterization domain and the surface should be topologically equivalent. Many results are available for parameterization of surfaces of disc-like [Floater, 1997, Levy et al., 2002, Sander et al., 2001] or spherical topology [Brechbühler et al., 1995, Praun and Hoppe, 2003, Gotsman et al., 2003, Gu et al., 2004]. Surfaces of other topologies are handled by dividing the surface in charts of disc-like topology and subsequently parameterizing these charts to the plane [Eck et al., 1995, Sander et al., 2001, Levy et al., 2002, Lamecker et al., 2002, Grimm, 2004, Lamecker et al., 2004].

There has been little research in parameterization of surfaces of cylindrical topology [Haker et al., 2000a, Zöckler et al., 2000, Antiga and Steinman, 2004, Grimm, 2004, Hong et al., 2006], although surfaces of this kind are commonly encountered in the real world: blood vessels, the trachea, the colon, cochlear canals, etc. Cylindrical parameterization can even be used for certain elongated spherical surfaces after topological modification [Huysmans et al., 2006].

The methods found in the literature often fail in keeping the introduced area or angle distortion within acceptable bounds. Some rely on a two step procedure involving cutting of the surface which may result in increased distortions along the cut [Haker et al., 2000a, Grimm, 2004]. In this work, two complementary methods are introduced. One method, is based on nonlinear optimization and succeeds in generating parameterizations with low angle and area distortions, even for very deformed surfaces. It constructs the parameterization in a hierarchical way to make it efficient and robust. For less convoluted surfaces, the use of the other method provided in this chapter is advised. It is a very fast method since it is based on the solution of a linear system and it provides parameterizations with minimal angle distortions and low area distortions for these surfaces. In order to generate a parameterization with the least possible distortion, both proposed methods also automatically choose the optimal length, in terms of their distortion measure, of the cylindrical parameterization domain.

2.1.1 Contributions

The main contributions of this work are as follows.

(a) In section 2.5, a nonlinear parameterization approach for surfaces of cylindrical topology is introduced. To our knowledge, this is the only cylindrical parameterization method to date that allows direct optimization of a balanced distortion measure, e.g. stretch [Sander et al., 2001]. Nonlinear parameterization methods, in comparison with linear methods [Haker et al., 2000a, Zöckler et al., 2000, Hong et al., 2006], are computationally more complex but they produce maps with much more balanced angle and area distortion, especially for surfaces that require large deformations in order to be parameterized.

(b) The cylindrical parameterization methods introduced in sections 2.4 and 2.5 take the periodicity of the angular parameter of the cylindrical domain directly into account. In most previous methods, this periodicity was removed by cutting the surface open prior to parameterization [Haker et al., 2000a, Zöckler et al., 2000, Grimm, 2004]. This, however, over-constrains the parameterization and may introduce unwanted distortions. Since the methods in this chapter do not use such a cutting strategy, these distortions are certainly avoided.

(c) Most previously reported cylindrical parameterization methods do not give an estimate of the optimal length of the parameterization cylinder [Zöckler et al., 2000, Grimm, 2004]. As a consequence, for elongated surfaces the resulting parameterizations are highly distorted. Both methods introduced in this chapter automatically determine the optimal length of the parameterization cylinder with respect to their distortion measure as part of the optimization. The resulting parameterization will therefore be of minimal distortion over all possible lengths of the cylinder.

(d) The formulation of conformal cylindrical parameterization, introduced in Section 2.4, as a constrained optimization problem allows seamless integration of extra constraints. This allows direct construction of parameterizations with consistent landmark mapping which is useful in surface correspondence construction. This is not possible with previous parameterization methods for the cylinder.

2.2 Related Work

For excellent and extensive reviews of parameterization methods and their applications, the interested reader is referred to [Floater and Hormann, 2002, Floater et al., 2005, Sheffer et al., 2006].

Many parameterization methods directly minimize some measure of deformation in order to keep the metric distortion under control [Degener et al., 2003, Hormann and Greiner, 2000, Sander et al., 2001, Sheffer and de Sturler, 2001, Sorkine et al., 2002, Zhang et al., 2005, Yoshizawa et al., 2004]. The optimization problem associated with these parameterization methods is usually a highly nonlinear one. Therefore, considerable effort has been dedicated to the development of the non-linear solution methods. A particularly simple but efficient approach is the hierarchical solution method proposed by Hormann et al. [1999] which was extended to the spherical domain in Praun and Hoppe [2003]. The nonlinear parameterization technique of this chapter is closely related to the spherical parameterization method of Praun and Hoppe [2003] since we also use a progressive mesh to construct a hierarchy. For the measure of distortion, the nonlinear method of this work uses a symmetric version of the stretch measure of Sander et al. [2001].

Linear parameterization methods, such as proposed by Eck et al. [1995], Haker et al. [2000b], Pinkall and Polthier [1993], Desbrun et al. [2002], Levy et al. [2002], Gu and Yau [2003], are popular since they are very fast and generate parameterizations with low distortion in case the surfaces are well-behaved. Usually, the parameterization is obtained by solving the Laplace equation on the surface for both parameter coordinates while enforcing certain boundary constraints. Depending on the actual discretisation of the Laplace operator, different realisations of the system matrix are possible. Among the most celebrated are cotangent weighting [Pinkall and Polthier, 1993], resulting in a harmonic map, and mean value weighting [Floater, 2003]. Often, the boundary mapping of the parameterization is defined beforehand which thus results in a boundary value problem. Free boundary parameterizations, where the boundary of the parameterization is allowed to move freely together with the interior, are achieved using natural boundary conditions, see for example Levy et al. [2002], Desbrun et al. [2002] and Kami et al. [2005]. The length optimization of the linear method proposed in this chapter is closely related to the free boundary problem. A notable difference of cylindrical parameterization with the abovementioned linear planar parameterization techniques, is the periodicity of the angular parameter.

As first noted by Brechbühler et al. [1995] in their work on spherical parameterization, the periodic part of a parameter can be factored out of the linear system. This technique was later used for toric parameterization [Steiner and Fischer, 2004] and to globally align the parameterizations of different charts on a surface [Tong et al., 2006]. The linear method of this work also adopts this approach for the angular parameter.

For cylindrical parameterization, a number of approaches have been proposed in the past:

- Haker et al. [2000a] solve two boundary value problems in order to obtain a conformal parameterization of the surface. First, the axial parameterization is obtained. Then, the surface is dissected into a topological disc and a conjugate angular parameterization is derived. The linear method proposed in this chapter is closely related to Haker et al. [2000a], but the parameterization is obtained in a single step by taking into account the periodicity of the angular parameter using the method of Steiner and Fischer [2004]. Also, and in contrast to the linear method of this chapter, the way in which the surface is dissected in Haker's method influences the quality of the final parameterization.

- Another two stage approach is proposed in Zöckler et al. [2000]: first, the surface is cut and mapped to a square. Then, the square is stitched into a cylinder and the parameterization is iteratively relaxed. This method suffers from the same drawbacks as Haker et al. [2000a] and the iterative relaxation is slower than solving a linear system.

- The method of Antiga and Steinman [2004] maps segments of blood vessels to the cylinder by first mapping the axial coordinate using a harmonic function, similar to Haker et al. [2000a], and then mapping the angular coordinate using a heuristic method. Although this approach provides nice results for vessels, it can only be applied to surfaces of cylindrical topology with star shaped cross sections.

- Grimm [2004] proposes a method to map surfaces to certain manifolds. For the cylinder manifold, the surface is first divided into a number of charts, which are then parameterized separately and stitched together. The parameterization is then relaxed along the chart boundaries to remove the high distortion. Unfortunately, this relaxation is only local and, therefore, the resulting parameterization can be suboptimal with respect to the distortion measure.

- In Hong et al. [2006], a parameterization of the colon is obtained using holomorphic one-forms on a dual covering of the colon surface. They obtain similar results as our linear method but at the expense of duplicating surface geometry for the double covering. Furthermore, positional landmark constraints can only be satisfied using a second optimization, as opposed to our method, where they can be directly incorporated.

2.3 Cylindrical Parameterization

A surface has cylindrical topology if it can be continuously deformed, without tearing or gluing, to an open ended cylinder. More formally, only orientable manifolds $\mathscr{M}$ with two boundaries, denoted $\partial^0_{\mathscr{M}}$ and $\partial^1_{\mathscr{M}}$, and without handles are considered. The parameterization domain is the two-dimensional open-ended right circular cylinder with unit radius and length h, denoted by $\mathscr{C}^2_h$. It also has two boundaries: $\partial^0_{\mathscr{C}^2_h}$ and $\partial^1_{\mathscr{C}^2_h}$. The domain $\mathscr{C}^2_h$ itself is parameterized by an angular coordinate $u^{(0)} \in [0, 2\pi)$ and an axial coordinate $u^{(1)} \in [0, h]$.

A cylindrical parameterization of $\mathscr{M}$ is any homeomorphic map $\boldsymbol{x}$ from cylinder $\mathscr{C}^2_h$ to the surface $\mathscr{M}$, i.e. $\boldsymbol{x} : [0, 2\pi) \times [0, h] \to \mathscr{M} \subset \mathbb{R}^3$. For $\boldsymbol{x}$ to be a homeomorphism, it must be a bijective, continuous function, and have a continuous inverse. If the topology of $\mathscr{M}$ is consistent, such a homeomorphism can always be obtained although a solution is not unique. This can be seen from the fact that the composition $\boldsymbol{x} \circ \boldsymbol{\rho}$ of any automorphism $\boldsymbol{\rho}$ of the cylinder with the parameterization $\boldsymbol{x}$ of the surface $\mathscr{M}$, is a different parameterization of the same surface. The particular solution that a parameterization technique will propose is usually the result of the minimization of a certain energy functional. Different functionals result in different parameterizations. Figure 2.1 shows an example parameterization.

In this work, the map $\boldsymbol{x}$ is represented by embedding the connectivity graph of the surface $\mathscr{M}$ in the parameterization domain $\mathscr{C}^2_h$. Suppose the surface $\mathscr{M}$ is described by the pair (K, M) where K is the simplicial complex containing the vertices, edges and faces of the surface mesh and $M = (\boldsymbol{x}_0, \ldots, \boldsymbol{x}_{n-1})$ are the coordinates of the vertices of the surface in $\mathbb{R}^3$. Then, the parameterization $\boldsymbol{x}$ is represented by the embedding $\mathscr{U} = (K, U)$, where $U = (\boldsymbol{u}_0, \ldots, \boldsymbol{u}_{n-1})$ are the coordinates of the vertices of the mesh on the cylinder $\mathscr{C}^2_h$. When an embedding is established, the parameterization is defined at the vertices as $\boldsymbol{x}(\boldsymbol{u}_i) = \boldsymbol{x}_i$ and extended to the triangles by interpolation: a point $\boldsymbol{p}$ in a parametric triangle $\boldsymbol{u}_i \boldsymbol{u}_j \boldsymbol{u}_k$ with barycentric coordinates $(\beta_i, \beta_j, \beta_k)$ is mapped to

$$\begin{aligned} \boldsymbol{x}(\boldsymbol{p}) &= \boldsymbol{x}(\beta_i \boldsymbol{u}_i + \beta_j \boldsymbol{u}_j + \beta_k \boldsymbol{u}_k) \\ &= \beta_i \boldsymbol{x}_i + \beta_j \boldsymbol{x}_j + \beta_k \boldsymbol{x}_k. \end{aligned}$$

Note that the inverse of the piecewise linear map $\boldsymbol{x}$ exists and that it will be denoted by $\boldsymbol{u} : \mathscr{M} \to \mathscr{C}^2_h$.

In the following sections, a linear and a nonlinear parameterization method will be proposed. Both methods find a parameterization for a surface $\mathscr{M}$ by constructing the cylindrical embedding $\mathscr{U}$ or, equivalently, the map $\boldsymbol{u}$. The actual parameterization may then be obtained as the inverse of this map, i.e. $\boldsymbol{x} = \boldsymbol{u}^{-1}$.

2.4 Linear Parameterization Method

In this section, a method is introduced for the construction of a cylindrical parameterization by means of a conformal map $\boldsymbol{u} = (u^{(0)}, u^{(1)})$. A map $\boldsymbol{u}$ is conformal if the separate coordinate maps $u^{(0)}$ and $u^{(1)}$ satisfy the Cauchy-Riemann

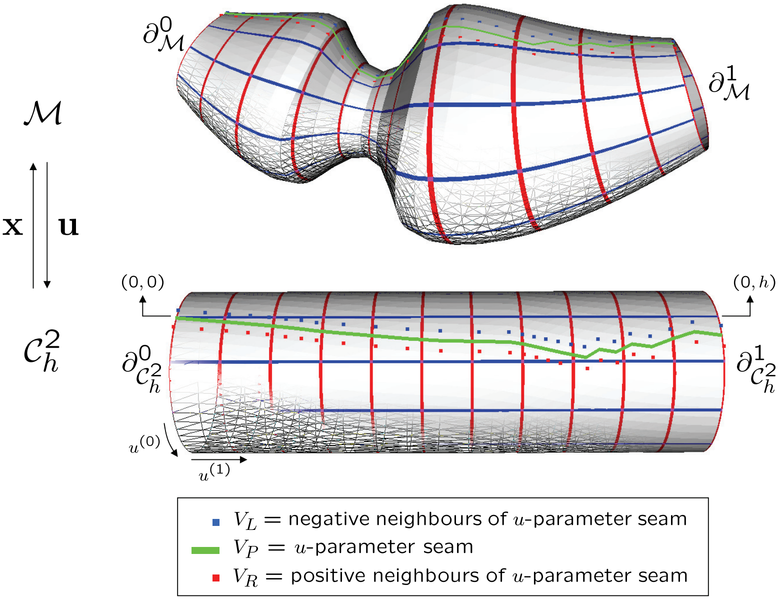

Figure 2.1: Top: an example surface $\mathscr{M}$ with boundaries $\partial^0_{\mathscr{M}}$ and $\partial^1_{\mathscr{M}}$. The parameterization $\boldsymbol{x}$, or its inverse $\boldsymbol{u}$, is visualised using a texture: iso-parametric curves are shown in red and blue lines. The vertex path, used to tackle the periodicity problem, is shown in green and the right and left neighbouring vertices are shown in red and blue, respectively. Bottom: the parameterization domain $\mathscr{C}^2_h$ with boundaries $\partial^0_{\mathscr{C}^2_h}$ and $\partial^1_{\mathscr{C}^2_h}$. The location on $\mathscr{C}^2_h$ of the vertex path and its neighbours is also shown.

equations:

$$\frac{\partial u^{(0)}}{\partial e^{(0)}} = \frac{\partial u^{(1)}}{\partial e^{(1)}} \quad , \quad \frac{\partial u^{(0)}}{\partial e^{(1)}} = -\frac{\partial u^{(1)}}{\partial e^{(0)}} \tag{2.1}$$

where $(e^{(0)}, e^{(1)})$ is a parameterization of the local frame on $\mathscr{M}$. In this work, each of the coordinate maps $u^{(0)}$ and $u^{(1)}$ are constructed as a harmonic function. Harmonic functions minimize the Dirichlet energy or, equivalently, are a solution to the Laplace equation:

$$\boldsymbol{\Delta}_{\mathscr{M}} \boldsymbol{u} = \boldsymbol{0}. \tag{2.2}$$

By imposing suitable boundary conditions, harmonic coordinate maps can be obtained which together satisfy the conformality condition of Eq. (2.1). Moreover, the optimal length h of the cylindrical parameter domain can also be obtained automatically by enforcing conformality. The problem of finding a conformal solution of the Laplace equation can be stated as a linearly constrained

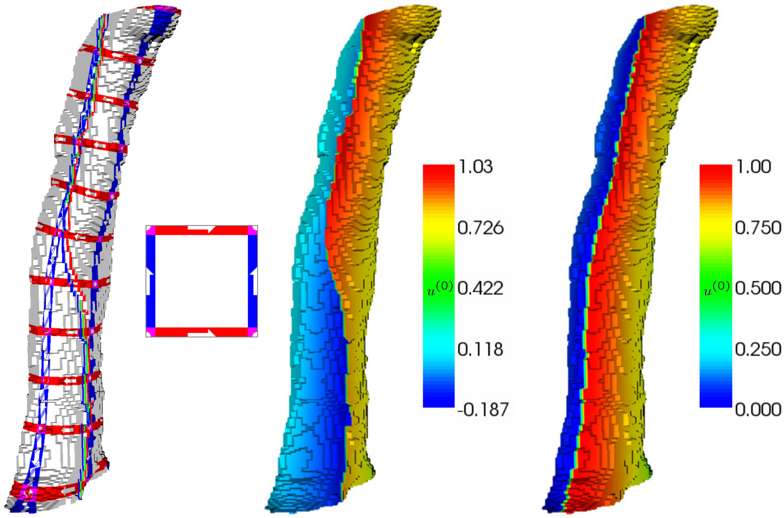

Figure 2.2: Cylindrical parameterization of the human trachea using a conformal map $\boldsymbol{u}$. On the left, the parameterized trachea surface is shown. A texture is used to reveal the parameterization: blue iso-$u^{(0)}$ lines and red iso-$u^{(1)}$ lines can be seen. Also, the path V_P is shown in green and the vertex neighbours V_L and V_R are marked in blue and red. In the middle, the trachea is shown with a color indicating the value of the periodic coordinate $u^{(0)}$. It can be seen that the parametric jump is located along the vertex path V_P. Also, it can be seen that the actual values of $u^{(0)}$, at which the jump occurs, differ along the seam. On the right, the periodic coordinate $u^{(0)}$ is mapped into $[0, 2\pi)$ in order to have the parametric jump at $u^{(0)} = 0 = 2\pi$.

convex quadratic minimization problem. In what follows, the construction of the linear system, solving this optimization problem, will be explained in detail. But first, the periodicity of the parameterization domain is tackled.

2.4.1 Edge Vectors in $\mathscr{C}_h^2$ and the Periodicity of $u^{(0)}$

The Dirichlet energy, the Laplacian operator, and the boundary conditions will all be formulated in terms of the lengths of the edges $\boldsymbol{u}_{ij}$ of the embedding of K in $\mathscr{C}_h^2$. The length of $\boldsymbol{u}_{ij}$ can be calculated using the coordinates of the end points $\boldsymbol{u}_i$ and $\boldsymbol{u}_j$ of the edge, i.e.

$$
\begin{aligned}
||\boldsymbol{u}_{ij}||^2 &= ||\boldsymbol{u}_i - \boldsymbol{u}_j||^2 \\
&= (u_i^{(0)} - u_j^{(0)})^2 + (u_i^{(1)} - u_j^{(1)})^2.
\end{aligned}
\tag{2.3}
$$

Since the parameterization domain is periodic along parameter $u^{(0)}$, some edges will cross the parametric seam $u^{(0)} = 0 = 2\pi$. For those edges, the above expression does not calculate the correct length.

Similar periodicity problems have been addressed in Brechbühler et al. [1995], Steiner and Fischer [2004], Tong et al. [2006] and the same strategy is applied here. Given a surface $\mathscr{M}$, a vertex path V_P, connecting $\partial^0_{\mathscr{M}}$ with $\partial^1_{\mathscr{M}}$, is introduced on the surface. The path V_P should not self-intersect and it can have only one vertex on each boundary. The neighbouring vertices of the path V_P are divided in two groups: V_L are the neighbours on the left side and V_R are the neighbours on the right side of the path. In Figure 2.1, an example surface is shown with vertex path V_P marked in green and the path neighbours V_R and V_L marked in red and blue, respectively. The path and neighbours are also shown on the embedding in $\mathscr{C}^2_h$.

Now, any given cylindrical map $\boldsymbol{u}$ can be modified to have its parametric jump along any path V_P. This can be accomplished without affecting the edge lengths $\boldsymbol{u}_{ij}$ and, as a consequence, also without affecting the Dirichlet energy of the map. Therefore, only maps $\boldsymbol{u}$ are considered with the 2π parametric jump occurring along the vertex path V_P instead of at $u^{(0)} = 0 = 2\pi$ and this without loss of generality.

Requiring the map to have the parametric jump along the V_P will result in values for $u^{(0)}$ exceeding the interval $[0, 2\pi)$. They are mapped back into the interval afterwards using the modulo-2π operator. Figure 2.2 shows an example embedding with one map having the parameter jump along the path V_P and the other map having the parameter jump at $u^{(0)} = 0 = 2\pi$. With this setting, a general formula for the vector $\boldsymbol{u}_{ij}$ can be derived for which Eq. (2.3) will always give the correct length:

$$\boldsymbol{u}_{ij} = \begin{cases} \begin{pmatrix} u_i^{(0)} - u_j^{(0)} - 2\pi \\ u_i^{(1)} - u_j^{(1)} \end{pmatrix} & \text{if } i \in V_L \text{ and } j \in V_P \\ \begin{pmatrix} u_i^{(0)} - u_j^{(0)} + 2\pi \\ u_i^{(1)} - u_j^{(1)} \end{pmatrix} & \text{if } i \in V_P \text{ and } j \in V_L \\ \begin{pmatrix} u_i^{(0)} - u_j^{(0)} \\ u_i^{(1)} - u_j^{(1)} \end{pmatrix} & \text{otherwise} \end{cases} . \tag{2.4}$$

Note, that any path, without self intersections, connecting $\partial^0_{\mathscr{M}}$ with $\partial^1_{\mathscr{M}}$, can be used in this strategy and this without influencing the final parameterization. In this work, the vertex path with the shortest geodesic distance between the two boundaries is used [Kimmel and Sethian, 1998].

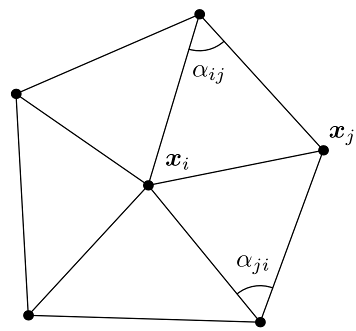

Figure 2.3: A vertex one-ring on $\mathscr{M}$. The angles α_{ij} and α_{ji} are the angles of the corners opposite to edge (i,j).

2.4.2 Harmonicity of the Coordinate Maps

For a given map $\boldsymbol{u}$, the Dirichlet energy ξ_D is defined as:

$$\xi_D(\boldsymbol{u}) = \frac{1}{2}\int_{\mathscr{M}} ||\nabla \boldsymbol{u}||^2 = \frac{1}{4}\sum_{(i,j)\in K} \omega_{ij}||\boldsymbol{u}_{ij}||^2, \tag{2.5}$$

where the integral becomes a sum because, within a triangle, the map is linear and has constant gradient [Pinkall and Polthier, 1993]. The weights ω_{ij} are the harmonic weights [Pinkall and Polthier, 1993]:

$$\omega_{ij} = \begin{cases} \frac{1}{2}(\cot\alpha_{ij} + \cot\alpha_{ji}) & \text{if } (i,j) \text{ internal} \\ \frac{1}{2}\cot\alpha_{ij} & \text{if } (i,j) \text{ on boundary} \end{cases}, \tag{2.6}$$

where α_{ij} and α_{ji} are the angles on $\mathscr{M}$ opposite to the edge (i,j) in the two triangles adjacent to the edge (i,j) as shown in Figure 2.3. For each edge (i,j), $\boldsymbol{u}_{ij}$ is the vector connecting both vertices of the edge in the parameter space $\mathscr{C}_h^2$ as defined in Eq. (2.4).

The discrete Laplace operator $\boldsymbol{\Delta}_{\mathscr{M}}$ is defined as the derivative of the discrete Dirichlet energy ξ_D. The Laplacian of a map $\boldsymbol{u}$ at vertex i on the surface $\mathscr{M}$ is defined as:

$$(\boldsymbol{\Delta}_{\mathscr{M}}\boldsymbol{u})_i = \frac{\partial \xi_D(\boldsymbol{u})}{\partial \boldsymbol{u}_i} = \frac{1}{2}\sum_{j\in\mathscr{N}_i} \omega_{ij}\boldsymbol{u}_{ij}, \tag{2.7}$$

where $\mathscr{N}_i = \{j|(i,j)\in K\}$ is the set of 1-ring neighbours of vertex i [Pinkall and Polthier, 1993].

A harmonic map $\boldsymbol{u}$ can now be obtained as a minimizer of the Dirichlet energy, or, equivalently, as the solution of the Laplace equation:

$$(\boldsymbol{\Delta}_{\mathscr{M}}\boldsymbol{u})_i = \sum_{j\in\mathscr{N}_i} \omega_{ij}\boldsymbol{u}_{ij} = \boldsymbol{0}, \quad \forall i. \tag{2.8}$$

This system of linear equations can be formulated as $\boldsymbol{Au} = \boldsymbol{b}$. Here,

$$\boldsymbol{u} = (u_0^{(0)}, u_0^{(1)}, \ldots, u_{n-1}^{(0)}, u_{n-1}^{(1)})^T$$

is the vector of unknowns defining the map. The system matrix $\boldsymbol{A}$ is sparse with non-zeros

$$\begin{aligned} A_{2i,2j} &= A_{2i+1,2j+1} \\ &= \begin{cases} -\sum_{k\in\mathcal{N}_i}\omega_{ik} & \text{if } i = j \\ \omega_{ij} & \text{if } j \in \mathcal{N}_i \end{cases} \quad, \forall i, \forall j. \end{aligned} \tag{2.9}$$

The right-hand side $\boldsymbol{b} = (b_0, \ldots, b_{2n-1})$ is also sparse. The non-zeros relate to the parametric jump along the path V_P and correspond to the constant parts of the $\boldsymbol{u}_{ij}$'s brought to the right side of Eq. (2.8). If vertex i is in V_L or V_P and has neighbours in V_P or V_L, respectively, then b_{2i} will be non-zero:

$$\begin{aligned} b_{2i} = {} & 2\pi |\{j | i \in V_L \text{ and } j \in \mathcal{N}_i \cap V_P\}| \\ & - 2\pi |\{j | i \in V_P \text{ and } j \in \mathcal{N}_i \cap V_L\}|, \quad \forall i. \end{aligned} \tag{2.10}$$

In its current form, the linear system $\boldsymbol{Au} = \boldsymbol{b}$ is singular and has infinitely many solutions due to the periodicity. Suitable boundary conditions will reduce the solution set to a singleton.

2.4.3 Conformality of Combined Coordinate Map

In Desbrun et al. [2002], the conformality of the harmonic coordinate maps for disc-like surfaces is obtained by enforcing the following condition along the surface boundary:

$$\boldsymbol{\nabla_n u} = (\boldsymbol{\nabla_t u})^{\perp}, \tag{2.11}$$

where $\boldsymbol{\nabla_\bullet}$ is the directional derivative, $\boldsymbol{n}$ is the direction normal to the boundary, $\boldsymbol{t}$ is the direction tangential to the boundary, and $\perp$ is a 90° counterclockwise rotation, i.e. $(x, y)^{\perp} = (-y, x)$. In this work, their strategy is adopted and the boundary condition of Eq. (2.11) is enforced at $\partial^0_{\mathcal{M}}$ and $\partial^1_{\mathcal{M}}$.

Let the set of vertices on boundary $\partial^0_{\mathcal{M}}$ and $\partial^1_{\mathcal{M}}$ be denoted as V_B. Then, the conformality condition is captured in following system of equations:

$$\sum_{j\in\mathcal{N}_i} \omega_{ij}\boldsymbol{u}_{ij} = (\boldsymbol{u}_{i_{n_i}i} + \boldsymbol{u}_{ii_1})^{\perp}, \quad \forall i \in V_B, \tag{2.12}$$

where i_1 and i_{n_i} are the first and the last neighbouring boundary vertices of i when traversing the neighborhood of vertex i counter-clockwise. Now, given a boundary vertex $i \in V_B$, let $\imath$ be the corresponding index in the set V_B. Then, these constraints can be formulated as a linear system $\boldsymbol{Cu} = \boldsymbol{d}$, where the system matrix is sparse and has non-zeros

$$\begin{aligned} C_{2\imath,2i_1+1} = C_{2\imath+1,2i_1} &= -1, \quad \forall i \in V_B, \\ C_{2\imath,2i_{n_i}+1} = C_{2\imath+1,2i_{n_i}} &= 1, \quad \forall i \in V_B, \end{aligned}$$

$$C_{2\imath,2j} = C_{2\imath+1,2j+1}$$
$$= \begin{cases} -\sum_{k\in\mathcal{N}_i} \omega_{ik} & \text{if } i = j \\ \omega_{ij} & \text{if } j \in \mathcal{N}_i \backslash \{i_1, i_{n_i}\} \end{cases}, \forall i \in V_B, \forall j. \tag{2.13}$$

and the right-hand side is also sparse and has non-zeros

$$\begin{aligned} d_{2\imath} &= 2\pi|\{j|i \in V_L \text{ and } j \in \mathcal{N}_i \cap V_P\}| \\ &\quad - 2\pi|\{j|i \in V_P \text{ and } j \in \mathcal{N}_i \cap V_L\}|, \quad \forall i \in V_B, \\ d_{2\imath+1} &= \begin{cases} 2\pi & \text{if } i \in V_L \text{ and } i_1 \in V_P \\ -2\pi & \text{if } i_{n_i} \in V_L \text{ and } i \in V_P \end{cases}, \quad \forall i \in V_B. \end{aligned} \tag{2.14}$$

2.4.4 Automatic Length Optimization

The Dirichlet energy of Eq. (2.5) under the conformal boundary constraints of Eq. (2.11) still has multiple minima because the Dirichlet energy is invariant with respect to translations of the map $\boldsymbol{u}$ on the cylinder. These degrees of freedom, however, can be removed by fixing a single point of the parameterization. Here, the point at the intersection of the boundary $\partial^0_{\mathcal{M}}$ with the path V_P is chosen and it will be fixed at $\mathbf{0}$. Also, in order to have a bijective map between the surface $\mathcal{M}$ and the cylinder $\mathcal{C}^2_h$ of length h, the image of boundary $\partial^0_{\mathcal{M}}$ and $\partial^1_{\mathcal{M}}$ needs to be constrained to boundary $\partial^0_{\mathcal{C}^2_h}$ and $\partial^1_{\mathcal{C}^2_h}$ respectively. This leads to the following boundary constraints:

$$\begin{cases} u^{(1)}_i &= u^{(1)}_j, \quad \forall i \in V_{B_0}, \forall j \in V_{B_0}, \\ u^{(1)}_i &= u^{(1)}_j, \quad \forall i \in V_{B_1}, \forall j \in V_{B_1}, \\ \boldsymbol{u}_i &= \mathbf{0}, \qquad \text{for } i = V_{B_0} \cap V_P. \end{cases}, \tag{2.15}$$

where V_{B_0} is the set of vertices on boundary $\partial^0_{\mathcal{M}}$ and V_{B_1} is the set of vertices on boundary $\partial^1_{\mathcal{M}}$. Note, that with these constraints, the vertices of boundary $\partial^0_{\mathcal{M}}$ will be mapped to the iso-circle $u^{(1)} = 0$ on $\mathcal{C}^2_h$. The vertices on $\partial^1_{\mathcal{M}}$ will be mapped to the iso-circle $u^{(1)} = h$, but without fixing h. In this way, the length h of the cylindrical domain, resulting in a map with minimal Dirichlet energy, will be chosen automatically.

The constraints of Eq. (2.15) can be formulated as a linear system $\boldsymbol{E}\boldsymbol{u} = \mathbf{0}$, where the system matrix is sparse and has following non-zeros

$$\begin{aligned} E_{\imath,i} = -E_{\imath,i_1} &= 1, & &\forall i \in V_B \\ E_{|V_B|,i} &= 1, & &\text{for } i = V_{B_0} \cap V_P \\ E_{|V_B|+1,i+1} &= 1, & &\text{for } i = V_{B_0} \cap V_P \end{aligned} \tag{2.16}$$

where $\imath$ is the index in V_B for vertex i and i_1 is the first encountered boundary vertex when the neighbourhood of vertex i is traversed in counter-clockwise direction.

Note that one can drop the first two constraint sets of Eq. (2.15) in order to obtain a free-boundary parameterization on the cylinder. By trimming both ends of the resulting parameterization, a one-to-one map between the trimmed surface and the cylinder can be obtained. Such an approach is useful to avoid large distortions at jagged surface boundaries when an exact correspondence between the surface boundary and the domain boundary is not required.

2.4.5 Final Linear System

Finally, the problem of obtaining a conformal harmonic map $\boldsymbol{u}: \mathcal{M} \to \mathcal{C}_h^2$ with optimal length h can be formulated as the following optimization problem:

$$\begin{aligned} \min_{\boldsymbol{u}_k, h} \xi_D(\boldsymbol{u}) &= \frac{1}{4} \sum_{(i,j)\in K} \omega_{ij} ||\boldsymbol{u}_{ij}||^2 \\ \text{subject to } u_i^{(1)} &= u_j^{(1)}, && \forall i \in V_{B_0}, \forall j \in V_{B_0}, \\ u_i^{(1)} &= u_j^{(1)}, && \forall i \in V_{B_1}, \forall j \in V_{B_1}, \\ \boldsymbol{u}_i &= \boldsymbol{0}, && \text{for } i = V_{B_0} \cap V_P. \\ \sum_{j\in\mathcal{N}_i} \omega_{ij}\boldsymbol{u}_{ij} &= (\boldsymbol{u}_{i_{n_i} i} + \boldsymbol{u}_{i i_0})^{\perp}, && \forall i \in V_B, \end{aligned} \tag{2.17}$$

This is a convex quadratic programming problem with linear equality constraints. This problem can be transformed in to a linear system by the use of Lagrange multipliers:

$$\begin{bmatrix} \boldsymbol{A} & \boldsymbol{C}^T & \boldsymbol{E}^T \\ \boldsymbol{C} & 0 & 0 \\ \boldsymbol{E} & 0 & 0 \end{bmatrix} \cdot \begin{bmatrix} \boldsymbol{u} \\ \boldsymbol{\lambda_1} \\ \boldsymbol{\lambda_2} \end{bmatrix} = \begin{bmatrix} \boldsymbol{b} \\ \boldsymbol{d} \\ \boldsymbol{0} \end{bmatrix} \tag{2.18}$$

where the system matrix is the Karush-Kuhn-Tucker (KKT) matrix associated with the quadratic programming problem [Nocedal and Wright, 1999]. The solution $(\boldsymbol{u}^*, \boldsymbol{\lambda}_1^*, \boldsymbol{\lambda}_2^*)$ of this system provides the conformal map $\boldsymbol{u}^*$ and the optimal Lagrange multipliers $(\boldsymbol{\lambda}_1^*, \boldsymbol{\lambda}_2^*)$ for the constraints. In this work, LU-decomposition is used to solve the above system.

The parametric jump of the obtained map $\boldsymbol{u}^*$ occurs along the path V_P. The modulo-2π operator is applied to the values of the map $\boldsymbol{u}^*$ in order to obtain a map $\boldsymbol{u}$ that is within $[0, 2\pi) \times [0, h]$. Finally, the parameterization is obtained as $\boldsymbol{x} = \boldsymbol{u}^{-1}$.

Note that it is possible to subject the optimization problem of Eq. (2.17) to additional constraints, simply by extending the KKT system of Eq. (2.18). For example, by using appropriate constraints, one could fix the certain landmarks to a predetermined position on the parameterization domain. This is particularly useful for constructing landmark based correspondences between tubular surfaces. This is not possible with the conformal method of Hong et al. [2006].

2.5 Nonlinear Parameterization Method

The method proposed in this section enables the parameterization of geometrically complex cylindrical surfaces while keeping the distortion, in both angles and areas, to a minimum. The method of Section 2.4 generates parameterizations with minimal angle distortion. As a consequence, for surfaces with substantial variation in cross-sectional diameter, the parameterizations exhibit large distortion in areas. In this section, this problem is overcome by using a distortion measure that penalizes angle and area deformations in a balanced way. The employed distortion measure is derived from the celebrated stretch measure of Sander et al. [2001]. See Figure 2.4 for the comparison between the linear and the nonlinear method for a surface with substantial variation in cross-sectional diameter.

The downside of using such a measure is that it takes the parameterization problem into the domain of non-linear optimization. In order to robustly and efficiently solve the optimization problem, this work adopts the approach of Hormann et al. [1999] by constructing the parameterization in a hierarchical way: the method starts with a simplified version of the surface, which exhibits a trivial parameterization, and gradually refines the parameterization until all details of the surface are incorporated.

2.5.1 Distortion Measure

Given a surface $\mathscr{M}$ with parameterization $\boldsymbol{u}$, let the distortion at a point $\boldsymbol{x}$ on the surface $\mathscr{M}$ be denoted as $\xi_S(\boldsymbol{u}|_{\boldsymbol{x}})$. The total amount of distortion exhibited by the parameterization can then be obtained by integrating this measure over the entire surface:

$$\xi_S(\boldsymbol{u}) = \frac{1}{A_{\mathscr{M}}} \int_{\mathscr{M}} \xi_S(\boldsymbol{u}|_{\boldsymbol{x}})\, d\boldsymbol{x}, \tag{2.19}$$

where $A_{\mathscr{M}}$ denotes the area of the surface $\mathscr{M}$. Following Sander et al. [2001], the distortion $\xi_S(\boldsymbol{u}|_{\boldsymbol{x}})$ of a parameterization $\boldsymbol{u}$ is measured in terms of the singular values of the Jacobian of $\boldsymbol{u}$. This Jacobian is piecewise constant because, within each triangle, the map $\boldsymbol{u}$ is affine. Taking this into account, Eq. (2.19) becomes:

$$\xi_S(\boldsymbol{u}) = \frac{1}{A_{\mathscr{M}}} \sum_{t \in K} A_t \xi_S(\boldsymbol{u}|_t). \tag{2.20}$$

Now, for each triangle $t \in K$, let γ_t and Γ_t be the smallest and the largest singular value, respectively, of the Jacobian of the affine map $\boldsymbol{u}\big|_t$. Then, the distortion measure of Sander et al., at any point in this triangle, is defined as $\sqrt{\gamma_t^2 + \Gamma_t^2}$. It penalizes undersampling or, equivalently, compression of triangles. In this work, a measure is sought after that penalizes both compression and expansion. Such a measure is obtained by making Sander's measure symmetric w.r.t. the

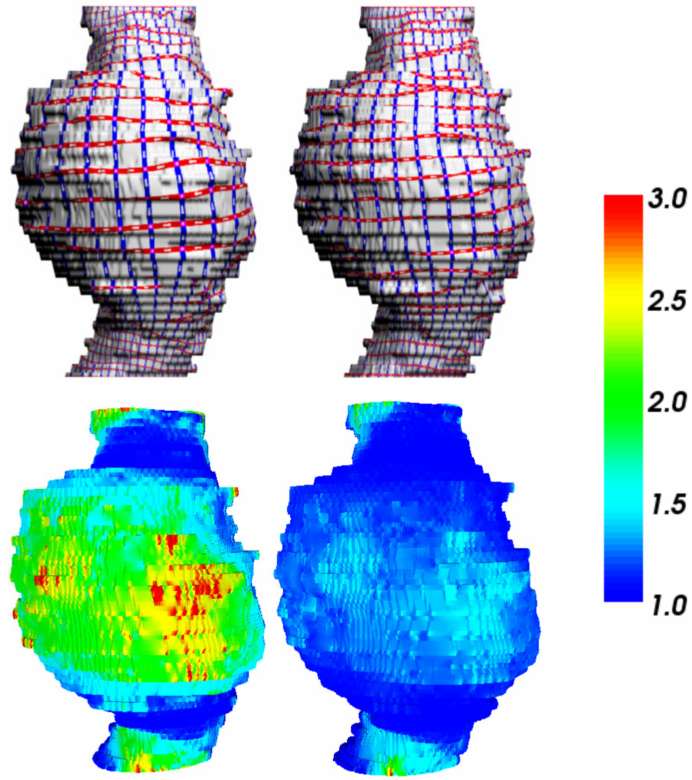

Figure 2.4: Comparison of the parameterization generated by the linear (left) and nonlinear (right) method for a thrombus surface with substantial variation in cross-sectional diameter. Top: visualization of the parameterization through iso-parametric lines. Bottom: visualization of the distortion ξ_A of the triangle area.

singular values, i.e.

$$\xi_S(\boldsymbol{u}|_t) = \frac{\sqrt{2}}{4}\left(\sqrt{\gamma_t^2 + \Gamma_t^2} + \sqrt{\frac{1}{\gamma_t^2} + \frac{1}{\Gamma_t^2}}\right), \tag{2.21}$$

which has a minimum of 1 when there is no distortion. Finally, the total distortion $\xi_S(\boldsymbol{u})$ introduced by a parameterization $\boldsymbol{u} : \mathscr{C}_h^2 \to \mathscr{M}$ can be evaluated as:

$$\xi_S(\boldsymbol{u}) = \frac{\sqrt{2}}{4A_{\mathscr{M}}} \sum_{t\in K} A_t \left(\sqrt{\gamma_t^2 + \Gamma_t^2} + \sqrt{\frac{1}{\gamma_t^2} + \frac{1}{\Gamma_t^2}}\right). \tag{2.22}$$

It should be noted that this measure is not invariant under scaling of the surface $\mathscr{M}$. This can be remedied easily by scaling the singular values with a factor

$\sqrt{\frac{A_{\mathscr{C}_h^2}}{A_{\mathscr{M}}}}$, where $A_{\mathscr{C}_h^2}$ is the area of the cylindrical domain $\mathscr{C}_h^2$.

2.5.2 Progressive Construction

Finding an embedding $\mathscr{U}$ of K on the cylinder $\mathscr{C}_h^2$ for a given surface $\mathscr{M}$ that minimizes the nonlinear distortion measure of Eq. (2.22) is a large and challenging optimization problem. If the surface $\mathscr{M}$ has n vertices, then approximately $2n$ variables need to be optimized simultaneously. Furthermore, such an optimization does not necessarily result in a valid parameterization because the one-to-one property of the resulting map is not enforced by Eq. (2.22). Constrained optimization is a possible answer to this problem, but, in this work, a more efficient method utilizing a surface hierarchy, is proposed.

The method starts by constructing a surface hierarchy

$$(\mathscr{M}^0, \{\text{vsplit}_1, \ldots, \text{vsplit}_m\})$$

called the progressive mesh [Hoppe, 1996] of surface $\mathscr{M}$. It is obtained from the original surface $\mathscr{M}$ by successively collapsing edges into vertices, i.e.

$$\mathscr{M} \equiv \mathscr{M}^m \xrightarrow{\text{ecol}_m} \mathscr{M}^{m-1} \xrightarrow{\text{ecol}_{m-1}} \ldots \xrightarrow{\text{ecol}_1} \mathscr{M}^0, \tag{2.23}$$

where ecol_i is the inverse operation of vsplit_i. With every surface $\mathscr{M}^i$ in the hierarchy corresponds a simplicial mesh, i.e. $\mathscr{M}^i = (K^i, M^i)$, where K^i contains the vertex connectivity and $M^i \subset M$ are the positions in $\mathbb{R}^3$ of the vertices. As in Garland and Heckbert [1997], the order of the edge collapses is determined by a quadratic error metric which penalizes deviation from the original surface. Additionally, for the method of this section, a collapse is subject to a number of conditions: an edge collapse should not result in (1) non-manifold geometry, (2) degenerate triangles, and (3) triangles that have all three vertices at the same boundary. Also, (4) boundary vertices should only be collapsed into vertices of the same boundary. Any violation of these conditions will result in an invalid parameterization.

The obtained hierarchy is now utilized to construct a parameterization of $\mathscr{M}$ in a progressive way. First, the embedding $\mathscr{U}^0$ of K^0 in $\mathscr{C}_h^2$ is found. This defines a parameterization of the base mesh $\mathscr{M}^0$. It turns out, that for surfaces of cylindrical topology, the base mesh $\mathscr{M}^0$, as generated by a progressive mesh that takes into account conditions (1)-(4), contains six vertices, namely three at each boundary. As a consequence, a valid embedding $\mathscr{U}^0$ can be established trivially by evenly distributing the vertices of the base mesh $\mathscr{M}^0$ over the boundaries of $\mathscr{C}_h^2$.

The obtained parameterization $\mathscr{U}^0$ of the base mesh $\mathscr{M}^0$ provides a valid starting point for further refinement of the parameterization. By applying vertex split vsplit_i to the embedding $\mathscr{U}^{i-1}$ of the level $i-1$ surface $\mathscr{M}^{i-1}$, an embedding $\mathscr{U}^i$ of level i surface $\mathscr{M}^i$ is obtained. The initial position of the newly

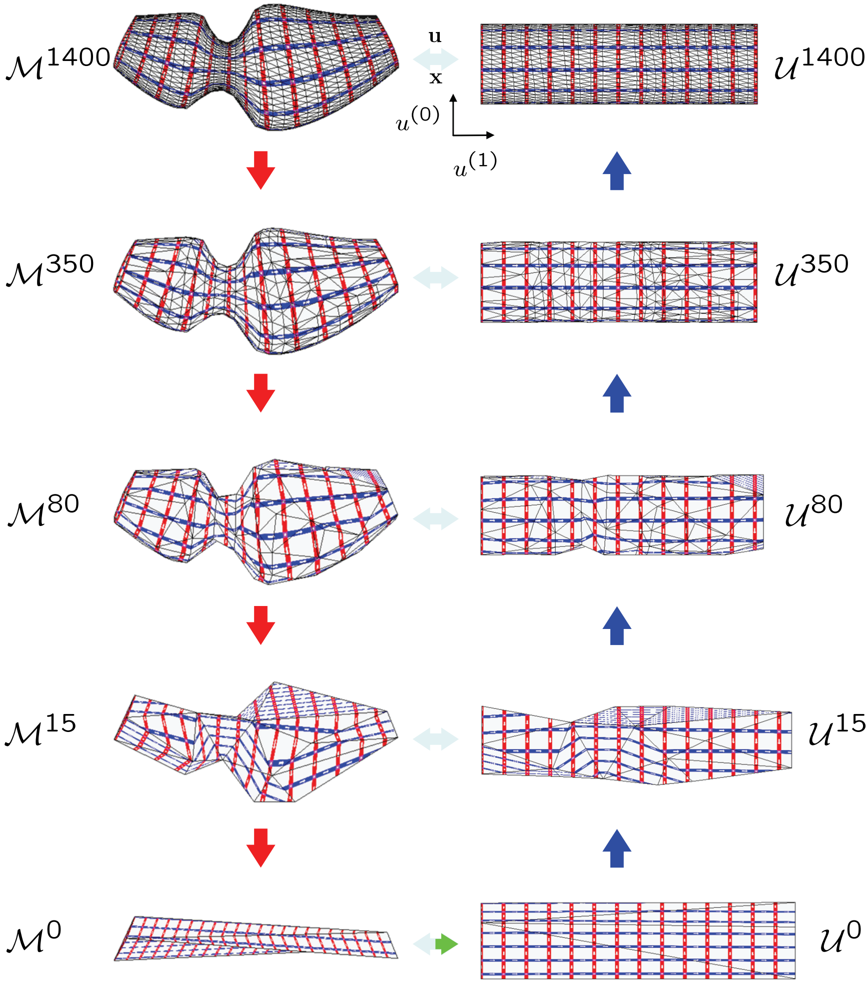

Figure 2.5: A depiction of the parameterization process for a sample surface using the nonlinear method. The algorithm starts with the original surface $\mathcal{M} \equiv \mathcal{M}^{1400}$, shown at the top left. A surface hierarchy is constructed by successively applying edge collapses (red arrows). On the bottom left, the lowest surface in the hierarchy is shown, denoted $\mathcal{M}^0$. Its embedding $\mathcal{U}^0$ on the cylinder is trivial (green arrow) and it is shown at the bottom right. Now, the inverse operations of the edge collapses, namely vertex splits, are applied to the embedding and the vertex positions are optimized with respect to the distortion measure (blue arrows). This results in progressively finer embeddings. The final embedding $\mathcal{U}^{1400} \equiv \mathcal{U}$, shown at the top right, together with the original surface $\mathcal{M} \equiv \mathcal{M}^{1400}$ define the final parameterization. At each level, the iso-parametric lines of the cylinder are shown on both the embedding and the surface in order to reveal the current mapping.

introduced vertex v_i is chosen at the center of the kernel of its 1-ring neighbourhood on the cylinder $\mathscr{C}_h^2$. This initialization always provides a valid embedding $\mathscr{U}^i$. The position of the vertex v_i is then further optimized, with respect to the distortion measure ξ_S, using gradient descent within the bounds of the kernel. Note, that the distortion measure can be evaluated efficiently because movements of v_i only affect the triangles of its 1-ring neighbourhood.

Occasionally, when the amount of vertices has increased with a certain factor (e.g. 1.1), a full optimization is run, this in order to allow larger adjustments. In a full optimization run, all vertices are being optimized, one by one, within the kernel of their 1-ring neighbourhood. This process is repeated until the improvement in distortion drops below a certain value (e.g. 0.001). The order in which each vertex is optimized is determined by the distortion reduction that vertex caused in the previous optimization. Note that, by optimizing each vertex inside the kernel of their 1-ring, triangle flips are avoided and the embedding is kept valid. Optimizing all vertices simultaneously would also be possible but then a constrained optimization technique would have to be used.

When all vertex splits have been applied, the embedding $\mathscr{U}^m \equiv \mathscr{U}$ of surface $\mathscr{M}^m \equiv \mathscr{M}$ is obtained. It should be noted that an embedding obtained in this way is valid by construction. For a depiction of the progressive construction of the parameterization for a sample surface, see Figure 2.5.

2.5.3 Length Optimization

Similar to the linear method of section 2.4, the length h of the cylindrical domain $\mathscr{C}_h^2$ is a variable in the optimization problem. The length h that gives rise to the parameterization $\boldsymbol{u}$ with minimal distortion, in terms of ξ_S, is considered optimal.

One possible approach is to calculate the optimal parameterization of $\mathscr{M}$ on a cylindrical domain of length $h = 2\pi$ and optimize the length afterwards. For surfaces where the length/circumference-ratio is approximately one, this approach will generate good results. But, for elongated surfaces, where the length is a multiple of the circumference, large distortions will be introduced into the parameterization and the length can not be estimated accurately. This is due to the fact that, during the construction of the embedding on the cylinder of length $h = 2\pi$, the triangles will become squashed in the $u^{(1)}$-direction, to such an extent, that even numerical problems may arise.

This work proposes a different strategy. The length is optimized, using Brent's 1D minimization method, at several stages during the progressive construction of the parameterization, namely after each full run of vertex optimizations. In this way, an accurate estimate of the length of the domain is obtained early in the hierarchy. As a consequence, the above-mentioned problem does not occur. Moreover, since an accurate estimate is obtained early in the hierarchy, subsequent optimizations converge in a few iterations.

The method can be made even more efficient by storing the current Jacobian for each triangle during the full vertex optimization. These Jacobians can then be used to optimize the length: scaling the length of the domain with a factor s simply results in new Jacobians

$$J_i^s = J_i \cdot \begin{bmatrix} 1 & 0 \\ 0 & \frac{1}{s} \end{bmatrix},$$

from which the singular values, required for the computation of the distortion ξ_s, can easily be derived.

2.5.4 Final Algorithm

The final optimization problem can be stated as follows

$$\underset{\boldsymbol{u}_k,\, h}{\arg\min}\ \xi_S(\boldsymbol{u}) = \frac{\sqrt{2}}{4A_{\mathcal{M}}} \sum_{t\in K} A_t \left(\sqrt{\gamma_t^2 + \Gamma_t^2} + \sqrt{\frac{1}{\gamma_t^2} + \frac{1}{\Gamma_t^2}} \right)$$

$$\begin{aligned} \text{subject to } u_i^{(1)} &= 0, \qquad && \forall i \in V_{B_0}, \\ u_i^{(1)} &= h, && \forall i \in V_{B_1}. \end{aligned} \tag{2.24}$$

The nonlinear parameterization method that solves this problem is laid out in Algorithm 1. For a visualization of the major steps of this algorithm, the reader is referred to Figure 2.5.

2.6 Results and Discussion

In this section, the linear and the nonlinear parameterization method proposed in this chapter, are analysed in terms of different distortion measures and execution time. Also, as a reference, the performance is compared with a conformal parameterization method from the literature. The method of Haker et al. [2000a] is chosen because it is easy to implement and results in maps equal to those generated by the method of Hong et al. [2006]. This method is also linear and constructs a conformal parameterization in three steps. First the $u^{(1)}$-coordinate is found as the solution of a Dirichlet problem. Then, the surface is dissected along a gradient descent path of $u^{(1)}$ from $\partial^1_{\mathcal{M}}$ to $\partial^0_{\mathcal{M}}$. Finally, the $u^{(0)}$-coordinate is obtained by a second Dirichlet problem, where the boundary conditions are provided by the conformality condition. It should be noted that a slightly improved version of Haker's algorithm is used here. Haker suggested using a vertex based gradient descent path, while in this work a smooth gradient descent path is obtained by interpolating the $u^{(1)}$-coordinate over the triangles. The choice of the path is important in Haker's method, because it will be the $u^{(0)} = 0$ iso line and it directly influences the final parameterization result. Note that for the linear method of this chapter the choice of the path does not influence the final result.

Algorithm 1 Parameterize $\mathscr{M}$ with distortion measure ξ_S

Input: $\mathscr{M}$
Output: $\boldsymbol{x}$

build progressive mesh of $\mathscr{M}$:
$\mathscr{M} \equiv \mathscr{M}^m \xrightarrow{\text{ecol}_m} \mathscr{M}^{m-1} \xrightarrow{\text{ecol}_{m-1}} \dots \xrightarrow{\text{ecol}_1} \mathscr{M}^0$
map base mesh $\mathscr{M}^0$ to $\mathscr{C}_h^2$: $\mathscr{M}^0 \to \mathscr{U}^0$
for $i = 1$ to m **do**
  introduce new vertex v_i by applying vsplit$_i$ to $\mathscr{U}^{i-1}$:
  $\mathscr{U}^{i-1} \xrightarrow{\text{vsplit}_i} \mathscr{U}^i$
  provide initial position $\boldsymbol{u}_i^0$ for v_i
  optimize position of v_i on $\mathscr{C}_h^2$, starting from $\boldsymbol{u}_i^0$:
  $\hat{\boldsymbol{u}}_i = \arg\min_{\boldsymbol{u}_i} \xi_S(\boldsymbol{u})$
  if significant increase in detail **then**
    while improvement **do** $\hat{\boldsymbol{u}}_j = \arg\min_{\boldsymbol{u}_j} \xi_S(\boldsymbol{u}),\ \forall j$
    optimize length h of $\mathscr{C}_h^2$: $h = \arg\min_h \xi_S(\boldsymbol{u})$
  end if
end for
return $\boldsymbol{x} = \boldsymbol{u}^{-1}$

population	size	avg(n)
clavicles	20	$61k$
cochleas	6	$256k$
thrombi	25	$83k$
tracheas	20	$36k$
colons	2	$650k$

Table 2.1: Data sets used in the evaluation.

2.6.1 Data Sets

A large number of data sets were used in the comparison, this in order to provide a reliable evaluation of the performance of the different methods. By the use of the marching cubes algorithm [Lorensen and Cline, 1987], the following data sets were derived from segmented ct-scans of human tissue and bone: a set of clavicles which are topologically modified to cylinders, a set of cochlear channels, a set of aortic sections with a thrombus, a set of tracheas, and two colon data sets. The number of data sets in each population together with the average number of vertices for a surface in each population is shown in Table 2.1. The methods were tested on all of these surfaces and distortion measures and execution times are reported per population, allowing for a statistical comparison.

2.6.2 Distortion Measures

In this work, the quality of a parameterization is evaluated using four distortion measures: the total Dirichlet energy ξ_D, the total stretch distortion ξ_S, the total area distortion ξ_A, and the total angle distortion ξ_C. All measures can be expressed in function of the singular values, γ_t and Γ_t, of the Jacobian of the affine maps $\boldsymbol{u}\big|_t$:

$$\xi_D(\boldsymbol{u}) = \frac{1}{2A_{\mathcal{M}}} \sum_{t \in K} \left(\gamma_t^2 + \Gamma_t^2\right) \tag{2.25}$$

$$\xi_S(\boldsymbol{u}) = \frac{\sqrt{2}}{4A_{\mathcal{M}}} \sum_{t \in K} A_t \left(\sqrt{\gamma_t^2 + \Gamma_t^2} + \sqrt{\frac{1}{\gamma_t^2} + \frac{1}{\Gamma_t^2}}\right) \tag{2.26}$$

$$\xi_A(\boldsymbol{u}) = \frac{1}{2A_{\mathcal{M}}} \sum_{t \in K} A_t \left(\gamma_t \Gamma_t + \frac{1}{\gamma_t \Gamma_t}\right) \tag{2.27}$$

$$\xi_C(\boldsymbol{u}) = \frac{1}{2A_{\mathcal{M}}} \sum_{t \in K} A_t \left(\frac{\gamma_t}{\Gamma_t} + \frac{\Gamma_t}{\gamma_t}\right) \tag{2.28}$$

All these measures have a minimal value of 1. For harmonic maps, ξ_D is minimal. When a map has no angle distortion, it is conformal and minimizes ξ_C. The area distortion measure ξ_A, on the other hand, is minimized for authalic maps. A map that preserves both angles and areas is isometric and minimizes the stretch measure ξ_S. Note that only developable surfaces can be parameterized isometrically. For a selection of parameterizations, the contribution of each triangle to the above measures will be visualized on the surface by the use of a color map. A high quality parameterization should have balanced angle and area distortions.

2.6.3 Quantitative Comparison

Each surface of the populations listed in Table 2.1 is parameterized using the linear and the nonlinear method of this chapter and also with Haker's linear method. In Figure 2.6, a box plot of the distortion measures ξ_D, ξ_S, ξ_A, and ξ_C is shown for each population and method. Figure 2.7 shows a boxplot of the execution time of each method for each population. In Figure 2.8, 2.9, and 2.10 the contribution of each triangle to the distortion measures is visualized for a sample of the trachea population, the thrombus population, and the colon population, respectively.

It should be noted that some outliers were left out of the analysis in Figure 2.6. This is done because the influence of extreme outliers on the average case would be out of proportion. These outliers are the result of jagged geometry at the boundaries of the surfaces that can only be mapped to the circular cylinder boundary with large distortions. Extreme distortions were observed at very small parts of a few surfaces and only for the linear methods. This is not surprising because strict adherence to the conformality constraint can result in extreme area distortion. From a total of 885 measurements, 15 were considered as extreme outliers.

From Figure 2.6, a number of observations can be made. On one hand, the linear methods, in comparison with the nonlinear method, generate parameterizations with less angle distortion and lower Dirichlet energy. The lowest stretch and area distortions, on the other hand, are always obtained by the nonlinear parameterization method. This is because the methods generate parameterizations by optimizing these respective measures. It can also be observed that the nonlinear method generates parameterizations that are more balanced, in terms of area and angle distortions, compared to the linear methods. This is particularly true for surfaces with large variations in cross-sectional diameter, e.g. the thrombus data sets and the colon data sets. See Figure 2.9 for a visualization of the distortions for a sample thrombus data set. In case of the colon, the area distortions were too large to visualize in the graph for the linear methods. These large distortions in area can be observed in Figure 2.10. Note that the area distortions are much smaller with the nonlinear method. This is important if the parameterization is employed for virtual colon flattening because large area distortions can result in down-sizing of important features that should not be missed during inspection. For surfaces of more or less constant circumference, both the linear and nonlinear methods generate parameterizations with low distortion. In Figure 2.8, a visual comparison is made of the parameterizations of a trachea generated by the different methods.

For conformal harmonic parameterizations, as generated by the linear methods, the Dirichlet energy ξ_D should be approximately 1. For most surfaces, this is the case for both the linear method of this chapter and the method of Haker. However, for some surfaces an increased energy was observed, particularly with Haker's method. The increased energy is caused by poor estimation of the length of the parameterization domain. The length is estimated by enforcing the conformality condition at the boundary. The method of Haker uses the boundary triangles for the conformality condition whereas the linear method of this chapter uses all triangles neighbouring a boundary vertex for the conformality condition. This difference explains the poor estimation of the length for some surfaces with Haker's method. Note that, as with the linear method of this chapter, the method of Hong et al. [2006] normally should not suffer from this problem.

From Figure 2.7, it can be seen that the nonlinear method is an order of magnitude slower compared to the linear methods. However, parameterizations with more balanced distortions are obtained in return. It can also be seen that the linear method of this work is slightly slower than Haker's method. This is due to the slow calculation of the surface path, connecting both boundaries, which is based on slow geodesic distance computations. This, however, could be replaced by a much faster path calculation, e.g. Dijkstra's shortest path algorithm, without any influence on the resulting parameterizations. The linear system of the linear method proposed in this chapter is larger compared to Haker's system, therefore, also more time is spent in solving that system.

As a closing remark, we note that both the linear conformal parameterization technique and the nonlinear stretch based parameterization technique, proposed in this chapter, are useful in their own right. The choice as to use the linear method or the nonlinear method depends on the targeted application. For example, the conformal parameterization can be employed to translate a surface based PDE into a modified 2D PDE, which is much easier to solve [Lui et al., 2005]. In this case, the introduced area distortions do not influence the result. In other applications, where area distortions are to be kept to a minimum, e.g. statistical shape modeling, one should use the nonlinear method. However, some surfaces can be mapped conformally to the cylinder without introducing large area distortions. For such cases, the conformal method can still be used. The trachea data sets, used in this chapter, are a good example of such a case.

2.7 Conclusions

In this work, two complementary methods were proposed for the parameterization of surfaces of cylindrical topology to the cylinder of length h. The proposed linear method generates harmonic conformal maps using a linear system. It can therefore generate high quality parameterizations very efficiently. In comparison with the method of Haker et al. [2000a], the linear method of this chapter turned out to be the method of choice. On one hand, the conformality condition is obeyed more closely, especially when few boundary vertices exist. On the other hand, our results do not rely on the employed path tracing method. For surfaces with large variation in cross-sectional diameter, the linear methods suffer from increased area distortions and the use of a nonlinear method is advised. It was observed that the nonlinear method of this chapter succeeds in generating parameterizations with low angle and area distortion, even for very convoluted surfaces, at the cost of a longer execution time. In contrast to previous methods, the nonlinear method of this chapter is not subject the constraints of prior surface chartifications and directly optimizes the distortion on the cylinder. Also, both the linear and the nonlinear method, proposed in this work, automatically determine the optimal length of the parameterization domain, resulting in parameterizations with the least possible distortion.

For future work, it would be interesting to develop the ultimate method that combines the speed of the linear method with the low distortions of the nonlinear method. In this respect, the work of Dong and Garland [2007] is worth noting. For surfaces of disk-like topology, low distortion parameterizations are efficiently obtained by solving a sequence of linear systems where the edge weights of the linear systems are obtained by local non-linear optimizations. All the necessary components to extend this approach to surfaces of cylindrical topology are available from this work.

Another interesting direction would be to add a constraint mechanism to

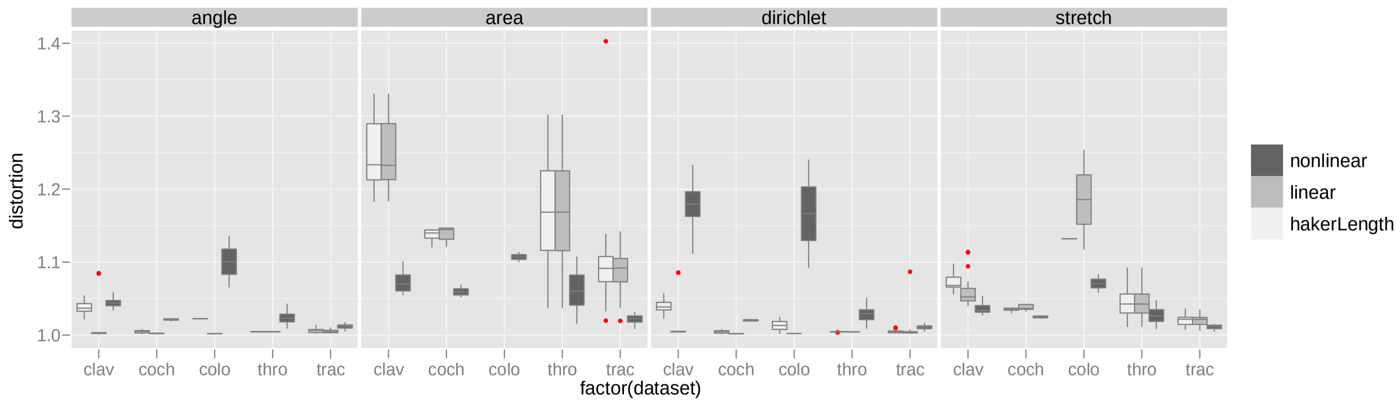

Figure 2.6: Comparison of the distortion measures for the different methods and populations. Note that a few extreme outliers were left out of the analysis. From left to right: angle distortion ξ_C, area distortion ξ_A, Dirichlet energy ξ_D, and stretch distortion ξ_S. Within each panel, the measures are grouped per population and for each population the distortions for the three methods are given in the following order, from left to right: Haker's linear method followed by the linear and the nonlinear method of this chapter.

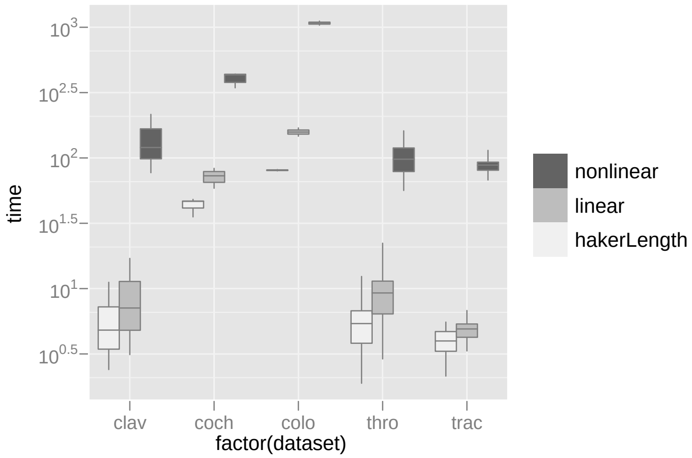

Figure 2.7: The execution time (in seconds) for the parameterization of a single surface, reported for the different populations and methods. The linear methods generate parameterizations in a matter of seconds while the nonlinear method takes a few minutes.

the parameterization methods in order to be able to predefine the map $\boldsymbol{u}$ for certain points of the surface $\mathscr{M}$. This would be particularly useful for the construction of consistent parameterizations which are used in shape modeling and analyses applications. The way that the linear parameterization problem is formulated in this work allows the addition of constraints simply by adding extra linear equations. Moreover, since the linear parameterization method of this work determines both parameterization coordinates simultaneously, it is even possible to add constraints that relate these two constraints. This is something that is not possible with previous methods.

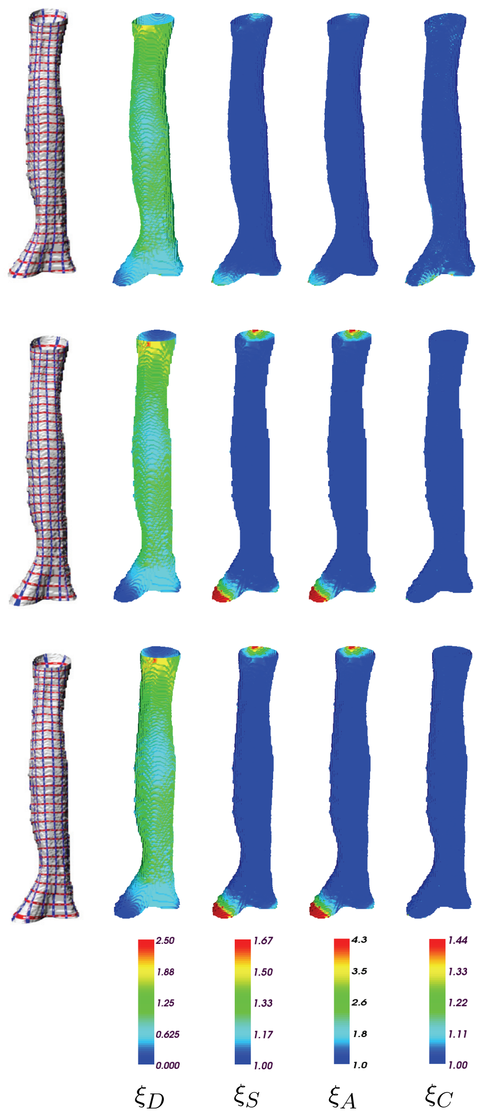

Figure 2.8: A visualization of the parameterization of a trachea surface and the contribution of the triangles to the different distortion measures. From top to bottom: parameterization generated by the nonlinear method, the linear method, and Haker's method. From left to right: a visualization of the parameterization through iso-parametric lines, followed by the visualisation of the per triangle contribution of the distortion measures ξ_D, ξ_S, ξ_A, and ξ_C. The surface has approximately constant cross-sectional diameter (except for the lowest part, where the trachea bifurcates). As a result, all methods generate acceptable parameterizations.

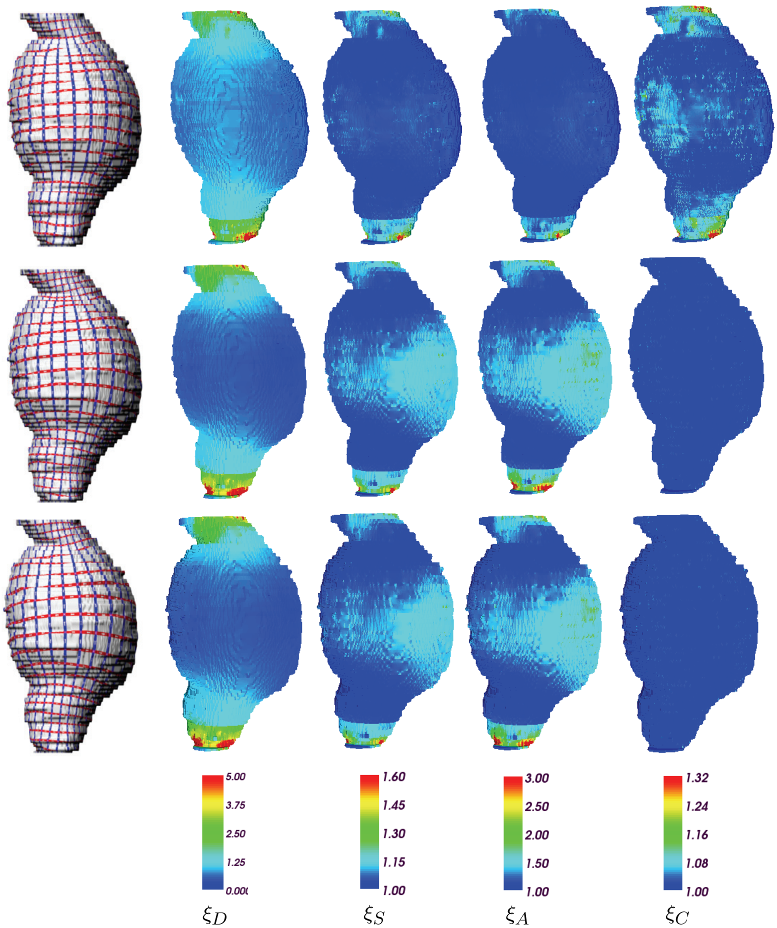

Figure 2.9: A visualization of the parameterization of a thrombus surface and the contribution of the triangles to the different distortion measures. From top to bottom: parameterization generated by the nonlinear method, the linear method, and Haker's method. From left to right: a visualization of the parameterization through iso-parametric lines, followed by the visualisation of the per triangle contribution of the distortion measures ξ_D, ξ_S, ξ_A, and ξ_C. The thrombus surface has a large variation in cross-sectional diameter. As a consequence, the linear parameterization methods suffer from significant area distortions over the whole of the surface.

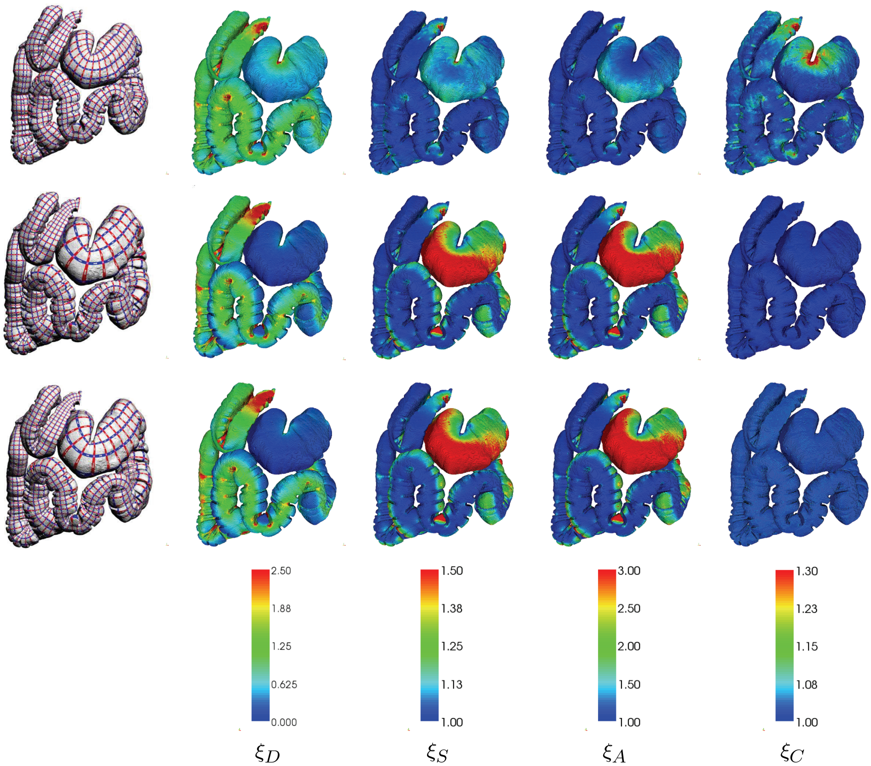

Figure 2.10: A visualization of the parameterization of a colon surface and the contribution of the triangles to the different distortion measures. From top to bottom: parameterization generated by the nonlinear method, the linear method, and Haker's method. From left to right: a visualization of the parameterization through iso-parametric lines, followed by the visualisation of the per triangle contribution of the distortion measures ξ_D, ξ_S, ξ_A, and ξ_C. The colon surface is a very convoluted surface, as a consequence, the linear parameterization methods suffer from significant area distortions over the whole of the surface.

CHAPTER 3

AUTOMATIC CONSTRUCTION OF CORRESPONDENCES FOR TUBULAR SURFACES

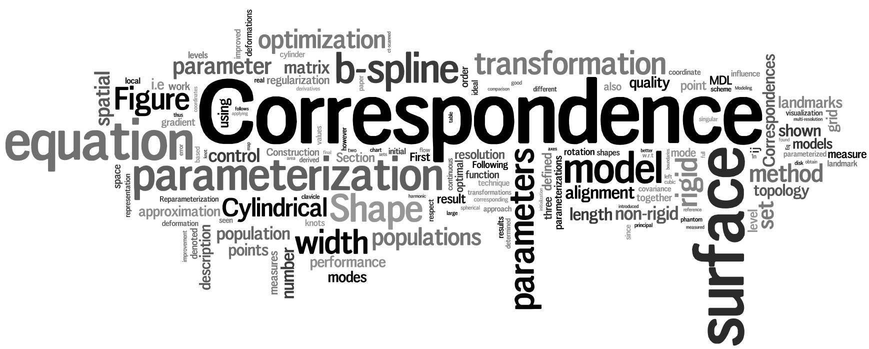

The work in this chapter has been accepted for publication in Special Issue on Shape Modeling and Analysis of the IEEE Transactions of Pattern Analysis and Machine Intelligence:

Toon Huysmans, Jan Sijbers, and Brigitte Verdonk, "Automatic Construction of Correspondences for Tubular Surfaces", 2009.

Abstract

Statistical shape modeling is an established technique and is used for a variety of tasks in medical image processing, such as image segmentation and analysis. A challenging task in the construction of a shape model is establishing a good correspondence across the set of training shapes. Especially for shapes of cylindrical topology, very little work has been done. This chapter describes an automatic method to obtain a correspondence for a set of cylindrical shapes. The method starts from an initial correspondence which is provided by cylindrical parameterization. The quality, measured in terms of the description length, of the obtained correspondence is then improved by deforming the parameterizations using cylindrical b-spline deformations and by optimization of the spatial alignment of the shapes. In order to allow efficient gradient guided optimization, an analytic expression is provided for the gradient of this quality measure with respect to the parameters of the parameterization deformation and the spatial alignment. A comparison is made between models obtained from the correspondences before and after the optimization. The results show that, in comparison with parameterization based correspondences, this new method establishes correspondences that generate models with significantly increased performance in terms of reconstruction error, generalization ability, and specificity.

3.1 Introduction

Shape correspondences and the derived statistical shape models have a wide range of applications in medical image computing [Cootes et al., 1995, Dryden and Mardia, 1998]. They have been used to analyze shape differences between different classes of objects, for example, the lateral ventricles of schizophrenics versus a healthy group [Styner et al., 2005]. They have also been employed to gain more knowledge about the anatomical variability of certain organs or bones as for example the human ear canal [Paulsen et al., 2002]. Such knowledge can in turn be used to reconstruct malformed, missing, or fractured bone structures [Zachow et al., 2005]. A widespread application of statistical shape models is their use as prior knowledge in automatic image segmentation [Kelemen et al., 1999, Cootes et al., 1994, de Bruijne et al., 2004]. The probability density function of the shape is estimated from a set of manual segmentations. This knowledge is then used to guide the segmentation process of an unseen instance and to restrict the segmentation result to the class of plausible shapes.

The major hurdle in the construction of a statistical shape model is establishing a dense correspondence over the surfaces of a large set of training shapes. These correspondences should be of high quality, i.e. the correspondence should match anatomically equivalent points over the surfaces. If this requirement is not met, artificial modes of variation are introduced into the shape model and this has a negative effect on the performance of the model when used for image segmentation or interpretation [Styner et al., 2003].

For 2D shapes, a correspondence between the boundary curves of the individual shapes is often defined by manual landmarking [Bookstein, 1991]. Although this approach is feasible, it turns out to be a time consuming and error prone task. In principle, the approach can be extended to 3D but it becomes highly impractical due to the large amount of landmarks that need to be located and the increased level of difficulty in pin-pointing them. Several approaches have been proposed to automate this labor intensive procedure.

A relatively simple but effective approach is to establish the sought-after correspondence by means of surface parameterization [Floater, 1997, Brechbühler et al., 1995, Praun and Hoppe, 2003, Huysmans et al., 2005, Eck et al., 1995, Lamecker et al., 2002, 2004]. Thereby, a one-to-one map is constructed between each surface of the set and some common, predefined and usually mathematically simple parameter domain, such as a planar disc or a sphere. For each surface, the obtained one-to-one map associates a 2D parameter coordinate with each point of the 3D surface. The surface-to-surface correspondence is then defined by the assigned parameter values i.e., points between the surfaces correspond when they share the same parameters.

Although the parameterization approach produces valid correspondences, there is still room for improvement. The parameterization of each shape in the training set is done independently of the other shapes, thus correlations between the shapes are not taken into account. When an approach takes this extra information into account, it can obtain better correspondences. Surface parameterization can provide a good initial correspondence for such a method. Such a correspondences method was developed in Davies et al. [2002b]. They use the description length of the derived shape model as a measure of correspondence quality and optimize the correspondences with respect to this criterion. To date, their minimum description length (MDL) approach is considered the method of choice for the construction of correspondences [Styner et al., 2003].

Most of the aforementioned techniques focus on sets of surfaces of *spherical* topology since these are prevalent in biomedical image processing, e.g. kidneys, liver, and brain ventricles. Nonetheless, the developed principles can be translated to surfaces of other topologies. More specifically, this chapter deals with the translation of these principles to sets of surfaces of *cylindrical* topology, such as the trachea, cochlear channels, aortic aneurysms and the rectum. For such surfaces, the cylinder is the natural choice for the parameter domain. An initial correspondence is obtained by specialized cylindrical parameterization techniques. Following this, the correspondence is improved by an optimization framework that adopts the MDL criterion as a measure of correspondence quality.

The remainder of this chapter is organized as follows. Related work is discussed in Section 3.1.1. An overview of the correspondence method is given in Section 3.2. Parameterization of surfaces of cylindrical topology is discussed in Section 3.3. The measure of correspondence quality, namely description length, is treated in Section 3.4. Section 3.5 details the procedure of how an initial correspondence is obtained and Section 3.6 elaborates on the correspondence optimization. Experimental results of applying the method to a number of phantoms and real data sets are presented and discussed in Section 3.7. Section 3.8

concludes the chapter.

3.1.1 Related Work

Parameterization of surfaces with disc-like topology onto a planar convex region has been addressed in Floater [1997]. A parameterization technique to parameterize surfaces of spherical topology onto the sphere has been developed in Brechbühler et al. [1995] and is known as SPHARM. This was later used to model the shape of brain structures for segmentation [Kelemen et al., 1999] and analysis [Styner et al., 2005]. Conformal parameterization techniques for surfaces of spherical topology were introduced in Hurdal et al. [1999], Gotsman et al. [2003], Gu et al. [2004]. A more efficient alternative to SPHARM, utilizing a progressive surface representation, was provided by Praun and Hoppe [2003]. Based on this spherical parameterization technique, Huysmans et al. [2005] have developed a cylindrical parameterization technique to parameterize tubular surfaces onto the cylinder in a progressive way. Conformal parameterization of surfaces of cylindrical topology was addressed in Haker et al. [2000a], Hong et al. [2006], Huysmans and Sijbers [2009]. Algorithms for more complex topologies (genus-n) have also been proposed [Eck et al., 1995, Lamecker et al., 2002, 2004] but, from a correspondence optimization point of view, these algorithms are suboptimal since they rely on a heuristic or manually defined surface chartification. In Jin et al. [2008], Ricci flow is used to construct a seamless periodic tiling of a genus-n surface in the plane, sphere, or hyperbolic space and it is known as the universal covering space. The obtained map is angle preserving and can be used to construct harmonic maps between surfaces of the same topology [Li et al., 2008].

Kotcheff and Taylor [1998] used the determinant of the landmark covariance matrix as an optimization objective. Based on their ideas, Davies et al. [2002b] developed a minimum description length (MDL) formulation for the assessment of correspondence quality for 2D curves, which was later simplified by Thodberg [2003]. The method for building MDL correspondences has been extended to surfaces of spherical topology [Davies et al., 2002a], which was later improved in Heimann et al. [2005] in terms of computational efficiency. Horkeaw and Yang applied the MDL principle to surfaces of disc-like topology [Horkaew and Yang, 2004] and an extension to more complex topologies was obtained by cutting surfaces into topological discs prior to optimization [Horkaew and Yang, 2003a]. This of course constrains the optimization along the cuts. In the recent work of Li et al. [2008], a globally optimal map, in terms of harmonic energy, is obtained between two surfaces sharing arbitrary complex topology. An extension of their method to populations of surfaces and to other correspondence metrics, e.g. MDL, is, however, not addressed. Recently introduced point-based correspondence techniques can also handle arbitrary topology. In Ferrarini et al. [2007], self organising maps were used to obtain a pairwise correspondence between each population member and a template. In

Cates et al. [2007], particle systems were used to optimize geometry sampling and groupwise correspondence with respect to an information theoretic measure comparable to MDL. Point-based correspondence techniques are promising but problems occurring with highly convoluted surfaces still need to be addressed.

Little work has been done in shape modeling for cylindrical surfaces. In de Bruijne et al. [2003], an improved modeling scheme for tubular objects was proposed. They used a manually determined correspondence. Some of the previously discussed techniques could be employed to build a correspondence for a set of cylindrical shapes. For example, the spherical MDL framework can be applied when the holes of the cylindrical shapes are closed but this can result in an invalid correspondence at the boundaries and this approach will not perform well for elongated surfaces [Huysmans et al., 2006]. The correspondence methods that rely on chartification [Horkaew and Yang, 2003a, Lamecker et al., 2002] could also be applied to cylindrical surfaces but obviously the performance of the chartification heuristic will influence the final quality. The method proposed in this chapter does not suffer from these drawbacks since, here, the description length minimization method is translated specifically to treat sets of surfaces of cylindrical topology.

3.2 Method Outline

The method, treated in this chapter, constructs a dense surface correspondence together with an optimal spatial alignment for an arbitrary population of cylindrical surfaces. It proceeds in two steps. First, a correspondence is derived from the surface parameterizations by alignment of the surfaces and parameterizations. The result is referred to as the *rigid correspondence*. Then, the rigid correspondence is improved by applying local, non-rigid, deformations to the parameterizations while keeping the surfaces optimally aligned. The finally obtained correspondence is referred to as the *non-rigid correspondence*. An overview of these two steps can be found in Figure 3.1 and Figure 3.2.

The input to the method is a set of n_s triangle surfaces $\{\mathcal{M}_1, \ldots, \mathcal{M}_{n_s}\}$ of cylindrical topology. Each surface $\mathcal{M}_i$ is defined by a tuple (V_i, T_i), where V_i is the set of n_{V_i} vertices $\{\boldsymbol{v}_1^i, \ldots, \boldsymbol{v}_{n_{V_i}}^i\}$ with $\boldsymbol{v}_j^i \in \mathbb{R}^3$ and T_i is the set of n_{T_i} triangles $\{t_1^i, \ldots, t_{n_T}^i\}$.

The construction of the rigid correspondence is covered by the flow chart in Figure 3.1 and presented in detail in Section 3.5. The rigid correspondence, denoted as $\{\boldsymbol{x}_1, \ldots, \boldsymbol{x}_{n_s}\}$, is obtained by parameterization of the surfaces $\mathcal{M}_i$, followed by rigid alignment of the surfaces and their parameter spaces. The spatial transformations for the alignment of the surfaces are denoted $\boldsymbol{\tau}^\circ(\bullet|\boldsymbol{\Phi}_i^{\tau^\circ})$ and the parameterization transformations for the parameter space alignments are denoted $\boldsymbol{\rho}^\circ(\bullet|\boldsymbol{\Phi}_i^{\rho^\circ})$. In order to avoid convergence to local minima, the optimal parameters $\hat{\boldsymbol{\Phi}}_i^{\tau^\circ}$ and $\hat{\boldsymbol{\Phi}}_i^{\rho^\circ}$ of these transformations are obtained by a number of consecutive optimizations with respect to the MDL correspondence quality criterion, denoted μ. The construction pipeline for the rigid correspondence comprises following steps:

1. A cylindrical parameterization $\boldsymbol{x}_i^\circ$ is constructed for each surface $\mathscr{M}_i$. It constitutes a one-to-one map between the surface $\mathscr{M}_i$ and the open-ended cylinder $\mathscr{C}_h^2$ of height h.
2. A smooth b-spline approximation $\tilde{\boldsymbol{x}}_i^\circ$ is constructed for each surface. The b-spline representation results in smooth optimization objectives and provides a multi-resolution representation of the surface.
3. An initial spatial alignment of the surfaces is obtained by alignment of their principal axes.
4. While keeping the spatial alignment fixed, an alignment of the parameterizations is determined by optimization with respect to MDL.
5. Both the spatial and parameter space alignments are improved by simultaneous optimization with respect to MDL.

In order to obtain the rigid correspondence, the optimal spatial transformations and parameterization transformations are applied to the b-spline approximations of each of the parameterized surfaces:

$$\boldsymbol{x}_i = \boldsymbol{\tau}^\circ(\bullet|\hat{\boldsymbol{\Phi}}_i^{\tau^\circ}) \circ \tilde{\boldsymbol{x}}_i^\circ \circ \boldsymbol{\rho}^\circ(\bullet|\hat{\boldsymbol{\Phi}}_i^{\rho^\circ}). \tag{3.1}$$

The construction of non-rigid correspondence is covered by the flow chart in Figure 3.2 and is presented in detail in Section 3.6. The non-rigid correspondence is obtained as an improvement of the rigid correspondence by applying a non-rigid b-spline transformation to the parameter space of each surface and simultaneously optimizing their spatial alignment. Again, the MDL correspondence criterion was used as the optimization objective. For reasons of efficiency and in order to avoid local minima, the optimization is done successively at a number of resolution levels. With each resolution level L, the grid size $m_{u^{(0)}}^L \times m_{u^{(1)}}^L$ for the b-spline approximation $\tilde{\boldsymbol{x}}_i^L$ of $\boldsymbol{x}_i$ and the grid size $n_{u^{(0)}}^L \times n_{u^{(1)}}^L$ for the b-spline parameterization deformation $\boldsymbol{\rho}^L(\bullet|\boldsymbol{\Phi}_i^{\rho^L})$ is doubled, allowing for a more detailed correspondence improvement. Also, the number of landmarks n_p^L used to calculate the shape model is increased and the convergence tolerance becomes more strict. The spatial transformation $\boldsymbol{\tau}(\bullet|\boldsymbol{\Phi}_i^{\tau^L})$ is rigid and has optimal parameters $\boldsymbol{\Phi}_i^{\tau^L}$. The optimization of a resolution level L is initialized with the result from the previous resolution level $L-1$. The final correspondence is obtained from the optimal transformation parameters $\hat{\boldsymbol{\Phi}}_i^{\tau^L}$ and $\hat{\boldsymbol{\Phi}}_i^{\rho^L}$ of the last resolution level:

$$\hat{\boldsymbol{x}}_i^L = \boldsymbol{\tau}(\bullet|\hat{\boldsymbol{\Phi}}_i^{\tau^L}) \circ \tilde{\boldsymbol{x}}_i^L \circ \boldsymbol{\rho}^L(\bullet|\hat{\boldsymbol{\Phi}}_i^{\rho^L}). \tag{3.2}$$

From the final correspondence $\{\hat{\boldsymbol{x}}_1, \ldots, \hat{\boldsymbol{x}}_{n_s}\}$, a map from surface $\mathscr{M}_i$ to surface $\mathscr{M}_j$ can be obtained by composition of the inverse of parameterization $\hat{\boldsymbol{x}}_i$ with the parameterization $\hat{\boldsymbol{x}}_j$, i.e. $\boldsymbol{q} = \hat{\boldsymbol{x}}_j \circ \hat{\boldsymbol{x}}_i^{-1}(\boldsymbol{p})$, where $\boldsymbol{p} \in \mathscr{M}_i$ and the corresponding point $\boldsymbol{q} \in \mathscr{M}_j$.

3.3 Surface Representation

3.3.1 Parameterization

Starting from a cylindrical surface $\mathscr{M}$ defined by its vertices V and triangles T, a parameterized version $\boldsymbol{x}$ of $\mathscr{M}$ is obtained by assigning a unique pair of cylindrical coordinates to each point of the surface $\mathscr{M}$. Usually, the parameter coordinates are only defined explicitly at the vertices of $\mathscr{M}$ and the extension over the triangles is implied by barycentric interpolation of the parameter coordinates at the vertices. To be more precise, for surfaces of cylindrical topology, the parameterization $\boldsymbol{x}$ is a homeomorphic function from $\mathscr{C}_h^2$ to the surface $\mathscr{M}$, i.e.:

$$\begin{aligned} \boldsymbol{x} \quad &: \quad [0, 2\pi] \times [0, h] \to \mathscr{M} \subset \mathbb{R}^3 \\ &: \quad \boldsymbol{u} \to \boldsymbol{x}(\boldsymbol{u}), \end{aligned}$$

where $\mathscr{C}_h^2$ denotes the open-ended two-dimensional cylinder of length h with unit radius, which is parameterized by an angular coordinate $u^{(0)}$ and an axial coordinate $u^{(1)}$, i.e. $\boldsymbol{u} = (u^{(0)}, u^{(1)})$. For $\boldsymbol{x}$ to be a homeomorphism, it must be a bijective, continuous function, and have a continuous inverse. If the topology of $\mathscr{M}$ is consistent, such a homeomorphism can always be obtained although a solution is not unique. This can be seen from the fact that the composition $\boldsymbol{x} \circ \boldsymbol{\rho}$ of any automorphism $\boldsymbol{\rho}$ of the cylinder with the parameterization $\boldsymbol{x}$ of the surface $\mathscr{M}$, again is a valid parameterization of the same surface. The particular solution that a parameterization technique will propose is usually the result of the minimization of an energy functional. Different functionals result in different parameterizations, the quality of which depends on the actual application.

In order to obtain good correspondences between surfaces, a parameterization technique should create similar maps for similar surfaces. In addition, it is also desirable that it retains relative areas and angles as much as possible (i.e. distortion). When the parameterizations systematically suffer from large area distortions, undersampling of parts of the surface can occur in the final correspondence. For a tubular surface with an approximately constant width, the use of an harmonic parameterization technique is recommended, e.g. [Haker et al., 2000a, Hong et al., 2006]. The harmonic cylindrical parameterization is uniquely defined as the solution of a system of linear equations. As a consequence, it is computationally very efficient. However, it fails to keep area distortions within acceptable bounds when large variation in cross-sectional diameter is present. For these cases, the progressive non-linear cylindrical parameterization technique from Huysmans et al. [2005] is a better alternative. It

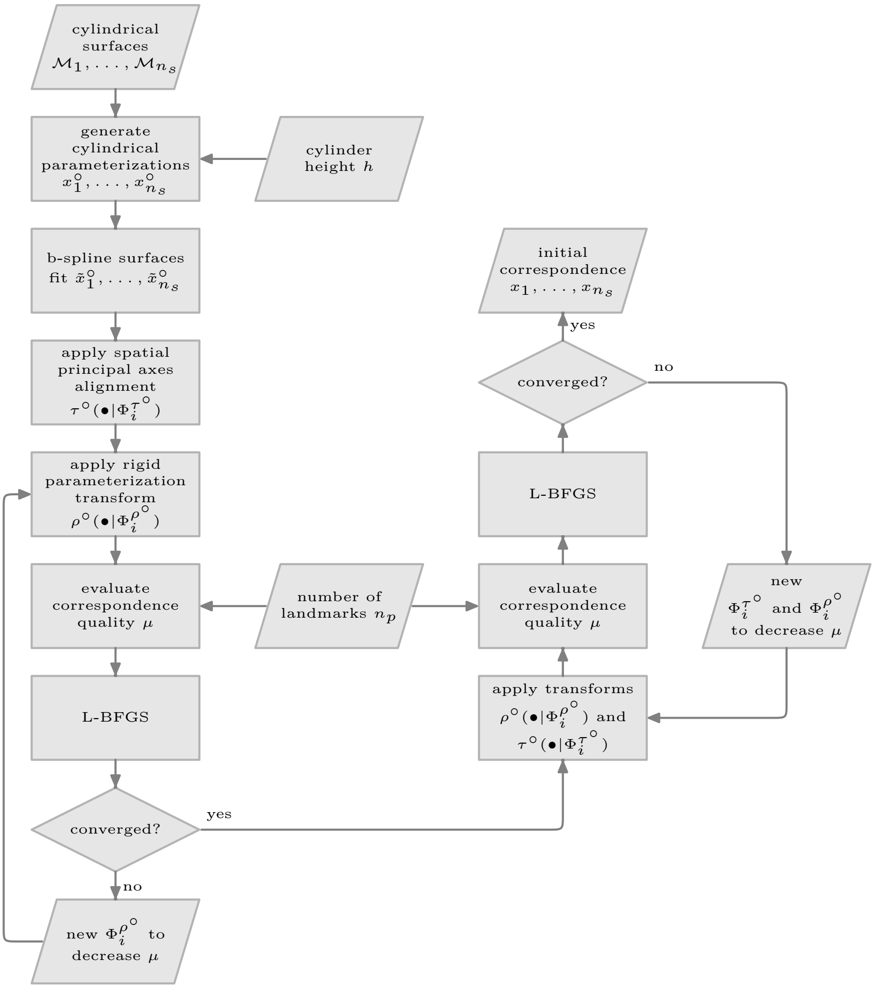

Figure 3.1: Flow chart visualization of the rigid correspondence construction. First, each surface is equipped with a cylindrical parameterization and approximated with a b-spline surface. Then, the surfaces are brought into a reference coordinate system by alignment of their principal axes. This is followed by the alignment of the parameter spaces of the surfaces by optimization w.r.t. the correspondence quality i.e., model description length. Finally, the rigid correspondence is obtained after a second optimization, where both the spatial and parameterization alignment parameters are set free.

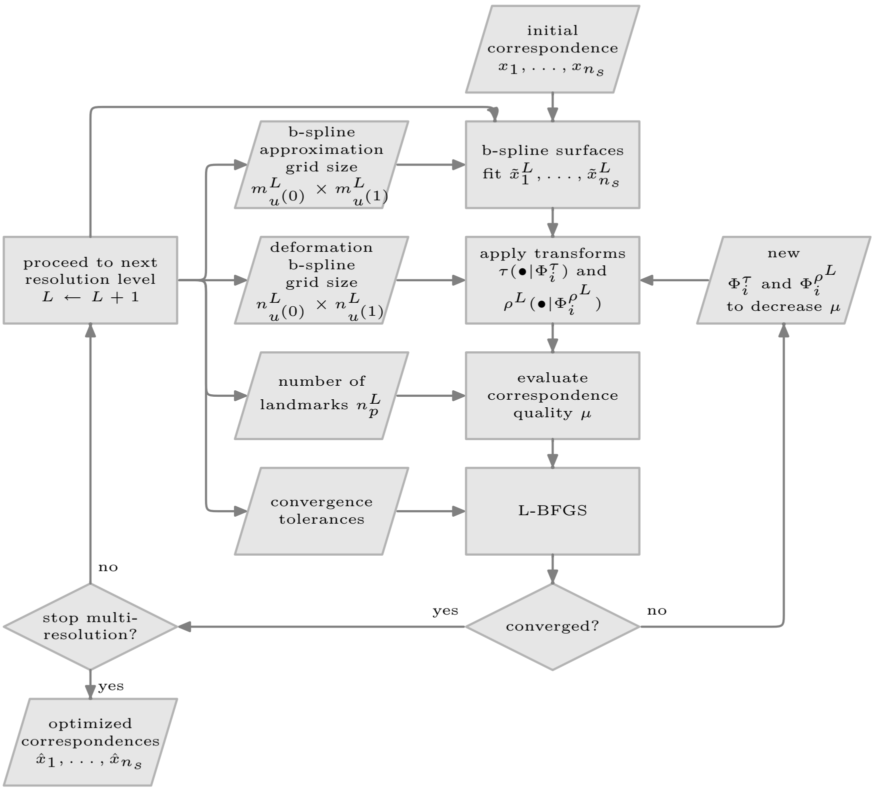

Figure 3.2: Flow chart visualization of the non-rigid correspondence improvement. The correspondence is improved by simultaneously optimizing the parameters of the spatial alignments and the b-spline parameterization deformations w.r.t. the correspondence quality. The optimization is performed at multiple resolution levels sequentially, starting at the lowest level with coarse deformations and gradually adding more detail with each new level. Finally, the non-rigid correspondence is obtained.

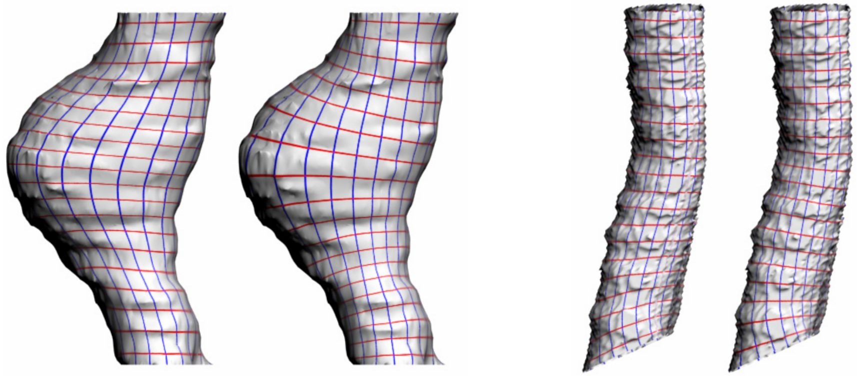

(a) (b)

Figure 3.3: A qualitative comparison of the harmonic parameterization method with the non-linear parameterization method. The parameterization of each surface is visualized by the blue and red lines which correspond to the iso-$u^{(0)}$ and iso-$u^{(1)}$ lines of the cylinder, respectively. In (a), two parameterizations of a surface with a large variation in cross-sectional diameter are shown. It is clearly visible that the harmonic parameterization (right) has large area distortions at the bulge compared to the non-linear method (left), so the non-linear method is preferred for this kind of surfaces. In (b), two parameterizations of a surface with an approximately constant cross section diameter are shown. For this surface, both methods can be used since they approximately perform equally well.

allows control over the trade-off between angle and area distortions, at the cost of an increased computation time. See Figure 3.3 for a comparison of the two methods.

3.3.2 B-Spline Representation

Since the surface $\mathscr{M}$ is a piecewise linear surface, the partial derivatives of the surface coordinates with respect to the parameter coordinates ($\frac{\partial \boldsymbol{x}}{\partial u^{(0)}}$ and $\frac{\partial \boldsymbol{x}}{\partial u^{(1)}}$) are discontinuous at the triangle boundaries, excluding boundaries between coplanar triangles. This is undesirable since these partial derivatives are utilized in the gradient guided optimization of the correspondences. Using cubic b-splines, approximation of $\boldsymbol{x}$ will result in a surface $\tilde{\boldsymbol{x}}$ that is $\mathscr{C}^2$ continuous within the b-spline patches and $\mathscr{C}^1$ continuous at the patch boundaries. By varying the number of control points used for the approximation, a multiresolution representation of the surface can be obtained. Moreover, evaluation of the b-spline representation $\tilde{\boldsymbol{x}}$ is much faster than evaluation of the triangle based representation $\boldsymbol{x}$. This is because point location in a regular grid is far more efficient than point location in a triangulation. A good b-spline approximation of $\boldsymbol{x}$ can be achieved with a number of control points much lower than the original number of vertices that $\boldsymbol{x}$ comprises, resulting also in better memory efficiency.

The approximation uses a 2D tensor product b-spline surface. The cubic b-spline kernel, denoted β, is defined as in Bartels et al. [1987]:

$$\beta(u) = \begin{cases} \frac{1}{6}(3|u|^3 - 6u^2 + 4), & |u| \in [0,1[\\ \frac{1}{6}(2-|u|)^3, & |u| \in [1,2[\\ 0, & |u| \in [2,\infty[\end{cases} . \tag{3.3}$$

The b-spline surface is defined by a uniform grid of knots $K = \{\boldsymbol{k}_{ij}\}$ positioned on the cylinder $\mathscr{C}_h^2$ and a corresponding grid of control points $P = \{\boldsymbol{p}_{ij}\}$ in $\mathbb{R}^3$. An example knot grid is shown in Figure 3.5a. The b-spline surface then has the following form:

$$\tilde{\boldsymbol{x}}(\boldsymbol{u}|K,P) = \sum_{i=-1}^{m_{u^{(0)}}+1} \sum_{j=-1}^{m_{u^{(1)}}} \beta\left(\frac{\boldsymbol{u}-\boldsymbol{k}_{ij}}{\boldsymbol{\Delta}}\right)\boldsymbol{p}_{ij}, \tag{3.4}$$

where $m_{u^{(0)}}$ is the number of knots in the $u^{(0)}$-direction and $m_{u^{(1)}}$ is the number of knots in $u^{(1)}$-direction that are within the range $[0,2\pi] \times [0,h]$. The 2D cubic b-spline kernel $\beta(\boldsymbol{u})$ is separable, i.e. $\beta(\boldsymbol{u}) = \beta(u^{(0)})\beta(u^{(1)})$ and the grid spacing is denoted as $\boldsymbol{\Delta} = (\frac{2\pi}{n_{u^{(0)}}}, \frac{h}{n_{u^{(1)}}-1})$. The division in the argument of the b-spline kernel is executed element-wise. In order to obtain a closed and smooth surface at the parameter boundary $u^{(0)} = 2\pi$, the control points satisfy the the following conditions:

$$\begin{cases} \boldsymbol{p}_{-1,j} & = & \boldsymbol{p}_{m_{u^{(0)}}-1,j} \\ \boldsymbol{p}_{m_{u^{(0)}},j} & = & \boldsymbol{p}_{0,j} \\ \boldsymbol{p}_{m_{u^{(0)}}+1,j} & = & \boldsymbol{p}_{1,j} \end{cases} \tag{3.5}$$

Least squares fitting is used in order to find a set of $m_{u^{(0)}}(m_{u^{(1)}}+2)$ control points that provides a good approximation to the surface $\boldsymbol{x}$. For this purpose, a set of m_p uniformly distributed parameter locations is chosen on the cylinder: $\boldsymbol{U}^{m_p} = \{\boldsymbol{u}_1,\ldots,\boldsymbol{u}_{m_p}\} \subset \mathscr{C}_h^2$. Using these parameter locations, the approximation error can be determined as the sum of the squared distances between the points on the original surface and the points on the approximating surface at corresponding parameter locations. The set of control points $\hat{P}$ for which this error is minimal, is regarded as the optimal set in a least squares sense:

$$\hat{P} = \arg\min_P \sum_{i=1}^{m_p} ||\tilde{\boldsymbol{x}}(\boldsymbol{u}_i|K,P) - \boldsymbol{x}(\boldsymbol{u}_i)||^2 \tag{3.6}$$

The minimum is found as the solution of the system $BP = X$, where X is a $m_p \times 3$ matrix having surface points $\{\boldsymbol{x}(\boldsymbol{u}_i)\}$ as its rows, P is a $m_{u^{(0)}}(m_{u^{(1)}}+2)\times 3$ matrix having the control points $\{\boldsymbol{p}_{ij}\}$ as its rows, and B is a $m_p \times m_{u^{(0)}}(m_{u^{(1)}}+2)$ matrix.

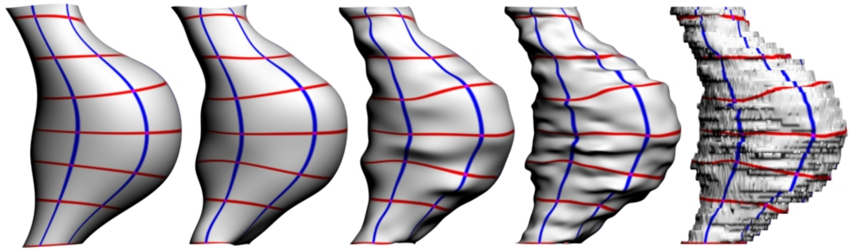

Figure 3.4: Approximation of a parameterized surface using a b-spline surface with an increasing number of control points (indicated as $m_{u^{(0)}} \times m_{u^{(1)}}$).

Note that B_{kl} is the contribution of the l-th control point P_l to the approximation of the k-th surface point X_k. The solution is obtained efficiently from the normal equations $B^T BP = B^T X$ [Lloyd et al., 1997]. In Figure 3.4, a surface is shown together with four cylindrical b-spline approximations obtained using an increasing number of control points.

3.4 Correspondence Quality Measure

In this work, the quality of the correspondence of a set of surfaces is measured by the description length of the shape model that was built from the correspondence. The actual computation of the description length can be divided into three steps. First, each surface is represented with a set of corresponding landmarks. Then, the point distribution model (PDM) is calculated from these landmarks. This PDM consists of a mean surface, a set of shape modes and, the variance expressed by each of these modes. Finally, the description length is calculated from the obtained shape mode variances. The following three sections expound these steps.

3.4.1 Statistical Modeling

In order to build a statistical shape model or a point distribution model [Cootes et al., 1995] for a set of n_s surfaces $\{\mathcal{M}_i\}$, a correspondence needs to be established and the surfaces have to be aligned in a common reference coordinate system. Suppose that $\{\boldsymbol{x}_i\}$ are the parameterizations that express this correspondence in the common reference coordinate system. Then, the goal of statistical shape modeling is to capture the shape present in the set of surfaces with a probability density function. Here, a distribution is assumed that is symmetric about its mean namely a multivariate Gaussian distribution and the actual distribution parameters are obtained using principal components analysis (PCA) [Jolliffe, 2002].

In this work, the computation of the PCA is done by means of singular value decomposition (SVD). This is more efficient than the traditional method where an eigenvalue decomposition of the large covariance matrix is used. The SVD method also allows the computation of the partial derivatives of the shape mode variances w.r.t. the landmark positions, which is important for the gradient based optimization. A matrix representation of the set of surfaces $\{\boldsymbol{x}_i\}$ is obtained by sampling each surface at a set of uniformly distributed cylindrical parameter locations $\boldsymbol{U}^{n_p} = \{\boldsymbol{u}_1, \ldots, \boldsymbol{u}_{n_p}\}$. For each surface, the coordinates of the n_p landmarks are concatenated and a $3n_p$ row vector $\dot{\boldsymbol{x}}_i$, representing the surface $\boldsymbol{x}_i$, is obtained:

$$\dot{\boldsymbol{x}}_i = [\boldsymbol{x}_i(\boldsymbol{u}_1) \ldots \boldsymbol{x}_i(\boldsymbol{u}_{n_p})]. \tag{3.7}$$

The landmark matrix $\boldsymbol{X}$ is then obtained from the n_s shape vectors as $\boldsymbol{X} = [\dot{\boldsymbol{x}}_1^T \ldots \dot{\boldsymbol{x}}_{n_s}^T]$, resulting in a matrix of dimensions $3n_p \times n_s$. The mean shape vector $\bar{\boldsymbol{x}}$ is computed as

$$\bar{\boldsymbol{x}} = \frac{1}{n_s} \sum_{i=1}^{n_s} \dot{\boldsymbol{x}}_i \tag{3.8}$$

and the row centered landmark matrix is obtained by subtracting this mean shape from each column of $\boldsymbol{X}$, i.e.

$$\boldsymbol{X}_c = [\dot{\boldsymbol{x}}_1^T - \bar{\boldsymbol{x}}^T \ldots \dot{\boldsymbol{x}}_{n_s}^T - \bar{\boldsymbol{x}}^T]. \tag{3.9}$$

Now, let the SVD of the centered landmark matrix be defined as

$$\frac{1}{\sqrt{n_s - 1}} \boldsymbol{X}_c = \boldsymbol{P}\boldsymbol{S}\boldsymbol{Q}^T, \tag{3.10}$$

where $\boldsymbol{P}$ is a $3n_p \times 3n_p$ orthonormal matrix containing the left singular vectors $\boldsymbol{p}_j$ as its columns, $\boldsymbol{S}$ is a $3n_p \times n_s$ diagonal matrix where the diagonal elements are the singular values σ_j in descending order, and $\boldsymbol{Q}$ is an $n_s \times n_s$ orthonormal matrix with the right singular vectors $\boldsymbol{q}_j$ as its columns. The $n_s \times n_s$ surface covariance matrix $\boldsymbol{D}$ is defined as

$$\boldsymbol{D} = \frac{1}{n_s - 1} \boldsymbol{X}_c^T \boldsymbol{X}_c = \boldsymbol{Q}\boldsymbol{S}^2\boldsymbol{Q}^T \tag{3.11}$$

and its SVD can be calculated efficiently. The first m columns of $\boldsymbol{P}$, denoted as $\boldsymbol{P}_m$, contain the m shape modes $\boldsymbol{p}_j$ and they are obtained from the SVD of $\boldsymbol{D}$ as

$$\boldsymbol{P}_m = \frac{1}{\sqrt{n_s - 1}} \boldsymbol{X}_c \boldsymbol{Q} \boldsymbol{S}_m^{-1}, \tag{3.12}$$

where $\boldsymbol{S}_m$ is the matrix that contains the first m rows of $\boldsymbol{S}$. The first m corresponding shape mode variances λ_j are also obtained from Eq. (3.11) as the first m squared non-zero singular values σ_j^2.

Using the obtained shape modes $\boldsymbol{p}_j$ and the corresponding mode variances λ_j, a new shape instance $\dot{\boldsymbol{x}}$ can be obtained by adding a linear combination of the principal shape modes to the mean surface:

$$\dot{\boldsymbol{x}} = \bar{\boldsymbol{x}} + \sum_{j=1}^{n_s-1} \boldsymbol{p}_j b_j, \tag{3.13}$$

where b_j is the contribution of the j-th principal shape mode to $\dot{\boldsymbol{x}}$. Equation (3.13) defines a shape space spanned by the shape parameters b_j and with the mean shape as the origin. The bounds on the shape parameters of the shape space are usually chosen as a small multiple of the standard deviation of the point cloud along that direction, i.e. $-3\sqrt{\lambda_j} \leq b_j \leq +3\sqrt{\lambda_j}$.

In what follows, $\boldsymbol{\Lambda}$ will denote the function that maps a set of corresponded surfaces to the mode variances of their derived shape model:

$$(\lambda_1, \ldots, \lambda_{n_s-1}) = \boldsymbol{\Lambda}(\boldsymbol{x}_1, \ldots, \boldsymbol{x}_{n_s} | \boldsymbol{U}^{n_p}). \tag{3.14}$$

3.4.2 Description Length

In Davies et al. [2002b], a correspondence measure for curves and surfaces is introduced which is regarded as the current standard for correspondence optimization. Their measure is adopted here but in a simplified form. The original measure is based on the minimum description length principle: the sampled surfaces are coded in a message where the encoding is determined by the PCA model built from the correspondence. The total message length of the encoded surfaces, together with the encoded model, determine the quality of the model and therefore also the quality of the correspondence. In this way, a trade-off is made between model complexity and goodness-of-fit. Over the years, the MDL measure has been tuned and in this work the simplified MDL measure, introduced in [Thodberg, 2003], is used. It is a function of the shape mode variances λ_j and is defined as follows:

$$\mu(\lambda_1, \ldots, \lambda_{n_s-1}) = \sum_{\lambda_i \geq \lambda_c} \left(1 + \log \frac{\lambda_i}{\lambda_c}\right) + \sum_{\lambda_i < \lambda_c} \frac{\lambda_i}{\lambda_c}, \tag{3.15}$$

The free parameter λ_c is set to be the expected noise variance in the data. The variation captured by all modes with an eigenvalue (variance) below λ_c is thus considered noise. As can be seen from the first and the second term in Equation (3.15) respectively, the benefit of decreasing normal modes is logarithmic while for noise modes it is constant. Furthermore, the quality measure μ goes to zero when all eigenvalues go to zero, i.e. it favors compact models. Also, both μ and its partial derivatives $\frac{\partial \mu}{\partial \lambda_i}$ are continuous. This is an attractive property for optimization. Note that shorter description length, i.e. a lower value of μ, indicates better quality of correspondence.

3.4.3 Gradient of Description Length

The L-BFGS minimizer used in this work requires not only the value of the objective μ but also the gradient $\nabla\mu$. In this section, the gradient with respect to the landmark positions x_{ij} is derived. In Ericsson and Åström [2003], it is explained how to obtain the partial derivatives of the description length μ w.r.t. centered the landmark positions x^c_{ij}. Their derivation is based on a result obtained in Papadopoulo and Lourakis [2000]. This result is a simple expression, in function of the elements p_{ik} of $\boldsymbol{P}$ and q_{kj} of $\boldsymbol{Q}$, for the derivative of the singular values σ_k of X_c w.r.t. the matrix values x^c_{ij}, namely:

$$\frac{\partial \sigma_k}{\partial x^c_{ij}} = p_{ik} q_{kj}. \tag{3.16}$$

The partial derivatives of the description length w.r.t. the non-centered landmarks x_{ij} can be obtained as:

$$\frac{\partial \mu}{\partial x_{ij}} = \sum_{\lambda_k \geq \lambda_c} \frac{1}{\lambda_k} \frac{\partial \lambda_k}{\partial x_{ij}} + \sum_{\lambda_k < \lambda_c} \frac{1}{\lambda_c} \frac{\partial \lambda_k}{\partial x_{ij}}. \tag{3.17}$$

The derivatives of the shape mode variances λ_k can be refined into:

$$\frac{\partial \lambda_k}{\partial x_{ij}} = 2\sigma_k p_{ik} q_{kj} - \frac{2}{n_s} \sigma_k p_{ik} \sum_{\jmath} q_{k\jmath}, \tag{3.18}$$

where Equation (3.16) was used together with the fact that

$$\frac{\partial x^c_{\imath\jmath}}{\partial x_{ij}} = \begin{cases} 1 - \frac{1}{n_s} & \text{if } \imath = i \text{ and } \jmath = j \\ -\frac{1}{n_s} & \text{if } \imath = i \text{ and } \jmath \neq j \\ 0 & \text{if } \imath \neq i \end{cases}. \tag{3.19}$$

Hereby the gradient of the description length w.r.t. the landmarks are obtained. The gradient with respect to the transformation parameters $\boldsymbol{\Phi}$ can be obtained by multiplying the landmark gradient with the Jacobian of the function that maps the transformation parameters to the landmark positions.

3.5 Rigid Correspondence

Establishing an initial correspondence for a set of surfaces $\{\mathcal{M}_1, \ldots, \mathcal{M}_{n_s}\}$ starts by parameterizing each surface onto the cylinder. The parameterized piecewise linear surfaces $\{\boldsymbol{x}^\circ_1, \ldots, \boldsymbol{x}^\circ_{n_s}\}$ are then approximated using b-splines, resulting in the smooth surfaces $\{\tilde{\boldsymbol{x}}^\circ_1, \ldots, \tilde{\boldsymbol{x}}^\circ_{n_s}\}$. Details on this can be found in Section 3.3. The approximation uses a grid of $m^\circ_{u^{(0)}} \times m^\circ_{u^{(1)}}$ control points. It was observed that accurate approximations are achieved with a grid size of the order $32 \times \frac{h}{2\pi} 32$ for all surfaces considered in this work. An initial correspondence, denoted $\{\hat{\boldsymbol{x}}_1^\circ, \ldots, \hat{\boldsymbol{x}}_{n_s}^\circ\}$, is obtained from the b-spline surfaces after applying a spatial alignment $\boldsymbol{\tau}^\circ(\bullet|\hat{\boldsymbol{\Phi}}_i^{\tau^\circ})$ and parameter space rotation $\boldsymbol{\rho}^\circ(\bullet|\hat{\Phi}_i^{\rho^\circ})$ to each of the surfaces $\tilde{\boldsymbol{x}}_i^\circ$. The optimal transformation parameters $\hat{\boldsymbol{\Phi}}_i^{\tau^\circ}$ and $\hat{\Phi}_i^{\rho^\circ}$ are determined by optimization w.r.t. the model description length μ. The objective μ contains multiple local minima and therefore suitable initialization for the transformation parameters is required. First the spatial transformation parameters are initialized by principal axes alignment of the surfaces. This is followed by initialization of the parameterization rotation parameters by running a description length optimization for the parameterization rotations while keeping the spatial transformation parameters fixed. Finally, starting from these initial parameters, the full optimization of the description length, where both spatial transformation parameters and parameterization rotation parameters are set free, is executed. This results in the desired rigid correspondence $\{\hat{\boldsymbol{x}}_1^\circ, \ldots, \hat{\boldsymbol{x}}_{n_s}^\circ\}$. An overview of establishing a rigid correspondence is given in the flow chart of Figure 3.1.

3.5.1 Spatial Alignment Initialization

The spatial transformation $\boldsymbol{\tau}^\circ(\bullet|\boldsymbol{\Phi}^{\tau^\circ}) : \mathbb{R}^3 \to \mathbb{R}^3$, used for the alignment of the surfaces, is a 3D rigid transformation. It is composed of a 3D rotation around the surface center followed by a 3D translation. The rotation is parameterized by a unit quaternion $\boldsymbol{q} = (w, q_x, q_y, q_z) \in \mathscr{S}^3$, where $\mathscr{S}^3$ is the three-sphere. In order to be of unit length, the quaternion should adhere to the following constraint:

$$\sqrt{\boldsymbol{q}\boldsymbol{q}^T} = 1. \tag{3.20}$$

Quaternion parameterization for rotation does not suffer from the singularities encountered with Euler angles. The translation is parameterized by a 3d vector $\boldsymbol{t} = (t_x, t_y, t_z)$. The transformation $\boldsymbol{\tau}^\circ$ is thus controlled by seven parameters: $\boldsymbol{\Phi}^{\tau^\circ} = (\boldsymbol{q}, \boldsymbol{t})$.

Let

$$\hat{\boldsymbol{x}}_i^\circ(\bullet|\boldsymbol{\Phi}_i^{\tau^\circ}) = \boldsymbol{\tau}^\circ(\bullet|\boldsymbol{\Phi}_i^{\tau^\circ}) \circ \tilde{\boldsymbol{x}}_i^\circ \tag{3.21}$$

be a shorthand notation for the surface obtained after applying the spatial transformation $\boldsymbol{\tau}^\circ$ to the surface $\tilde{\boldsymbol{x}}_i^\circ$, for given parameters $\boldsymbol{\Phi}_i^{\tau^\circ}$. Then, the parameters $\{\boldsymbol{\Phi}_1^{\tau^\circ}, \ldots, \boldsymbol{\Phi}_{n_s}^{\tau^\circ}\}$ are chosen so that the surfaces $\{\hat{\boldsymbol{x}}_1^\circ(\bullet|\boldsymbol{\Phi}_1^{\tau^\circ}), \ldots, \hat{\boldsymbol{x}}_{n_s}^\circ(\bullet|\boldsymbol{\Phi}_{n_s}^{\tau^\circ})\}$ have their principal axes aligned with the axes of the reference coordinate system. The translation vector $\boldsymbol{t}_i$ for surface $\tilde{\boldsymbol{x}}_i^\circ$ centers the surface at the origin of the coordinate system, i.e $\boldsymbol{t}_i = -\bar{\boldsymbol{v}}^i = -\frac{1}{n_{V_i}} \sum_{j=1}^{n_{V_i}} \boldsymbol{v}_j^i$ where $\bar{\boldsymbol{v}}^i$ is the average of the vertices $\boldsymbol{v}_j^i$ of surface $\tilde{\boldsymbol{x}}_i^\circ$. The rotation for the surface is obtained using singular value decomposition. Let $\boldsymbol{V}_i = [(\boldsymbol{v}_1^i - \bar{\boldsymbol{v}}^i)^T \ldots (\boldsymbol{v}_{n_{V_i}}^i - \bar{\boldsymbol{v}}^i)^T]^T$ be the matrix that has the centered vertices of $\mathscr{M}_i$ as its rows and let the singular value decomposition of the coordinate covariance matrix be defined as $\frac{1}{n_{V_i}-1} \boldsymbol{V}_i^T \boldsymbol{V}_i = \boldsymbol{U}_i \boldsymbol{S}_i^2 \boldsymbol{U}_i^T$.

Then, $\boldsymbol{U}_i$ is the rotation matrix that aligns the principal axes of the surface with the reference coordinate axes. Note that the rotation matrix $\boldsymbol{U}_i$ is not uniquely defined since the singular vectors are defined up to their sign. Thus there are eight possible rotations, from which four can be eliminated since they produce a mirrored surface. From the four remaining rotations, the one is chosen that best matches a reference surface $\mathscr{M}_r$ in terms of the following error:

$$\sum_{j=1}^{n_p} \left[D(\hat{\boldsymbol{x}}_i^\circ(\boldsymbol{u}_j|\boldsymbol{\Phi}_i^{\tau^\circ}), \mathscr{M}_r) \right]^2, \tag{3.22}$$

where $D(\boldsymbol{p}, \mathscr{M})$ measures the distance from $\boldsymbol{p}$ to the closest point on $\mathscr{M}$. The quaternion $\boldsymbol{q}_i$ that represents the best rotation together with the translation $\boldsymbol{t}_i$ form the initialization for the spatial transformation parameter set, i.e. $\boldsymbol{\Phi}_i^{\tau^\circ} = (\boldsymbol{q}_i, \boldsymbol{t}_i)$.

3.5.2 Parameterization Alignment Initialization

The parameterization transformation $\boldsymbol{\rho}^\circ(\bullet|\Phi^{\rho^\circ})$, used to align the parameterizations, is a parameter space rotation and it is controlled by a single parameter $\Phi^{\rho^\circ} \in [0, 2\pi]$, defining the angle of rotation. The transformation has the following form:

$$\boldsymbol{\rho}^\circ(\bullet|\Phi^{\rho^\circ}) \quad : \quad \mathscr{C}_h^2 \mapsto \mathscr{C}_h^2 \tag{3.23}$$

$$\quad : \quad \boldsymbol{u} \mapsto (u^{(0)} + \Phi^{\rho^\circ}, u^{(1)}). \tag{3.24}$$

Similar to Equation (3.21), a shorthand notation for the surface obtained after applying the spatial and parameterization transformation, for given parameters $\boldsymbol{\Phi}_i^{\rho^\circ}$ and $\boldsymbol{\Phi}_i^{\tau^\circ}$, is as follows:

$$\hat{\boldsymbol{x}}_i^\circ(\bullet|\boldsymbol{\Phi}_i^{\rho^\circ}, \boldsymbol{\Phi}_i^{\tau^\circ}) = \boldsymbol{\tau}^\circ(\bullet|\boldsymbol{\Phi}_i^{\tau^\circ}) \circ \tilde{\boldsymbol{x}}_i^\circ \circ \boldsymbol{\rho}^\circ(\bullet|\Phi_i^{\rho^\circ}). \tag{3.25}$$

The initial values for the parameterization rotation parameters $\{\Phi_1^{\rho^\circ}, \ldots, \Phi_{n_s}^{\rho^\circ}\}$ are then obtained by solving the following optimization problem:

$$\underset{\Phi_i^{\rho^\circ}, \forall i}{\arg\min}\, \mu \circ \Lambda(\ldots, \hat{\boldsymbol{x}}_i^\circ(\bullet|\Phi_i^{\rho^\circ}, \boldsymbol{\Phi}_i^{\tau^\circ}), \ldots | \boldsymbol{U}^{n_\circ}). \tag{3.26}$$

where the $\boldsymbol{\Phi}_i^{\tau^\circ}$ are the initial spatial alignment parameters obtained in the previous section.

3.5.3 Full Alignment

Now, starting from the initial spatial transformation parameters $\{\boldsymbol{\Phi}_1^{\tau^\circ}, \ldots, \boldsymbol{\Phi}_{n_s}^{\tau^\circ}\}$ and the initial parameterization rotation parameters $\{\Phi_1^{\rho^\circ}, \ldots, \Phi_{n_s}^{\rho^\circ}\}$, obtained in the previous two sections, the full description length minimization with rigid transformations can be solved:

$$\underset{\mathbf{\Phi}_i^{\rho^\circ}, \mathbf{\Phi}_i^{\tau^\circ}, \forall i}{\arg\min} \left\{ \mu \circ \Lambda(\ldots, \hat{\boldsymbol{x}}_i^\circ(\bullet|\mathbf{\Phi}_i^{\rho^\circ}, \mathbf{\Phi}_i^{\tau^\circ}), \ldots |\boldsymbol{U}^{n_\circ}) + \frac{\alpha^\tau}{n_s} \sum_j \eta^\tau(\mathbf{\Phi}_j^{\tau^\circ}) \right\}. \tag{3.27}$$

Here, the regularization term $\eta^\tau(\mathbf{\Phi}_j^{\tau^\circ})$ penalizes parameter sets with a quaternion that violates Equation (3.20). The penalty for a quaternion $\boldsymbol{q}$ is measured as $(1 - \sqrt{\boldsymbol{q}\boldsymbol{q}^T})^2$. The regularization term attains its minimum when all quaternions are in $\mathscr{S}^3$ and smoothly penalizes any deviation from this. In all the experiments a regularization factor $\alpha^\tau = 10^6$ was used. The parameters that solve Equation (3.27) are denoted $\{\hat{\mathbf{\Phi}}_1^{\tau^\circ}, \hat{\Phi}_1^{\rho^\circ}, \ldots, \hat{\mathbf{\Phi}}_{n_s}^{\tau^\circ}, \hat{\Phi}_{n_s}^{\rho^\circ}\}$ and they provide the final rigid correspondence $\{\hat{\boldsymbol{x}}_1^\circ(\bullet|\hat{\mathbf{\Phi}}_1^{\rho^\circ}, \hat{\mathbf{\Phi}}_1^{\tau^\circ}), \ldots, \hat{\boldsymbol{x}}_{n_s}^\circ(\bullet|\hat{\mathbf{\Phi}}_{n_s}^{\rho^\circ}, \hat{\mathbf{\Phi}}_{n_s}^{\tau^\circ})\}$.

3.6 Non-rigid Correspondence

In the previous section, an rigid correspondence $\{\boldsymbol{x}_1, \ldots, \boldsymbol{x}_{n_s}\}$ was produced by applying the optimal rigid spatial transformations and rigid parameterization transformations to the parameterized surfaces. An improvement over this rigid correspondence can be obtained by allowing local deformations of the parameterizations. Such local deformations can be realized by a non-rigid parameterization transformation. Here, a cylindrical b-spline parameterization deformation $\boldsymbol{\rho}^L$ is used, where L indicates the level of resolution of the deformation. The spatial transformation $\boldsymbol{\tau}$ is the same as in Section 3.5. The optimal non-rigid parameterization deformations, together with the spatial transformation parameters, are determined by optimization. The optimization is done at increasing levels of resolution, sequentially, to avoid convergence to a local optimum. The flow chart in Figure 3.2 gives an overview of the multi-resolution correspondence optimization.

At every resolution level L, the optimal transformation parameters for that level are determined in the following manner: First, each surface $\boldsymbol{x}_i$, obtained from the rigid correspondence procedure, is approximated with a b-spline surface, denoted $\tilde{\boldsymbol{x}}_i^L$. The approximation uses a $m_{u^{(0)}}^L \times m_{u^{(1)}}^L$ grid of control points. Here, $m_{u^{(0)}}^L = 3 \cdot 2^{L-1}$ and $m_{u^{(1)}}^L = \left\lfloor \frac{h}{2\pi} m_{u^{(0)}}^L \right\rfloor$ is used, thus the resolution is approximately isotropic and doubled from one level to the next. Each surface $\tilde{\boldsymbol{x}}_i^L$ is transformed according to the spatial transformation parameters $\mathbf{\Phi}_i^{\tau^L}$ and parameterization transformation parameters $\mathbf{\Phi}_i^{\tau^L}$ as follows:

$$\hat{\boldsymbol{x}}_i^L(\bullet|\mathbf{\Phi}_i^{\rho^L}, \mathbf{\Phi}_i^{\tau^L}) = \boldsymbol{\tau}(\bullet|\mathbf{\Phi}_i^{\tau^L}) \circ \tilde{\boldsymbol{x}}_i^L \circ \boldsymbol{\rho}^L(\bullet|\Phi_i^{\rho^L}). \tag{3.28}$$

The level-L b-spline parameterization transformation $\boldsymbol{\rho}^L$ is defined by a grid of $n_{u^{(0)}}^L \times n_{u^{(1)}}^L$ control points. Similar to the approximation b-spline, the transformation b-spline has an isotropic resolution that is doubled at each new level, i.e.

$n^L_{u^{(0)}} = 3 \cdot 2^{L-1}$ and $n^L_{u^{(1)}} = \left\lfloor \frac{h}{2\pi} n^L_{u^{(0)}} \right\rfloor$. Using the notation from Equation (3.28), the optimal level-L transformation parameters are determined by solving the following optimization problem:

$$\operatorname*{arg\,min}_{\boldsymbol{\Phi}_i^{\rho^L}, \boldsymbol{\Phi}_i^{\tau^L}, \forall i} \Bigg\{ \mu \circ \Lambda(\ldots, \hat{\boldsymbol{x}}_i^L(\bullet | \boldsymbol{\Phi}_i^{\rho^L}, \boldsymbol{\Phi}_i^{\tau^L}), \ldots | \boldsymbol{U}^{n_p^L}) \\ + \frac{\alpha^\tau}{n_s} \sum_j \eta^\tau(\boldsymbol{\Phi}_j^{\tau^L}) + \frac{\alpha^\rho}{n_s} \sum_j \eta^{\rho^L}(\boldsymbol{\Phi}_j^{\rho^L}) \Bigg\}. \quad (3.29)$$

Here, η^τ is the regularization for the spatial transformations, as defined in Section 3.5.3, and η^{ρ^L} is the regularization for the parameterization deformations in order to avoid overfitting. The experimentally determined regularization constants are $\alpha^\tau = 10^6$ and $\alpha^\rho = 0.2$. The set of parameter coordinates $\boldsymbol{U}^{n_p^L}$, used to estimate the shape covariance matrix, contains $n_p^L = 250 \cdot 4^{L-1}$ parameter locations. Thus, the number of samples per area increases fourfold with every new level. This mirrors the doubling of the resolution of the surface approximation and parameterization transformation. Note that the optimal transformation parameters for the optimization problem of level $L-1$ are used to initialize the parameters of current the level L. To initialize the b-spline parameterization transformation parameters $\boldsymbol{\Phi}_j^{\rho^L}$ from $\hat{\boldsymbol{\Phi}}_j^{\rho^{L-1}}$ the b-spline upsampling technique from Catmull and Clark [1978] is used. The initialization of the spatial transformations is trivial, i.e $\boldsymbol{\Phi}_j^{\tau^L} = \hat{\boldsymbol{\Phi}}_j^{\tau^{L-1}}$. In this work, three levels of resolution were used and thus the optimal transformation parameters $\{\hat{\boldsymbol{\Phi}}_1^{\tau^3}, \hat{\Phi}_1^{\rho^3}, \ldots, \hat{\boldsymbol{\Phi}}_{n_s}^{\tau^3}, \hat{\Phi}_{n_s}^{\rho^3}\}$ of the third level optimization problem are the final transformation parameters. These provide the final correspondence $\{\hat{\boldsymbol{x}}_1, \ldots, \hat{\boldsymbol{x}}_{n_s}\}$.

In the following two sections, the actual form of the parameterization transformation will be detailed and a suitable regularizer is introduced.

3.6.1 Reparameterization Transformation

The parameterization space $\mathscr{C}_h^2$ is deformed using a parameterization transformation $\boldsymbol{\rho}^L(\boldsymbol{u}|\boldsymbol{\Phi}^{\rho^L})$, where L denotes the level of resolution. The transformation is an automorphism of the parameter space, i.e. $\boldsymbol{\rho}^L$ constitutes a continuous one-to-one map of $\mathscr{C}_h^2$. The space of possible reparameterizations is spanned by the transformation parameters $\boldsymbol{\Phi}^{\rho^L}$. Different bases can be used to represent a reparameterization function [Davies et al., 2002b,a, Heimann et al., 2005, Horkaew and Yang, 2003b]. In this work, $\boldsymbol{\rho}^L$ is a 2d cubic b-spline function with knot positions on a regular grid. Such a representation has a number of convenient properties: (1) cubic b-spline deformations are C^2 continuous with respect to their parameters within the patches and C^1 continuous at the patch boundaries. This is required for efficient, gradient guided, optimization. (2) it has compact support which makes it fast to evaluate and allows local control. And, (3) it can be used in a multi-resolution method by refining the grid that controls the shape of the deformation.

The b-spline deformation function $\boldsymbol{\rho}^L$ is defined by a set of knots $\boldsymbol{K}^L = \{\boldsymbol{\kappa}_{ij}^L\}$ and a set of control point displacements $\boldsymbol{\Phi}^{\rho^L} = \{\boldsymbol{\delta}_{ij}^L\}$:

$$\boldsymbol{\rho}^L(\boldsymbol{u}|\boldsymbol{\Phi}^{\rho^L}) = \sum_{i=-1}^{n_{u^{(0)}}^L+1} \sum_{j=-1}^{n_{u^{(1)}}^L} \beta\left(\frac{\boldsymbol{u}-\boldsymbol{\kappa}_{ij}^L}{\boldsymbol{\Delta}^L}\right)(\boldsymbol{\kappa}_{ij}^L + \boldsymbol{\delta}_{ij}^L) \mod^{(0)} 2\pi \tag{3.30}$$

Where the modulo operator, $\mathrm{mod}^{(0)}$, acts on the first coordinate of the parameter space and keeps the deformed parameter within the bounds $[0, 2\pi]$. $\boldsymbol{\beta}$ is the 2D separable cubic b-spline kernel from Equation (3.3). The knots and the corresponding control points are arranged on a regular $n_{u^{(0)}}^L \times n_{u^{(1)}}^L$ grid on the cylinder $\mathscr{C}_h^2$. The spacing between the knots is denoted as $\boldsymbol{\Delta}^L = (\frac{2\pi}{n_{u^{(0)}}^L}, \frac{h}{n_{u^{(1)}}^L - 1})$.

The following constraints on the control point displacements $\boldsymbol{\delta}_{ij}$ make sure that $\boldsymbol{\rho}^L$ is periodic and continuous at the parameter boundary $u^{(0)} = 2\pi$:

$$\begin{cases} \boldsymbol{\delta}_{-1,j} & = & \boldsymbol{\delta}_{n_{u^{(0)}}-1,j} \\ \boldsymbol{\delta}_{0,j} & = & \boldsymbol{\delta}_{n_{u^{(0)}},j} \\ \boldsymbol{\delta}_{1,j} & = & \boldsymbol{\delta}_{n_{u^{(0)}}+1,j} \end{cases}, \forall j. \tag{3.31}$$

In order to make $\boldsymbol{\rho}^L$ one-to-one along the boundaries of $\mathscr{C}_h^2$, the following constraints are also enforced:

$$\begin{cases} \delta_{i,-1}^{(1)} & = & -\delta_{i,1}^{(1)} \\ \delta_{i,n_{u^{(0)}}}^{(1)} & = & -\delta_{i,n_{u^{(0)}}-2}^{(1)} \\ \delta_{i,0}^{(1)} & = & 0 \\ \delta_{i,n_{u^{(0)}}-1}^{(1)} & = & 0 \end{cases}, \forall i. \tag{3.32}$$

In this work, the same arrangement of knots $\boldsymbol{K}^L$ is used for the reparameterization of each surface $\boldsymbol{x}_k$. Only the control point displacements $\boldsymbol{\Phi}_k^{\rho^L} = \{\boldsymbol{\delta}_{ij,k}^L\}$ differ from surface to surface. Figure 3.5a shows a 3×4 cylindrical grid of knots in an unfolded view and Figure 3.5b shows a grid of control points for that knot grid, where the control points are obtained by adding the control point displacement to the knot location, i.e. $\boldsymbol{\kappa}_{ij}^L + \boldsymbol{\delta}_{ij}^L$. Observe that both the knots and the control points reside on the parameter domain $\mathscr{C}_h^2$. The b-spline function $\boldsymbol{\rho}^L$ thus defines a reparameterization function of the cylindrical parameter domain $\mathscr{C}_h^2$.

3.6.2 Reparameterization Regularization

From Equation (3.30), it can be seen that the reparameterization transformation $\boldsymbol{\rho}^L$ is a linear combination of translated versions of the cubic b-spline kernel β.

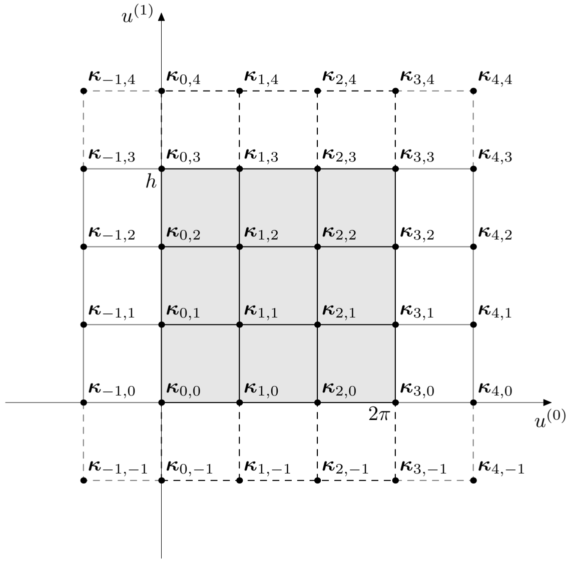

(a) knot grid

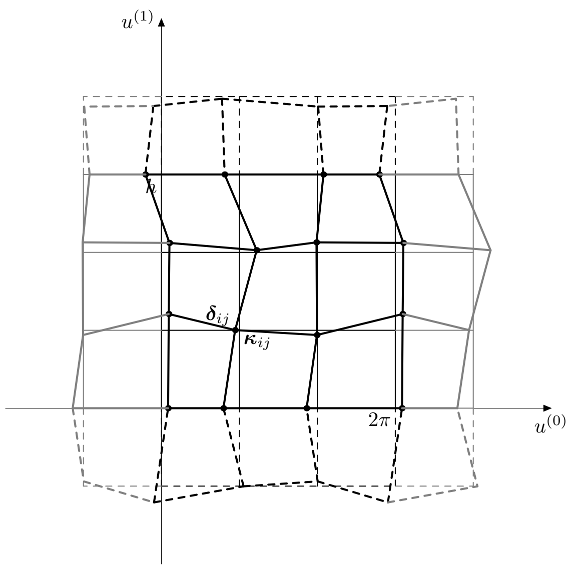

(b) control points

Figure 3.5: (a) A 3 × 4 grid of knots on $\mathscr{C}_h^2$. The knots $\boldsymbol{\kappa}_{i,-1}$ and $\boldsymbol{\kappa}_{i,4}$ ensure that the cubic b-spline can be evaluated over the whole domain of $\mathscr{C}_h^2$ (indicated as the shaded area) and the knots $\boldsymbol{\kappa}_{-1,j}$, $\boldsymbol{\kappa}_{3,j}$, and $\boldsymbol{\kappa}_{4,j}$ make the b-spline periodic in the $u^{(0)}$-direction. (b) An example grid of b-spline control points overlaid on the knot grid. Together these define a cylindrical parameterization transformation. The shape of the transformation is controlled by the displacements $\boldsymbol{\delta}_{ij}$ from the corresponding knots $\boldsymbol{\kappa}_{ij}$.

As a result, the reparameterization transformation is C^2 continuous within the patches and C^1 continuous at the patch boundaries. The inherent smoothness of the b-spline transformation is convenient but it does not avoid overfitting by the b-spline transform. Overfitting is perceived as an irregular local deformation and occurs in regions where μ is insensitive to local deformations, e.g. when a b-spline kernel is not supported by any landmark samples in the calculation of $\mathbf{\Lambda}$.

To counter these irregularities, a regularization term is introduced, denoted η^ρ. For b-splines, a number of regularization terms have been used in the past [Loeckx, 2006, Rueckert et al., 1999]. Here, a simple regularizer is chosen that measures the Dirichlet energy of the parameterization displacement function. This displacement function, denoted ϱ can be derived easily from Equation 3.30:

$$\varrho(\boldsymbol{u}|\mathbf{\Phi}^\rho) = \sum_{i=-1}^{n_{u^{(0)}}+1} \sum_{j=-1}^{n_{u^{(1)}}} \beta\left(\frac{\boldsymbol{u}-\boldsymbol{\kappa}_{ij}}{\mathbf{\Delta}}\right)\boldsymbol{\delta}_{ij} \tag{3.33}$$

The regularization term η^ρ for the deformation is then defined as:

$$\eta(\mathbf{\Phi}^\rho) = \iint_{\mathscr{C}_h^2} \left(\left| \frac{\partial \varrho(\boldsymbol{u}|\mathbf{\Phi}^\rho)}{\partial u^{(0)}} \right|^2 + \left| \frac{\partial \varrho(\boldsymbol{u}|\mathbf{\Phi}^\rho)}{\partial u^{(1)}} \right|^2 \right) \mathrm{d}\boldsymbol{u} \tag{3.34}$$

In what follows, $\beta^i_{u^{(c)}} = \beta\left(\frac{u^{(c)}}{\Delta^{(c)}} - i\right)$ is used as a shorthand notation and the prime mark symbol denotes the derivative. Substituting the b-spline transformation into Equation (3.34) results in:

$$\begin{aligned}\eta(\mathbf{\Phi}^\rho) = &\sum_{ij}\sum_{kl} \boldsymbol{\delta}_{ij}\boldsymbol{\delta}^T_{kl} \\ &\left(\frac{1}{\Delta^{(0)2}} \int_0^{2\pi} \beta^{i'}_{u^{(0)}}\beta^{k'}_{u^{(0)}} \mathrm{d}u^{(0)} \int_0^h \beta^{j}_{u^{(1)}}\beta^{l}_{u^{(1)}} \mathrm{d}u^{(1)} \right. \\ &\left. + \frac{1}{\Delta^{(1)2}} \int_0^{2\pi} \beta^{i}_{u^{(0)}}\beta^{k}_{u^{(0)}} \mathrm{d}u^{(0)} \int_0^h \beta^{j'}_{u^{(1)}}\beta^{l'}_{u^{(1)}} \mathrm{d}u^{(1)} \right)\end{aligned} \tag{3.35}$$

From this, the derivatives of the smoothness energy w.r.t. the control point displacements are easily derived:

$$\begin{aligned}\frac{\partial \eta}{\partial \delta^{(0)}_{kl}} = &2\sum_{ij} \delta^{(0)}_{ij} \\ &\left(\frac{1}{\Delta^{(0)2}} \int_0^{2\pi} \beta^{i'}_{u^{(0)}}\beta^{k'}_{u^{(0)}} \mathrm{d}u^{(0)} \int_0^h \beta^{j}_{u^{(1)}}\beta^{l}_{u^{(1)}} \mathrm{d}u^{(1)} \right. \\ &\left. + \frac{1}{\Delta^{(1)2}} \int_0^{2\pi} \beta^{i}_{u^{(0)}}\beta^{k}_{u^{(0)}} \mathrm{d}u^{(0)} \int_0^h \beta^{j'}_{u^{(1)}}\beta^{l'}_{u^{(1)}} \mathrm{d}u^{(1)} \right)\end{aligned} \tag{3.36}$$

Equations (3.35) and (3.36) can be evaluated analytically and, as a result, they can be used efficiently with a gradient based optimization method. For a more

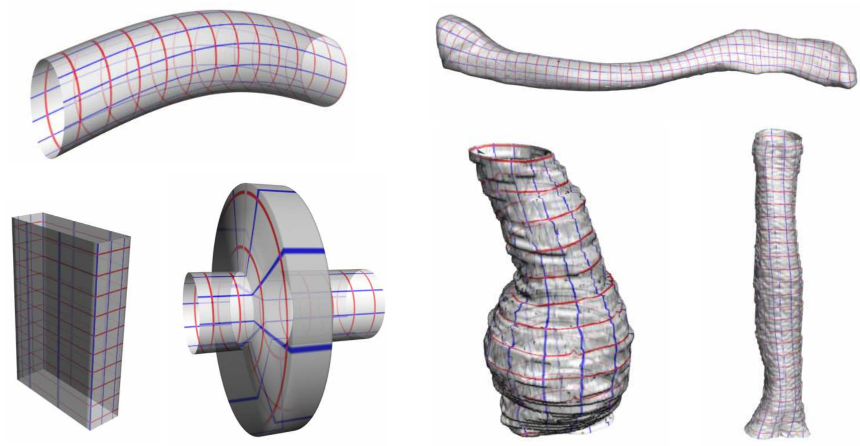

(a) synthetic (b) real

Figure 3.6: From each of the six considered surface populations one random surface is shown here. Each surface is textured with the iso-contours of its parameter coordinates obtained after parameterization. The three populations of synthetic surfaces, in clockwise order in (a) are cylinders, disks, and beams. The three populations of real surfaces, in clockwise order in (b) are clavicles, tracheas, and thrombi.

elaborate discussion on the derivation of Eq. (3.35) and (3.36), the reader is referred to Appendix A.

3.7 Results and Discussion

3.7.1 Data Sets

In this work, six populations of surfaces were used to test the proposed correspondence method. Three of these are phantom populations, each consisting of 30 surfaces: a population of disks where the position of the disk on the cylinder is variable, a population of beams with varying width and depth, and a population of cylinder-like bent surfaces with elliptic cross-section where the width and height of the cross-section is variable together with the amount of bending. A sample surface of each of these populations is shown in Figure 3.6a. There are also three populations of real, ct-scanned, surfaces: a population of 25 clavicles, a population of 23 tracheas and a population of 50 aortic sections with a thrombus. A sample surface of each of the real populations can be found in Figure 3.6b. All surfaces of these populations have cylindrical topology except the clavicles which are of spherical topology. The clavicles are made cylindrical by

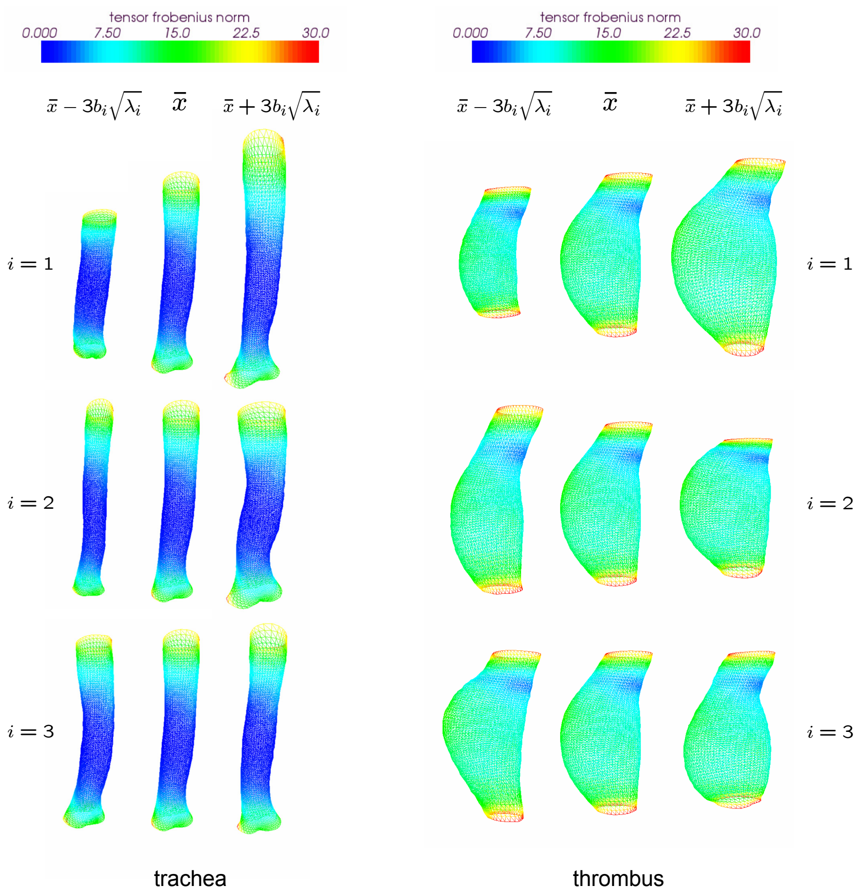

Figure 3.7: A visualization of the modes of models obtained with the approach of this chapter. The color coding represents the frobenius norm of the landmark covariance matrix and is a measure of the local variability of the surface. The first three modes are shown for the CT-scanned trachea and the thrombus populations. For each mode i, the average shape $\bar{\boldsymbol{x}}$ is shown together with the positive and negative offset in the direction of mode i: $\bar{\boldsymbol{x}} \pm 3\boldsymbol{b}_i\sqrt{\lambda_i}$.

puncturing both ends of the clavicle.

3.7.2 Performance Measures

In what follows, different correspondences will be constructed for the above-mentioned populations. The quality of the established correspondences is evaluated by deriving a PCA-model from the correspondence and reporting perfor-

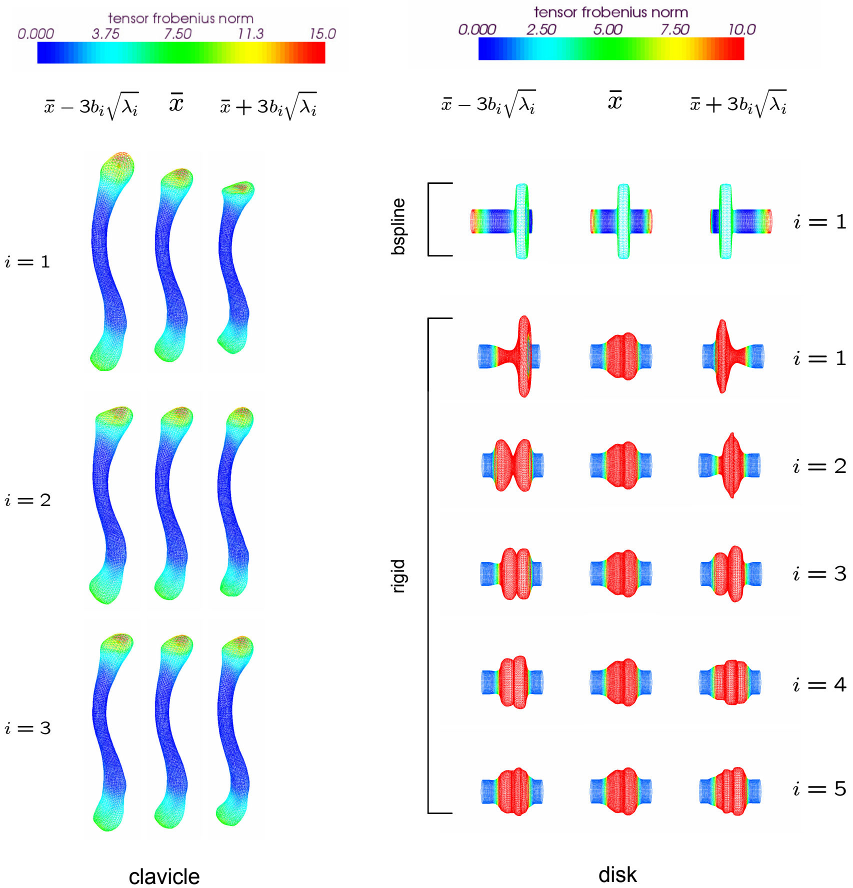

Figure 3.8: A visualization of the modes of models obtained with the approach of this chapter. The color coding represents the frobenius norm of the landmark covariance matrix and is a measure of the local variability of the surface. On the left, the first three modes are shown for the CT-scanned clavicle population For each mode i, the average shape $\bar{x}$ is shown together with the positive and negative offset in the direction of mode i: $\bar{x} \pm 3\boldsymbol{b}_i\sqrt{\lambda_i}$. On the right, the modes of model for the disk population is shown. On top, the b-spline optimized model is shown. At the bottom, the model of the rigid correspondence is shown. Clearly, the b-spline optimization dramatically improved the correspondence.

mance measures for the obtained model. The performance of a model is measured here by the compactness, reconstruction ability, generalization ability and specificity of the model. The performance measures are reported for the full k-mode model and all restricted m-mode, $m < k$, versions of the PCA-model. In a comparison, the correspondence having the best performance measures, for its derived model, is considered the best correspondence.

Now, given a set of surfaces $\{\mathcal{M}_1,\dots,\mathcal{M}_{n_s}\}$, let the correspondence be denoted as $\{\boldsymbol{x}_1,\dots,\boldsymbol{x}_{n_s}\}$ and the derived shape model as $\dot{\boldsymbol{x}}^m$, where m is the number of modes of the shape model. Then the *compactness* of a model is measured as the cumulative variance:

$$C(m) = \sum_{i=1}^{m} \lambda_i, \tag{3.37}$$

where λ_i is the variance of the i-th shape mode. The *reconstruction ability* indicates how good a model is able to reconstruct the surfaces that were used to build the model. It is measured as the average approximation error after fitting the model to each of the surfaces $\{\mathcal{M}_1,\dots,\mathcal{M}_{n_s}\}$:

$$R(m) = \frac{1}{n_s}\sum_{i=1}^{n_s} \min_{\boldsymbol{\Phi}^{\boldsymbol{\tau}},\boldsymbol{b}} D(\boldsymbol{\tau}(\boldsymbol{\Phi}^{\boldsymbol{\tau}}) \circ \dot{\boldsymbol{x}}^m(\boldsymbol{b}), \mathcal{M}_i), \tag{3.38}$$

where $\boldsymbol{\Phi}^{\boldsymbol{\tau}}$ are the parameters of the rigid transformation $\boldsymbol{\tau}$, $\boldsymbol{b}$ are model parameters, and $D(\boldsymbol{x},\boldsymbol{y})$ measures the average closest point distance from surface $\boldsymbol{y}$ to surface $\boldsymbol{x}$. The optimal parameters $\boldsymbol{\Phi}^{\boldsymbol{\tau}}$ and $\boldsymbol{b}$, resulting in the best model-to-surface fit, are determined iteratively by alternately estimating $\boldsymbol{\Phi}^{\boldsymbol{\tau}}$ and $\boldsymbol{b}$ in a least squares sense. The *generalization ability* of a model determines how well the model generalizes to unseen instances of the modeled class. It is measured as the average approximation error after fitting leave-one-out versions of the model to the left out surfaces:

$$G(m) = \frac{1}{n_s}\sum_{i=1}^{n_s} \min_{\boldsymbol{\Phi}^{\boldsymbol{\tau}},\boldsymbol{b}} D(\boldsymbol{\tau}(\boldsymbol{\Phi}^{\boldsymbol{\tau}}) \circ \dot{\boldsymbol{x}}_i^m(\boldsymbol{b}), \mathcal{M}_i), \tag{3.39}$$

where $\dot{\boldsymbol{x}}_i^m$ is the m-mode model where the i-th surface was left out, i.e. it is built from the corresponded surfaces $\{\boldsymbol{x}_1,\dots,\boldsymbol{x}_{i-1},\boldsymbol{x}_{i+1},\dots,\boldsymbol{x}_{n_s}\}$. The model *specificity* measures how much random samples, generated by the model, resemble the original surfaces:

$$S(m) = \frac{1}{n_t}\sum_{i=1}^{n_t} \min_{j,\boldsymbol{\Phi}^{\boldsymbol{\tau}}} D(\boldsymbol{\tau}(\boldsymbol{\Phi}^{\boldsymbol{\tau}}) \circ \dot{\boldsymbol{x}}^m(\boldsymbol{b}_i^m), \mathcal{M}_j), \tag{3.40}$$

where the $\boldsymbol{b}_i^m$ are random Gaussian model parameters for the sample of the i-th trial and n_t is the number of random samples used to estimate the specificity. Note that the model performance measures from Davies et al. [2002b] result in a bias towards the MDL-optimized models. The model performance measures in Eq. (3.38), (3.39), and (3.40) do not suffer from this drawback. The compactness

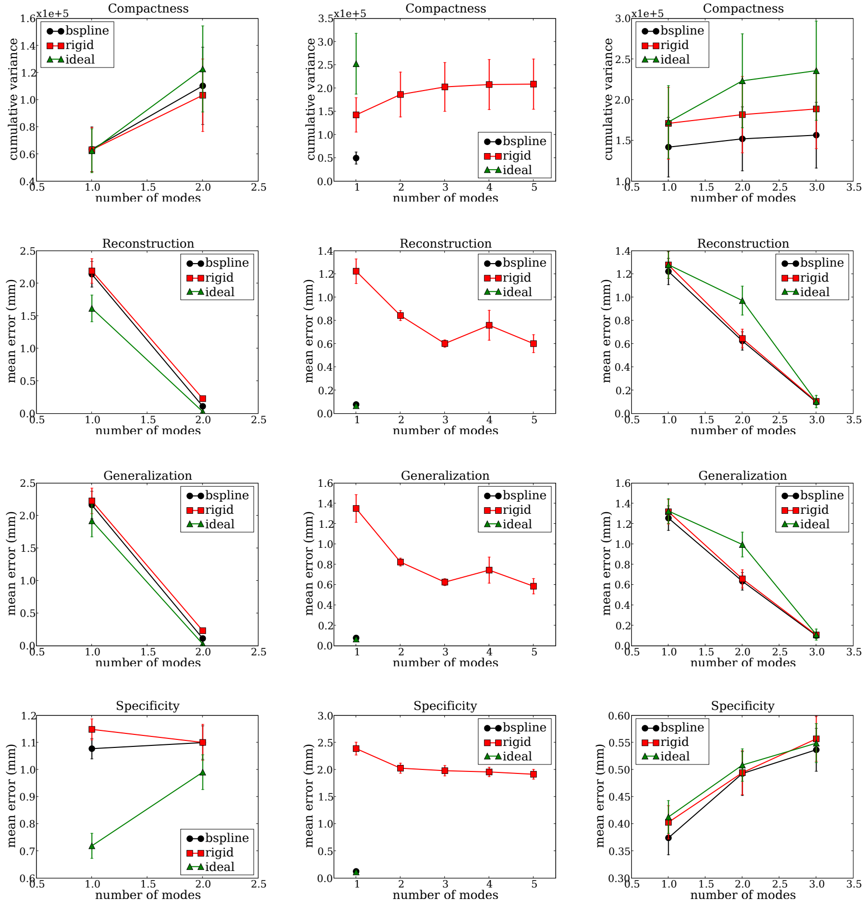

Figure 3.9: The model performance measures, together with the standard error, for the phantom populations. From left to right: beams, disks and cylinders populations. From top to bottom: compactness, reconstruction, generalization and specificity measure. In each graph a comparison is made of the ideal correspondence (green), the rigid correspondence (red) is and the non-rigid correspondence (black). For each model, the first *m* modes are shown that capture 99% of the total variance in the model.

measure from Eq. (3.37) is closely related to the MDL-measure and therefore biased. It is, however, reported here because it contains important information of how a model captures the variation of a population.

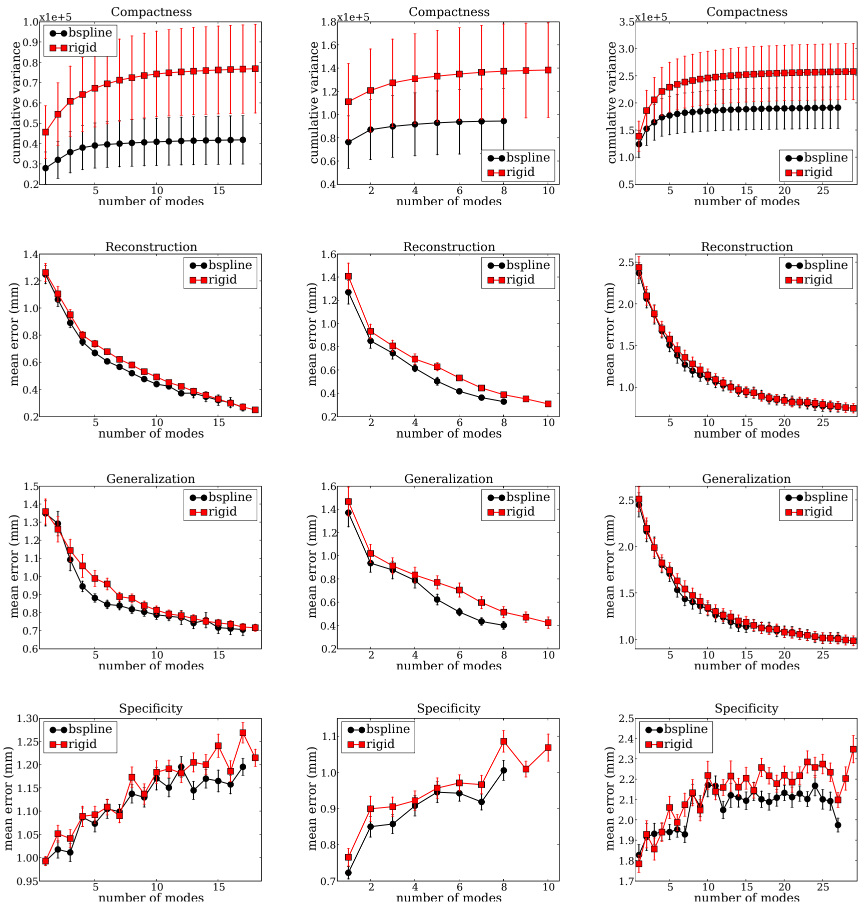

Figure 3.10: Different model performance measures, together with the standard error, for the real data sets. From left to right: clavicles, tracheas and thrombi populations. From top to bottom: compactness, reconstruction, generalization and specificity measure. In each graph the rigid correspondence (red) is compared to the non-rigid correspondence (black). For each model, the first m modes are shown that capture 99% of the total variance in the model.

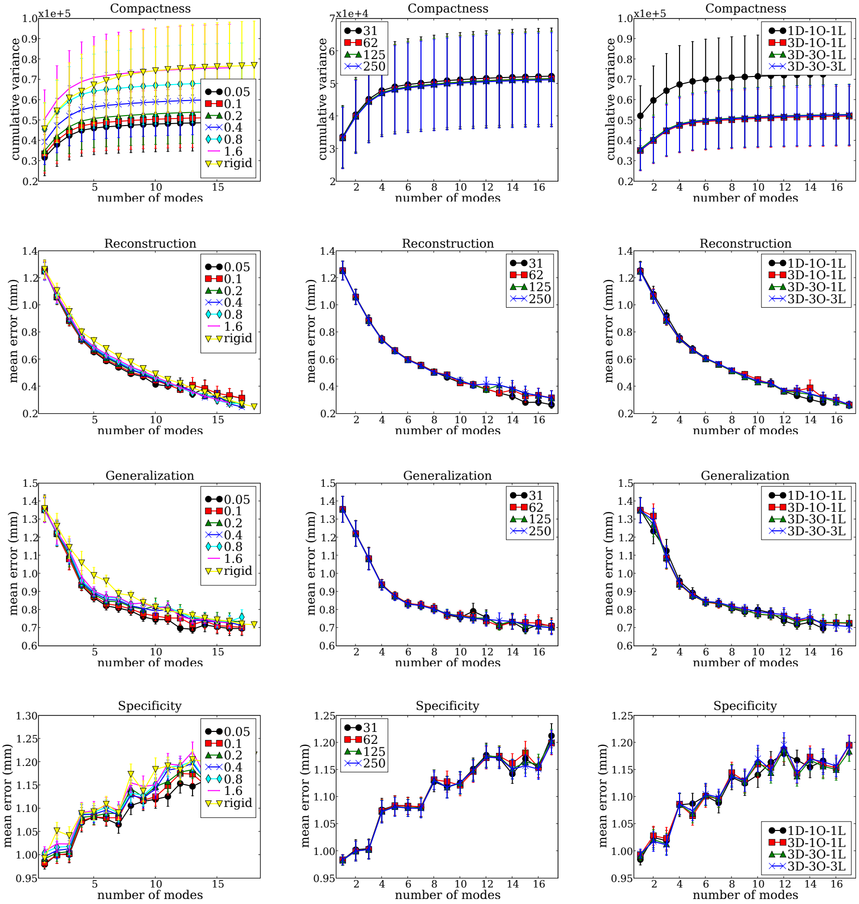

Figure 3.11: Influence of the method parameters on the model performance for the clavicle data set. Left: influence of the b-spline deformation regularization factor α^ρ. Seven models with regularisations from $\alpha^\rho = 0.05$ to $\alpha^\rho = 1.6$ are compared. The rigid case, i.e. $\alpha^\rho = \infty$, is provided as a reference. It can be observed that models with less regularisation tend to perform better. However, too low values for α^ρ may result in irregularities. Middle: influence of the number of landmarks n_p used in the estimation of the shape covariance matrix. Four models are shown with number of landmarks from $n_p^L = 31 \cdot 4^{L-1}$ to $n_p^L = 250 \cdot 4^{L-1}$. It can be seen that the performance is insensitive to this parameter. However, for certain populations, using too few landmarks may result in degraded models due to undersampling of highly variable surface regions. Right: influence of the multi-resolution scheme. The scheme encoded as aD-bO-cL uses a levels for the b-spline deformation, b levels for the surface approximation, and c levels for the number of landmarks. It can be observed that the single resolution scheme 1D-1O-1L generates a degraded model and that the other schemes result in comparable models. The full scheme 3D-3O-3L is preferred because it is computationally less expensive.

			MDL			
population	n_s	h	ideal	rigid	non-rigid	time (min.)
disks	30	2π	6.2	17.2	4.6	66
beams	30	2π	9.6	9.8	9.5	19
cylinders	30	2π	13.6	11.7	10.9	82
clavicles	25	8π		61.9	41.5	157
trachea	23	4π		47.2	33.3	385
thrombi	50	2π		39.1	28.0	411

Table 3.1: Ideal, rigid and non-rigid correspondence results.

3.7.3 Rigid versus Non-Rigid Correspondence

The surfaces of each of the six phantom and real populations were parameterized using the progressive parameterization technique of Huysmans et al. [2005]. The chosen height h of the cylinder for each of the populations can be found in Table 3.1. From the parameterized surfaces, a $16 \times 16\frac{h}{2\pi}$ b-spline representation was computed for each surface using $m_p = 10.000$ points. This was followed by the construction of the rigid correspondence. The number of landmarks to estimate the covariance was $n_p = 4000$ for all populations. Starting from the rigid correspondence, the non-rigid correspondence was calculated. In this construction, a b-spline regularization factor of $\alpha^\rho = 0.2$ was used for all populations. Three levels of scale were used for the b-spline surface, the reparameterization transformation and for the number of landmarks. On the coarsest scale, a 4×4 b-spline surface, together with a 4×4 reparameterization transformation, was the covariance matrix was estimated based on 250 landmarks. At each new resolution level the values are increased as detailed in Section 3.6. All optimizations problems were solved with the L-BFGS routine [Liu and Nocedal, 1989]. For the alignment initialization (Eq. 3.26) and full alignment (Eq. 3.27) a gradient tolerance of 0.01 was used to determine convergence. For the multi-resolution correspondence optimization (Eq. 3.29) a gradient tolerance of 0.01×2^{-L} was used. The quality of the obtained correspondences was assessed using the above-mentioned model performance measures. The results are shown in Figure 3.9 for the phantom populations and in Figure 3.10 for the real populations.

In Figure 3.9, the ideal (intuitive), the rigid and the non-rigid correspondence for the phantom populations are compared. For the disk population, it can be seen that the non-rigid and the ideal correspondence are of comparable quality. The rigid correspondence on the other hand is much worse. This is due to the fact that the parameterization technique maps the disk part of the surfaces to a different location in the parameter space. The non-rigid correspondence improvement, on the other hand, moves the disks to the same part of the parameter space and this results in an optimal correspondence. See Figure

3.8 for a visualization of the rigid and b-spline optimized model. The improved compactness of the non-rigid over the ideal correspondence can be attributed to the reduced area that the disk part of the surface for the non-rigid correspondence takes in the parameter-space. For the beam population, the quality of the correspondences is comparable, with a slight advantage for the ideal, since the parameterization technique already generates a good correspondence. The most notable difference is the improved specificity of the ideal model, which is due to the fact that the other models can generate samples with rounded corners. For the cylinders population, it can be seen that the non-rigid correspondence is an improvement over the ideal, which is mainly due to the improved spatial alignment of the surfaces.

In Figure 3.7 and Figure 3.8, a visualization of the first few modes of the models of the CT-scanned populations can be found. In Figure 3.10, the model performance measures for the rigid and the non-rigid correspondence are shown for the CT-scanned populations. It is more difficult to analyze these results because there is no ideal correspondence available. It can be seen though that the rigid correspondence generates good models for all three populations and that the non-rigid correspondence is a significant improvement in most cases. Compared to the clavicle and trachea populations, the approximation errors for the thrombi population errors are higher. This can be attributed to the large variability that is present in the thrombi population, together with the lower resolution of the ct-scans, that is $0.5 \times 0.5 \times 0.5mm^3$ versus $0.5 \times 0.5 \times 2.0mm^3$.

In Table 3.1, the MDL values for the ideal (when available), the rigid, and the non-rigid correspondences can be found for all populations. It can be seen that the b-spline correspondence optimization always succeeds in decreasing the MDL-value. Such a decrease indicates that the resulting shape model became less complex. This is most apparent for the disk population: the five modes of the rigid model (MDL-value of 17.2) are reduced to a single mode by the b-spline optimization (MDL-value of 4.6). Table 3.1 also reports the execution time for the construction of the correspondences, once the parameterizations are obtained. About 10% of the time is taken by the rigid correspondence construction. The correspondences for the phantom populations are constructed more efficiently compared with the CT-scanned populations. This is because the phantom shape models are relatively simple, i.e. they have a small number of modes. The construction for the CT-scanned populations takes a couple of hours. Together with the construction of the parameterizations, a correspondence can easily be established overnight.

3.7.4 Influence of Parameters

In this section, the influence of the method parameters on the resulting correspondence is investigated. Figure 3.11 shows the model performance parameters for the clavicle population when using different values for the most important parameters: (a) the b-spline deformation regularization controlled by

number of levels				
reparameterization	surface	landmarks	MDL	time(h)
1	1	1	42.6	4.5
3	1	1	41.3	7.5
3	3	1	41.3	7.5
3	3	3	41.5	2.5

Table 3.2: Influence of the multi-level scheme for the clavicle population.

factor α^ρ in Eq. (3.29), (b) the number of landmarks to estimate the shape covariance matrix, controlled by n_p in Eq. (3.14), and (c) the number of scale levels L for the b-spline surface approximation, the b-spline parameterization transform and the landmarks.

In the first column of Figure 3.11, the influence of the b-spline regularization factor α^ρ is shown and it can be seen that, as expected, lower regularization, i.e. smaller α^ρ, generates better models. However, the regularization can not be lowered too much since then irregularities can appear. No irregularities were noted with regularization factors $\alpha^\rho \leq 0.2$ for all considered populations.

In the second column of Figure 3.11, it can be seen that the influence of the number of landmarks n_p is negligible for the clavicle population. It can, however, happen that using too few landmarks results in undersampling of highly variable parts of the surface, which, in turn, will result in a degraded correspondence. This was observed for the thrombi population, where $n_p^L = 250 \cdot 4^{L-1}$ landmarks generated a significantly better correspondence than $n_p^L = 31 \cdot 4^{L-1}$ landmarks (result not shown). Using less landmarks reduces computation time, but it can also result in a degraded correspondences.

In the last column of Figure 3.11, the model performance measures for different multi-scale schemes are shown and in Table 3.2 the corresponding MDL values are listed. Four different schemes are shown: 1D-1O-1L optimizes the correspondence using a single resolution, 3D-1O-1L uses three resolution levels for the deformations, 3D-3O-1L uses three levels for the deformations and the surfaces, and 3D-3O-3L is the full multi-resolution scheme using three levels for the deformations, the surfaces, and the landmarks. It can be seen that, for the clavicle, the single scale scheme generates a degraded correspondence and the three other schemes generate comparable correspondences. However, the full 3-scale scheme is considerably faster. For the disk population, the performance degradation of the single scale method was even more notable since, as opposed to the three other schemes, it did not successfully correspond the disk parts of the surface (result not shown).

3.8 Conclusions

In this work, the minimum description length approach for shape modeling was translated to surfaces of cylindrical topology. The proposed method establishes an alignment and a correspondence for a population of surfaces of cylindrical topology. It generates a rigid correspondence based on cylindrical surface parameterizations and an improved correspondence using multi-level b-spline reparameterizations. Care was taken to ensure that the objective functions are differentiable with respect to the alignment and reparameterization parameters and, where necessary, an expression for the gradient was provided. It was shown that the method produces correspondences that agree with the intuitive correspondence and that the derived shape models generate small approximation errors.

The cylindrical correspondence method of this work, together with the spherical correspondence methods from Davies et al. [2002a] and Heimann et al. [2005], and the disc-like correspondence method of Horkaew and Yang [2004], already cover a wide range of biomedical surfaces. However, it would be interesting to extend the method to other topologies. The method of this chapter can be trivially extended to surfaces of genus-1 topology where the torus can be used as the parametric domain. More complex topologies can be treated by decomposing the surfaces in a consistent set of discs and tubes. Populations of tubular structures with bifurcations could be handled well with this approach. However, arbitrary complex surfaces will suffer from the boundary constraints imposed by the surface decomposition. The development of a method that can handle arbitrary topology, without constraints, is a very challenging problem to be solved in the future.

PART III

APPLICATIONS

CHAPTER 4

STRETCH OPTIMIZED COLON FLATTENING

Parts of this chapter have been included in the following patent application:

T. Huysmans and J. Sijbers, "Method for Mapping Tubular Surfaces to a Cylinder", European patent application number EP09162289.4, submitted June 9, 2009.

Abstract

Virtual colonoscopy (VC) is a minimally-invasive alternative for conventional optical colonoscopy to detect diseases of the colon, including polyps, diverticulosis, and cancer. In VC, computer tomography is combined with specialized visualization techniques in order to provide the physician with a comprehensive view of the colon wall. Due to the tortuous nature of the colon, the traditionally used fly-through visualization is time consuming and error prone. The recently emerging colon dissection or flattening visualization, on the other hand, results in a full coverage of the colon with a reduced inspection time. However, the unfolding is a complicated process that introduces distortions and care must be taken not to repeat or miss parts.

In this chapter, a new technique is proposed for virtual colon unfolding. Where previous techniques either preserve angles or areas, this new technique strives to balance angular and areal distortions. In this way, down-scaling of polyps in the flattened representation is avoided while the local shape is preserved as much as possible. This leads to significantly improved visibility of certain classes of polyps. The unfolding is realized in two steps: a cylindrical parameterization is calculated for the colon, together with the optimal length of the cylindrical domain. This is followed by dissection of the surface and transformation to a rectangle in the plane. The obtained planar colon representation is equipped with appropriate normals that in combination with parallel projection rendering result in centerline-view shading. A comparison between the new flattening technique and conformal flattening, in terms of metric distortion and visual quality, demonstrates the advantages of this new approach.

4.1 Introduction

Computed Tomography Colonography (CTC) or Virtual Colonoscopy (VC) is a minimally-invasive alternative to conventional optical colonoscopy to detect polyps of the colon wall. Optical colonoscopy is an invasive procedure requiring the patient to undergo a colon-cleansing regimen in preparation and to be sedetad during the procedure. CTC, on the other hand, is a patient friendly technique since the colon-cleansing regime is less rigorous, the patient does not need to be sedated, and the procedure is noninvasive and requires less time. CTC is also highly accurate [Pickhardt et al., 2003] and allows a full coverage of the colon wall.

CTC was invented by Vining and Gelfand [1994] and has significantly evolved since then. It is now emerging as a promising screening technique for colorectal cancer [Levin et al., 2008]. The CTC technique combines computer tomography of the abdomen with specialized visualization techniques in order to provide the physician with 2D and 3D views of the colon targeting a complete coverage of the colon wall. Traditionally, 2D axial images synchronised with 3D rendered fly-through navigation of the colon is used for virtual inspection. The length of the colon and its convoluted nature, however, make such an inspection process tedious and error-prone. Moreover, a polyp, hidden behind a fold, can easily be missed with this approach. Virtual colon flattening or virtual colon dissection is a recently emerging visualization technique for colon inspection, resulting in 100% surface coverage and a significantly reduced inspection time [Juchems et al., 2006]. The virtual flattening is achieved by unfolding the entire surface of the colon to the 2D plane and imposing from-the-centerline-view lighting on the unfolded colon. The resulting view resembles pathological preparation or dissection of the colon, hence the name virtual colon dissection.

A popular approach to generate an unfolded view of the colon starts by uniformly sampling the centerline of the colon. This is followed by computation of a cross section at each centerline point using ray casting. Then, the unfolded view is obtained by unfolding and concatenating the obtained cross sections. The main disadvantage of such a technique is that, in high curvature regions of the centerline, polyps may be missed or single polyps may occur multiple times. This happens because, at high curvature regions, the distance between neighbouring cross sections can become too large or intersections of neighbouring cross section occur. Several approaches have been introduced to overcome these problems [Wang et al., 1998, Bartrolí et al., 2001, Balogh et al., 2002, Shin et al., 2009]. However, these approaches can introduce large distortions.

Colon flattening through surface parameterization is a technique that directly generates a guaranteed one-to-one flattening of the whole colon surface. In this way, polyps are never repeated or missed. Previous techniques either preserve angles [Haker et al., 2000a, Hong et al., 2006, Wang et al., 2008] or areas [Zhu et al., 2005] in the flattening process. Angle preservation preserves local shape but it can result in significant down-scaling of a polyp in the flattened representation which, in turn, can result in overlooking of the polyp during inspection. The increased distortion resulting from strict area preservation, on the other hand, may also lead to difficulties in the detection of polyps. In this chapter, a flattening technique is proposed that minimizes a measure of metric distortion, referred to as *stretch* [Sander et al., 2001]. It is generally considered to be a good trade off between area and angle distortions and it thus lends itself to flattening of the colon. The flattening technique, presented here, is based on an improved version of the cylindrical parameterization technique of Huysmans et al. [2005]. In comparison to this previous parameterization technique, the new method is more robust, utilizes an improved distortion measure, and automatically determines the optimal length of the parameterization domain.

4.2 Methods

This section details the new method to generate a dissection view of the colon. It starts from the surface of the colon wall that has the topology of an open ended cylinder. This surface is first progressively parameterized to an open-ended cylinder of optimal length h, while keeping the introduced stretch to a minimum. Then, the cylinder is cut such that it is topologically equivalent to a disc and unfolded to a planar rectangle of length h. In order to obtain from-the-centerline-view lighting, the unfolded mesh is equipped with appropriate normals. A high quality dissection view can be obtained from flattened surface using standard surface rendering software. The parameterization of the colon surface to the cylinder is explained in Section 4.2.1. Mapping the cylindrically parameterized surface to the planar rectangle is discussed in Section 4.2.2. Finally, Section 4.2.3 expounds on the centerline-view rendering of the unfolded surface.

4.2.1 Cylindrical Parameterization

The colon surface is an orientable manifold $\mathscr{M}$ with two boundaries, denoted $\partial^0_{\mathscr{M}}$ and $\partial^1_{\mathscr{M}}$, and no topological handles. The parameterization domain is the two-dimensional open-ended, right circular cylinder with unit radius and length h, denoted by $\mathscr{C}^2_h$, and it has boundaries $\partial^0_{\mathscr{C}^2_h}$ and $\partial^1_{\mathscr{C}^2_h}$. The parameterization domain $\mathscr{C}^2_h$ is parameterized by an angular coordinate $u^{(0)} \in [0, 2\pi[$ and an axial coordinate $u^{(1)} \in [0, h]$. A cylindrical parameterization of $\mathscr{M}$ is any homeomorphic map $\boldsymbol{x}$ from the cylinder $\mathscr{C}^2_h$ to the surface $\mathscr{M}$, i.e. $\boldsymbol{x} : [0, 2\pi[\times [0, h] \to \mathscr{M} \subset \mathbb{R}^3$. In this chapter, the map $\boldsymbol{x}$ is represented by embedding the connectivity graph of the surface $\mathscr{M}$ in the parameterization domain $\mathscr{C}^2_h$. The colon $\mathscr{M}$ is described by the pair (K, M) where K is the simplicial complex containing the vertices, edges and faces of the surface mesh and $M = (\boldsymbol{x}_0, \ldots, \boldsymbol{x}_{n-1})$ are the coordinates of the vertices of the colon in $\mathbb{R}^3$. The parameterization $\boldsymbol{x}$ is represented by the embedding $\mathscr{U} = (K, U)$, where $U = (\boldsymbol{u}_0, \ldots, \boldsymbol{u}_{n-1})$ are the coordinates of the vertices of the mesh on the cylinder $\mathscr{C}^2_h$. When an embedding is established, the parameterization is defined at the vertices as $\boldsymbol{x}(\boldsymbol{u}_i) = \boldsymbol{x}_i$ and extended to the triangles by barycentric interpolation. The inverse of the piecewise linear map $\boldsymbol{x}$ exists and it is denoted by $\boldsymbol{u} : \mathscr{M} \to \mathscr{C}^2_h$.

Measuring Distortion

Given a surface $\mathscr{M}$ with parameterization $\boldsymbol{u}$, let the distortion at a point $\boldsymbol{x}$ on the surface $\mathscr{M}$ be denoted as $\xi_S(\boldsymbol{x}|\boldsymbol{u})$. The total amount of distortion exhibited by the parameterization can then be computed by integrating this measure over the entire surface:

$$\xi_S(\boldsymbol{u}) = \frac{1}{A_{\mathscr{M}}} \int_{\mathscr{M}} \xi_S(\boldsymbol{x}|\boldsymbol{u}) d\boldsymbol{x}, \tag{4.1}$$

where $A_{\mathscr{M}}$ denotes the area of the surface $\mathscr{M}$. Following Sander et al. [2001], the distortion $\xi_S(\bullet|\boldsymbol{u})$ of a parameterization $\boldsymbol{u}$ is measured in terms of the singular values of the Jacobian of $\boldsymbol{u}$. For each triangle $t \in K$, let γ_t and Γ_t be the smallest and the largest singular value of the Jacobian of the linear map $\boldsymbol{u}\big|_t$, respectively.

Then, a measure that penalizes both compression and expansion is obtained by making the stretch measure of Sander et al. [2001] symmetric with respect to the singular values, i.e.

$$\xi_S\big|_t(\bullet|\boldsymbol{u}) = \frac{\sqrt{2}}{4}\left(\sqrt{\gamma_t^2+\Gamma_t^2}+\sqrt{\frac{1}{\gamma_t^2}+\frac{1}{\Gamma_t^2}}\right), \tag{4.2}$$

which has a minimum of 1 when there is no distortion. The total distortion $\xi_S(\boldsymbol{u})$ introduced by a parameterization $\boldsymbol{u}: \mathscr{C}_h^2 \to \mathscr{M}$ can be evaluated as:

$$\xi_S(\boldsymbol{u}) = \frac{\sqrt{2}}{4A_{\mathscr{M}}}\sum_{t\in K} A_t\left(\sqrt{\gamma_t^2+\Gamma_t^2}+\sqrt{\frac{1}{\gamma_t^2}+\frac{1}{\Gamma_t^2}}\right), \tag{4.3}$$

where the surface integral of Eq. (4.1) becomes a sum over the triangles because, within each triangle, the map $\boldsymbol{u}$ is linear and, as a result, the singular values are constant. To make the above measure invariant under scaling of the surface $\mathscr{M}$, the singular values are scaled with a factor $\sqrt{\frac{A_{\mathscr{C}_h^2}}{A_{\mathscr{M}}}}$, where $A_{\mathscr{C}_h^2}$ is the area of the cylindrical domain $\mathscr{C}_h^2$.

Progressive Construction

Finding an embedding $\mathscr{U}$ of K on the cylinder $\mathscr{C}_h^2$ for the colon surface $\mathscr{M}$ that minimizes the nonlinear distortion measure of Eq. (4.3) is a large and challenging optimization problem. In this work, the approach of Hormann et al. [1999] is followed by utilizing a surface hierarchy in the construction of the parameterization. The method starts by constructing a surface hierarchy $(\mathscr{M}^0, \{\text{vsplit}_1, \ldots, \text{vsplit}_m\})$ called the progressive mesh [Hoppe, 1996] of surface $\mathscr{M}$, where vsplit_i denotes the vertex splitting operation that turns level $i-1$ of the progressive mesh into level i. It is obtained from the original surface $\mathscr{M}$ by successively collapsing edges into vertices, i.e.

$$\mathscr{M} \equiv \mathscr{M}^m \xrightarrow{\text{ecol}_m} \mathscr{M}^{m-1} \xrightarrow{\text{ecol}_{m-1}} \ldots \xrightarrow{\text{ecol}_1} \mathscr{M}^0, \tag{4.4}$$

where ecol_i is the inverse operation of vsplit_i, i.e., the edge collapse that turns level i of the progressive mesh into level $i-1$. With every surface $\mathscr{M}^i$ in the hierarchy corresponds a simplicial mesh, i.e. $\mathscr{M}^i = (K^i, M^i)$, where K^i contains the vertex connectivity and $M^i \subset M$ are the positions in $\mathbb{R}^3$ of the vertices. As in Garland and Heckbert [1997], the order of the edge collapses is determined by a quadratic error metric which penalizes deviation from the original surface. Additionally, a collapse is subject to a number of conditions: an edge collapse should not result in (1) non-manifold geometry, (2) degenerate triangles, or (3) triangles that have all three vertices at the same boundary. Also, (4) boundary vertices should only be collapsed into vertices of the same boundary. Any violation of these conditions will result in an invalid parameterization.

The obtained hierarchy is now utilized to construct a parameterization of $\mathscr{M}$ in a progressive way. First, the embedding $\mathscr{U}^0$ of K^0 in $\mathscr{C}_h^2$ is found. This defines a parameterization of the base mesh $\mathscr{M}^0$. It turns out that, for surfaces of cylindrical topology, the base mesh $\mathscr{M}^0$, as generated by a progressive mesh that takes into account conditions (1)-(4), contains six vertices, namely three at each boundary. As a consequence, a valid embedding $\mathscr{U}^0$ can be established trivially by evenly distributing the vertices of the base mesh $\mathscr{M}^0$ over the boundaries of $\mathscr{C}_h^2$.

The obtained parameterization $\mathscr{U}^0$ of the base mesh $\mathscr{M}^0$ provides a valid starting point for further refinement of the parameterization. By applying vertex split vsplit_i to the embedding $\mathscr{U}^{i-1}$ of the level $i-1$ surface $\mathscr{M}^{i-1}$, an embedding $\mathscr{U}^i$ of level i surface $\mathscr{M}^i$ is obtained. The initial position of the newly introduced vertex v_i is chosen at the center of the kernel of its 1-ring neighbourhood on the cylinder $\mathscr{C}_h^2$. This initialization always provides a valid embedding $\mathscr{U}^i$. The position of the vertex v_i is then further optimized, with respect to the distortion measure ξ_S, using gradient descent within the bounds of the kernel. Note that the distortion measure can be evaluated efficiently because movements of v_i only affect the triangles of its 1-ring neighbourhood.

Occasionally, when the amount of vertices has increased with a certain factor (e.g. 1.1), a full optimization is run, this in order to allow larger adjustments. In a full optimization run, all vertices are optimized one by one, within the kernel of their 1-ring neighbourhood. This process is repeated until the improvement in distortion drops below a certain value (e.g. 0.001). The order in which each vertex is optimized is determined by the distortion reduction that vertex caused in the previous optimization.

When all vertex splits have been applied, the embedding $\mathscr{U}^m \equiv \mathscr{U}$ of surface $\mathscr{M}^m \equiv \mathscr{M}$ is obtained. It should be noted that an embedding obtained in this way is valid by construction.

Length Optimization

The length h of the cylindrical domain $\mathscr{C}_h^2$ is a variable in the optimization problem. The length h that gives rise to the parameterization $\boldsymbol{u}$ with minimal distortion, in terms of ξ_S, is considered optimal. Here, the length is optimized, using Brent's method, at several stages during the progressive construction of the parameterization, namely after each full run of vertex optimizations. In this way, an accurate estimate of the length of the domain is obtained early in the hierarchy and subsequent optimizations converge in a few iterations. The method is made efficient by storing the current Jacobian for each triangle during the full vertex optimization. These Jacobians can then be used to optimize the length: scaling the length of the domain with a factor s simply results in new Jacobians $J_i^s = J_i \cdot \begin{bmatrix} 1 & 0 \\ 0 & \frac{1}{s} \end{bmatrix}$, from which the singular values, required for the computation of the distortion ξ_s, can easily be derived.

Final Algorithm

The final optimization problem can be stated as follows

$$\underset{\boldsymbol{u}_k, h}{\arg\min}\, \xi_S(\boldsymbol{u}) \quad \text{subject to} \quad \begin{array}{lll} u_i^{(1)} & = 0, & \forall\, i \in V_{B_0}, \\ u_i^{(1)} & = h, & \forall\, i \in V_{B_1}, \end{array}$$

where V_{B_0} is the set of vertices on boundary $\partial^0_{\mathcal{M}}$ and V_{B_1} is the set of vertices on boundary $\partial^1_{\mathcal{M}}$. The nonlinear parameterization method that solves this problem is laid out in Algorithm 2.

Algorithm 2 Parameterize $\mathcal{M}$ with distortion measure ξ_S

Input: $\mathcal{M}$
Output: $\boldsymbol{x}$

build progressive mesh of $\mathcal{M}$: $\mathcal{M} \equiv \mathcal{M}^m \xrightarrow{\text{ecol}_m} \mathcal{M}^{m-1} \xrightarrow{\text{ecol}_{m-1}} \dots \xrightarrow{\text{ecol}_1} \mathcal{M}^0$
map base mesh $\mathcal{M}^0$ to $\mathcal{C}_h^2$: $\mathcal{M}^0 \to \mathcal{U}^0$
for $i = 1$ to m **do**
  introduce new vertex v_i by applying vsplit$_i$ to $\mathcal{U}^{i-1}$: $\mathcal{U}^{i-1} \xrightarrow{\text{vsplit}_i} \mathcal{U}^i$
  provide initial position $\boldsymbol{u}_i^0$ for v_i
  optimize position of v_i on $\mathcal{C}_h^2$, starting from $\boldsymbol{u}_i^0$: $\hat{\boldsymbol{u}}_i = \arg\min_{\boldsymbol{u}_i} \xi_S(\boldsymbol{u})$
  if number of vertices increased with factor 1.1 **then**
    while improvement **do** $\hat{\boldsymbol{u}}_j = \arg\min_{\boldsymbol{u}_j} \xi_S(\boldsymbol{u})$, $\forall\, j$
    optimize length h of $\mathcal{C}_h^2$: $h = \arg\min_h \xi_S(\boldsymbol{u})$
  end if
end for
return $\boldsymbol{x} = \boldsymbol{u}^{-1}$

4.2.2 Unfolding to a Planar Rectangle

Using the inverse map $\boldsymbol{u}$ of the cylindrical parameterization $\boldsymbol{x}$, the colon surface $\mathcal{M}$ can easily be unfolded into a planar rectangle. The $u^{(0)} = 0$ iso-line is traced over the surface $\mathcal{M}$ going from $\boldsymbol{u} = (0, h)$ on boundary $\partial^1_{\mathcal{M}}$ to $\boldsymbol{u} = (0, 0)$ on boundary $\partial^0_{\mathcal{M}}$ by following the direction $(\nabla u^{(0)})^{\perp}$, where $\perp$ is a 90° counter-clockwise rotation. The colon surface is then cut open along the traced iso-line. Finally, the obtained topological disc is unfolded to a planar $2\pi \times h$ rectangle by putting each vertex $\boldsymbol{p}$ at the position determined by the inverse of the parameterization: $\boldsymbol{u}(\boldsymbol{p})$.

4.2.3 Visualization

In order to add shape information to the flattened colon, it is shaded as if each point was observed from the centerline. Such shading is obtained by equipping

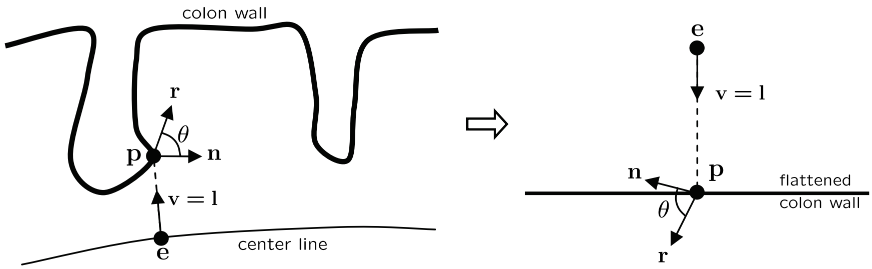

Figure 4.1: Left: The 3D colon surface vertex $\boldsymbol{p}$, with normal vector $\boldsymbol{n}$, is observed from the corresponding point $\boldsymbol{e}$ of the centerline. The position of the point light is fixed to the view point $\boldsymbol{e}$, thus the light vector $\boldsymbol{l}$ coincides with the view vector $\boldsymbol{v}$. In such a configuration, the angle θ (or equivalently the dot product) between the normal $\boldsymbol{n}$ and the reflection vector $\boldsymbol{r}$ completely determines the lighting at point $\boldsymbol{p}$. Right: Choosing the normal at the vertex of the 2D flattened colon surface to have the same angle θ with the reflection vector results in the exact same lighting as in the 3D scene.

the vertices of the flattened colon with appropriate normal vectors. A parametric centerline of the colon can be obtained from the parameterization $\boldsymbol{x}$ by integration over the first parameter:

$$\boldsymbol{c}(t) = \frac{1}{2\pi} \int_0^{2\pi} \boldsymbol{x}(s,t)\, ds. \tag{4.5}$$

The normals at the vertices of the 3D colon surface are obtained from the gradient of the CT image. The angle θ between the surface normal and the viewing direction, with the camera positioned at the corresponding centerline point, is calculated. The vertex in the flattened colon surface is assigned a normal that results in the same angle θ and thus also the same lighting. See Figure 4.1. Finally, the flattened colon is visualized by ordinary surface rendering in parallel projection with a single headlight and Phong fragment shading provides fine-grain realism.

4.3 Results and Discussion

The topologically cylindrical colon surface $\mathcal{M}$, counting $1.3M$ triangles, was extracted from a CT data set of the abdomen. The CT volume measured $512 \times 512 \times 532$ voxels of size $0.78 \times 0.78 \times 0.8 mm^3$. The colon surface was parameterized using the progressive stretch minimization technique and also using the conformal method of Haker et al. [2000a]. Both parameterizations were unfolded to the plane and rendered with the techniques of Section 4.2.2 and Section 4.2.3. The resulting unfolding is shown in Figure 4.2.

	method	
	conformal	stretch
angle	1.002	1.068
area	106.671	1.091
time (s)	100	924

Table 4.1: Calculation time and distortion measures for conformal flattening and the stretch optimized flattening.

The angle distortion ξ_C and the area distortion ξ_A, introduced by the flattening, are calculated as follows:

$$\xi_C(\boldsymbol{u}) = \frac{1}{2A_{\mathcal{M}}} \sum_{t\in K} A_t \left(\frac{\gamma_t}{\Gamma_t} + \frac{\Gamma_t}{\gamma_t} \right) \tag{4.6}$$

$$\xi_A(\boldsymbol{u}) = \frac{1}{2A_{\mathcal{M}}} \sum_{t\in K} A_t \left(\gamma_t \Gamma_t + \frac{1}{\gamma_t \Gamma_t} \right). \tag{4.7}$$

The distortion values for both techniques are reported in Table 4.1. It can be seen that the conformal method introduces severe area distortions in order to keep the angle distortions to a minimum. The method of this work, on the other hand, keeps both the area and angle distortion low. This can also be observed in figure 4.2, where the flattened colon is overlaid with the local area and angle distortion. The subfigures 4.2(e) and 4.2(f) show a part of the flattened colon image that corresponds to severe protrusions. In the stretch optimized flattening the protrusions are clearly visible, but in the conformal flattening they have almost entirely disappeared.

The conformal flattening is based on the solution of a large but sparse linear system and thus very efficient. The method of this chapter is based on non-linear optimization and is computationally more complex, but it can be seen from Table 4.1 that the computation time for this colon, counting 1.3M triangles, is less than 14 minutes. In exchange for an improved visibility of certain polyps, this increased computation time certainly is justified.

4.4 Conlusion

In this chapter, a new method for flattening of the colon was introduced. The flattening is obtained by minimization of the non-linear stretch measure and the method is made robust and efficient through utilization of a surface hierarchy. In this way, the flattening is generated within minutes. The resulting flattenings are low in both angle and area distortion. As opposed to traditional conformal flattening techniques, which often introduce large area distortions, the new method avoids severe down-scaling even for very pronounced protrusions, increasing the detection probability.

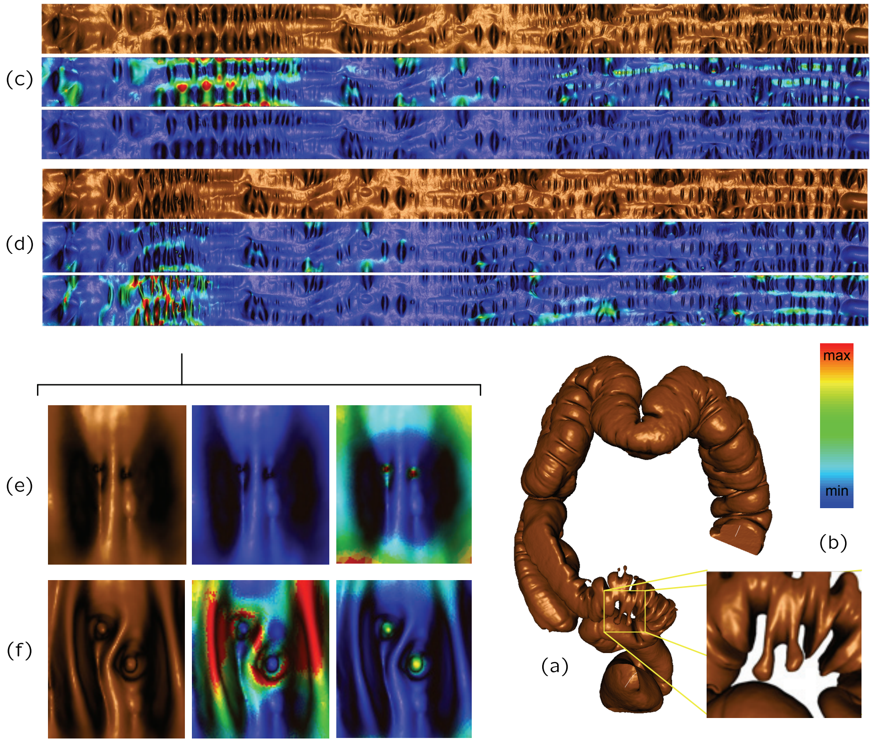

Figure 4.2: Conformal versus stretch optimized colon flattening: (a) Surface of the colon. (b) Magnification of part of the colon surface that exhibits significant down-sizing in the conformal flattening. (c) Flattened colon using conformal method. The final rendering is shown at the top and a map of the area distortion and the angle distortion is shown at the bottom. (d) same as in (c) but for the stretch optimization method. (e) Magnification of part of the conformally flattened colon, corresponding to the part of the colon shown in (b), From left to right: final rendering, angle distortion, and area distortion. (f) Same as in (e) but for the stretch optimization method. From (e) and (f) it can be seen that narrow protruding parts are significantly down-sized. This is not the case with the method of this chapter.

4.5 Future Work

For future work, it would be interesting to increase the performance of the method even further. There are a number of possible optimizations:

- The work of Dong and Garland [2007] is worth noting. For surfaces of disk-like topology, low distortion parameterizations are efficiently obtained by solving a sequence of linear systems where the edge weights of the linear systems are obtained by local non-linear stretch optimizations. All the necessary components to extend this approach to surfaces of cylindrical topology are available from this work.

- The linear system solver involved in the iterative construction can be further improved by making use of a multi-level mechanism. This was done for planar meshes in Aksoylu et al. [2005] and is easily extendible to surfaces of cylindrical topology.

- All of the above methods can be implemented on the GPU and in that way enjoy massive parallelism. Sparse linear system solvers and multigrid solvers are readily available from Bolz et al. [2003]. The nonlinear minimization of the vertices within their respective 1-rings can also be solved in parallel by conjugate gradient on the GPU.

Chapter 5

Shape Modeling of the Human Clavicle: Application to Anatomical Precontouring of Osteosynthesis Plates

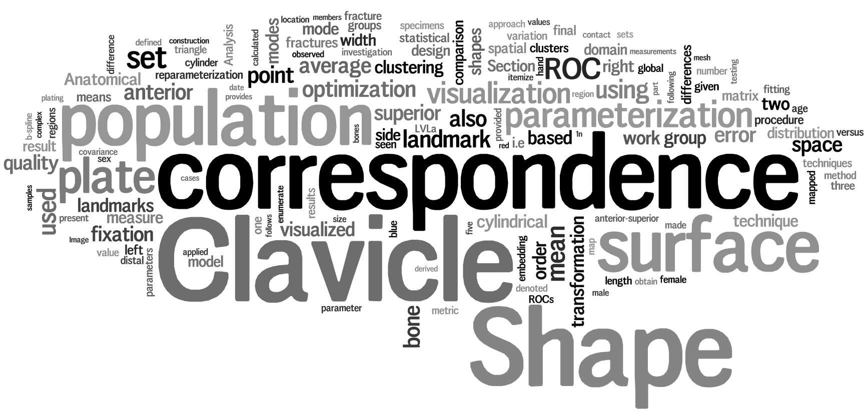

The work in this chapter has been submitted to Elsevier Medical Image Analysis as:

Toon Huysmans, Amit Bernat, Rômulo Pinho, Francis Van Glabbeek, and Jan Sijbers, "Shape Modeling of the Human Clavicle: Application to Anatomical

Precontouring of Osteosynthesis Plates", 2009.

Abstract

The clavicle is among the most frequently fractured bones in the human body and there is an increasing number of indications for surgical treatment of clavicular fractures. Due to the complex shape of the clavicle and its large variability, the design of osteosynthesis hardware is a very challenging task. Extensive knowledge of the anatomy of the clavicle clearly contributes to the improvement of such hardware. In this work, a methodology is proposed to facilitate the investigation of the anatomical shape of the clavicle of a given population. First, a new method is proposed to establish a dense correspondence for a population of clavicles, based on surface parameterization. Next, on the obtained correspondence, group-based local statistical analyses are performed to assess shape differences with respect to sex, direction, and date of birth. The correspondence is also employed to develop a set of precontoured osteosynthesis plates, covering the population under consideration with small error. The devised method is based on clustering and extracts a set of precontoured osteosynthesis plates from the distribution of clavicles in shape space. Experiments on a population of 90 clavicles are conducted to demonstrate the developed methods. The quality of the established correspondence and derived plates is also assessed.

5.1 Introduction

The clavicle is an S-shaped bone serving several functions in the human body. It stabilizes the shoulder girdle, protects the neurovascular bundle, and transmits physical impacts from the upper limb to the axial skeleton. In this last capacity, the clavicle is often subject to fracture. Although, in many cases, conservative treatment is satisfactory [Neer, 1960, Nordqvist et al., 1998], there are many indications for surgical intervention [McKee et al., 2006, 2003, Nowak et al., 2005, Wick et al., 2001]. From a variety of surgical treatment options, fixation through plating has the best outcome [Society, 2007, Golish et al., 2008, Endrizzi et al., 2008]. Knowledge of the specific shape of the clavicle and its possible variations is extremely valuable in the design of new treatment hardware. Furthermore, knowledge of, for example, skeletal asymmetries, gender related shape differences, or ethnicity related shape differences contributes to the field of human anatomy in general.

In comparison to other long bones, the shape of the clavicle is rather complex and it shows many variations. This complicates the investigation of its three-dimensional shape. In this work, a methodology is set forth that makes such an investigation possible with minimal effort from the user. The main application targeted in this chapter is the design of a set of plates for mid-shaft clavicular fracture fixation. Prior to the actual plate design, an investigation is made of the influence of sex, direction, and date of birth on the shape of the clavicle and, consequently, the shape of the fixation plates. This investigation will be carried out by means of statistical group testing combined with a qualitative exploration of the shape space.

The major hurdle in population-based shape investigation is the construction of a correspondence between the population members. In the case of a population of clavicles, a correspondence should provide a one-to-one map between the surfaces of any two clavicles in the population. Infinitely many such correspondences are possible and which specific correspondence is desired actually depends on the targeted application. Since this work is concerned with the design of tightly fitting fracture fixation plates, the design is mainly driven by the global shape of the clavicle and to a lesser extent by the local features. A correspondence technique that provides a good global match is the minimum description length (MDL) technique from Davies et al. [2002a]. Their approach will be followed in this work. Recently, the MDL-technique was extended to include local shape information [Styner et al., 2008], providing a trade-off between matching global or local features. The latter is, however, not aimed for in this work.

This work will set forth an approach to obtain a surface-based correspondence for a given population of clavicles with a good global match. The correspondence is obtained by mapping each surface to a common and mathematically simple parameter domain, followed by an optimization procedure that improves the alignment of the surfaces in the spatial and parametric domain. Since the shape of the clavicle is elongated, the cylinder is chosen as the common parameter domain. The cylindrical parameterization technique of Huysmans et al. [2009] will be used to construct the initial maps to the cylinder and a modified version of the technique of Huysmans and Sijbers [2009] is used to optimize the correspondence.

The correspondence, obtained with the proposed technique, will be employed for further analysis and modeling. The shape of the clavicle will be explored by visualization of the average clavicle shape and the main modes of variation present in the population. In addition, the shape asymmetry, shape differences between genders, and the influence of the date of birth will be assessed by permutation group testing using the Hotelling T^2 distance measure. As noted, the obtained correspondence will also be used to generate a set of fracture fixation plate shapes. As an input the procedure takes a desired region of contact, between bone and plate, defined on the average clavicle. A clustering technique is, then, used to extract a set of plate shapes that covers the whole population with a small fitting error.

It is noted, that the applicability of the methods developed in this work is not restricted to populations of clavicles. The methodology can also be applied to other populations of elongated bones, such as the humerus, radius, ulna, femur, tibia, and finger bones. The only condition is that there is a consistently identifiable point at both ends of the bone. For these elongated bones, possible applications are implant design, skeletal asymmetry studies, automatic shape guided image segmentation, and operative planning.

5.1.1 Related Work

To date, there has been no full 3D analysis of the anatomy of the clavicle. All of the following studies analyze and model the clavicle through a sparse set of measurements and mostly in 2D projections. In Huang et al. [2007], the inferior bow of the distal extremity and the angulations of the medial and lateral curves were measured using a digitizer and goniometer, followed by an analysis of differences between black and white specimens and between male and female specimens. Proportions and characteristics of the English clavicle were studied in Parsons [1916] and even an average contour was constructed in two orthogonal planes. Directional asymmetry of the clavicle was studied in Mays et al. [1999], Auerbach and Raxter [2008]. Length, curvatures, diameters, bone density and cortical thickness were studied in Andermahr et al. [2007], in the view of intramedullary nailing of midclavicular fractures. Due to the sparsity of the measurements, the analyses and modeling of these works do not cover the complete 3D anatomy of the clavicle and the information provided is insufficient to derive suitable precontouring for fixation plates.

The techniques proposed in this work use a dense set of 3D measurements in their analyses and modeling, which are derived from the correspondence. There are several possibilities for the representation and construction of a correspondence for a population of objects:

- image registration based techniques, e.g., Rueckert et al. [2001], Frangi et al. [2001], Frangi et al. [2002], Joshi et al. [2004], and Cootes et al. [2004],
- point-based techniques, e.g., Cates et al. [2007], Ferrarini et al. [2007], and Dalai et al. [2007],
- surface parameterization based techniques, e.g., Brechbühler et al. [1995], Zöckler et al. [2000], Lamecker et al. [2002], Lamecker et al. [2004], and Huysmans et al. [2006],
- surface reparameterization based techniques, e.g., Davies et al. [2002a], Horkaew and Yang [2003a], Horkaew and Yang [2004], Heimann et al. [2005], and Huysmans et al. [2009].

In this work, the cylindrical parameterization approach of Huysmans et al. [2009] will be used together with a modified version of the cylindrical surface reparameterization based approach from Huysmans and Sijbers [2009]. Compared to other approaches, it has the following advantages:

- For the targeted applications, only the shape of the outer surface of the clavicle is important. Therefore, it is more efficient to use a 2D surface based technique instead of a 3D image based technique.

- Each clavicle is represented by an irregular triangle mesh. The resolution of the triangle mesh locally adapts to the amount of detail present as opposed to an image based representation that would use a regular grid over the whole object. The triangle based representation is thus more efficient.

- The surface reparameterization approach results in a one-to-one correspondence. Point based correspondence techniques do not make assumptions about the topology of the surfaces. These techniques can therefore be applied to complex topologies but the one-to-one property can not be ensured.

- The reparameterization approach directly optimizes a group based correspondence measure based on the obtained shape space of the population. The parameterization based correspondence techniques do not optimize a group based measure. Image based registration techniques, on the other hand, are based on image intensities and do not take into account the shape space of the final population.

- The reparameterization technique used in this chapter is specifically designed for populations of surfaces of cylindrical topology. The use of a cylindrical domain for elongated surfaces results in maps from the cylinder to the clavicles that are smooth and low in distortion.

5.1.2 Clinical Background on Mid-shaft Clavicle Fracture Treatment

The clavicle is a complex S-shaped bone serving a stabilizing role in the human body. It is the only bony connection between the axial skeleton and the upper limb and it has various muscles and ligaments attached to it. The clavicle transmits loads on the upper limb to the axial skeleton [Harrington et al., 1993]. Heavy impacts often result in clavicular fractures. These account for 2% to 5% of all adult fractures and occur more commonly in younger individuals [Allman, 1967, Nordqvist and Petersson, 1994, Postacchini et al., 2002]. Most common are mid-shaft fractures, where the fracture occurs in the middle third of the bone, accounting for 80% of all clavicular fractures [Allman, 1967, Nordqvist and Petersson, 1994]. The study presented here concentrates on this type of fractures, but the developed techniques could also be employed for the development of fixation plates for fractures of the medial or lateral third.

Mostly, mid-shaft clavicle fractures are treated conservatively since they heal well [Neer, 1960, Nordqvist et al., 1998]. Although infrequent, malunions and nonunions can lead to substantial long term sequelae, including persistent pain, weakness, and loss of range of motion [McKee et al., 2006, 2003, Nowak et al., 2005, Wick et al., 2001]. Moreover, recent studies have demonstrated nonunion rates of more than 15% for displaced mid-shaft clavicle fractures when treated non-operatively [Hill et al., 1997, Zlowodzki et al., 2005]. There is an increasing number of indications for operative treatment: neurovascular injury, open injury, tented or necrotic skin, irreducible displaced mid-shaft clavicular fracture, nonunion or malunion, polytrauma, significant shortening and athletes with high activity level [Khan and Lucas, 1977, Poigenfürst et al., 1992, Schwarz and Höcker, 1992, Tavitian et al., 2002, Kabak et al., 2004, Verborgt et al., 2005]. Surgical options for the treatment of clavicle fractures include pins, Kirschner wires, and various plates. Although pins are a minimally invasive option, they suffer from inferior axial and rotational stability and there is a serious risk of pin migration [Marchi et al., 2008]. Plate fixation, on the other hand, has superior biomechanic properties and results in a high success rate [Society, 2007, Golish et al., 2008, Endrizzi et al., 2008].

Various plates are available: dynamic compression plates (DC), limited contact dynamic compression plates (LCDC), reconstruction plates (Recon), and, more recently, anatomical precontoured plates. In Iannotti et al. [2002], biomechanical testing demonstrated that LCDC delivers better stability compared with DC and Recon plates and this is supported clinically by Kabak et al. [2004]. Due to the complex anatomy of the clavicle, contouring such a plate during surgery to match the patient specific anatomy can be technically challenging. Precontoured plates are being developed to overcome this difficulty. In Huang et al. [2007], the quality of the precontoured Locking Clavicle Plates (Acumed, Hillsboro, Oregon) were assessed qualitatively by manually overlaying the Acumed templates with the 2D radiographs and judging the best fit result. While the plate provided a good fit to most male specimens, substantial plate overhang was observed for white female specimens. It is clear that a thorough understanding of the complex 3D anatomy of the clavicle is paramount for the development of an optimal set of fixation plates. The methodology proposed in this work provides the necessary tools to achieve such an understanding.

Several approaches exist to plating the clavicle: anterior, superior, and superior distal to anterior proximal plating. Currently, there is no consensus on the method of preference. In Iannotti et al. [2002], biomechanical testing showed that superior plating is preferred over anterior plating in terms of biomechanical stability. In Collinge et al. [2006], on the other hand, excellent results were observed with anterior plating. The latter also received better Visual Analog Scale patient symptom scores [Zlowodzki et al., 2005]. With the technique of Shen et al. [2008], the plate covers the superior distal and the anterior proximal part of the clavicle which have a thicker cortex. A shorter time to union and less complications were observed. The techniques developed in this work are independent of the above approaches and are able to derive sets of fixation plates for any of these configurations.

5.1.3 Contributions

The main contributions of the work presented in this work can be summarized as follows:

- A set of techniques that is specifically designed for the analysis and modeling of populations of cylindrical or elongated surfaces, such as long bones.
- The first automatic and dense investigation of the 3D morphology of the clavicle.
- The first automated precontouring technique for clavicle plates, taking into account the shape present in a population of clavicles.

5.1.4 Organization of the Chapter

The remainder of this chapter is organized as follows. Section 5.2 provides an overview of the data sets used in this study and details the preprocessing steps that were applied to these data sets. In Section 5.3, the representation of the surfaces and the associated correspondence is introduced. The construction of a correspondence for a population is detailed in Section 5.4, followed by a discussion of the group analysis and shape template generation techniques in Section 5.5. The performed experiments and the obtained results are discussed in Section 5.6. Section 5.7 concludes the chapter.

5.2 Data Sets and Preprocessing

For the experiments of this study, a population of 90 human clavicles was used. The clavicles, provided by the Faculty of Medicine of the University of Antwerp, were dissected from 32 male and 19 female human cadavers. The age of the specimens ranged from 25 years to 99 years with an average age of 71 years. The population of clavicles contains 38 left/right-pairs and 14 individual clavicles. An overview of the population of clavicles can be found in Table 5.1.

All clavicles were mounted on cardboard in a standard pose, easing later surface alignment. For each clavicle, 3D-scanning and reconstruction was performed with a GE Lightspeed VCT system at a spatial resolution of $0.5 \times 0.5 \times 0.6\,mm^3$. The reconstructed 3D-volumes were segmented into two complementary regions: the inside of the clavicle and tissue/air. The use of a highly concentrated zinc chloride solution in the embalming procedure of the cadavers resulted in an increased x-ray absorption rate for tissue. In case of an unembalmed specimen, any volume intensities above $400HU$ were assumed to be bone. In the embalmed situation, tissue intensities were observed as high as $1000HU$. This resulted in a large overlap between bone and tissue in the intensity histogram, effectively making histogram based threshold estimation

<table>
<tr><th>id</th><td>1</td><td>2</td><td>3</td><td>4</td><td>5</td><td>6</td><td>7</td><td>8</td><td>9</td><td>10</td><td>11</td><td>12</td></tr>
<tr><th>sex</th><td>M</td><td>M</td><td>M</td><td>M</td><td>M</td><td>M</td><td>M</td><td>M</td><td>M</td><td>M</td><td colspan="2">M</td></tr>
<tr><th>age</th><td>35</td><td>29</td><td>50</td><td>27</td><td>42</td><td>25</td><td>45</td><td>76</td><td>36</td><td>41</td><td colspan="2">80</td></tr>
<tr><th>side</th><td>R</td><td>R</td><td>R</td><td>R</td><td>R</td><td>R</td><td>R</td><td>R</td><td>R</td><td>R</td><td>R</td><td>L</td></tr>
</table>

<table>
<tr><th>id</th><td>13</td><td>14</td><td>15</td><td>16</td><td>17</td><td>18</td><td>19</td><td>20</td><td>21</td><td>22</td><td>23</td><td>24</td></tr>
<tr><th>sex</th><td colspan="2">F</td><td colspan="2">F</td><td colspan="2">M</td><td colspan="2">F</td><td colspan="2">F</td><td colspan="2">F</td></tr>
<tr><th>age</th><td colspan="2">84</td><td colspan="2">77</td><td colspan="2">76</td><td colspan="2">71</td><td colspan="2">99</td><td colspan="2">58</td></tr>
<tr><th>side</th><td>R</td><td>L</td><td>R</td><td>L</td><td>R</td><td>L</td><td>R</td><td>L</td><td>R</td><td>L</td><td>R</td><td>L</td></tr>
</table>

<table>
<tr><th>id</th><td>25</td><td>26</td><td>27</td><td>28</td><td>29</td><td>30</td><td>31</td><td>32</td><td>33</td><td>34</td><td>35</td><td>36</td></tr>
<tr><th>sex</th><td colspan="2">M</td><td colspan="2">M</td><td colspan="2">F</td><td colspan="2">F</td><td colspan="2">M</td><td colspan="2">M</td></tr>
<tr><th>age</th><td colspan="2">83</td><td colspan="2">91</td><td colspan="2">80</td><td colspan="2">85</td><td colspan="2">78</td><td colspan="2">71</td></tr>
<tr><th>side</th><td>R</td><td>L</td><td>R</td><td>L</td><td>R</td><td>L</td><td>R</td><td>L</td><td>R</td><td>L</td><td>R</td><td>L</td></tr>
</table>

<table>
<tr><th>id</th><td>37</td><td>38</td><td>39</td><td>40</td><td>41</td><td>42</td><td>43</td><td>44</td><td>45</td><td>46</td><td>47</td><td>48</td></tr>
<tr><th>sex</th><td colspan="2">M</td><td colspan="2">F</td><td colspan="2">M</td><td colspan="2">M</td><td colspan="2">F</td><td colspan="2">M</td></tr>
<tr><th>age</th><td colspan="2">77</td><td colspan="2">85</td><td colspan="2">74</td><td colspan="2">73</td><td colspan="2">85</td><td colspan="2">63</td></tr>
<tr><th>side</th><td>R</td><td>L</td><td>R</td><td>L</td><td>R</td><td>L</td><td>R</td><td>L</td><td>R</td><td>L</td><td>R</td><td>L</td></tr>
</table>

<table>
<tr><th>id</th><td>49</td><td>50</td><td>51</td><td>52</td><td>53</td><td>54</td><td>55</td><td>56</td><td>57</td><td>58</td><td>59</td><td>60</td></tr>
<tr><th>sex</th><td>F</td><td colspan="2">M</td><td>M</td><td colspan="2">M</td><td colspan="2">M</td><td colspan="2">M</td><td colspan="2">F</td></tr>
<tr><th>age</th><td>82</td><td colspan="2">67</td><td>60</td><td colspan="2">74</td><td colspan="2">69</td><td colspan="2">65</td><td colspan="2">87</td></tr>
<tr><th>side</th><td>R</td><td>R</td><td>L</td><td>R</td><td>R</td><td>L</td><td>R</td><td>L</td><td>R</td><td>L</td><td>R</td><td>L</td></tr>
</table>

<table>
<tr><th>id</th><td>61</td><td>62</td><td>63</td><td>64</td><td>65</td><td>66</td><td>67</td><td>68</td><td>69</td><td>70</td><td>71</td><td>72</td></tr>
<tr><th>sex</th><td colspan="2">F</td><td colspan="2">M</td><td colspan="2">M</td><td colspan="2">M</td><td colspan="2">M</td><td colspan="2">F</td></tr>
<tr><th>age</th><td colspan="2">43</td><td colspan="2">74</td><td colspan="2">85</td><td colspan="2">80</td><td colspan="2">88</td><td colspan="2">87</td></tr>
<tr><th>side</th><td>R</td><td>L</td><td>R</td><td>L</td><td>R</td><td>L</td><td>R</td><td>L</td><td>R</td><td>L</td><td>R</td><td>L</td></tr>
</table>

<table>
<tr><th>id</th><td>73</td><td>74</td><td>75</td><td>76</td><td>77</td><td>78</td><td>79</td><td>80</td><td>81</td><td>82</td><td>83</td></tr>
<tr><th>sex</th><td colspan="2">F</td><td colspan="2">F</td><td colspan="2">M</td><td>F</td><td colspan="2">F</td><td colspan="2">M</td></tr>
<tr><th>age</th><td colspan="2">82</td><td colspan="2">79</td><td colspan="2">64</td><td>93</td><td colspan="2">96</td><td colspan="2">81</td></tr>
<tr><th>side</th><td>R</td><td>L</td><td>R</td><td>L</td><td>R</td><td>L</td><td>L</td><td>R</td><td>L</td><td>R</td><td>L</td></tr>
</table>

<table>
<tr><th>id</th><td>84</td><td>85</td><td>86</td><td>87</td><td>88</td><td>89</td><td>90</td></tr>
<tr><th>sex</th><td colspan="2">M</td><td colspan="2">F</td><td colspan="2">F</td><td>F</td></tr>
<tr><th>age</th><td colspan="2">-</td><td colspan="2">88</td><td colspan="2">83</td><td>87</td></tr>
<tr><th>side</th><td>L</td><td>R</td><td>R</td><td>L</td><td>R</td><td>L</td><td>R</td></tr>
</table>

Table 5.1: An overview of the population of clavicles used in the experiments of the study. For each clavicle, an identifier (1-90) is provided together with the side of the body (Left/Right) from which it was extracted. For each single clavicle or clavicle L/R-pair, the sex (Male/Female) and age of the individual are also reported.

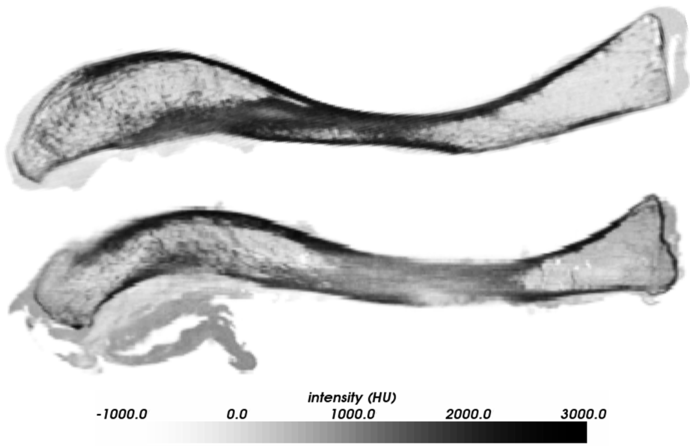

Figure 5.1: A slice through the reconstruction of a CT-scanned clavicle without (top) and with (bottom) embalming applied to the cadaver. The intensity overlap between bone and tissue complicates the segmentation procedure.

impossible. See Figure 5.1, for a comparison between a reconstruction of a CT-scanned clavicle from an unembalmed and an embalmed cadaver.

The above problem was addressed by the use of a semi-automatic segmentation procedure. Several thresholds were used in the segmentation and the user had to indicate the best result. The segmentations were generated by applying the following operations to the 3D-volumes:

1. Clipping of the volume to remove the scanning bed and the empty parts (air) of the volume.

2. Thresholding of the volume intensities. Different thresholds were used: $700HU$, $800HU$, $900HU$, $1000HU$, $1100HU$, $1200HU$, and $1300HU$.

3. Removal of small components by labeling connected components and removing components smaller than 50 voxels. In this way, unconnected small bone fragments present inside remaining tissue did not contribute to the final segmentation.

4. Padding the volume with zeros to avoid that the image dilation runs into the image boundary.

5. Ten dilations followed by ten erosions in order to close the interior of the clavicle

6. Ensuring 6-connectedness of the clavicle volume to ensure that the boundary surface is manifold. The NeuroLib toolbox (`http://www.ia.unc.edu/dev/`) is used to accomplish this.

For each clavicle, the best result of the different thresholds was chosen manually by inspection with the Avizo© segmentation viewer/editor and, where necessary, manual corrections were made. The boundary surface of the clavicle was extracted from the segmentation using the marching cubes algorithm [Lorensen and Cline, 1987]. Finally, all left clavicles were mirrored which allowed the construction of a correspondence and an analysis of the shape for the whole population of clavicles.

The correspondence technique detailed in this chapter requires that the surfaces in the population are of cylindrical topology. However, after extraction of the outer surface, the clavicles naturally have a spherical topology. Therefore, the topology of the clavicles is modified by punching a hole through the surfaces at the center of both the distal and proximal extremities. Using surface visualization combined with orthogonal volume slice visualization, an expert marked these locations for each member of the population.

5.3 Surface and Correspondence Representation

Each clavicle surface $\mathscr{M}_i$ of the population $\{\mathscr{M}_1,\dots,\mathscr{M}_{n_s}\}$ is represented with a triangle mesh. The triangle mesh is described by the pair (K_i, M_i), where K_i is the simplicial complex containing the vertices, edges, and faces of the surface mesh and $X_i = (\boldsymbol{x}_1^i,\dots,\boldsymbol{x}_{n_i}^i)$ are the coordinates of the n_i vertices of the surface in $\mathbb{R}^3$.

In order to obtain a correspondence between the surfaces in the population, each surface $\mathscr{M}_i$ is equipped with an appropriate cylindrical parameterization. A cylindrical parameterization of $\mathscr{M}_i$ is any homeomorphic map $\boldsymbol{x}_i$ from the cylinder $\mathscr{C}_h^2$ to the surface $\mathscr{M}_i$, i.e., $\boldsymbol{x}_i : [0,2\pi)\times[0,h] \to \mathscr{M}_i \subset \mathbb{R}^3$. Here, $\mathscr{C}_h^2$ is the parameterization domain and it is a two-dimensional open-ended right circular cylinder with unit radius and length h. The parameterization $\boldsymbol{x}_i$ is obtained by embedding the connectivity graph of the surface $\mathscr{M}_i$ in the parameterization domain $\mathscr{C}_h^2$. The embedding is denoted $\mathscr{U}_i = (K_i, U_i)$, where K_i again is the simplicial complex of the surface mesh and $U_i = (\boldsymbol{u}_1^i,\dots,\boldsymbol{u}_{n_i}^i)$ are the coordinates of the vertices of the mesh on the cylinder $\mathscr{C}_h^2$. When an embedding is established, the parameterization is defined at the vertices as $\boldsymbol{x}_i(\boldsymbol{u}_j^i) = \boldsymbol{x}_j^i$ and extended to the triangles by interpolation: a point $\boldsymbol{p}$ in a parametric triangle $\boldsymbol{u}_{k_1}^i\boldsymbol{u}_{k_2}^i\boldsymbol{u}_{k_3}^i$ with barycentric coordinates $(\beta_{k_1},\beta_{k_2},\beta_{k_3})$ is mapped to

$$\begin{aligned}\boldsymbol{x}_i(\boldsymbol{p}) &= \boldsymbol{x}_i(\beta_{k_1}\boldsymbol{u}_{k_1}^i + \beta_{k_2}\boldsymbol{u}_{k_2}^i + \beta_{k_3}\boldsymbol{u}_{k_3}^i)\\ &= \beta_{k_1}\boldsymbol{x}_{k_1}^i + \beta_{k_2}\boldsymbol{x}_{k_2}^i + \beta_{k_3}\boldsymbol{x}_{k_3}^i.\end{aligned}$$

The inverse of the piecewise linear map $\boldsymbol{x}_i$ exists and it will be denoted by $\boldsymbol{u}_i : \mathscr{M}_i \to \mathscr{C}_h^2$. See Figure 5.2 for a visualization of the maps $\boldsymbol{u}_i$ and $\boldsymbol{x}_i$ for a clavicle surface $\mathscr{M}_i$. Now it can be seen that the parameterizations $\{\boldsymbol{x}_1,\dots,\boldsymbol{x}_{n_s}\}$ of the clavicle population $\{\mathscr{M}_1,\dots,\mathscr{M}_{n_s}\}$ provide a correspondence:

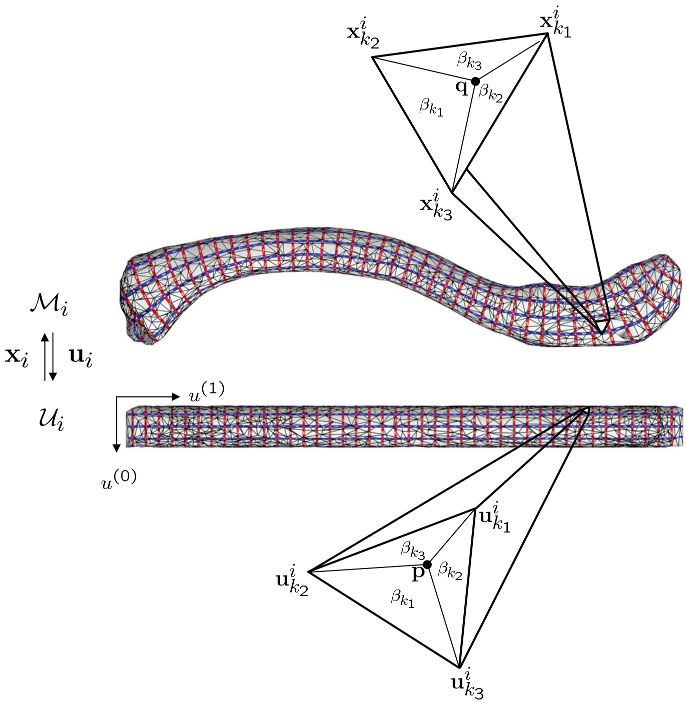

Figure 5.2: A clavicle surface $\mathscr{M}_i$ is shown together with its embedding $\mathscr{U}_i$ on the parameterization domain $\mathscr{C}^2_h$. The realisation of the simplicial complex K_i is overlaid on both domains. A given point $\boldsymbol{p}$ in a certain parametric triangle $\boldsymbol{u}^i_{k_1}\boldsymbol{u}^i_{k_2}\boldsymbol{u}^i_{k_3}$, shown at the bottom, with barycentric coordinates β_{k_j}, corresponds by the parameterization to the point $\boldsymbol{q}$ located in the corresponding spatial triangle $\boldsymbol{x}^i_{k_1}\boldsymbol{x}^i_{k_2}\boldsymbol{x}^i_{k_3}$, shown at the top, at the same barycentric coordinates.

- A point $\boldsymbol{p}$ on the surface of clavicle $\mathscr{M}_i$ corresponds to the point $\boldsymbol{q}$ on the surface of clavicle $\mathscr{M}_j$ iff $\boldsymbol{q} = \boldsymbol{x}_j \circ \boldsymbol{u}_i(\boldsymbol{p})$, where '$\circ$' denotes function composition.

- Any parameter location $\boldsymbol{u}$ on the cylinder $\mathscr{C}^2_h$ defines a point $\boldsymbol{x}_i(\boldsymbol{u})$ on each surface $\mathscr{M}_i$ and these points mutually correspond.

At certain stages in the processing pipeline, e.g, when evaluating the quality of a correspondence, it is useful to represent a clavicle with a point set instead of a parameterized surface. From a given parameterization $\boldsymbol{x}_i$ of the surface $\mathscr{M}_i$, such a point set representation $\dot{\boldsymbol{x}}_i$ can be easily obtained by sampling the surface at a set of n_p uniformly distributed cylindrical parameter locations $\boldsymbol{V}^{n_p} = \{\boldsymbol{v}_1, \ldots, \boldsymbol{v}_{n_p}\}$.

5.4 Correspondence Construction

Establishing a correspondence for the set of clavicles comes down to spatially aligning the surfaces in a common reference coordinate system and constructing a consistent parameterization for each surface. The approach taken in this work is based on the nonlinear cylindrical parameterization technique from Huysmans and Sijbers [2009] and a modified version of the cylindrical correspondence optimization technique from Huysmans et al. [2009]. The correspondence optimization technique is based on the minimum description length (MDL) technique of Davies et al. [2002a]. In that work, the quality of a given correspondence is calculated from the shape model derived from that correspondence. This approach will be adopted here.

For a population of clavicle surfaces $\{\mathscr{M}_1, \ldots, \mathscr{M}_{n_s}\}$, a correspondence is established as follows. First, each surface $\mathscr{M}_i$ is equipped with a parameterization $\boldsymbol{x}_i^\circ$ using a cylindrical parameterization method. Afterwards, each parameterization is modified by a reparameterization transformation in order to obtain a better matching between the surfaces as dictated by the correspondence quality measure. The reparameterization transformation, denoted $\boldsymbol{\rho}(\bullet|\boldsymbol{\Phi}_i^\rho)$, is a bijective map from and to the cylinder and it is modeled using a uniform b-spline network. The parameters $\boldsymbol{\Phi}_i^\rho$ of the reparameterization function are the control point positions on $\mathscr{C}_h^2$ of the b-spline network. In order to align the surfaces of the population, each surface $\mathscr{M}_i$ has its pose altered by a rigid spatial transformation $\boldsymbol{\tau}(\bullet|\boldsymbol{\Phi}_i^\tau)$, with $\boldsymbol{\Phi}_i^\tau$ its rotation and translation parameters. A correspondence is obtained for the population of clavicles by choosing the optimal spatial and parameterization transformation parameters for each surface in the population.

In addition to the method of Huysmans et al. [2009], which uses one spatial transformation and one parameterization transformation for each surface, here also a single global parameterization transform is applied to each surface. The purpose of this global transform, denoted $\bar{\boldsymbol{\rho}}(\bullet|\boldsymbol{\Phi}^{\bar{\rho}})$, is to maintain a uniform distribution of samples on the surfaces. Applying the same global transformation $\bar{\boldsymbol{\rho}}$ to each surface in the population does not change the correspondence between the surfaces. Only the correspondence with the cylindrical domain is altered. Thus, $\bar{\boldsymbol{\rho}}$ can be used to alter the distribution of samples on the surfaces without modifying the actual correspondence. The global reparameterization transformation is also represented using a uniform b-spline network with $\boldsymbol{\Phi}^{\bar{\rho}}$ as its control point locations on the cylinder.

Composition of the global transformation $\bar{\boldsymbol{\rho}}(\bullet|\boldsymbol{\Phi}^{\bar{\rho}})$, the reparameterization transformation $\boldsymbol{\rho}(\bullet|\boldsymbol{\Phi}_i^\rho)$, and the spatial transformation $\boldsymbol{\tau}(\bullet|\boldsymbol{\Phi}_i^\tau)$ together with the initial parameterization $\boldsymbol{x}_i^\circ$ results in the final parameterization $\boldsymbol{x}_i$ for surface $\mathscr{M}_i$, i.e.,

$$\boldsymbol{x}_i \equiv \boldsymbol{x}_i(\bullet|\boldsymbol{\Phi}_i^\tau, \boldsymbol{\Phi}_i^\rho, \boldsymbol{\Phi}^{\bar{\rho}}) = \boldsymbol{\tau}(\bullet|\boldsymbol{\Phi}_i^\tau) \circ \boldsymbol{x}_i^\circ \circ \boldsymbol{\rho}(\bullet|\boldsymbol{\Phi}_i^\rho) \circ \bar{\boldsymbol{\rho}}(\bullet|\boldsymbol{\Phi}^{\bar{\rho}}). \tag{5.1}$$

In other words, the correspondence $\{\boldsymbol{x}_1, \ldots, \boldsymbol{x}_{n_s}\}$ for a set of clavicles

$\{\mathcal{M}_1,\ldots,\mathcal{M}_{n_s}\}$ is determined by the initial parameterizations $\{\boldsymbol{x}_1^\circ,\ldots,\boldsymbol{x}_{n_s}^\circ\}$ and the parameters $\{\boldsymbol{\Phi}^{\bar{\rho}},\boldsymbol{\Phi}_1^{\tau},\boldsymbol{\Phi}_1^{\rho},\ldots,\boldsymbol{\Phi}_{n_s}^{\tau},\boldsymbol{\Phi}_{n_s}^{\rho}\}$ of the transformations.

In the remainder of this section, it will be shown how to obtain a shape model from a given correspondence and how to calculate the correspondence quality from this model. Then, it will be shown how to obtain good initial parameterizations and how to use the correspondence quality measure to find the optimal spatial and parameterization transformation parameters.

5.4.1 Statistical Shape Model

From a set of clavicle surfaces $\{\mathcal{M}_1,\ldots,\mathcal{M}_{n_s}\}$ aligned in a common reference coordinate system, together with a correspondence $\{\boldsymbol{x}_1,\ldots,\boldsymbol{x}_{n_s}\}$, a statistical shape model or a point distribution model [Cootes et al., 1995] can be calculated. The statistical shape model captures the average shape and the main shape variations, present in the population of clavicles, with a probability density function. A multivariate Gaussian distribution is used and the distribution parameters are obtained using singular value decomposition (SVD):

1. Each clavicle $\mathcal{M}_i$ is represented with a point set shape vector $\dot{\boldsymbol{x}}_i$ by sampling each parameterization $\boldsymbol{x}_i$ at the set of cylindrical parameter locations $\boldsymbol{V}^{n_p}$ and concatenating the coordinates of the n_p landmarks into a $3n_p$ column vector:

$$\dot{\boldsymbol{x}}_i = [\boldsymbol{x}_i(\boldsymbol{v}_1)\ldots\boldsymbol{x}_i(\boldsymbol{v}_{n_p})]^T. \tag{5.2}$$

   The clavicle population is represented by a single $3n_p \times n_s$ landmark matrix $\boldsymbol{X}$, obtained by concatenation of the n_s shape vectors, i.e.,

$$\boldsymbol{X} = [\dot{\boldsymbol{x}}_1\ldots\dot{\boldsymbol{x}}_{n_s}]. \tag{5.3}$$

2. The mean shape vector $\bar{\boldsymbol{x}}$ is computed as

$$\bar{\boldsymbol{x}} = \frac{1}{n_s}\sum_{i=1}^{n_s}\dot{\boldsymbol{x}}_i \tag{5.4}$$

   and the row centered landmark matrix is obtained by subtracting this mean shape from each column of $\boldsymbol{X}$, i.e.,

$$\boldsymbol{X}_c = [\dot{\boldsymbol{x}}_1-\bar{\boldsymbol{x}}\ldots\dot{\boldsymbol{x}}_{n_s}-\bar{\boldsymbol{x}}]. \tag{5.5}$$

3. The SVD of the centered landmark matrix is defined as

$$\frac{1}{\sqrt{n_s-1}}\boldsymbol{X}_c = \boldsymbol{P}\boldsymbol{S}\boldsymbol{Q}^T, \tag{5.6}$$

   where $\boldsymbol{P}$ is a $3n_p \times 3n_p$ orthonormal matrix containing the left singular vectors $\boldsymbol{p}_j$ as its columns, $\boldsymbol{S}$ is a $3n_p \times n_s$ diagonal matrix where the diagonal elements are the singular values σ_j in descending order, and $\boldsymbol{Q}$

is an $n_s \times n_s$ orthonormal matrix with the right singular vectors $\boldsymbol{q}_j$ as its columns.

The shape model is represented by the mean clavicle $\bar{\boldsymbol{x}}$ and the shape modes $\boldsymbol{p}_j$ with corresponding mode variances $\lambda_j = \sigma_j^2$. New clavicle instances $\dot{\boldsymbol{x}}$ can be obtained by adding a linear combination of the shape modes to the mean clavicle:

$$\dot{\boldsymbol{x}} = \bar{\boldsymbol{x}} + \sum_{j=1}^{n_s-1} \boldsymbol{p}_j b_j, \tag{5.7}$$

where b_j is the contribution of the j-th principal shape mode to $\dot{\boldsymbol{x}}$. Eq. (5.7) defines a shape space spanned by the shape parameters b_j and with the mean shape as the origin. The bounds on the shape parameters of the shape space are usually chosen as a small multiple of the standard deviation of the point cloud along that direction, i.e., $-3\sqrt{\lambda_j} \leq b_j \leq +3\sqrt{\lambda_j}$.

In what follows, $\boldsymbol{\Lambda}$ will denote the function that maps a corresponded clavicle population to the mode variances of the derived shape model, under a given sampling $\boldsymbol{V}^{n_p}$:

$$(\lambda_1, \ldots, \lambda_{n_s-1}) = \boldsymbol{\Lambda}(\boldsymbol{x}_1, \ldots, \boldsymbol{x}_{n_s} | \boldsymbol{V}^{n_p}). \tag{5.8}$$

5.4.2 Correspondence Quality Measure

The quality of the spatial alignment and the correspondence of the clavicles in a population will be assessed by applying the description length principle to the derived shape model. This approach was introduced by Davies et al. [2002b] and later simplified by Thodberg [2003]. The correspondence quality measure is a function of the shape mode variances λ_j and is defined as follows:

$$\mu(\lambda_1, \ldots, \lambda_{n_s-1}) = \sum_{\lambda_i \geq \lambda_c} \left(1 + \log \frac{\lambda_i}{\lambda_c}\right) + \sum_{\lambda_i < \lambda_c} \frac{\lambda_i}{\lambda_c}, \tag{5.9}$$

where the free parameter λ_c is the expected noise variance in the data. Correspondences and alignments that generate more compact shape models, i.e., models with lower total variance or with variance spread over fewer modes, result in lower values of μ which indicates an improved quality.

5.4.3 Parameterization

The nonlinear cylindrical parameterization method of Huysmans and Sijbers [2009] is used to find an initial parameterization $\boldsymbol{x}_i^\circ$ for the surface $\mathscr{M}_i$. This method constructs an embedding $\mathscr{U}_i^\circ = (K_i, U_i^\circ)$ of $\mathscr{M}_i$ on $\mathscr{C}_h^2$ that produces the least metric distortion, as measured by symmetric stretch. The method also calculates the optimal length h, in terms of stretch, of the parameterization domain $\mathscr{C}_h^2$. Using a geometric distortion measure to obtain an embedding will result in a good initial correspondence because similar embeddings are obtained for surfaces with a similar shape.

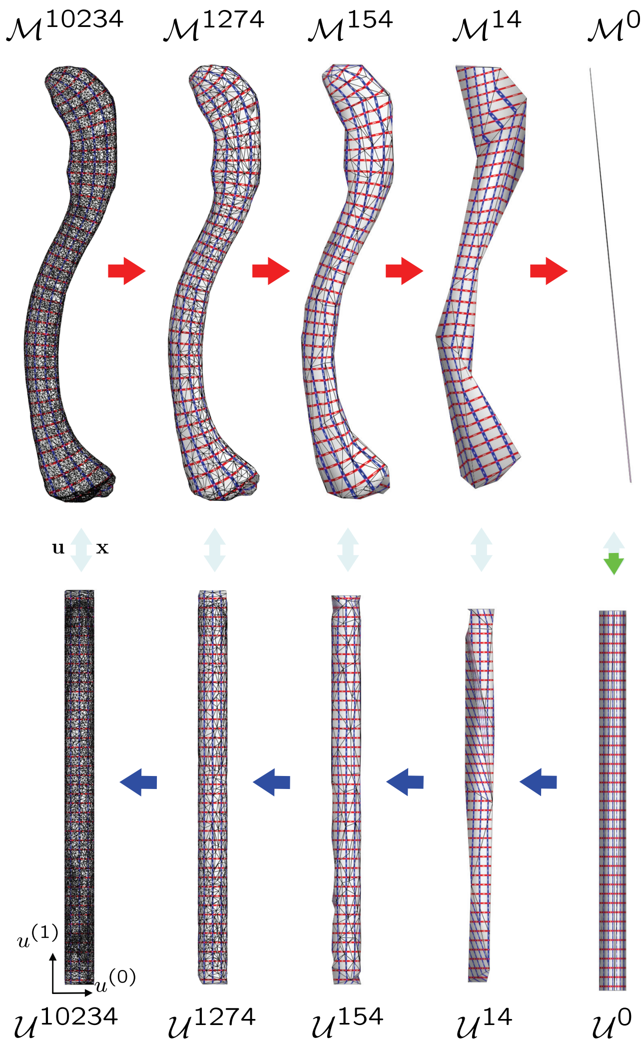

Figure 5.3: A depiction of the parameterization process for an example clavicle. The algorithm starts with the original surface $\mathscr{M} \equiv \mathscr{M}^{10234}$, shown at the top left. A surface hierarchy is constructed by successively applying edge collapses (red arrows). On the top right, the coarsest surface in the hierarchy is shown, denoted $\mathscr{M}^0$. Its embedding $\mathscr{U}^0$ on the cylinder is trivial (green arrow) and it is shown at the bottom right. Now, the inverse operations of the edge collapses, namely vertex splits, are applied to the embedding and the vertex positions are optimized with respect to the distortion measure (blue arrows). This results in progressively finer embeddings. The final embedding $\mathscr{U}^{10234} \equiv \mathscr{U}$, shown at the bottom left, together with the original surface $\mathscr{M}^{10234} \equiv \mathscr{M}$ define the final parameterization. At each level, the iso-parametric lines of the cylinder are shown on both the embedding and the clavicle in order to reveal the current mapping.

For a given parameterization $\boldsymbol{x} = \boldsymbol{u}^{-1}$ of a surface $\mathcal{M} = (K, M)$, the distortion is measured as

$$\xi_S(\boldsymbol{x}) = \frac{\sqrt{2}}{4A_{\mathcal{M}}} \sum_{t \in K} A_t \left(\sqrt{\gamma_t^2 + \Gamma_t^2} + \sqrt{\frac{1}{\gamma_t^2} + \frac{1}{\Gamma_t^2}} \right), \tag{5.10}$$

where $A_{\mathcal{M}}$ is the surface area of $\mathcal{M}$, A_t is the area of triangle t on $\mathcal{M}$, and γ_t and Γ_t are the smallest and largest singular value of the Jacobian of the affine map $\boldsymbol{u}|_t$, respectively. In order to make the distortion measure in Eq. (5.10) invariant under scaling of the surface $\mathcal{M}$, the singular values are scaled with a factor $\sqrt{\frac{A_{\mathcal{C}_h^2}}{A_{\mathcal{M}}}}$, where $A_{\mathcal{C}_h^2}$ is the area of the cylindrical domain $\mathcal{C}_h^2$.

The embedding $\mathcal{U}_i^\circ = (K_i, U_i^\circ)$ is then found by solving the following optimization problem:

$$\begin{aligned} \mathcal{U}_i^\circ &= \underset{h,\, \boldsymbol{u}_k^i, \forall k}{\arg\min}\, \xi_S(\boldsymbol{x}) \\ \text{subject to } u_j^{(1)} &= 0, \quad \forall j \in V_{B_0}^i, \\ u_j^{(1)} &= h, \quad \forall j \in V_{B_1}^i, \end{aligned} \tag{5.11}$$

where $V_{B_0}^i$ and $V_{B_1}^i$ are the sets of boundary vertices of the surface $\mathcal{M}_i$. This optimization problem is solved in a hierarchical way by means of the progressive mesh of the surface. The lowest level of the progressive mesh can be parameterized easily. The parameterizations for each of the following levels in the hierarchy are obtained by starting the optimization from the result of the previous level in the hierarchy. See Figure 5.3 for a depiction of the parameterization procedure. For further details, the reader is referred to Huysmans and Sijbers [2009].

5.4.4 Correspondence Optimization

Given a set of initial parameterizations $\{\boldsymbol{x}_1^\circ, \ldots, \boldsymbol{x}_{n_s}^\circ\}$ for $\{\mathcal{M}_1, \ldots, \mathcal{M}_{n_s}\}$, a correspondence $\{\boldsymbol{x}_1, \ldots, \boldsymbol{x}_{n_s}\}$ is to be obtained that, on the one hand, matches the surfaces spatially as well as parametrically and, on the other hand, results in a uniform distribution of samples on these surfaces. The former is achieved by optimizing the transformation parameters $\{\boldsymbol{\Phi}_1^\tau, \boldsymbol{\Phi}_1^\rho, \ldots, \boldsymbol{\Phi}_{n_s}^\tau, \boldsymbol{\Phi}_{n_s}^\rho\}$ of the spatial and parameterization transformations with respect to the correspondence quality measure μ defined in Eq. (5.9). Each spatial transformation is represented using a quaternion and to ensure that the optimized parameters form a valid unit length quaternion, a regularization term η^τ is introduced. Also, in order to avoid over-fitting, a regularization term η^ρ is introduced for each b-spline reparameterization transformation. This term measures the Dirichlet energy of the transformation, thereby penalizing excessive deformation. The optimization with respect to the correspondence quality measure μ can thus be stated as:

$$\underset{\Phi_i^{\rho},\Phi_i^{\tau},\forall i}{\arg\min}\left\{\mu\circ\Lambda(\ldots,\boldsymbol{x}_i(\bullet|\Phi_i^{\tau},\Phi_i^{\rho},\Phi^{\bar{\rho}}),\ldots|\boldsymbol{V}^{n_p}) + \frac{\alpha^{\tau}}{n_s}\sum_j \eta^{\tau}(\Phi_j^{\tau}) + \frac{\alpha^{\rho}}{n_s}\sum_j \eta^{\rho}(\Phi_j^{\rho})\right\}. \tag{5.12}$$

Here, the first term measures the actual quality of the correspondence and the last two terms are the spatial and parameterization regularization terms with factors α^{τ} and α^{ρ}, respectively. In this work, $\alpha^{\tau} = 10^5$ and $\alpha^{\rho} = 0.2$ was chosen. For a discussion of the regularisation factors, see Huysmans et al. [2009].

The uniformity of the distribution of samples on the surfaces is measured here using the stretch measure ξ_S defined in Eq. (5.10). This measure balances area and angle deformations and therefore enforces uniformity in the distribution of samples without introducing too much angle distortions. In order to make the optimization efficient, the measure is evaluated on the average surface $\bar{\boldsymbol{x}}$. In order to improve the uniformity, the global transformation parameters $\Phi^{\bar{\rho}}$ are optimized with respect to the stretch measure ξ_S of this average surface:

$$\underset{\Phi^{\bar{\rho}}}{\arg\min}\ \left\{\xi_S(\bar{\boldsymbol{x}}) + \alpha^{\bar{\rho}}\eta^{\bar{\rho}}(\Phi^{\bar{\rho}})\right\}, \tag{5.13}$$

where $\eta^{\bar{\rho}}$ is a regularization term for the b-spline transformation $\bar{\rho}$ that helps to avoid over-fitting. A regularisation factor $\alpha^{\bar{\rho}} = 10^3$ provided good results in the experiments of this work.

The optimization problems stated in Eq. (5.12) and Eq. (5.13) are solved using the LBFGS optimizer. Both problems are solved in a multi-resolution fashion using an increasing grid size for the b-spline transformations. Moreover, the problems are competing optimizations since the correspondence quality measure is sensitive to the distribution of samples. This competing optimization problem is handled by running a uniformity optimization before and after the correspondence optimization, and this at each resolution level.

See Figure 5.4 for a depiction of the correspondence optimization process.

5.5 Statistical Shape Analysis and Modeling

What follows is a discussion on how to visualize the shape space for a population of clavicles, how to compare the shape present in subgroups of the population, and how to derive a set of fracture fixation plate shapes from the population.

5.5.1 Shape Space Visualization

Once a population $\{\mathcal{M}_1,\ldots,\mathcal{M}_{n_s}\}$ is provided with a correspondence $\{\boldsymbol{x}_1,\ldots,\boldsymbol{x}_{n_s}\}$, a statistical shape model can be constructed using SVD, as

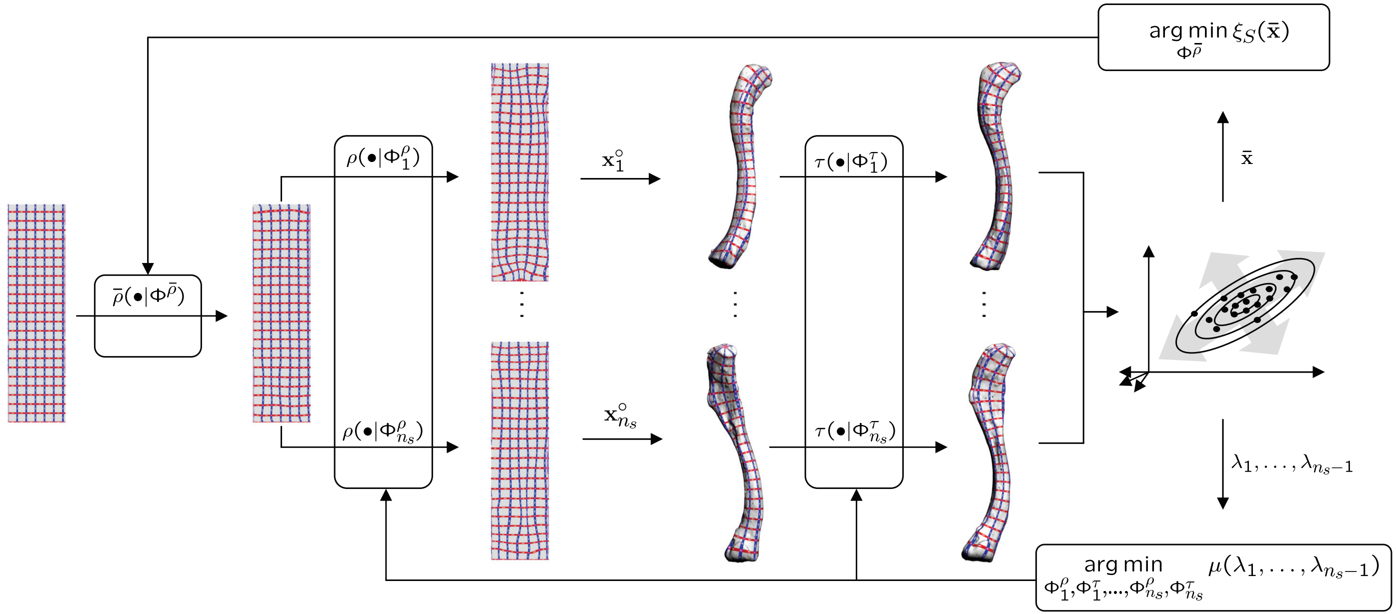

Figure 5.4: A depiction of the correspondence optimization process for the population of clavicles. On the right, the cylindrical domain is visualized as a planar patch, periodic in the horizontal direction. In this domain, the grid of uniformly distributed samples is defined. A texture is overlaid on the cylindrical domain in order to show the result of subsequent reparameterization transformations. This domain is transformed by the global transformation $\bar{\rho}$ in order to obtain a good distribution of samples on the average clavicle. Then, for each clavicle $\mathscr{M}_i$, the parameterization $\boldsymbol{x}_i^{\circ}$ is composed with a reparameterization function ρ in order to improve the alignment of the surfaces in the parameter space. Finally, a spatial transformation τ is applied to each clavicle in order to improve the spatial alignment of the clavicles. From the obtained correspondence, a shape model is calculated. The shape mode variances λ_j are used to assess the correspondence quality and the average clavicle $\bar{\boldsymbol{x}}$ is used to assess the uniformity of the distribution of samples. An optimal correspondence is obtained by optimization of the transform parameters with respect to the quality measures μ and ξ_S.

detailed in Section 5.4.1. In order to obtain an insight into the shape present in the population, a visualization can be made of the shape space. In this work, the following three visualizations will be employed:

- The distribution of the population in the shape space can be shown using scatter plots. The position $\boldsymbol{b}_i$ in shape space for each $\boldsymbol{x}_i$ is obtained as $\boldsymbol{b}_i = \boldsymbol{P}_{n_s-1}{}^T(\dot{\boldsymbol{x}}_i - \bar{\boldsymbol{x}})$, where $\dot{\boldsymbol{x}}_i$ is the point based representation of $\boldsymbol{x}_i$ and $\boldsymbol{P}_{n_s-1}$ is the matrix with the $n_s - 1$ shape modes as its columns. For each combination of two of the first few shape modes, a 2D scatter plot is made of the population members $\{\boldsymbol{b}_1,\ldots,\boldsymbol{b}_{n_s}\}$.

- The influence of each individual shape mode on the shape of the surface is also visualized. This is done for each mode $\boldsymbol{p}_j$ by displaying the average surface $\bar{\boldsymbol{x}}$ together with the offset surfaces $\bar{\boldsymbol{x}} \pm 3\sqrt{\lambda_j}\boldsymbol{p}_j$.

- The variation of the position of a point on the surface can be visualized by a landmark covariance tensor. For a given parameter location $\boldsymbol{u}$, the corresponding landmarks $\boldsymbol{x}_i(\boldsymbol{u})$ are centered and concatenated in a $3 \times n_s$ landmark matrix

$$\boldsymbol{L} = [(\boldsymbol{x}_1(\boldsymbol{u}) - \bar{\boldsymbol{x}}(\boldsymbol{u}))^T \ldots (\boldsymbol{x}_{n_s}(\boldsymbol{u}) - \bar{\boldsymbol{x}}(\boldsymbol{u}))^T], \tag{5.14}$$

  where

$$\bar{\boldsymbol{x}}(\boldsymbol{u}) = \frac{1}{n_s}\sum_{i=1}^{n_s} \boldsymbol{x}_i(\boldsymbol{u}) \tag{5.15}$$

  is the average of the landmarks. The landmark covariance matrix is then calculated as $\boldsymbol{C} = \frac{1}{n_s-1}\boldsymbol{L}\boldsymbol{L}^T$. Finally, the landmark covariance tensor is obtained from the eigenvalues and eigenvectors of this 3×3 matrix C and it is visualized for each landmark in $\boldsymbol{V}^{n_p}$, along with the average surface $\bar{\boldsymbol{x}}$. The mean surface can be color coded with the Frobenius norm of the landmark covariance matrix $||\boldsymbol{C}||_F$, which is a measure of the total variability for that landmark.

5.5.2 Statistical Shape Discrimination

In this section, two statistical test procedures are discussed. A framework similar to the approach of Ferrarini et al. [2007] and Styner et al. [2007] is used. On the one hand, there is the comparison of two groups in which the members of one group are not paired to the members of the other group. This unpaired testing procedure is employed for the comparison of clavicles of male and female specimens and for the comparison between old and more recent clavicles. On the other hand, there is the comparison of subgroups with members of one group paired to the members of the other group. This paired testing procedure is used for studying the left-right asymmetry of clavicle pairs.

In each case, the shape comparison is done in a local fashion, i.e., a statistical test is run at each point of the surface. First, a correspondence is established for the two to be compared groups. Then, for each parametric location $\boldsymbol{v} \in \boldsymbol{V}^{n_p}$, two sets of corresponding surface landmarks are derived, one for each group. Finally, for each parametric location, a statistical test decides whether (alternative-hypothesis) are not (null-hypothesis) the means of the two landmark sets differ in location. As a result, a scalar map of significance values on the surface will be obtained. This significance map can be visualized on the average surface of one of the subgroups and this can be complemented with an visualization of both group averages. In this way, the location and the extent of the shape differences is revealed.

The robust Hotelling T^2 metric will be used to measure the difference between the landmark sets and, since no assumptions will be made on the underlying distribution, permutation testing will be used to obtain the distribution of the test statistic T^2. The outline of the statistical procedure for two unpaired groups is as follows:

1. Let the two groups of surfaces be denoted as

$$\{\mathscr{M}_1, \ldots, \mathscr{M}_{n_s}\} \text{ and } \{\mathscr{N}_1, \ldots, \mathscr{N}_{n_s}\}.$$

   Let their common correspondence be denoted as $\{\boldsymbol{x}_1, \ldots, \boldsymbol{x}_{n_x}, \boldsymbol{y}_1, \ldots, \boldsymbol{y}_{n_y}\}$.

2. For a given parameter location $\boldsymbol{v}$, the average point position in each group is obtained as

$$\bar{\boldsymbol{x}}(\boldsymbol{v}) = \frac{1}{n_x} \sum_{i=1}^{n_x} \boldsymbol{x}_i(\boldsymbol{v}) \quad \text{and} \quad \bar{\boldsymbol{y}}(\boldsymbol{v}) = \frac{1}{n_y} \sum_{i=1}^{n_y} \boldsymbol{y}_i(\boldsymbol{v}). \tag{5.16}$$

   The landmark matrices $\boldsymbol{L_x}$ and $\boldsymbol{L_y}$ can then be obtained as

$$\begin{aligned} \boldsymbol{L_x} &= [(\boldsymbol{x}_1(\boldsymbol{v}) - \bar{\boldsymbol{x}}(\boldsymbol{v}))^T \ldots (\boldsymbol{x}_{n_x}(\boldsymbol{v}) - \bar{\boldsymbol{x}}(\boldsymbol{v}))^T] \\ \boldsymbol{L_y} &= [(\boldsymbol{y}_1(\boldsymbol{v}) - \bar{\boldsymbol{y}}(\boldsymbol{v}))^T \ldots (\boldsymbol{y}_{n_y}(\boldsymbol{v}) - \bar{\boldsymbol{y}}(\boldsymbol{v}))^T]. \end{aligned} \tag{5.17}$$

   The covariance matrices are defined as

$$\boldsymbol{C_x} = \frac{1}{n_x - 1} \boldsymbol{L_x} \boldsymbol{L_x}^T \quad \text{and} \quad \boldsymbol{C_y} = \frac{1}{n_y - 1} \boldsymbol{L_y} \boldsymbol{L_y}^T. \tag{5.18}$$

   The Hotelling T^2 metric is then calculated as [Seber, 1984]

$$t = (\bar{\boldsymbol{x}}(\boldsymbol{v}) - \bar{\boldsymbol{y}}(\boldsymbol{v})) \left(\frac{1}{n_x} \boldsymbol{C_x} + \frac{1}{n_y} \boldsymbol{C_y} \right)^{-1} (\bar{\boldsymbol{x}}(\boldsymbol{v}) - \bar{\boldsymbol{y}}(\boldsymbol{v}))^T. \tag{5.19}$$

3. Generate a large number, say m, of permutations of the two groups and evaluate the Hotelling T^2 metric for these new groups.

4. Let, t_{ref} be the metric value of the original groups and $t_1, \ldots, t_m$ the metric value for the m permutations. Then, the p-value is obtained as

$$\frac{|\{t_i \mid t_i > t_{\text{ref}}, i = 1 \ldots m\}|}{m}. \tag{5.20}$$

The outline of the paired statistical testing procedure is as follows:

1. Let the two groups of surfaces be denoted as

$$\{\mathcal{M}_1, \ldots, \mathcal{M}_{n_s}\} \text{ and } \{\mathcal{N}_1, \ldots, \mathcal{N}_{n_s}\}.$$

   Let their common correspondence be denoted as $\{\boldsymbol{x}_1, \ldots, \boldsymbol{x}_{n_s}, \boldsymbol{y}_1, \ldots, \boldsymbol{y}_{n_s}\}$. Let $\boldsymbol{z}_i(\boldsymbol{v}) = \boldsymbol{x}_i(\boldsymbol{v}) - \boldsymbol{y}_i(\boldsymbol{v})$ be the difference vector between the two paired group members.

2. For a given parameter location $\boldsymbol{v}$, the average difference vector is obtained as

$$\bar{\boldsymbol{z}}(\boldsymbol{v}) = \frac{1}{n_s} \sum_{i=1}^{n_s} \boldsymbol{z}_i(\boldsymbol{v}). \tag{5.21}$$

   The landmark matrix $\boldsymbol{L_z}$ can then be obtained as

$$\boldsymbol{L_z} = [(\boldsymbol{z}_1(\boldsymbol{v}) - \bar{\boldsymbol{z}}(\boldsymbol{v}))^T \ldots (\boldsymbol{z}_{n_s}(\boldsymbol{v}) - \bar{\boldsymbol{z}}(\boldsymbol{v}))^T]. \tag{5.22}$$

   The covariance matrix is defined as

$$\boldsymbol{C_z} = \frac{1}{n_s - 1} \boldsymbol{L_z} \boldsymbol{L_z}^T. \tag{5.23}$$

   The Hotelling T^2 metric for paired groups is then calculated as [Seber, 1984]

$$t = n_s \, \bar{\boldsymbol{z}}(\boldsymbol{v}) \, \boldsymbol{C_z}^{-1} \, \bar{\boldsymbol{z}}(\boldsymbol{v})^T. \tag{5.24}$$

3. Generate a large number, say m, of permutations of the two groups by randomly swapping the group membership of pairs and evaluate the Hotelling T^2 metric for these new groups.

4. Let, t_{ref} be the metric value of the original groups and $t_1, \ldots, t_m$ the metric value for the m permutations. Then, the p-value is obtained as

$$\frac{|\{t_i \mid t_i > t_{\text{ref}}, i = 1 \ldots m\}|}{m}. \tag{5.25}$$

For each landmark $\boldsymbol{v}_i \in \boldsymbol{V}^{n_p}$, the hypothesis test is executed and the resulting p-value is denoted as p_i. Since n_p is typically of the order of 10^3, multiple comparisons correction is a necessity. In this work, the false discovery rate (FDR) under the null-hypothesis will be controlled. In order to enforce an FDR value of α, the following procedure is applied to the p-values:

1. Sort the p-values p_i in ascending order and denote as $p_{(i)}$.
2. Find the index i_{FDR} as

$$i_{FDR} = \max\left\{0 \leq i \leq n_p \mid p_{(i)} \leq \alpha \frac{i}{n_p}\right\}. \tag{5.26}$$

3. Only $p_i \leq p_{(i_{FDR})}$ are considered significant.

5.5.3 Statistical Shape Template Generation

The goal of the shape template generation is to derive a set of indicative plate shapes that can be used to fixate fractures for a given population of clavicles with minimal error in fitting. The actual plate shapes for fixation of mid-shaft clavicle fractures depend on the targeted plating approach, e.g., anterior, superior, or superior distal to anterior proximal plating. The design of these different categories of plates is established by letting the user define the desired region of contact (ROC), between bone and plate, on the average bone of the population. The correspondence can be used to map this ROC from the average bone to each bone in the population. In this way, an ROC is obtained for each individual bone. A predefined number of plate shapes can then be extracted by using a clustering technique on the obtained ROC shapes.

Let the population of clavicles be denoted as $\{\mathscr{M}_1, \ldots, \mathscr{M}_{n_s}\}$ and its correspondence as $\{\boldsymbol{x}_1, \ldots, \boldsymbol{x}_{n_s}\}$. An ROC is obtained by interactive selection of a subset of landmarks $\boldsymbol{V} = \{\boldsymbol{v}_1, \ldots, \boldsymbol{v}_{n_v}\} \subset \boldsymbol{V}^{n_p}$ on the average clavicle $\bar{\boldsymbol{x}}$. For each surface $\mathscr{M}_i$, the individual ROC shape $\boldsymbol{r}'_i$ is obtained by mapping the landmarks $\boldsymbol{V}$ to the surface $\mathscr{M}_i$, i.e., $\boldsymbol{r}'_i = [\boldsymbol{x}_i(\boldsymbol{v}_1) \ldots \boldsymbol{x}_i(\boldsymbol{v}_{n_v})]^T$. Rigid alignment is applied to the ROCs $\{\boldsymbol{r}'_1, \ldots, \boldsymbol{r}'_{n_s}\}$ in order to obtain the final set of ROCs $\{\boldsymbol{r}_1, \ldots, \boldsymbol{r}_{n_s}\}$. The goal is to find n_t shape templates $\{\boldsymbol{c}_1, \ldots, \boldsymbol{c}_{n_t}\}$ that approximate the ROCs $\{\boldsymbol{r}_1, \ldots, \boldsymbol{r}_{n_s}\}$ as closely as possible. This problem is expressed by the following optimization problem:

$$\underset{\boldsymbol{c}_1, \ldots, \boldsymbol{c}_{n_t}}{\arg\min} \sum_{i=1}^{n_t} \int_{\mathscr{C}_i} \epsilon(\boldsymbol{c}_i, \boldsymbol{r}) p(\boldsymbol{r}) d\boldsymbol{r}, \tag{5.27}$$

where $\epsilon(\boldsymbol{c}_i, \boldsymbol{r})$ measures the mean squared error between the shape template $\boldsymbol{c}_i$ and the ROC $\boldsymbol{r}$, $\mathscr{C}_i$ is the Voronoi cell around $\boldsymbol{c}_i$, i.e., the set of shapes closest to $\boldsymbol{c}_i$, and $p(\boldsymbol{r})$ is the probability of occurrence of the ROC shape $\boldsymbol{r}$ in the population under consideration. In the discrete setting, the probability distribution p of ROC shapes is not available and replaced with an actual set of shapes. Then, the optimization problem can be solved with k-means clustering [MacQueen, 1967]. K-means clustering divides the population into n_t clusters $\{\boldsymbol{C}_1, \ldots, \boldsymbol{C}_{n_t}\}$ and the cluster centers define the template shapes $\{\boldsymbol{c}_1, \ldots, \boldsymbol{c}_{n_t}\}$. See Figure 5.5 for an overview of the shape template generation.

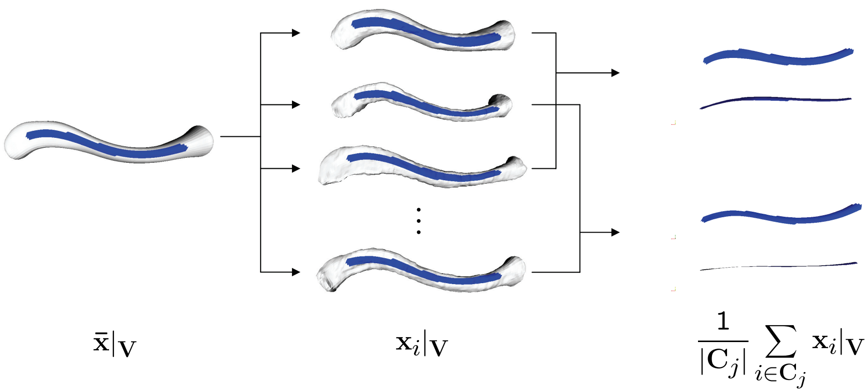

Figure 5.5: A depiction of the shape template generation process for the population of clavicles. First, the average surface $\bar{\boldsymbol{x}}$ of the population is calculated and a desired region of contact, between plate and bone, is selected by user interaction. The obtained ROC $\bar{\boldsymbol{x}}|_{\boldsymbol{V}}$ is shown in blue. The ROC is mapped through the correspondence to each surface of the population. These obtained ROC shapes $\boldsymbol{x}_i|_{\boldsymbol{V}}$ are superimposed on the original surfaces and shown in blue. Finally, k-means clustering divides the population in clusters and the cluster centers define the final shape templates. The final templates are shown from the top and the front.

5.6 Results and Discussions

Several experiments were conducted with the population of clavicles. For an overview of the properties of the clavicle population members and the necessary preprocessing steps applied to them, see Section 5.2. In Section 5.6.1, the construction of a correspondence is described for the whole clavicle population and the quality of this correspondence is assessed, both qualitatively and quantitatively. In Section 5.6.2, this is followed by an investigation of the shape differences between subgroups of the population, e.g., male versus female specimens, left versus right clavicles, and old versus more recent clavicles. Section 5.6.3 concludes the experiments by deriving a set of shape templates from the clavicle population for the fixation of mid-clavicular fractures.

5.6.1 Correspondence Quality

The size of the population of clavicles under investigation is 90. A closer inspection of each clavicle separately revealed that clavicles 38 and 44 had an abnormal shape. This is most likely due to a history of fracture. Therefore, these clavicles were left out of the population. A correspondence was constructed for the remaining population of 88 clavicles using the method described in Sec-

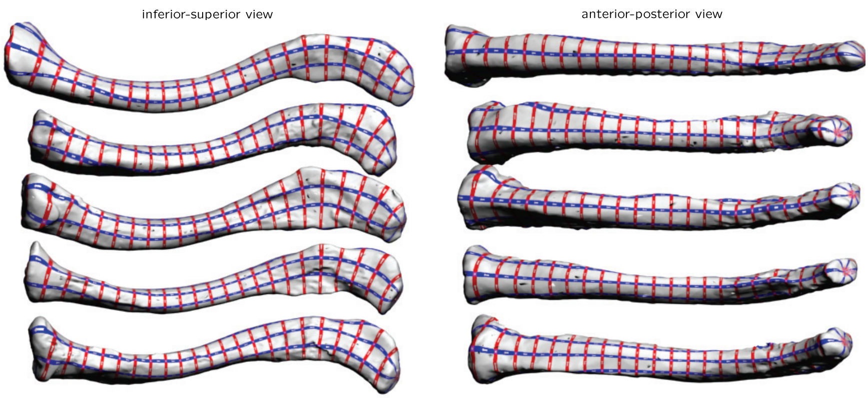

Figure 5.7: Visualization of the final correspondence for the first five clavicles of the population. The correspondence is shown on this surface by means of a texture: iso-$u^{(0)}$ and iso-$u^{(1)}$ lines of $\boldsymbol{x}_i$ are shown in blue and red, respectively. It can be seen that the correspondence matches anatomically equivalent regions>

tion 5.4. The parameterization of the 88 surfaces required 40 minutes on a 3.0 GHz processor. The width of the parameterization domain was fixed at 2π and an average length of $h = 23.81$ was observed. All the parameterizations were rescaled to this average length. A total of $n_p = 4000$ landmarks were uniformly distributed on this domain and further used in the optimization of the correspondence that required 8 hours of computation time.

In Figure 5.7, the resulting correspondence is visualized for the first five clavicles using a texture map. The cylindrical domain is periodically covered with the texture patch shown in Figure 5.6. Then, the texture of the cylinder is mapped onto the surface and, as a result, the iso-$u^{(0)}$ contours are shown as blue lines and the iso-$u^{(1)}$ contours are shown as red lines. These lines correspond. It can be seen from Figure 5.7 that the correspondence is a smooth map between the surfaces and that it globally matches anatomically equivalent regions. For a complete overview of the clavicle population and its correspondence, the reader is referred to Appendix B.

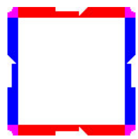

Figure 5.6: The texture that is used to visualize the correspondences.

The fact that the correspondence provides a global matching of anatomically equivalent regions can also be supported quantitatively. The following set of anatomical locations was identified:

TC or conoid tubercle is an eminence that surmounts the coracoid process of the scapula and gives attachment to the conoid ligament. The TC is marked with a point at its center.

LT or trapezoid line is an oblique ridge that attaches to the trapezoid ligament. Its most lateral end is marked with a point.

LVLa,b or deltoid tuberosity is a narrow ridge on the clavicle providing attachment to the deltoid muscle. It is located in the lateral arch. The medial and lateral ends are marked with points LVLa and LVLb, respectively.

ILCC or costal tuberosity, is an impression for the costoclavicular ligament. The center of the impression is marked with a point.

Each of these anatomical locations were marked by an expert on each clavicle of the population. Some cases, where the anatomical feature was missing or could not be clearly located, were left out of the analysis. Of the 88 cases, TC could be identified in all cases, LT in 75 cases, LVLa in 46 cases, LVLb in 45 cases, and ILCC in 23 cases.

The obtained markers for each surface were mapped, through the correspondence, to each other surface of the population. In this way, it is revealed how the correspondence maps the anatomically equivalent regions. In Figure 5.8, the clavicle with $id = 60$, together with the mapped markers, is visualized at two stages in the correspondence optimization: after applying only rigid transformations and after the full b-spline transformation optimization. It can be seen that, for each of the anatomical locations, the mapped markers form a compact group of points spread about the respective anatomical feature. The amount of spread depends on the variability of the anatomical feature and to a lesser extent on the error that the observer makes in pin-pointing the anatomical feature. The spread of the landmarks could be reduced by taking local shape information into account in the optimization of the correspondence. With the application of this work in mind, this is not aimed for. For example, the LVLa,b line exhibits a large variation in length. A correspondence that provides an exact match for the end points of this line would exhibit large dilations in the axial direction. In the application targeted here, i.e., generating fracture fixation plates, these dilations would influence the length of the fixation plates which is undesirable. It should be noted, however, that in applications where an exact match between the prominent anatomical features is required, one could introduce a curvature component in the MDL correspondence optimization problem of Equation 5.12 (as in Styner et al. [2008]).

For completeness, a quantitative assessment of the landmark correspondence is made and the results are provided in Table 5.2. For each anatomical feature on each clavicle, the mean geodesic distance (MGD) is calculated by averaging the distances between the point marked on that bone and the markers of each other bone mapped to that clavicle through the correspondence. The minimum, mean, and maximum MGD measured on the clavicles are then reported for each anatomical feature. The measurements are reported at two stages in the correspondence construction: after the optimization of the rigid spatial and parameter space alignment and after the b-spline correspondence

		MGD					
		min		mean		max	
marker	obs	rig	bsp	rig	bsp	rig	bsp
TC	1.37	3.39	3.15	5.16	5.44	12.00	12.63
LT	3.74	4.27	4.43	6.86	6.62	11.58	12.00
LVLa	5.75	6.49	6.38	9.17	8.94	16.85	16.45
LVLb	2.41	4.50	4.02	6.92	6.63	15.90	16.93
ILCC	1.85	6.58	5.86	9.09	9.02	18.97	15.00

Table 5.2: Measurements to assess the correspondence quality using anatomical landmarks. All measurements are reported in mm. On each clavicle, five landmarks were identified (TC, LT, LVLa, LVLb, and ILCC) and pin-pointed by an orthopedic expert. Cases where the landmark could not be clearly located were left out of the analysis. The measurements were repeated for 15 clavicles in order to estimate the selection error (obs) of the expert. Using the correspondence, all landmarks were mapped to each clavicle. On each clavicle, the mean geodesic distance (MGD) is calculated between the landmark pin-pointed on that clavicle and the landmarks of all the other clavicles, mapped to this clavicle through the correspondence. For each landmark. the minimum, mean, and maximum MGD is reported. The measurements are reported for both the rigid (rig) and the b-spline (bsp) correspondence.

optimization. Also, an estimate was made of the observer error by repeating the pin-pointing procedure for each anatomical feature on 15 of the clavicles and calculating the average of the distance between the obtained two markers.

As detailed in Section 5.5.1, the shape space, obtained from the final correspondence, can be visualized by displaying the mean surface and the offset surfaces for each mode of the shape space. This is done in order to show the shape variation present in the population. In Figure 5.9, the mean shape of the clavicle is visualized. The mean surface is color coded with the Frobenius norm of the landmark covariance matrix. This indicates the amount of variability of the landmarks at each location of the surface. Also, a visualization is made of the local landmark variability by displaying the tensor representation of the landmark covariance matrix for each point on the surface. It can be seen that the mean clavicle surface has a plausible shape, i.e., a typical S-shape is observed in the superior view, the inferior bow at the distal part of the clavicle is visible from the anterior view, and the typical bump at the TC site. This indicates that the correspondence is valid. A bad correspondence would average out much of the shape of the clavicle. From the tensor visualization, one can learn that most of the variability is normal to the surface.

In Figure 5.10, the first five shape modes are visualized using offset surfaces.

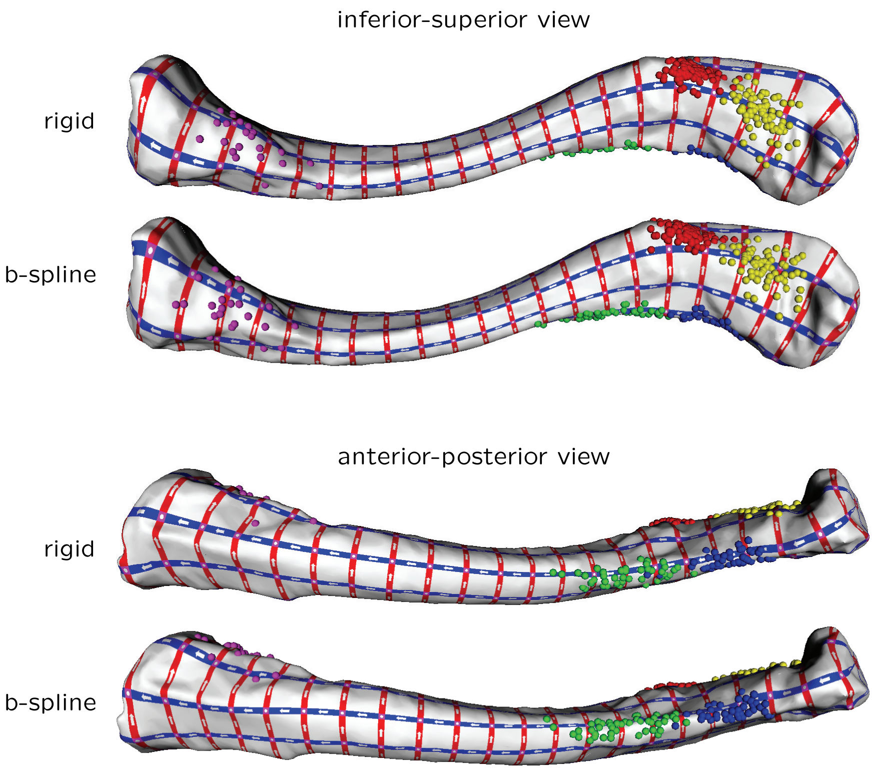

Figure 5.8: Visualization of a clavicle ($id = 60$) from the population. The final parameterization of this surface is visualized with a texture: iso-$u^{(0)}$ and iso-$u^{(1)}$ lines of $\boldsymbol{x}_{60}$ are shown in blue and red, respectively. On each clavicle of the population, five anatomical landmarks were identified and pin-pointed by an expert. These landmarks were mapped to the shown clavicle using the rigid and the b-spline correspondence and visualized, here, using small spheres: TC in red, LT in yellow, LVLa in green, LVLb in blue, and ILCC in magenta. It is clear that the obtained correspondence is anatomically consistent. However, it can be seen that the landmarks are not mapped exactly to each other. This is due to observer error in the pin-pointing procedure and also because the anatomy of the clavicle shows many variations.

In this figure, the correspondence is also revealed by the use of a texture. Each of these five modes captures, to some extent, an anatomically meaningful variation from the population. The first mode represents size. The second mode expresses a difference in the amount of bending of the lateral part of the clavicle, as can be seen in the anterior-posterior view. The third mode mainly captures the variation of the width of the lateral part. The fourth mode shows a difference in robustness of the clavicle. The fifth mode expresses a difference in the amount of bending of the S-curve. The fact that all these modes express plausible variations of the clavicle indicates that the obtained correspondence is valid.

5.6.2 Group Differences

In this section, several subgroups of the population of clavicles are compared in terms of shape. A comparison is made for the following subgroups: female versus male right clavicles, left versus right clavicles, and old (date of birth before or in 1926) versus more recent (date of birth after 1956) clavicles. Unpaired testing was used for the female versus male and the old versus recent comparison. For the comparison of right versus left clavicles, only pairs were used and thus paired testing became possible. In Figure 5.11, the means of the subgroups are compared and the p-values, obtained using 10^4 permutations and corrected for multiple comparisons using an FDR of 0.05, of the test are shown for each landmark of the surface.

The comparison of the right clavicles from female versus male specimens reveals a large difference. It can be seen from Figure 5.11 that the clavicles from female specimens are shorter and less robust. The p-value map shows that the difference in means between the two groups is significant at almost all landmarks. The fact that the clavicles of female individuals are, on average, shorter, means that one has to take into account both subgroups in the design of a fracture fixation plate.

The comparison of the mean left clavicle with the mean right clavicle, reveals that right clavicles are slightly longer. The mean of the right clavicles is also more robust at several parts of the surface. The observed differences are, however, not significant everywhere. A comparison of the dominant side with the non-dominant side may reveal larger and more consistent differences. Unfortunately, the dominance was known for none of the pairs. In any case, the differences between right and left clavicles are relatively small. Therefore, the design of the fracture fixation plates of one side can be mirrored from the other side.

In the last comparison, old clavicles were compared with more recent ones. The old clavicles are those from specimens with a date of birth before or in 1926. The more recent ones were chosen to be from specimens with a date of birth after 1956. Thus, there is a gap of 30 years in between. The mean of the old clavicles was found to be slightly shorter and more robust, but the effect was not

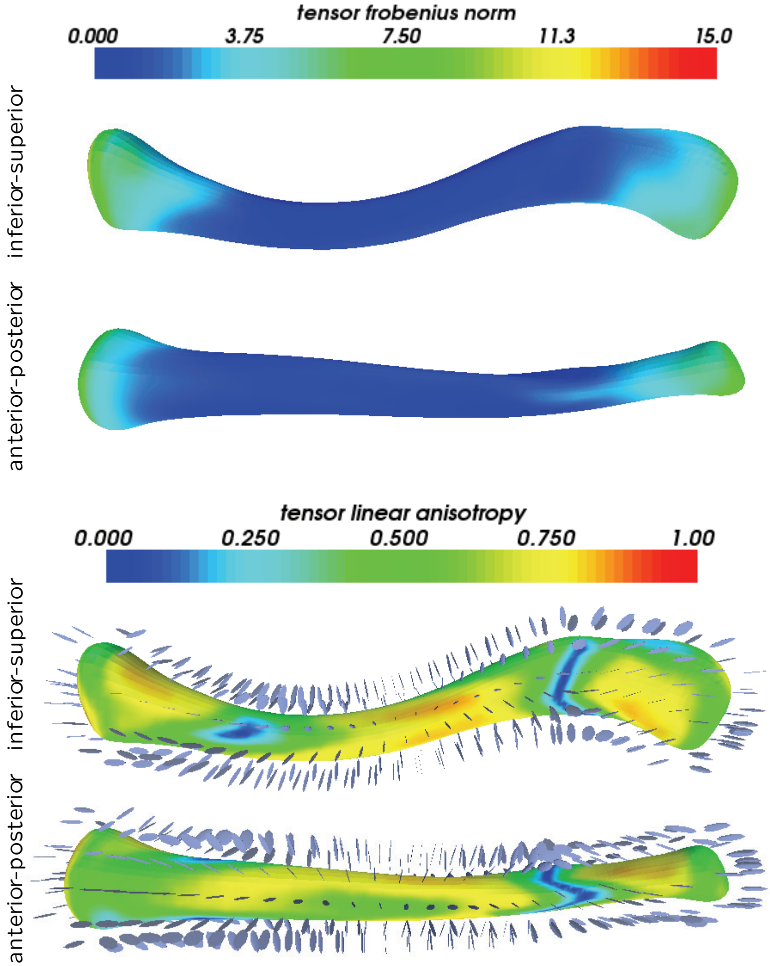

Figure 5.9: Visualization of a the mean surface of the shape model obtained from the final correspondence. On the left, the mean surface is color coded with the Frobenius norm of the landmark covariance matrix indicating the amount of variation present in the population at each point of the surface. On the right, a visualization is made of the landmark covariance matrices by means of tensors. The tensors are a visualization of the distribution of the landmarks within the population. The surface is color coded with the linear anisotropy of the tensors. It can be seen that most of the variation is normal to the surface.

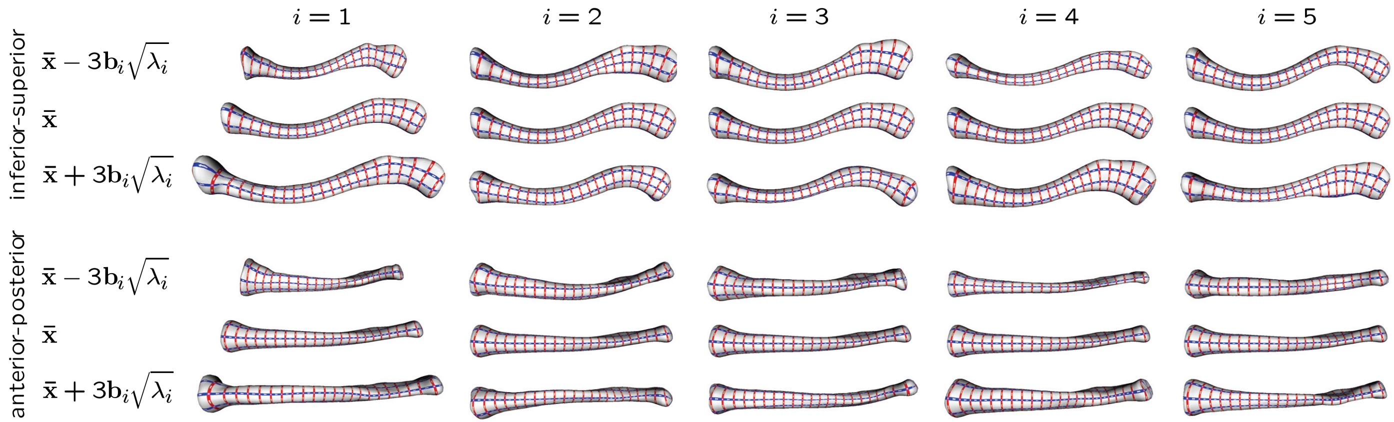

Figure 5.10: Visualization of a shape modes from the shape model obtained from the final correspondence of the population. The first five modes are shown. The correspondence is shown on each surface by means of a texture: iso-$u^{(0)}$ and iso-$u^{(1)}$ lines of $\boldsymbol{x}_i$ are shown in blue and red, respectively. At the top of the figure, the clavicles are viewed from the inferior side. At the bottom, an anterior view of the clavicles is provided.

significant. It should be noted that the groups were rather small in this test (7 versus 8 members). An investigation with more data sets is ongoing. However, it is not expected that age is an important factor in the design of clavicle fixation plates. That is, when considering specimens older than 25 years, i.e., when the clavicle is completely ossified.

5.6.3 Plate Shapes

In this section, three plate designs are derived from the population of clavicles: a superior plate, an anterior plate, and a proximal anterior to distal superior plate or anterior-superior plate in short. The desired region of contact (ROC) for each of these plates was delineated on the mean clavicle by an orthopedic expert. In Figure 5.12, the delineated region for each plate is shown. At this point, it is interesting to compare the three ROCs of Figure 5.12 with the visualization of the landmark variability on the mean clavicle in Figure 5.9. It can be seen that all landmarks inside the anterior-superior ROC exhibit low variability (indicated in blue). This is in contrast to the superior ROC and, to a lesser extent, also with the anterior ROC which are partly in higher variability regions (indicated in cyan). From a further analysis it will become clear that this influences the quality of fit to the clavicle population.

For each ROC, a single plate shape or a set of plate shapes can be derived that, together, cover the clavicle population with small error. As explained in Section 5.5.3, such a set is obtained through clustering. For each ROC, such a clustering was done for the number of templates n_t running from 1 to 20. Each obtained set of plate shapes is evaluated with three error measures: $E_{50\%}$, $E_{90\%}$, and $E_{100\%}$. These errors are calculated as

$$E_{q\%}(\boldsymbol{V}) = \frac{1}{n_s}\sum_{i=1}^{n_s} \overset{q\%}{\max_{\boldsymbol{v}\in\boldsymbol{V}}} ||\boldsymbol{c}_{(i)}(\boldsymbol{v}) - \boldsymbol{x}_i(\boldsymbol{v})||^2, \tag{5.28}$$

where $\boldsymbol{V}$ represents the ROC by its set of landmarks, n_s is the number of clavicles in the population, $\boldsymbol{x}_i$ is the i-th clavicle, $\boldsymbol{c}_{(i)}$ is the cluster center or plate shape of the cluster to which the clavicle $\boldsymbol{x}_i$ belongs, and $\overset{q\%}{\max}$ takes the maximum value of the q percent smallest values of its argument. In fact, $E_{50\%}$ and $E_{100\%}$ measure the median and maximum fitting error averaged over all clavicles. The error measure $E_{90\%}$, on the other hand, gives the maximal error with which 90% of the ROC is covered, averaged over the population. That is, $E_{90\%} = 1mm$ means that, on average, only 10% of the plate is subject to an error $\geq 1mm$. In Figure 5.13, the errors $E_{50\%}$, $E_{90\%}$, and $E_{100\%}$ are reported for the superior, anterior, and anterior-superior plate.

From Figure 5.13, it can be seen that the anterior-superior plate provides the tightest fit, as was anticipated. The superior plate provides the worst fit and this is due to the highly variable extremities of the clavicle to which the plate extends. The largest fitting errors occur at the distal part of the clavicle (result

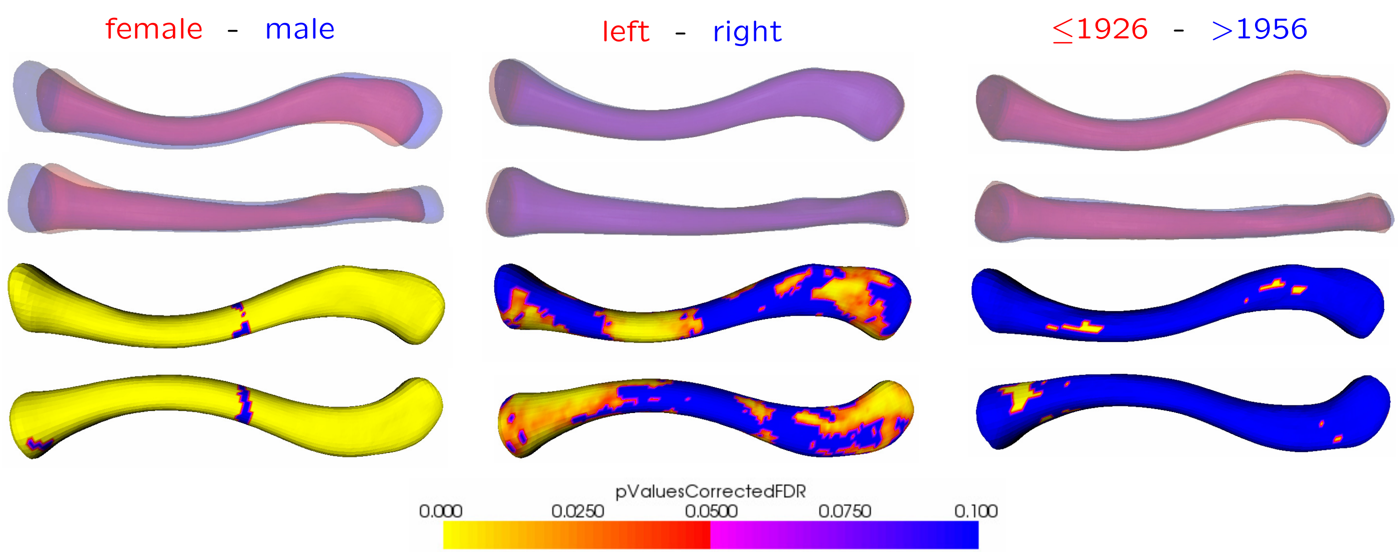

Figure 5.11: Visualization of the results of the difference in group means assessment. From left to right: female vs. male right clavicles, left vs right clavicles, and old versus recent male right clavicles. At the top, the group means are overlaid and rendered transparently from the inferior and the anterior side. At the bottom, the p-values are visualized on the mean surface of the first group, viewed from the inferior and superior side. These p-values express the significance of the difference between the group means at each location on the surface. Note, that the p-values displayed here are corrected for an FDR of 0.05.

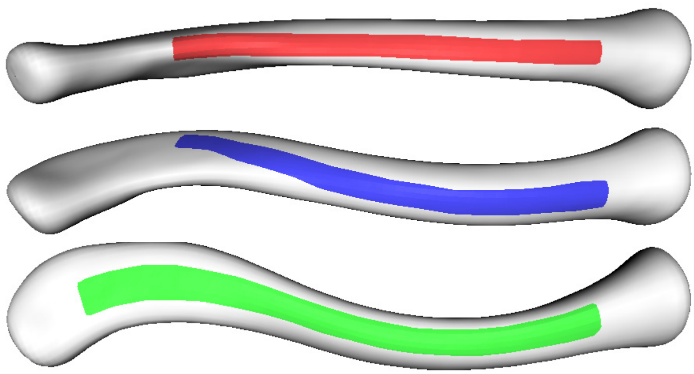

Figure 5.12: A visualization of the desired region of contact between bone and plate, as specified on the mean clavicle by an orthopedic expert. The regions, superimposed on the mean clavicle, are shown for three possible plate configurations. From top to bottom: an anterior ROC, an anterior-superior ROC, and a superior ROC.

not shown). The anterior plate is subject to the most variation at the LVLa,b line which is a highly variable part. Note that the variation of LVLa,b was expressed by the fifth shape mode in Figure 5.10. The three plate ROCs, however, all have a low mean and 90% error that rapidly approaches $1mm$ and less. In the plating practice, such an error can be considered negligible.

In what follows, the result of the clustering is discussed for the three ROCs with the number of shapes fixed at $n_t = 4$. In Figure 5.15 and Figure 5.16, the obtained clusters are visualized in the shape space of the population. In this way, it can be seen which shape variation (shape modes) of the clavicle influenced the clustering for a specific ROC. The actual shape of the plates corresponding to each of the clusters, i.e., the cluster centers, are visualized in 3D in Figure 5.14. For the anterior ROC, the best separation of the four obtained clusters is observed in the pairplot of the first and the fifth shape mode. This means that the clustering for the anterior ROC is most influenced by the length of the clavicle and by the prominence of the LVLa,b line. This is to be expected for an anterior plate, since a more prominent LVLa,b line requires a less curved plate. The first shape mode, expressing size differences, has a large influence on the clustering of all three ROCs. This is because size has the largest variation present in the population of clavicles and the derived population of ROCs. For the anterior-superior ROC, the best separation is observed in the pair plot of the first shape mode with the third or fifth shape mode. Again, size is an important factor for this plate but also the curvature of the clavicular bow plays a significant role. Finally, for the superior ROC, the first and second shape mode are most influential. Thus, apart from the size, also the amount of superior to inferior bend-

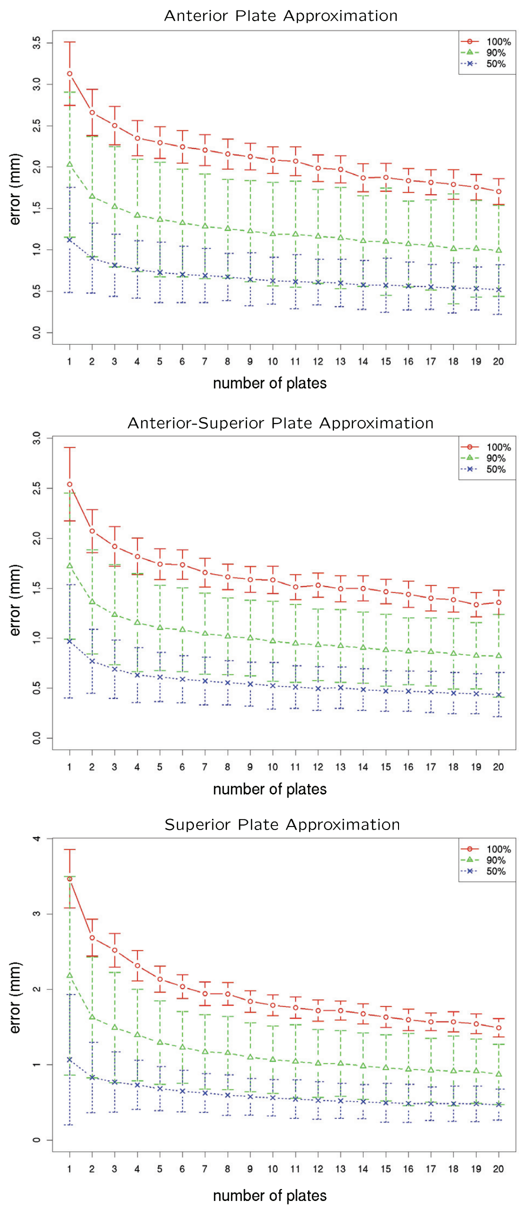

Figure 5.13: The fitting errors $E_{50\%}$ (blue and dotted), $E_{90\%}$ (green and dashed), and $E_{100\%}$ (red and solid) for the superior, anterior, and anterior-superior plate. The anterior-superior plate provides the best fit. This is followed by the anterior plate which experiences some error along the LVLa,b line. The superior plate is subject to the high variation at the extremities and therefore provides a worse fit.

ing of the distal part of the clavicle matters. The influence of the latter is more prominent with the superior ROC because, in comparison with the other ROCs, it extends further to the distal extremity of the clavicle. In Figure 5.14, the size and bending differences are noticeable in the different plates within the set.

Note that the error measures reported in Figure 5.13 are an estimation of the actual physical fitting error. On the one hand, the error is underestimated because, physically, the same degree of fitting can not be achieved as the plate can not run through the bone, which is the case with Procrustes alignment in the simulation. On the other hand, the error is overestimated because, in the simulation, the plate is restricted to the individual ROC of the bone, but in an actual situation, a slight translation of the plate along the bone can decrease the error and this is something that was not accounted for in the simulation.

5.7 Conclusions

In this work, a method was introduced to enable the construction of a dense correspondence for a population of long bones. After the selection of a landmark at both extremities of each bone, the construction of the correspondence was fully automatic. It was observed that, for the population of clavicles under consideration and for the targeted application, the method generated a good correspondence. The correspondence implied a shape space where all shape modes express plausible variations. An analysis of the correspondence of the most prominent anatomical features of the clavicle also demonstrated the matching quality of the proposed correspondence method.

Using the obtained correspondence, the shape present in different subgroups of the clavicle population was investigated. It was found that gender is an important factor in the shape of the clavicle. Directional differences and differences in date of birth, on the other hand, were much smaller and, therefore, considered negligible in the design of fixation plates.

The established correspondence was also used in the design of a set of fracture fixation plates for the clavicle. Three desired regions of contact, between fixation plate and bone, were defined on the mean clavicle of the population: one superiorly located region, an anteriorly located region, and also a region ranging from the proximal anterior part to the distal superior part of the clavicle. By mapping these three regions through the correspondence, each individual clavicle is equipped with three regions of contact. A clustering technique then provided a set of plate shapes that cover these regions with low fitting error. An analysis was made of the fitting error of these plate sets with respect to the number of plates in the set. The anterior-superior plate provided the lowest fitting error from the three suggested regions of contact. An investigation of the clustering result in the shape space and a visualization of the final plates, provided some insight into the factors that are most important in the design. It was found that the size of the clavicle and the curvatures of the clavicular bows were

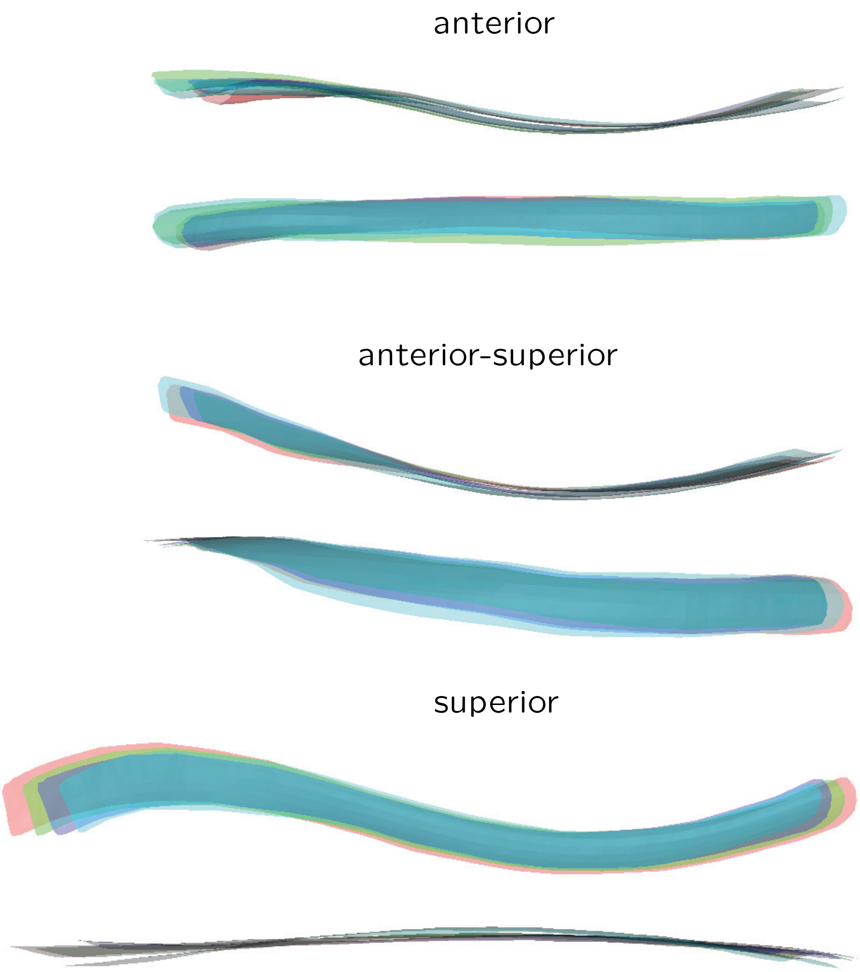

Figure 5.14: A 3D visualization of the set of plate shapes, obtained from the clustering procedure with the number of clusters $n_t = 4$, for each of the ROCs. In each case, the plates are shown from the superior side (top) and the anterior side (bottom). The four plates are visualized in different colors, matching the cluster colors in Figure 5.15 and Figure 5.16. It can be seen that the plates differ mainly in size and bow curvatures.

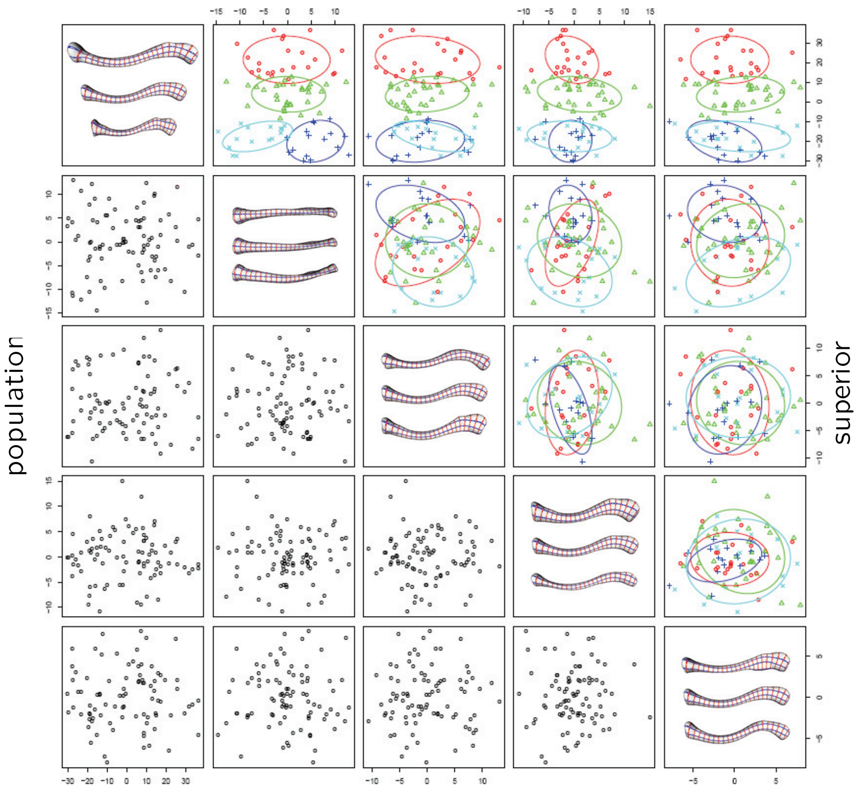

Figure 5.15: A visualization of the clustering result, with the number of clusters $n_t = 4$, for the superior ROC. The clusters are visualized in the shape space which is spanned by the shape modes. The space is restricted to the first five modes. This 5D space is visualized by projection on each combination of modes, i.e., using pair plots. The population is visualized in the lower triangle. In the upper triangle, the clustering result is visualized for the superior ROC. The different clusters are colored in red, green, blue, and cyan and these correspond to the 3D visualization of the cluster centers in Figure 5.14.

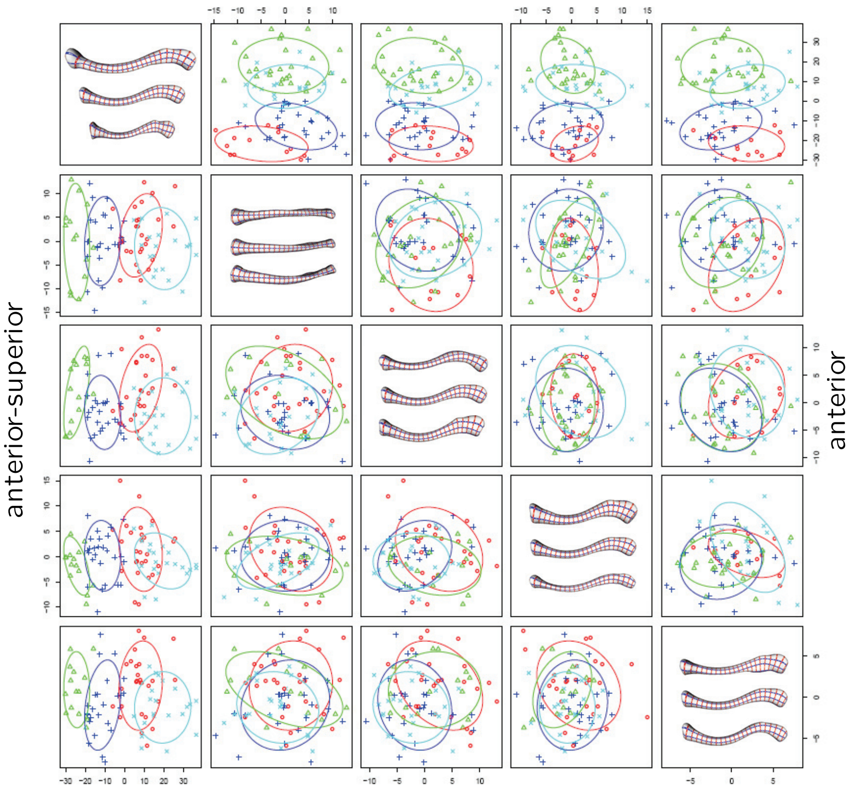

Figure 5.16: A visualization of the clustering result, with the number of clusters $n_t = 4$, for anterior and the anterior-superior ROCs. The clusters are visualized in the shape space which is spanned by the shape modes. The space is restricted to the first five modes. This 5D space is visualized by projection on each combination of modes, i.e., using pair plots. The result for anterior and the anterior-superior ROC are shown in the upper and lower triangle, respectively. The different clusters are colored in red, green, blue, and cyan and these correspond to the 3D visualization of the cluster centers in Figure 5.14.

dominating the design.

For future work, it would be interesting to use the framework to design clavicle fixation plates for fractures other then mid-shaft, i.e., fractures in the distal or proximal third of the clavicle. Furthermore, the framework should extend easily to other long bones and it could, thus, also be used in the design of fixation plates for other bones. A validation study with physical models is also a logical next step.

PART IV

SUMMARY AND CONCLUSIONS

CHAPTER 6

SUMMARY AND CONCLUSIONS

6.1 Summary and Conclusions

The goal of this manuscript was to provide a methodology for improved visualization, modeling, and analysis of tubular surfaces and to demonstrate its usefulness in some of its many applications. The main techniques underlying the proposed methodology are surface parameterization and correspondence construction. Most of the techniques that are available concentrate on surfaces of spherical or disc-like topology. For tubular surfaces, however, only a limited amount of research has been carried out while, in fact, many examples of structures of cylindrical topology are encountered in the biomedical field. Therefore, a methodology was proposed in this manuscript that is specifically designed for tubular surfaces.

In Chapter 2, two parameterization methods were developed that are specifically designed for surfaces of cylindrical topology. These methods establish a homeomorphic mapping between a surface of cylindrical topology and a cylindrical domain of a certain length and they also determine the optimal length of the cylindrical domain. Both methods establish the mapping by embedding the triangle mesh of the surface into the cylindrical domain while minimizing a certain measure of deformation to which the triangles are subjected. One method was proposed that minimizes angle deformations. The method is fast since it only requires the solution of a linear system. It was also shown to be more robust in comparison with a standard method from the literature. For surfaces with strong variation in diameter, this linear method, however, failed in keeping area distortions low. The other proposed parameterization method, which minimizes a balanced area and angle deformation measure, performed much better for such surfaces. The balanced distortion measure of this second method resulted in a nonlinear optimization problem that was solved using a hierarchical approach. It is the first cylindrical parameterization method that allows direct optimization of a balanced distortion measure that also provides the optimal length of the parameterization domain. The proposed cylindrical parameterization methods are considered complementary: the linear method generates low distortion parameterizations for well-behaved surfaces fast, while the slower, nonlinear method generates low distortion parameterizations even for the more challenging surfaces.

The differences between the two proposed parameterization methods were further highlighted in Chapter 4, where both methods were employed in a virtual inspection application for tubular organs. It was shown that the parameterization methods can be used to generate a virtual dissection view for a convoluted tubular organ and this without missing or repeating parts of the surface. In contrast with the nonlinear method, the linear parameterization resulted in severe downscaling of long protrusions. For virtual colonoscopy, this might result in certain elongated polyps being missed during the inspection procedure. Therefore, it was advised to used the nonlinear parameterization method of this manuscript.

The developed cylindrical parameterization techniques formed the basis for the cylindrical correspondence construction method developed in Chapter 3. In that chapter, the correspondence between a population of surfaces of cylindrical topology was represented by a set of cylindrical parameterizations. From a set of surface parameterizations, an initial correspondence was obtained by spatially and parameterically aligning the surfaces through optimization with respect to a celebrated correspondence quality measure from the literature. In a second stage, the obtained initial correspondence was further improved by nonrigid transformation of the parameterizations. The solution was found in a robust and efficient way by a multi-level approach and the use of gradient information. The developed method is specifically designed for surfaces of cylindrical topology and it, therefore, does not suffer from constraints imposed by surface chartifications. The method was evaluated on a large number of data sets and proved to generate high quality correspondences.

In Chapter 5, the cylindrical correspondence technique of this manuscript was used to construct a correspondence for a population of clavicles. The clavicles were modified to a cylindrical topology by opening them at both ends. It was shown that the obtained correspondence matched anatomically equivalent regions which is a requirement for meaningful shape analysis. Subsequently, different subgroups were compared in terms of shape and it was found that clavicles of males are significantly smaller that those of females. The chapter also presented a technique to extract a tightly fitting set of fracture fixation plates from a population of bones, given a desired region of contact. From all plating approaches, anterior-superior plating resulted in the smallest fitting errors. It was also shown that the clavicle length is the dominant factor in the plate shape design.

6.2 Possible Improvements and Future Prospects

The nonlinear cylindrical parameterization method developed in Chapter 2 succeeds in keeping both angle and area distortions low, even for surfaces with a large variation in cross-sectional diameter. This, however, comes at an increased computational cost. Therefore, it would be interesting to combine the quality of the nonlinear methods with the speed of the linear method. In this respect, the work of Dong and Garland [2007] is worth noting. For surfaces of disk-like topology, they obtain low distortion parameterizations efficiently by solving a sequence of linear systems where the edge weights of the linear systems are obtained by local, non-linear optimizations. All the necessary components to extend their approach to surfaces of cylindrical topology are, in fact, already available from this manuscript. A further speedup might even be obtained by porting the algorithm to the graphical processing unit (GPU) where it can enjoy massive parallelism.

Another useful extension of the cylindrical parameterization methods would be to allow the incorporation of constraints. The constraint mechanism could then be used to incorporate prior knowledge which is useful in, for example, the construction of a population correspondence. By predefining the parametric location of certain manually pin-pointed anatomical landmarks, a correspondence is obtained that provides a direct map between these landmarks across the surfaces in the population.

Further investigation is also needed to more accurately highlight the advantages and disadvantages of the nonlinear parameterization method for virtual organ inspection. "Which classes of pathologies can be more reliably identified with this method?" and "How likely are these pathologies to occur?" are relevant questions, here. In order to compete with current leading edge commercial software for virtual inspection, the inspection technique of Chapter 4 should also be augmented with computer aided detection (CAD) of pathologies.

In Chapter 5, the quality of the correspondence obtained with the methods of this manuscript for a population of clavicles was investigated based on manually defined anatomical markers. An investigation of the influence of the parameters of the correspondence method on the matching quality would be very useful. Furthermore, a comparison could be made with correspondences that are obtained using alternative quality measures such as the MDL measure with local geometry [Styner et al., 2008].

The parameterization techniques and correspondence technique developed in this manuscript can be trivially ported to the populations of genus-1 surfaces. In that case, the torus would be used as a parameter domain. It is also very likely that the methodology of this manuscript can be extended to populations of tubular surfaces with branches or even to populations of surfaces of genus-n topology, although further research is needed.

The automatic precontouring technique, developed in Chapter 5, is a promising tool for shortening of the design cycle of certain types of osteosynthesis hardware, such as plates and nails. However, there is still room for improvement: incorporating collision detection in the assessment of the plate fitting error could lead to a more accurate fitting error measure. It would also be very interesting to do a thorough comparison of the obtained plates for midclavicular fractures with currently available commercial fixation plates. It should not be too hard to implement an automated quality assessment tool for plates, based on the correspondence framework that was proposed in this manuscript. Finally, the proposed technique could also be applied to other bones such as the long bones in the upper and lower extremities or even less obvious elongated surfaces such as the mandible.

APPENDIX A

B-SPLINE REGULARISATION

Let the b-spline reparameterization function $\boldsymbol{\rho}$ with control point displacements $\boldsymbol{\delta}$ be defined as:

$$\boldsymbol{\rho}(\boldsymbol{u}|\boldsymbol{\delta}) = \sum_{i=-1}^{n_{u^{(0)}}+1} \sum_{j=-1}^{n_{u^{(1)}}} \beta\left(\frac{\boldsymbol{u}-\boldsymbol{\kappa}_{ij}}{\boldsymbol{\Delta}}\right)(\boldsymbol{\kappa}_{ij}+\boldsymbol{\delta}_{ij}) \mod^{(0)} 2\pi, \tag{A.1}$$

where β is a separable cubic b-spline kernel centered around the origin, $\boldsymbol{u} = (u^{(0)}, u^{(1)})$ is the position in parameter space, $\boldsymbol{\Delta} = (\Delta^{(0)}, \Delta^{(1)}) = (\frac{2\pi}{n_{u^{(0)}}}, \frac{h}{n_{u^{(1)}}-1})$ is the knot spacing in the $u^{(0)}$- and $u^{(1)}$-direction, $\boldsymbol{\kappa}_{ij} = (i\Delta^{(0)}, j\Delta^{(1)})$ are the knot positions and $\boldsymbol{\delta}_{ij}$ are the control point displacements at each knot.

From equation A.1 the parameterization displacement function $\boldsymbol{\varrho}$ can be derived:

$$\boldsymbol{\varrho}(\boldsymbol{u}|\boldsymbol{\delta}) = \sum_{i=-1}^{n_{u^{(0)}}+1} \sum_{j=-1}^{n_{u^{(1)}}} \beta\left(\frac{\boldsymbol{u}-\boldsymbol{\kappa}_{ij}}{\boldsymbol{\Delta}}\right)\boldsymbol{\delta}_{ij}. \tag{A.2}$$

Expanding the separable b-spline kernel β leads to:

$$\begin{aligned}
\boldsymbol{\varrho}(\boldsymbol{u}|\boldsymbol{\delta}) &= \sum_{i=-1}^{n_{u^{(0)}}+1} \sum_{j=-1}^{n_{u^{(1)}}} \beta\left(\frac{u^{(0)}-i\Delta^{(0)}}{\Delta^{(0)}}\right)\beta\left(\frac{u^{(1)}-j\Delta^{(1)}}{\Delta^{(1)}}\right)\boldsymbol{\delta}_{ij} \\
&= \sum_{i=-1}^{n_{u^{(0)}}+1} \sum_{j=-1}^{n_{u^{(1)}}} \beta\left(\frac{u^{(0)}}{\Delta^{(0)}}-i\right)\beta\left(\frac{u^{(1)}}{\Delta^{(1)}}-j\right)\boldsymbol{\delta}_{ij} \\
&= \sum_{ij} \beta^{i}_{u^{(0)}}\beta^{j}_{u^{(1)}}\boldsymbol{\delta}_{ij},
\end{aligned}$$

where $\beta^i_{u^{(c)}} \equiv \beta\left(\frac{u^{(c)}}{\Delta^{(c)}} - i\right)$ is used as a shorthand notation.

The regularisation η^ρ term for the deformation is defined as:

$$\eta^\rho(\boldsymbol{\delta}) = \int_{\mathscr{C}_h^2} \left(\left| \frac{\partial \varrho(\boldsymbol{u}|\boldsymbol{\delta})}{\partial u^{(0)}} \right|^2 + \left| \frac{\partial \varrho(\boldsymbol{u}|\boldsymbol{\delta})}{\partial u^{(1)}} \right|^2 \right) \mathrm{d}\boldsymbol{u}. \tag{A.3}$$

In what follows, the prime mark symbol will be used to denote the derivative. The first part of this integral is given by:

$$\begin{aligned}
\int_{\mathscr{C}_h^2} \left| \frac{\partial \varrho(\boldsymbol{u}|\boldsymbol{\delta})}{\partial u^{(0)}} \right|^2 \mathrm{d}\boldsymbol{u} &= \int_{\mathscr{C}_h^2} \left| \sum_{ij} \beta^{i'}_{u^{(0)}} \beta^{j}_{u^{(1)}} \frac{\boldsymbol{\delta}_{ij}}{\Delta^{(0)}} \right|^2 \mathrm{d}\boldsymbol{u} \\
&= \int_{\mathscr{C}_h^2} \sum_{ij} \sum_{kl} \beta^{i'}_{u^{(0)}} \beta^{k'}_{u^{(0)}} \beta^{j}_{u^{(1)}} \beta^{l}_{u^{(1)}} \frac{\boldsymbol{\delta}_{ij} \boldsymbol{\delta}_{kl}^T}{\left(\Delta^{(0)}\right)^2} \mathrm{d}\boldsymbol{u} \\
&= \sum_{ij} \sum_{kl} \frac{\boldsymbol{\delta}_{ij} \boldsymbol{\delta}_{kl}^T}{\left(\Delta^{(0)}\right)^2} \int_0^{2\pi} \beta^{i'}_{u^{(0)}} \beta^{k'}_{u^{(0)}} \mathrm{d}u^{(0)} \int_0^h \beta^{j}_{u^{(1)}} \beta^{l}_{u^{(1)}} \mathrm{d}u^{(1)}.
\end{aligned}$$

An analogous computation gives:

$$\int_{\mathscr{C}_h^2} \left| \frac{\partial \varrho(\boldsymbol{u}|\boldsymbol{\delta})}{\partial u^{(1)}} \right|^2 \mathrm{d}\boldsymbol{u} = \sum_{ij} \sum_{kl} \frac{\boldsymbol{\delta}_{ij} \boldsymbol{\delta}_{kl}^T}{\left(\Delta^{(1)}\right)^2} \int_0^{2\pi} \beta^{i}_{u^{(0)}} \beta^{k}_{u^{(0)}} \mathrm{d}u^{(0)} \int_0^h \beta^{j'}_{u^{(1)}} \beta^{l'}_{u^{(1)}} \mathrm{d}u^{(1)}.$$

So, the total smoothness energy becomes:

$$\begin{aligned}
\eta^\rho(\boldsymbol{\delta}) = \sum_{ij} \sum_{kl} \boldsymbol{\delta}_{ij} \boldsymbol{\delta}_{kl}^T \Bigg(&\frac{1}{\left(\Delta^{(0)}\right)^2} \int_0^{2\pi} \beta^{i'}_{u^{(0)}} \beta^{k'}_{u^{(0)}} \mathrm{d}u^{(0)} \int_0^h \beta^{j}_{u^{(1)}} \beta^{l}_{u^{(1)}} \mathrm{d}u^{(1)} \\
&+ \frac{1}{\left(\Delta^{(1)}\right)^2} \int_0^{2\pi} \beta^{i}_{u^{(0)}} \beta^{k}_{u^{(0)}} \mathrm{d}u^{(0)} \int_0^h \beta^{j'}_{u^{(1)}} \beta^{l'}_{u^{(1)}} \mathrm{d}u^{(1)} \Bigg).
\end{aligned} \tag{A.4}$$

The resulting integrals can be calculated analytically, and they become zero when $|i - j| \geq 4$:

$$\begin{aligned}
\int_0^{2\pi} \beta^{i}_{u^{(0)}} \beta^{j}_{u^{(0)}} \mathrm{d}u^{(0)} &= \int_0^{2\pi} \beta\left(\frac{n_{u^{(0)}}}{2\pi} u^{(0)} - i\right) \beta\left(\frac{n_{u^{(0)}}}{2\pi} u^{(0)} - j\right) \mathrm{d}u^{(0)} \\
&= \frac{2\pi}{n_{u^{(0)}}} \int_{-i}^{n_{u^{(0)}} - i} \beta\left(u^{(0)}\right) \beta\left(u^{(0)} + i - j\right) \mathrm{d}u^{(0)}
\end{aligned}$$

$$\begin{aligned}
\int_0^{2\pi} \beta^{i'}_{u^{(0)}} \beta^{j'}_{u^{(0)}} \mathrm{d}u^{(0)} &= \int_0^{2\pi} \beta'\left(\frac{n_{u^{(0)}}}{2\pi} u^{(0)} - i\right) \beta'\left(\frac{n_{u^{(0)}}}{2\pi} u^{(0)} - j\right) \mathrm{d}u^{(0)} \\
&= \frac{2\pi}{n_{u^{(0)}}} \int_{-i}^{n_{u^{(0)}} - i} \beta'\left(u^{(0)}\right) \beta'\left(u^{(0)} + i - j\right) \mathrm{d}u^{(0)}
\end{aligned}$$

$$\begin{aligned}\int_0^h \beta^i_{u^{(1)}}\beta^j_{u^{(1)}}\mathrm{d}u^{(1)} &= \int_0^h \beta\left(\frac{n_{u^{(1)}}-1}{h}u^{(1)}-i\right)\beta\left(\frac{n_{u^{(1)}}-1}{h}u^{(1)}-j\right)\mathrm{d}u^{(1)}\\ &= \frac{h}{n_{u^{(1)}}-1}\int_{-i}^{n_{u^{(1)}}-1-i}\beta\left(u^{(1)}\right)\beta\left(u^{(1)}+i-j\right)\mathrm{d}u^{(1)}\end{aligned}$$

$$\begin{aligned}\int_0^h \beta^{i'}_{u^{(1)}}\beta^{j'}_{u^{(1)}}\mathrm{d}u^{(1)} &= \int_0^h \beta'\left(\frac{n_{u^{(1)}}-1}{h}u^{(1)}-i\right)\beta'\left(\frac{n_{u^{(1)}}-1}{h}u^{(1)}-j\right)\mathrm{d}u^{(1)}\\ &= \frac{h}{n_{u^{(1)}}-1}\int_{-i}^{n_{u^{(1)}}-1-i}\beta'\left(u^{(1)}\right)\beta'\left(u^{(1)}+i-j\right)\mathrm{d}u^{(1)}.\end{aligned}$$

The derivatives of the smoothness energy w.r.t. the control point displacements are easily derived:

$$\frac{\partial\eta^\rho}{\partial\delta^{(0)}_{mn}}(\boldsymbol{\delta}) = 2\int_{\mathscr{C}_h^2}\frac{\partial\varrho(\boldsymbol{u}|\boldsymbol{\delta})}{\partial u^{(0)}}\cdot\frac{\partial^2\varrho(\boldsymbol{u}|\boldsymbol{\delta})}{\partial u^{(0)}\partial\delta^{(0)}_{mn}}+\frac{\partial\varrho(\boldsymbol{u}|\boldsymbol{\delta})}{\partial u^{(1)}}\cdot\frac{\partial^2\varrho(\boldsymbol{u}|\boldsymbol{\delta})}{\partial u^{(1)}\partial\delta^{(0)}_{mn}}\,\mathrm{d}\boldsymbol{u}. \tag{A.5}$$

This finally leads to:

$$\begin{aligned}\frac{\partial\eta^\rho}{\partial\delta^{(0)}_{mn}}(\boldsymbol{\delta}) = 2\sum_{ij}\delta^{(0)}_{ij}\Bigg(&\frac{1}{\Delta^{(0)2}}\int_0^{2\pi}\beta^{i'}_{u^{(0)}}\beta^{k'}_{u^{(0)}}\mathrm{d}u^{(0)}\int_0^h\beta^j_{u^{(1)}}\beta^l_{u^{(1)}}\mathrm{d}u^{(1)}\\ &+\frac{1}{\Delta^{(1)2}}\int_0^{2\pi}\beta^i_{u^{(0)}}\beta^k_{u^{(0)}}\mathrm{d}u^{(0)}\int_0^h\beta^{j'}_{u^{(1)}}\beta^{l'}_{u^{(1)}}\mathrm{d}u^{(1)}\Bigg).\end{aligned} \tag{A.6}$$

Appendix B

Population of Human Clavicles

What follows is a visualization of the clavicles of the population used in this manuscript. The final correspondence that was obtained for these surfaces is visualized by means of a texture.

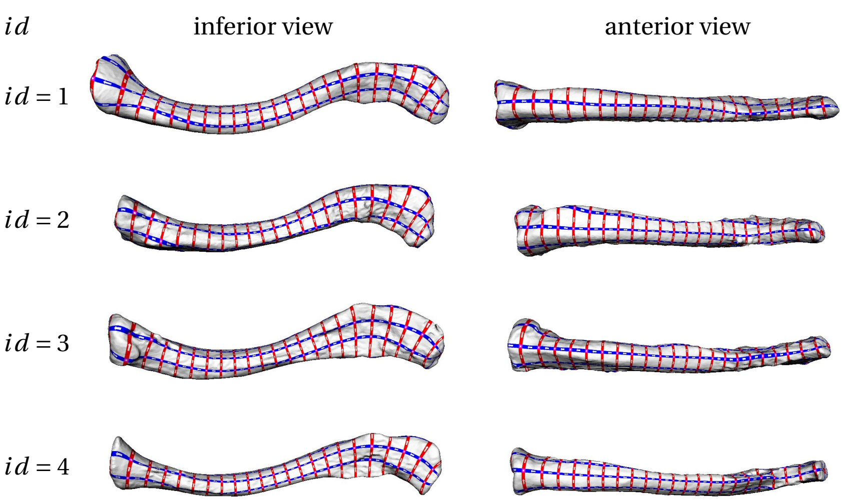

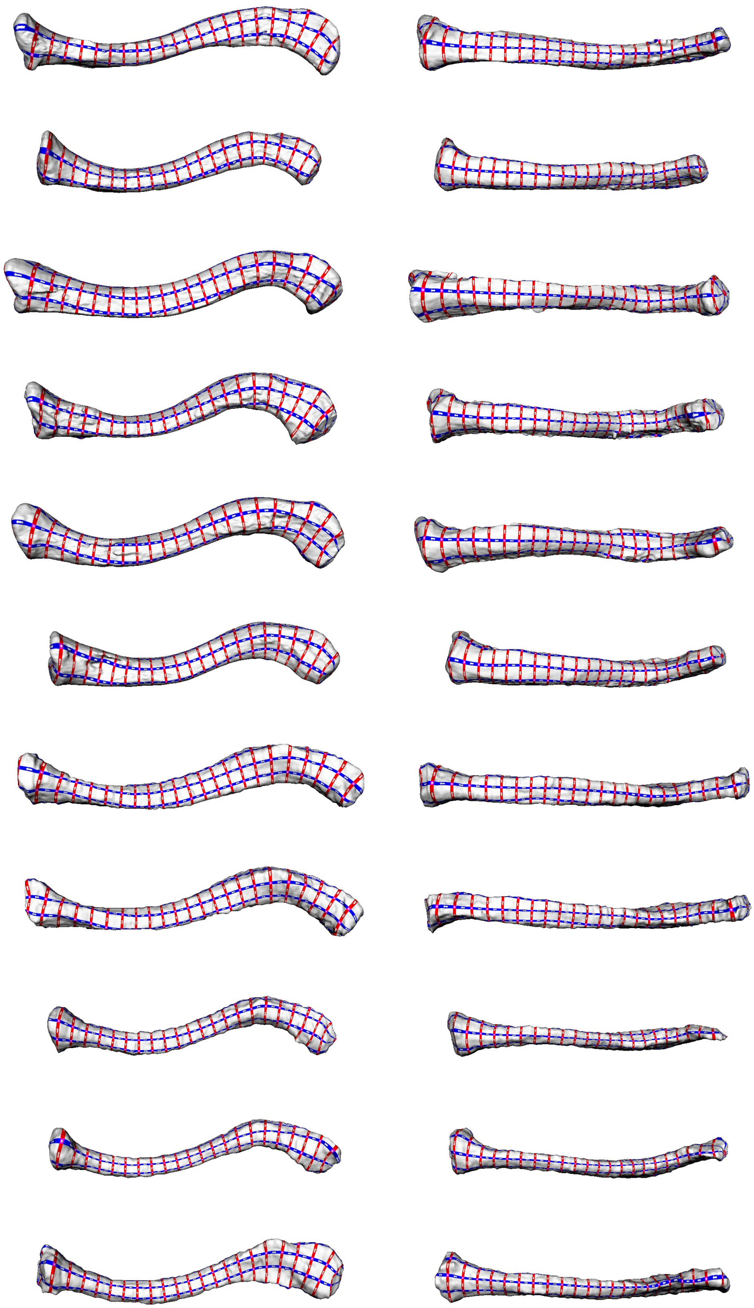

$id = 5$

$id = 6$

$id = 7$

$id = 8$

$id = 9$

$id = 10$

$id = 11$

$id = 12$

$id = 13$

$id = 14$

$id = 15$

$id = 16$

$id = 17$

$id = 18$

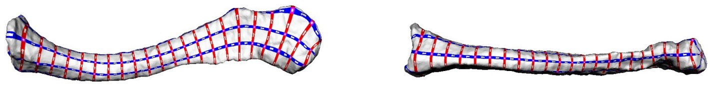

$id = 19$

$id = 20$

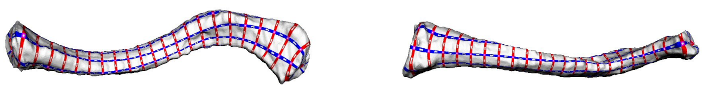

$id = 21$

$id = 22$

$id = 23$

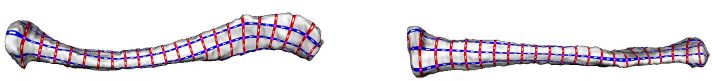

$id = 24$

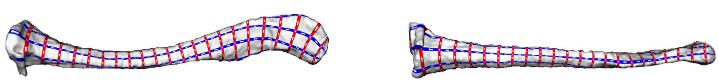

$id = 25$

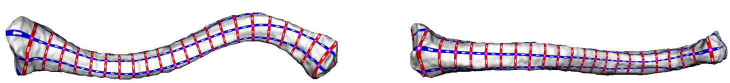

$id = 26$

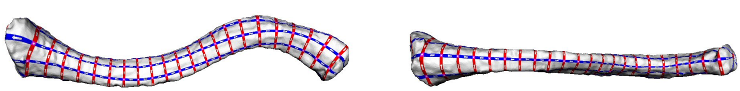

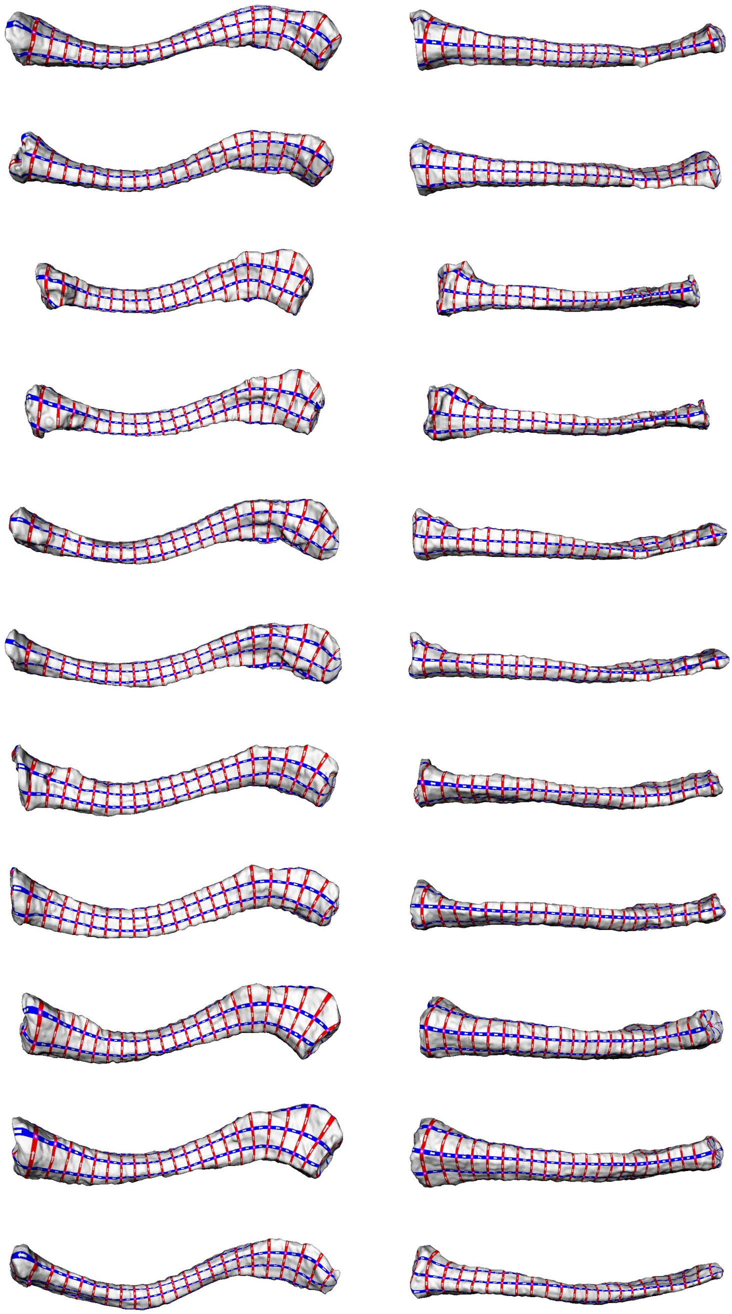

$id = 27$

$id = 28$

$id = 29$

$id = 30$

$id = 31$

$id = 32$

$id = 33$

$id = 34$

$id = 35$

$id = 36$

$id = 37$

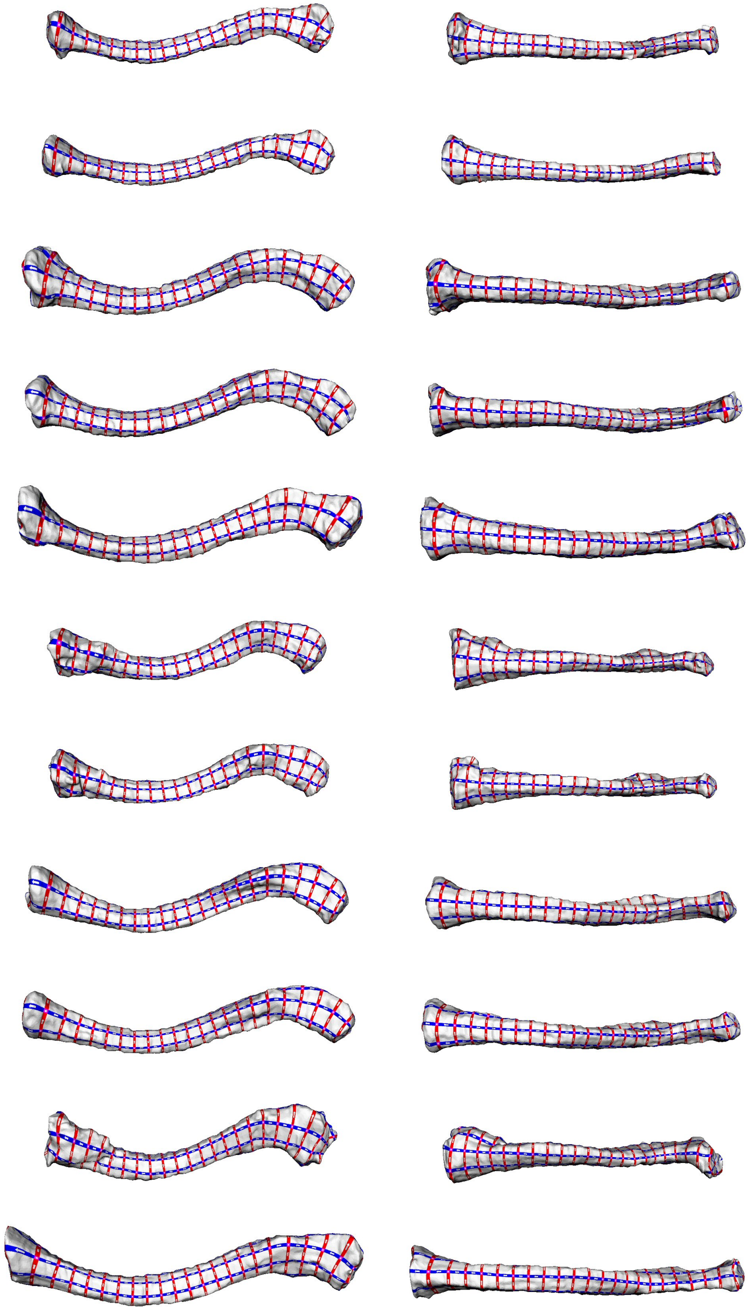

$id = 39$

$id = 40$

$id = 41$

$id = 42$

$id = 43$

$id = 45$

$id = 46$

$id = 47$

$id = 48$

$id = 49$

$id = 50$

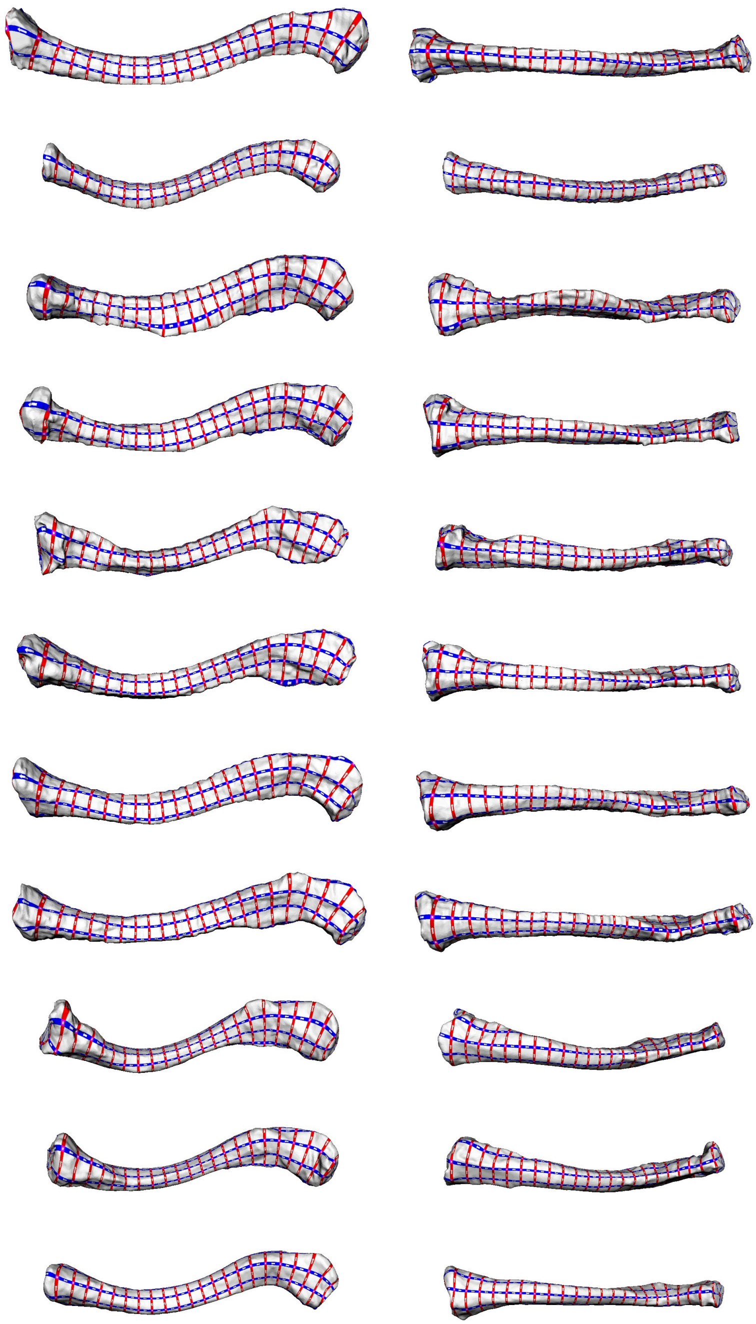

$id = 51$

$id = 52$

$id = 53$

$id = 54$

$id = 55$

$id = 56$

$id = 57$

$id = 58$

$id = 59$

$id = 60$

$id = 61$

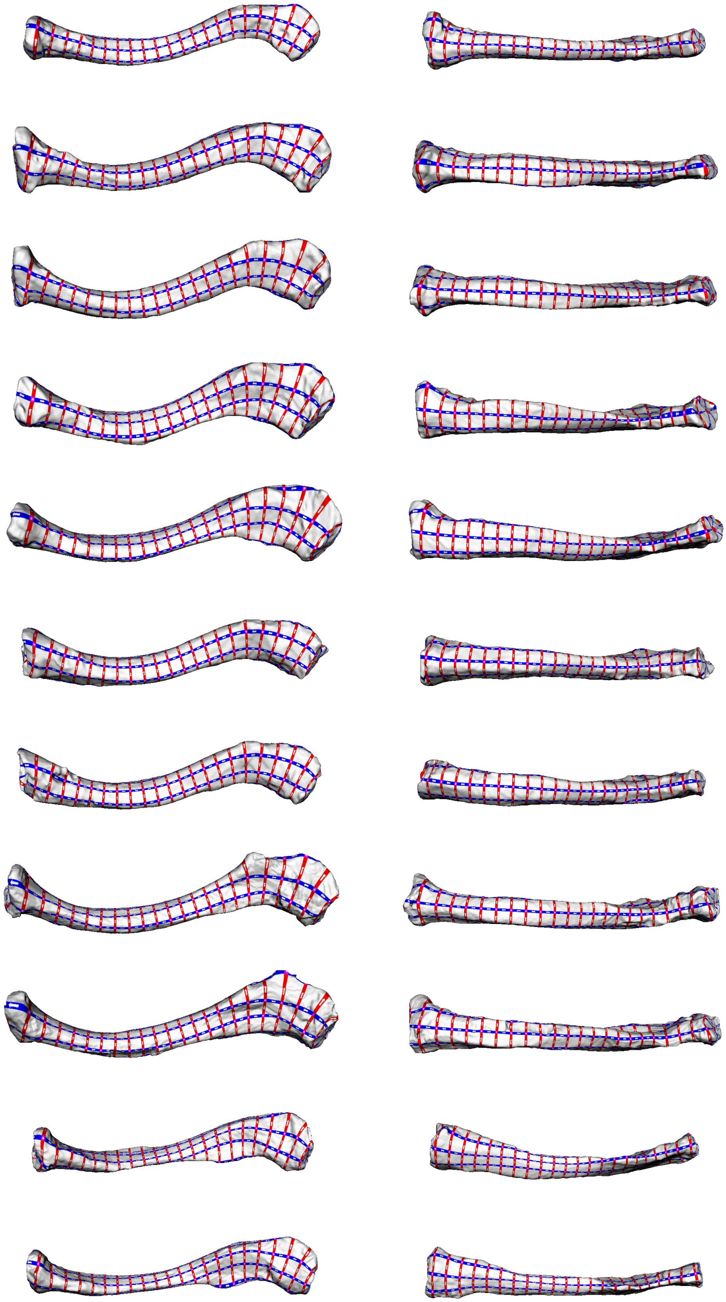

$id = 62$

$id = 63$

$id = 64$

$id = 65$

$id = 66$

$id = 67$

$id = 68$

$id = 69$

$id = 70$

$id = 71$

$id = 72$

$id = 73$


$id = 74$


$id = 75$


$id = 76$


$id = 77$
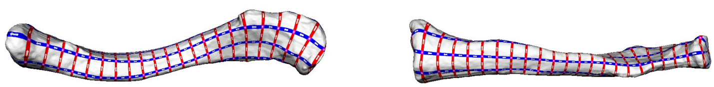

$id = 78$
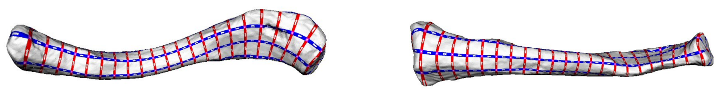

$id = 79$


$id = 80$


$id = 81$


$id = 82$


$id = 83$


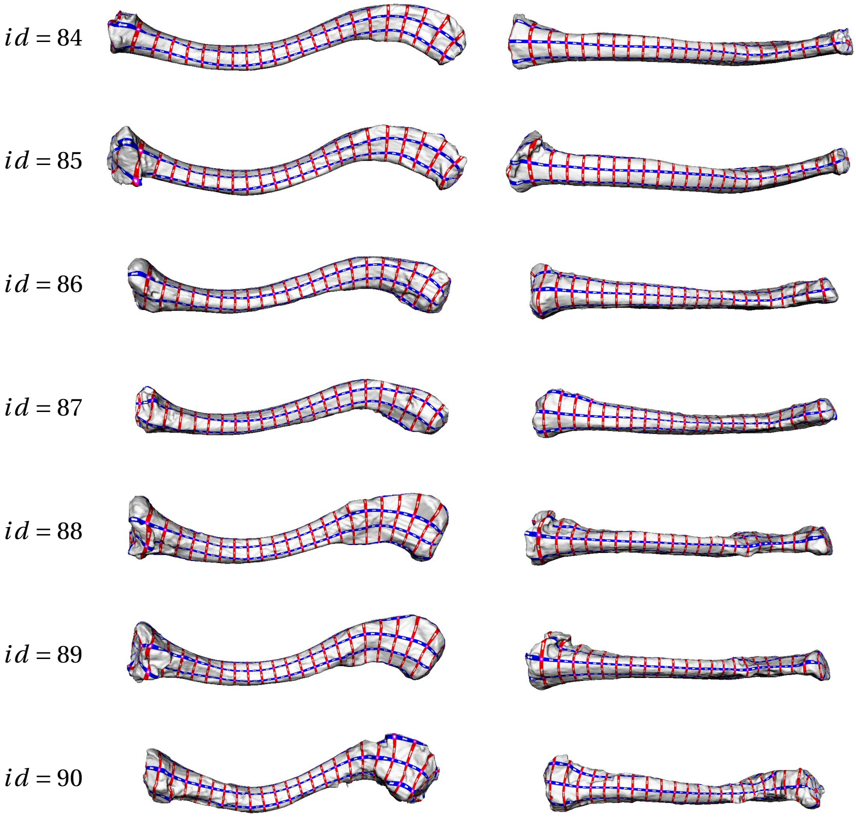
$id = 84$
$id = 85$
$id = 86$
$id = 87$
$id = 88$
$id = 89$
$id = 90$

NEDERLANDSE SAMENVATTING

De aard van een object komt tot uiting in de verschillende eigenschappen die het bezit, zoals kleur, textuur, gewicht en vorm. Elk van deze eigenschappen bevat een bron van informatie die mogelijk van belang is voor de waarnemer. Dit werk concentreert zich op de geometrische vorm van objecten voorgesteld aan de hand van een maas van driehoeken. Zulk een maas wordt over het algemeen bekomen met behulp van een beeldvormingstechniek (zoals MRI, CT of laserscanning) in combinatie met een waaier van voorverwerkingsoperaties (zoals ontruising, segmentatie en oppervlak extractie). In dit manuscript wordt de aandacht gevestigd op biomedische objecten, maar de ontwikkelde technieken zijn wel algemeen toepasbaar. Kennis van de vorm en de verschillende vormvariaties van een orgaan of bot is zeer nuttig en kan gebruikt worden in talloze toepassingen, zoals segmentatie, reconstructie en diagnose.

Het doel van dit manuscript is het uiteenzetten van een methodologie voor de verbeterde analyse, modellering en visualisatie van buisvormige objecten en de bruikbaarheid van deze methodologie aan te tonen in een aantal biomedische toepassingen. De belangrijkste onderliggende technieken van de methodologie zijn parameterisatie en correspondentie van oppervlakken. Daar waar voorgaand onderzoek vooral handelde over objecten die de topologie hebben van een sfeer of van een schijf, gaat in dit manuscript de aandacht uit naar objecten die de topologie van een cilinder hebben of objecten die topologisch gezien een sfeer zijn maar wel een langwerpige geometrie vertonen. Deze laatsten kunnen namelijk eenvoudig gewijzigd worden zodat ze eveneens de topologie van een cilinder verkrijgen door aan beide uiteinden van het oppervlak een gaatje te prikken. Hoewel er voor oppervlakken van cilindrische topologie slechts weinig onderzoek is verricht in het verleden, zijn er toch vele voorbeelden van buisvormige structuren terug te vinden in bijvoorbeeld het menselijk lichaam. Daarom wordt in dit manuscript een methodologie voorgesteld die specifiek ontwikkeld is voor dit type oppervlakken.

Hoofdstuk 1 vormt de introductie van dit manuscript. Eerst wordt kort het onderwerp ingeleid. Daarna wordt er een overzicht gegeven van de methodologie en de applicaties die in het manuscript ontwikkeld worden. Dit wordt gevolgd door een overzicht van voorgaand onderzoek dat verband houdt met het werk in dit manuscript. Het hoofdstuk wordt afgesloten met een bespreking van de bijdragen van dit manuscript.

In Hoofdstuk 2, worden twee parameterisatietechnieken voorgesteld die specifiek ontworpen zijn voor oppervlakken van cilindrische topologie. Beide methoden stellen een homeomorfe functie op die het oppervlak van cilindrische topologie afbeeldt op een cilindrisch domein met een bepaalde lengte. Bovendien bepalen deze methoden ook de optimale lengte van het cilindrisch domein. De parameterisatie wordt in beide gevallen bekomen door de maas van het oppervlak op een danige manier te vervormen naar het cilindrisch domein zodat een bepaalde maat voor vervorming, waar de driehoeken van het oppervlak aan onderhevig zijn, geminimaliseerd wordt. De eerste methode die geïntroduceerd wordt tracht de vervorming van de hoeken te minimaliseren. Het betreft een snelle methode omdat de parameterizatie bekomen wordt uit de oplossing van een systeem van lineaire vergelijkingen. Voor oppervlakken waarbij de diameter van de doorsnede sterk veranderlijk is, slaagt deze methode er helaas niet in om de vervorming in oppervlakte onder controle te houden. Daarom wordt er een tweede methode geïntroduceerd die de vervorming in oppervlakte en hoeken tracht te balanceren. De specifieke vervormingsmaat die zich bij deze techniek aandient, resulteert echter in een niet-lineair optimalisatieprobleem. Een hiërarchische oplossingsmethode lost het optimalisatieprobleem op een efficiënte en robuuste wijze op. Deze niet-lineaire techniek is bijgevolg trager dan de lineaire techniek, maar slaagt er wel in de hoek- en oppervlaktevervorming onder controle te houden bij oppervlakken waarbij de diameter van de doorsnede sterk veranderlijk is. We kunnen daarom de twee voorgestelde methoden als complementair beschouwen.

In Hoofdstuk 4, worden de ontwikkelde parameterisatietechnieken aangewend voor de virtuele inspectie van buisvormige organen. De parameterisatietechniek wordt gebruikt om de maas van het orgaan om te vormen in een cilinder. Vervolgens wordt die cilinder opengevouwen naar een rechthoek in het vlak en worden er normalen aangebracht die bij belichting de oorspronkelijke vorm van het orgaan weer naar voren brengen. De alzo bekomen virtuele dissectie geeft de wand van het, eventueel sterk gekronkelde, orgaan weer zonder delen te missen of te herhalen. Indien men de lineaire parameterisatietechniek gebruikt kunnen er wel sterke oppervlaktevervormingen optreden. Deze vervormingen zorgen ervoor dat lange uitsteeksels, zoals divertikels of lange poliepen, flink worden verkleind of zelfs volledig onzichtbaar worden. Dit kan als gevolg hebben dat tijdens de inspectie van het orgaan de pathologie in kwestie niet ontdekt wordt. Gebruikt men daarentegen de niet-lineaire parameterisatietechniek, dan zijn deze structuren veel beter zichtbaar.

De ontwikkelde parameterisatiemethoden vormen ook de basis voor de correspondentiemethode die in Hoofdstuk 3 wordt voorgesteld. De correspondentie voor een populatie van oppervlakken van cilindrische topologie wordt er namelijk voorgesteld door middel van cilindrische parameterisaties, één voor elk individu in de populatie. Door compositie van deze parameterisaties kan men rechtstreeks afbeeldingen bekomen tussen twee oppervlakken van de populatie. Het is de bedoeling de parameterisaties zodanig op te stellen dat overeenkomstige delen van de objecten op elkaar afgebeeld worden door de correspondentie. Een initiële correspondentie wordt verwezenlijkt door de objecten spatiaal uit te lijnen en eveneens de parmeterisaties uit te lijnen. De optimale uitlijning verkrijgt men door de parameters die de uitlijningen bepalen te optimaliseren naar een standaard kwaliteitsmaat voor correspondentie. De bekomen initiële correspondentie wordt nog verbeterd door een tweede optimalisatie waarbij er niet-rigide transformaties toegelaten zijn voor de parameterisaties. De oplossing van dit complex optimalisatieprobleem wordt op een robuuste en efficiënte manier gevonden door gebruik te maken van een multischaal aanpak, in combinatie met gradiënt informatie. De voorgestelde techniek wordt op een groot aantal datasets getest en de invloed van de parameters van het algoritme wordt eveneens onderzocht.

In Hoofdstuk 5 wordt de voorgestelde correspondentiemethode gebruikt om een correspondentie op te stellen voor een populatie van menselijke sleutelbeenderen. Een sleutelbeen kan voorgesteld worden aan de hand van een langwerpig oppervlak van sferische topologie. De topologie kan men echter eenvoudig op een consistente manier converteren naar die van een cilinder door aan de uiteinden een gaatje te prikken. Het wordt aangetoond dat de bekomen correspondentie van hoge kwaliteit is en dat ze anatomisch equivalente delen van de sleutelbeenderen met elkaar in overeenstemming brengt. De correspondentie wordt vervolgens gebruikt om verschillende deelpopulaties met elkaar te vergelijken: sleutelbeenderen van mannen versus vrouwen, oude versus recentere sleutelbeenderen en linker versus rechter sleutelbeenderen. Verder wordt er in dit hoofdstuk ook een techniek uiteengezet om automatisch steunplaatjes te genereren die bij een breuk van het sleutelbeen gebruikt kunnen worden om het bot te fixeren. Er wordt hiervoor eerst een gemiddeld sleutelbeen berekend. Vervolgens wordt er de gewenste regio op aangeduid waar er contact moet zijn tussen bot en steunplaat. Deze regio wordt dan via de correspondentie afgebeeld op alle botjes van de populatie. Hieruit wordt uiteindelijk een set van plaatjes afgeleid die samen de gewenste contactregio's met een kleine fout dekken.

Het manuscript wordt besloten met Hoofdstuk 6. Hierin wordt het manuscript kort samengevat en worden de belangrijkste conclusies nog eens op een rijtje gezet. Tot slot wordt er in dit hoofdstuk ook nog ingegaan op de eventuele verbeteringen die kunnen worden aangebracht en de verdere mogelijke uitbreidingen.

Bibliography

Burak Aksoylu, Andrei Khodakovsky, and Peter Schröder. Multilevel solvers for unstructured surface meshes. *SIAM J. Sci. Comput.*, 26(4):1146–1165, 2005. ISSN 1064-8275. doi: http://dx.doi.org/10.1137/S1064827503430138.

Marc Alexa. Recent advances in mesh morphing. *Computer Graphics Forum*, 21 (2):173–196, June 2002.

Pierre Alliez, Mark Meyer, and Mathieu Desbrun. Interactive geometry remeshing. In *Proceedings of the 29th annual conference on Computer graphics and interactive techniques*, pages 347–354. ACM Press, 2002.

Pierre Alliez, Marco Attene, Craig Gotsman, and Giuliana Ucelli. Recent advances in remeshing of surfaces. In Leila de Floriani and Michela Spagnuolo, editors, *Shape Analysis and Structuring, Mathematics and Visualization*, pages 828–839, Berlin, 2007. Springer.

F L Allman. Fractures and ligamentous injuries of the clavicle and its articulation. *The Journal of Bone and Joint Surgery. American Volume*, 49(4):774–84, June 1967.

Jonas Andermahr, Axel Jubel, Andreas Elsner, Jan Johann, Axel Prokop, Klaus Emil Rehm, and Juergen Koebke. Anatomy of the clavicle and the intramedullary nailing of midclavicular fractures. *Clinical Anatomy (New York, N.Y.)*, 20(1):48–56, 2007.

L. Antiga and D.A. Steinman. Robust and objective decomposition and mapping of bifurcating vessels. *Medical Imaging, IEEE Transactions on*, 23(6):704–713, 2004. ISSN 0278-0062.

Benjamin M. Auerbach and Michelle H. Raxter. Patterns of clavicular bilateral asymmetry in relation to the humerus: variation among humans. *Journal of Human Evolution*, 54(5):663–674, May 2008.

E Balogh, E Sorantin, L G Nyul, K Palagyi, A Kuba, G Werkgartner, and E Spuller. Colon unraveling based on electronic field: Recent progress and future work. In *Proceedings SPIE 4681*, pages 713–721, 2002.

Richard H. Bartels, John C. Beatty, and Brian A. Barsky. *An introduction to splines for use in computer graphics & geometric modeling.* Morgan Kaufmann Publishers Inc., San Francisco, CA, USA, 1987. ISBN 0-934613-27-3.

Anna Vilanova Bartrolí, Rainer Wegenkittl, Andreas König, and Eduard Gröller. Nonlinear virtual colon unfolding. In *VIS '01: Proceedings of the conference on Visualization '01*, pages 411–420, Washington, DC, USA, 2001. IEEE Computer Society. ISBN 0-7803-7200-X.

Jeff Bolz, Ian Farmer, Eitan Grinspun, and Peter Schröoder. Sparse matrix solvers on the gpu: conjugate gradients and multigrid. *ACM Trans. Graph.*, 22 (3):917–924, 2003. ISSN 0730-0301. doi: http://doi.acm.org/10.1145/882262.882364.

F.L. Bookstein. *Morphometric Tools for Landmark Data: Geometry and Biology.* Cambridge University Press, 1991.

Ch. Brechbühler, G. Gerig, and O. Kübler. Parametrization of closed surfaces for 3-d shape description. *Computer Vision and Image Understanding*, 61(2): 154–170, 1995.

Marleen De Bruijne, Bram Van Ginneken, Max A. Viergever, and Wiro J. Niessen. Adapting active shape models for 3d segmentation of tubular structures in medical images. In *in medical images,âĂİ in Information Processing in Medical Imaging*, pages 136–147. Springer, 2003.

Joshua Cates, P Thomas Fletcher, Martin Styner, Martha Shenton, and Ross Whitaker. Shape modeling and analysis with entropy-based particle systems. *Inf Process Med Imaging*, 20(NIL):333–45, 2007.

E. Catmull and J. Clark. Recursively generated b-spline surfaces on arbitrary topological meshes. *Computer-Aided Design*, 10(6):350–355, November 1978.

Cory Collinge, Scott Devinney, Dolfi Herscovici, Thomas DiPasquale, and Roy Sanders. Anterior-inferior plate fixation of middle-third fractures and nonunions of the clavicle. *Journal of Orthopaedic Trauma*, 20(10):680–6, 2006.

T. F. Cootes, A. Hill, C. J. Taylor, and J. Haslam. Use of active shape models for locating structures in medical images. *Image and Vision Computing*, 12(6): 355–365, 1994.

T. F. Cootes, C. J. Taylor, D. H. Cooper, and J. Graham. Active shape models: their training and application. *Computer Vision and Image Understanding*, 61(1): 38–59, 1995. ISSN 1077-3142.

T. F. Cootes, S. Marsl, C. J. Twining, K. Smith, and C. J. Taylor. Groupwise diffeomorphic non-rigid registration for automatic model building. In *In Proc. ECCV*, pages 316–327. Springer, 2004.

P. Dalai, B.C. Munsell, Song Wang, Jijun Tang, K. Oliver, H. Ninomiya, Xiangrong Zhou, and H. Fujita. A fast 3d correspondence method for statistical shape modeling. *Computer Vision and Pattern Recognition, 2007. CVPR '07. IEEE Conference on*, pages 1–8, June 2007.

R. H. Davies, C. J. Twining, T. F. Cootes, J. C. Waterton, and C. J. Taylor. 3d statistical shape models using direct optimisation of description length. In *Computer Vision - Eccv 2002 Pt Iii*, volume 2352 of *Lecture Notes in Computer Science*, pages 3–20. 2002a.

Rhodri H Davies, Carole J Twining, Tim F Cootes, John C Waterton, and Chris J Taylor. A minimum description length approach to statistical shape modeling. *IEEE Trans Med Imaging*, 21(5):525–537, May 2002b.

M. de Bruijne, B. van Ginneken, W.J. Niessen, and M.A. Viergever. Adapting Active Shape Models for 3D Segmentation of Tubular Structures in Medical Images. In C.J. Taylor and J.A. Noble, editors, *Information Processing in Medical Imaging*, volume 2732 of *Lecture Notes in Computer Science*, pages 136–147. Springer, 2003.

Marleen de Bruijne, Bram van Ginneken, Max A. Viergever, and Wiro J. Niessen. Interactive segmentation of abdominal aortic aneurysms in cta images. *Medical Image Analysis*, 8(2):127–138, 2004.

P. Degener, J. Meseth, and R. Klein. An adaptable surface parameterization method. In *In Proceedings of the 12th International Meshing Roundtable*, pages 201–213, 2003.

M. Desbrun, M. Meyer, and P. Alliez. Intrinsic parameterizations of surface meshes. *Computer Graphics Forum*, 21, 2002.

Shen Dong and Michael Garland. Iterative methods for improving mesh parameterizations. In *SMI '07: Proceedings of the IEEE International Conference on Shape Modeling and Applications 2007*, pages 199–210, Washington, DC, USA, 2007. IEEE Computer Society.

I. L. Dryden and K.V. Mardia. *Statistical Shape Analysis.* John Wiley Sons, 1998.

Matthias Eck, Tony DeRose, Tom Duchamp, Hugues Hoppe, Michael Lounsbery, and Werner Stuetzle. Multiresolution analysis of arbitrary meshes. In *SIGGRAPH '95: Proceedings of the 22nd annual conference on Computer graphics and interactive techniques*, pages 173–182, New York, NY, USA, 1995. ACM Press.

Donald P. Endrizzi, Raymond R. White, George M. Babikian, and Andrew B. Old. Nonunion of the clavicle treated with plate fixation: A review of forty-seven consecutive cases. *Journal of Shoulder and Elbow Surgery*, 17(6):951–953, 2008.

Anders Ericsson and Kalle Åström. Minimizing the description length using steepest descent. In *Proc. British Machine Vision Conference, Norwich, United Kingdom*, volume 2, pages 93–102, 2003.

L. Ferrarini, W. M. Palm, H. Olofsen, R. van der Landen, M. A. van Buchem, J. H. Reiber, and F. Admiraal-Behloul. Ventricular shape biomarkers for Alzheimer's disease in clinical MR images. *Magn Reson Med*, 59:260–267, Feb 2008.

Luca Ferrarini, Hans Olofsen, Walter M. Palm, Mark A. van Buchem, Johan H.C. Reiber, and Faiza Admiraal-Behloul. Games: Growing and adaptive meshes for fully automatic shape modeling and analysis. *Medical Image Analysis*, 11 (3):302 – 314, 2007.

M. S. Floater and K. Hormann. Parameterization of triangulations and unorganized points. In A. Iske, E. Quak, and M. S. Floater, editors, *Tutorials on Multiresolution in Geometric Modelling*, Mathematics and Visualization, pages 287–316. Springer, Berlin, Heidelberg, 2002.

Michael S. Floater. Mean value coordinates. *Comput. Aided Geom. Des.*, 20(1): 19–27, 2003. ISSN 0167-8396.

Michael S. Floater. Parametrization and smooth approximation of surface triangulations. *Computer Aided Geometric Design*, 14(3):231–250, 1997.

MS Floater, K Hormann, NA Dodgson, MS Floater, and MA Sabin. Surface parameterization: a tutorial and survey. *Advances in Multiresolution for Geometric Modelling*, pages 157–186, 2005.

A.F. Frangi, D. Rueckert, J.A. Schnabel, and W.J. Niessen. Automatic construction of multiple-object three-dimensional statistical shape models: application to cardiac modeling. *Medical Imaging, IEEE Transactions on*, 21(9):1151–1166, 2002.

Alejandro Frangi, Wiro Niessen, Daniel Rueckert, and Julia Schnabel. *Automatic 3D ASM Construction via Atlas-Based Landmarking and Volumetric Elastic Registration*, pages 78–91. 2001.

Michael Garland and Paul S. Heckbert. Surface simplification using quadric error metrics. In *SIGGRAPH '97: Proceedings of the 24th annual conference on Computer graphics and interactive techniques*, pages 209–216, New York, NY, USA, 1997. ACM Press/Addison-Wesley Publishing Co.

S Raymond Golish, Jason Oliviero, Eric Francke, and Mark Miller. A biomechanical study of plate versus intramedullary devices for midshaft clavicle fixation. *Journal of Orthopaedic Surgery and Research*, 3(1):28, 2008. ISSN 1749-799X.

C. Gotsman, X. Gu, and A. Sheffer. Fundamentals of spherical parameterization for 3d meshes. *ACM Transactions on Graphics*, 22, 2003.

Cindy Grimm. Parameterization using manifolds. *International Journal of Shape Modeling*, 10(1):51–80, June 2004.

Xianfeng Gu and Shing-Tung Yau. Global conformal surface parameterization. In *SGP '03: Proceedings of the 2003 Eurographics/ACM SIGGRAPH symposium on Geometry processing*, pages 127–137, Aire-la-Ville, Switzerland, Switzerland, 2003. Eurographics Association.

Xianfeng Gu, Steven J. Gortler, and Hugues Hoppe. Geometry images. In John Hughes, editor, *SIGGRAPH 2002 Conference Proceedings*, Annual Conference Series, pages 335–361. ACM Press/ACM SIGGRAPH, 2002.

Xianfeng Gu, Yalin Wang, T.F. Chan, P.M. Thompson, and Shing-Tung Yau. Genus zero surface conformal mapping and its application to brain surface mapping. *Medical Imaging, IEEE Transactions on*, 23(8):949–958, Aug. 2004.

S Haker, S Angenent, A Tannenbaum, and R Kikinis. Nondistorting flattening maps and the 3-D visualization of colon CT images. *IEEE Trans Med Imaging*, 19(7):665–670, Jul 2000a.

Steven Haker, Sigurd Angenent, Allen Tannenbaum, Ron Kikinis, Guillermo Sapiro, and Michael Halle. Conformal surface parameterization for texture mapping. *IEEE Transactions on Visualization and Computer Graphics*, 6(2): 181–189, 2000b. ISSN 1077-2626.

M. A. Harrington, T. S. Keller, J. G. Seiler, D. R. Weikert, E. Moeljanto, and H. S. Schwartz. Geometric properties and the predicted mechanical behavior of adult human clavicles. *Journal of Biomechanics*, 26(4-5):417–426, 1993.

Ying He, Xianfeng Gu, and Hong Qin. Rational spherical splines for genus zero shape modeling. In *SMI '05: Proceedings of the International Conference on Shape Modeling and Applications 2005*, pages 82–91, Washington, DC, USA, 2005. IEEE Computer Society. ISBN 0-7695-2379-X.

T Heimann, I Wolf, T Williams, and HP Meinzer. 3d active shape models using gradient descent optimization of description length. In *Information Processing in Medical Imaging*, volume 3565 of *Lecture Notes in Computer Science*, pages 566–577. 2005.

J M Hill, M H McGuire, and L A Crosby. Closed treatment of displaced middle-third fractures of the clavicle gives poor results. *The Journal of Bone and Joint Surgery. British Volume*, 79(4):537–9, July 1997.

Wei Hong, Xianfeng Gu, Feng Qiu, Miao Jin, and Arie Kaufman. Conformal virtual colon flattening. In *Proceedings of the 2006 ACM symposium on Solid and physical modeling*, pages 85–93, Cardiff, Wales, United Kingdom, 2006. ACM. ISBN 1-59593-358-1.

Hugues Hoppe. Progressive meshes. In *SIGGRAPH '96: Proceedings of the 23rd annual conference on Computer graphics and interactive techniques*, pages 99–108, New York, NY, USA, 1996. ACM Press.

P. Horkaew and G. Z. Yang. Optimal deformable surface models for 3d medical image analysis. In *Information Processing in Medical Imaging, Proceedings*, volume 2732 of *Lecture Notes in Computer Science*, pages 13–24. 2003a.

Paramate Horkaew and Guang-Zhong Yang. Optimal Deformable Surface Models for 3D Medical Image Analysis. In *Information Processing in Medical Imaging, IPMI 2003*, pages 13–24, 2003b.

Paramate Horkaew and Guang-Zhong Yang. Construction of 3D Dynamic Statistical Deformable Models for Complex Topological Shapes. In *7th International Conference on Medical Image Computing and Computer-Assisted Intervention (MICCAI 2004), Saint-Malo, France, September 26-29, 2004*, volume 3216, pages 217–224, September 2004.

K. Hormann and G. Greiner. MIPS: An efficient global parametrization method. In P.-J. Laurent, P. Sablonnière, and L. L. Schumaker, editors, *Curve and Surface Design: Saint-Malo 1999*, Innovations in Applied Mathematics, pages 153–162. Vanderbilt University Press, Nashville, TN, 2000.

K. Hormann, G. Greiner, and S. Campagna. Hierarchical parametrization of triangulated surfaces. In B. Girod, H. Niemann, and H.-P. Seidel, editors, *Proceedings of Vision, Modeling, and Visualization 1999*, pages 219–226, Erlangen, Germany, November 1999. infix.

Jerry I. Huang, Paul Toogood, Michael R. Chen, John H. Wilber, and Daniel R. Cooperman. Clavicular anatomy and the applicability of precontoured plates. *J Bone Joint Surg Am*, 89(10):2260–2265, October 2007.

Monica K. Hurdal, Philip L. Bowers, Ken Stephenson, De Witt L. Sumners, Kelly Rehm, Kirt Schaper, and David A. Rottenberg. Quasi-conformally flat mapping the human cerebellum. In *MICCAI '99: Proceedings of the Second International Conference on Medical Image Computing and Computer-Assisted Intervention*, pages 279–286, London, UK, 1999. Springer-Verlag. ISBN 3-540-66503-X.

T Huysmans, J Sijbers, and B Verdonk. Parameterization of tubular surfaces on the cylinder. *The journal of WSCG*, 13(3):97–104, 2005.

T. Huysmans, J. Sijbers, F. Vanpoucke, and B. Verdonk. Improved shape modeling of tubular objects using cylindrical parameterization. *Lecture Notes in Computer Science*, 4091:84–91, 2006.

Toon Huysmans and Jan Sijbers. Mapping tubular surfaces to the cylinder. *submitted to Medical Image Analysis*, march 2009.

Toon Huysmans, Jan Sijbers, and Brigitte Verdonk. Automatic construction of correspondences of tubular surfaces. *IEEE Transactions on Pattern Recognition and Machine Intelligence*, april 2009.

M. R. Iannotti, L. A. Crosby, P. Stafford, Greg Grayson, and R. Goulet. Effects of plate location and selection on the stability of midshaft clavicle osteotomies: A biomechanical study. *Journal of Shoulder and Elbow Surgery*, 11(5):457–462, October 2002.

M. Jin, J. Kim, F. Luo, and X. Gu. Discrete surface ricci flow. *Visualization and Computer Graphics, IEEE Transactions on*, 14(5):1030–1043, Sept.-Oct. 2008.

I. T. Jolliffe. *Principal Component Analysis*. Springer, October 2002. ISBN 0387954422.

S. Joshi, Brad Davis, Matthieu Jomier, and Guido Gerig. Unbiased diffeomorphic atlas construction for computational anatomy. *NeuroImage*, 23(Supplement 1):S151 – S160, 2004. Mathematics in Brain Imaging.

Markus S Juchems, Thorsten R Fleiter, Sandra Pauls, Stefan A Schmidt, Hans-JÃijrgen Brambs, and Andrik J Aschoff. Ct colonography: comparison of a colon dissection display versus 3d endoluminal view for the detection of polyps. *European Radiology*, 16(1):68–72, 2006.

Sevki Kabak, Mehmet Halici, Mehmet Tuncel, Levent Avsarogullari, and Sinan Karaoglu. Treatment of midclavicular nonunion: comparison of dynamic compression plating and low-contact dynamic compression plating techniques. *Journal of Shoulder and Elbow Surgery*, 13(4):396–403, 2004.

Dagmar Kainmüller, Thomas Lange, and Hans Lamecker. Shape constrained automatic segmentation of the liver based on a heuristic intensity model. *Proc. MICCAI Workshop 3D Segmentation in the Clinic: A Grand Challenge*, pages 109–116, 2007.

Z. Kami, C. Gotsman, and S.J. Gortler. Free-boundary linear parameterization of 3d meshes in the presence of constraints. In *Shape Modeling and Applications, 2005 International Conference*, pages 266–275, 2005.

A. Kelemen, G. Szekely, and G. Gerig. Elastic model-based segmentation of 3-d neuroradiological data sets. *Medical Imaging, IEEE Transactions on*, 18(10): 828–839, Oct 1999.

M.A. Ali Khan and H. Keith Lucas. Plating of fractures of the middle third of the clavicle. *Injury*, 9(4):263–267, 1977.

R. Kimmel and J. A. Sethian. Computing geodesic paths on manifolds. *Proceedings of the National Academy of Sciences of the United States of America*, 95 (15):8431–8435, 1998.

A. C. W. Kotcheff and C. J. Taylor. Automatic construction of eigenshape models by direct optimization. *Medical Image Analysis*, 2:303–314(12), 1998.

H. Lamecker, M. Seebaß, H.-C. Hege, and P. Deuflhard. A 3d statistical shape model of the pelvic bone for segmentation. In J.M. Fitzpatrick and M. Sonka, editors, *Proceedings of SPIE - Volume 5370 Medical Imaging 2004: Image Processing*, pages 1341–1351, May 2004.

Hans Lamecker, Thomas Lange, and Martin Seebaß. A statistical shape model for the liver. In Takeyoshi Dohi and Ron Kikinis, editors, *Medical Image Computing and Computer-Assisted Intervention - MICCAI 2002, 5th International Conference, Tokyo, Japan, September 25-28, 2002, Proceedings, Part II*, volume 2489 of *Lecture Notes in Computer Science*, pages 421–427. Springer, 2002.

Bernard Levin, David A Lieberman, Beth McFarland, Robert A Smith, Durado Brooks, Kimberly S Andrews, Chiranjeev Dash, Francis M Giardiello, Seth Glick, Theodore R Levin, Perry Pickhardt, Douglas K Rex, Alan Thorson, and Sidney J Winawer. Screening and surveillance for the early detection of colorectal cancer and adenomatous polyps, 2008: a joint guideline from the american cancer society, the us multi-society task force on colorectal cancer, and the american college of radiology. *CA: A Cancer Journal for Clinicians*, 58 (3):130–160, 2008.

Bruno Levy, Sylvain Petitjean, Nicolas Ray, and Jerome Maillot. Least squares conformal maps for automatic texture atlas generation. In *Proceedings of the 29th annual conference on Computer graphics and interactive techniques*, pages 362–371. ACM Press, 2002.

Xin Li, Yunfan Bao, Xiaohu Guo, Miao Jin, Xianfeng Gu, and Hong Qin. Globally optimal surface mapping for surfaces with arbitrary topology. *IEEE Transactions on Visualization and Computer Graphics*, 14(4):805–819, 2008. ISSN 1077-2626.

D. C. Liu and J. Nocedal. On the limited memory bfgs method for large scale optimization. *Math. Program.*, 45(3):503–528, 1989.

I. Lloyd, N. Trefethen, and David Bau. *Numerical Linear Algebra.* SIAM, 3600 University City Science Center, Philadelphia, PA, 1997.

Dirk Loeckx. *Automated nonrigid intra-patient image registration using B-splines.* PhD thesis, K.U.Leuven, Belgium, May 2006.

William E. Lorensen and Harvey E. Cline. Marching cubes: A high resolution 3d surface construction algorithm. *SIGGRAPH Comput. Graph.*, 21(4):163–169, 1987.

Lok Ming Lui, Yalin Wang, and Tony F. Chan. *Solving PDEs on Manifolds with Global Conformal Parametriazation*, pages 307–319. 2005.

J. B. MacQueen. Some methods for classification and analysis of multivariate observations. In L. M. Le Cam and J. Neyman, editors, *Proc. of the fifth Berkeley Symposium on Mathematical Statistics and Probability*, volume 1, pages 281–297. University of California Press, 1967.

Z. Mai, T. Huysmans, and J. Sijbers. Colon visualization using cylindrical parameterization. *Lecture Notes in Computer Science*, 4678:607–615, 2007.

Evaldo Marchi, Marcio P. Reis, and Marcus V. Carvalho. Transmediastinal migration of kirschner wire. *Interactive CardioVascular and Thoracic Surgery*, page icvts.2008.185850, July 2008.

Simon Mays, James Steele, and Mark Ford. Directional asymmetry in the human clavicle. *International Journal of Osteoarchaeology*, 9(1):28, 18, 1999.

Michael D. McKee, Lisa M. Wild, and Emil H. Schemitsch. Midshaft malunions of the clavicle. *J Bone Joint Surg Am*, 85(5):790–797, May 2003.

Michael D. McKee, Elizabeth M. Pedersen, Caroline Jones, David J.G. Stephen, Hans J. Kreder, Emil H. Schemitsch, Lisa M. Wild, and Jeffrey Potter. Deficits following nonoperative treatment of displaced midshaft clavicular fractures. *J Bone Joint Surg Am*, 88(1):35–40, 2006.

C S Neer. Nonunion of the clavicle. *Journal of the American Medical Association*, 172:1006–11, March 1960.

Jorge Nocedal and Stephen J. Wright. *Numerical Optimization.* Springer Series in Operations Research. Springer, New York, 1999.

A Nordqvist and C Petersson. The incidence of fractures of the clavicle. *Clinical Orthopaedics and Related Research*, (300):127–32, March 1994.

A Nordqvist, C J Petersson, and I Redlund-Johnell. Mid-clavicle fractures in adults: end result study after conservative treatment. *Journal of Orthopaedic Trauma*, 12(8):572–6, 1998.

Jan Nowak, Margareta Holgersson, and Sune Larsson. Sequelae from clavicular fractures are common: a prospective study of 222 patients. *Acta Orthopaedica*, 76(4):496–502, August 2005.

ThÃľodore Papadopoulo and Manolis I. A. Lourakis. Estimating the jacobian of the singular value decomposition: Theory and applications. In David Vernon, editor, *ECCV (1)*, volume 1842 of *Lecture Notes in Computer Science*, pages 554–570. Springer, 2000.

F G Parsons. On the proportions and characteristics of the modern english clavicle. *Journal of Anatomy*, 51(Pt 1):71–93, October 1916. PMID: 17103806.

R. R. Paulsen, R. Larsen, S. Laugesen, C. Nielsen, and B. K. Ersbøll. Building and testing a statistical shape model of the human ear canal. In *Medical Image Computing and Computer-Assisted Intervention - MICCAI 2002, 5th Int. Conference, Tokyo, Japan,*. Springer, 2002.

P. J. Pickhardt, J. R. Choi, I. Hwang, J. A. Butler, M. L. Puckett, H. A. Hildebrandt, R. K. Wong, P. A. Nugent, P. A. Mysliwiec, and W. R. Schindler. Computed tomographic virtual colonoscopy to screen for colorectal neoplasia in asymptomatic adults. *N. Engl. J. Med.*, 349:2191–2200, Dec 2003.

R. Pinho, J. Sijbers, and T. Huysmans. Segmentation of the human trachea using deformable statistical models of tubular shapes. In *Advanced Concepts for Intelligent Vision Systems (ACIVS) 2007, LNCS*, volume 4678, pages 531–542, August 2007.

R. Pinho, T. Huysmans, W. Vos, and J. Sijbers. Tracheal stent prediction using statistical deformable models of tubular shapes. In *Proceedings of SPIE Medical Imaging*, San Diego, CA, USA, February 2008. SPIE.

Ulrich Pinkall and Konrad Polthier. Computing discrete minimal surfaces and their conjugates. *Experimental Mathematics*, 2(1):15âĂŞ36, 1993.

J. Poigenfürst, G. Rappold, and W. Fischer. Plating of fresh clavicular fractures: results of 122 operations. *Injury*, 23(4):237–241, 1992.

Franco Postacchini, Stefano Gumina, Pierfrancesco De Santis, and Francesco Albo. Epidemiology of clavicle fractures. *Journal of Shoulder and Elbow Surgery*, 11(5):452–456, October 2002.

Emil Praun and Hugues Hoppe. Spherical parametrization and remeshing. *ACM Transactions on Graphics*, 22(3):340–349, 2003.

D. Rueckert, L. I. Sonoda, C. Hayes, D. L. Hill, M. O. Leach, and D. J. Hawkes. Nonrigid registration using free-form deformations: application to breast mr images. *IEEE Transactions on Medical Imaging*, 18(8):712–721, August 1999.

D. Rueckert, A. Frangi, and J. Schnabel. *Automatic Construction of 3D Statistical Deformation Models Using Non-rigid Registration*, pages 77–84. 2001.

Pedro V. Sander, John Snyder, Steven J. Gortler, and Hugues Hoppe. Texture mapping progressive meshes. In *SIGGRAPH '01: Proceedings of the 28th annual conference on Computer graphics and interactive techniques*, pages 409–416, New York, NY, USA, 2001. ACM Press. ISBN 1-58113-374-X.

N Schwarz and K Höcker. Osteosynthesis of irreducible fractures of the clavicle with 2.7-mm asif plates. *The Journal of Trauma*, 33(2):179–83, August 1992.

G. A. F. Seber. *Multivariate Observations*. Wiley, New York, 1984.

A. Sheffer and E. de Sturler. Parameterization of faceted surfaces for meshing using angle-based flattening. *Engineering with Computers*, 17:326–337, 2001.

Alla Sheffer, Emil Praun, and Kenneth Rose. Mesh parameterization methods and their applications. *Foundations and Trends in Computer Graphics and Vision*, 2(2):105–171, 2006.

J.-W. Shen, P.-J. Tong, and H.-B. Qu. A three-dimensional reconstruction plate for displaced midshaft fractures of the clavicle. *J Bone Joint Surg Br*, 90-B(11): 1495–1498, November 2008.

Byeong-Seok Shin, Sukhyun Lim, and Hye-Jin Lee. Efficient unfolding of virtual endoscopy using linear ray interpolation. *Computer Methods and Programs in Biomedicine*, 93(2):174–184, February 2009.

Jan Sijbers and Dirk Van Dyck. Efficient algorithm for the computation of 3-D fourier descriptors. In Guido M Cortelazzo and Concettina Guerra, editors, *Proceedings of the 1st International Symposium on* 3*-D Data Processing Visualization and Transmission (3DPVT-02)*, pages 640–643, Los Alamitos, CA, June 29–21 2002. IEEE Computer Society.

Canadian Orthopaedic Trauma Society. Nonoperative treatment compared with plate fixation of displaced midshaft clavicular fractures. a multicenter, randomized clinical trial. *J Bone Joint Surg Am*, 89(1):1–10, 2007.

Olga Sorkine, Daniel Cohen-Or, Rony Goldenthal, and Dani Lischinski. Bounded-distortion piecewise mesh parameterization. In *VIS '02: Proceedings of the conference on Visualization '02*, pages 355–362, Washington, DC, USA, 2002. IEEE Computer Society. ISBN 0-7803-7498-3.

D. Steiner and A. Fischer. Planar parameterization for closed 2-manifold genus-1 meshes. In *SM '04: Proceedings of the ninth ACM symposium on Solid modeling and applications*, pages 83–91, Aire-la-Ville, Switzerland, Switzerland, 2004. Eurographics Association. ISBN 3-905673-55-X.

M. Styner, I. Oguz, S. Xu, D. Pantazis, and G. Gerig. Statistical group differences in anatomical shape analysis using hotelling t2 metric. SPIE Med Imaging, 02 2007.

M. Styner, I. Oguz, T. Heimann, and G. Gerig. Minimum description length with local geometry. pages 1283–1286, May 2008.

Martin Styner. *Combined Boundary-Medial Shape Description of Variable Biological Objects*. PhD thesis, University of North Carolina, Dept. of Computer Science, June 2001.

Martin Styner, Jeffrey A Lieberman, Robert K McClure, Daniel R Weinberger, Douglas W Jones, and Guido Gerig. Morphometric analysis of lateral ventricles in schizophrenia and healthy controls regarding genetic and disease-specific factors. *Proc Natl Acad Sci U S A*, 102(13):4872–4877, Mar 2005.

Martin A Styner, Kumar T Rajamani, Lutz-Peter Nolte, Gabriel Zsemlye, Gabor Szekely, Chris J Taylor, and Rhodri H Davies. Evaluation of 3D correspondence methods for model building. *Inf Process Med Imaging*, 18:63–75, Jul 2003. Evaluation Studies.

J. Der Tavitian, J. N. S. Davison, and J. J. Dias. Clavicular fracture non-union surgical outcome and complications. *Injury*, 33(2):135–143, March 2002.

Hans Henrik Thodberg. Minimum Description Length Shape and Appearance Models. In *Information Processing in Medical Imaging, IPMI 2003*, 2003.

Y. Tong, P. Alliez, D. Cohen-Steiner, and M. Desbrun. Designing quadrangulations with discrete harmonic forms. In *SGP '06: Proceedings of the fourth Eurographics symposium on Geometry processing*, pages 201–210, Aire-la-Ville, Switzerland, Switzerland, 2006. Eurographics Association. ISBN 30905673-36-3.

Olivier Verborgt, Kathleen Pittoors, Francis Van Glabbeek, Geert Declercq, Rudy Nuyts, and Johan Somville. Plate fixation of middle-third fractures of the clavicle in the semi-professional athlete. *Acta Orthopaedica Belgica*, 71(1):17–21, February 2005.

D Vining and D Gelfand. Noninvasive colonoscopy using helical ct scanning, 3d reconstruction, and virtual reality. In *Meeting of the Society of Gastrointestinal Radiologists, February 13âĂŞ18*, Washington, DC, USA, 1994.

Ge Wang, G. McFarland, B.P. Brown, and M.W. Vannier. Gi tract unraveling with curved cross sections. *Medical Imaging, IEEE Transactions on*, 17(2):318–322, 1998.

Yalin Wang, Lok Ming Lui, Xianfeng Gu, K.M. Hayashi, T.F. Chan, A.W. Toga, P.M. Thompson, and Shing-Tung Yau. Brain surface conformal parameterization using riemann surface structure. *Medical Imaging, IEEE Transactions on*, 26 (6):853–865, June 2007.

Yalin Wang, Xiaotian Yin, Xianfeng Gu, Tony F. Chan, Paul M. Thompson, and Shing-Tung Yau. Colon flattening with discrete ricci flow. In *MICCAI08 Workshop: Computational and Visualization Challenges in the New Era of Virtual Colonoscopy*, New York, USA, Sep 6-10 2008.

M Wick, E J MÃijller, E Kollig, and G Muhr. Midshaft fractures of the clavicle with a shortening of more than 2 cm predispose to nonunion. *Archives of Orthopaedic and Trauma Surgery*, 121(4):207–11, 2001.

Shin Yoshizawa, Alexander Belyaev, and Hans-Peter Seidel. A fast and simple stretch-minimizing mesh parameterization. In *SMI '04: Proceedings of the Shape Modeling International 2004*, pages 200–208, Washington, DC, USA, 2004. IEEE Computer Society.

S. Zachow, H. Lamecker, B. Elsholtz, and M. Stiller. Reconstruction of mandibular dysplasia using a statistical 3d shape model. In *Proceedings of CARS (H. Lemke et al, eds.), Int. Congress Series (1281)*, pages 1238–1243. Elsevier, 2005.

Eugene Zhang, Konstantin Mischaikow, and Greg Turk. Feature-based surface parameterization and texture mapping. *ACM Trans. Graph.*, 24(1):1–27, 2005.

Lei Zhu, S. Haker, and A. Tannenbaum. Flattening maps for the visualization of multibranched vessels. *Medical Imaging, IEEE Transactions on*, 24(2):191–198, Feb. 2005.

Michael Zlowodzki, Boris A Zelle, Peter A Cole, Kyle Jeray, and Michael D McKee. Treatment of acute midshaft clavicle fractures: systematic review of 2144 fractures: on behalf of the evidence-based orthopaedic trauma working group. *Journal of Orthopaedic Trauma*, 19(7):504–7, August 2005.

Malte Zöckler, Detlev Stalling, and Hans-Christian Hege. Fast and intuitive generation of geometric shape transitions. *The Visual Computer*, 16(5):241–253, June 2000.

Developed Software

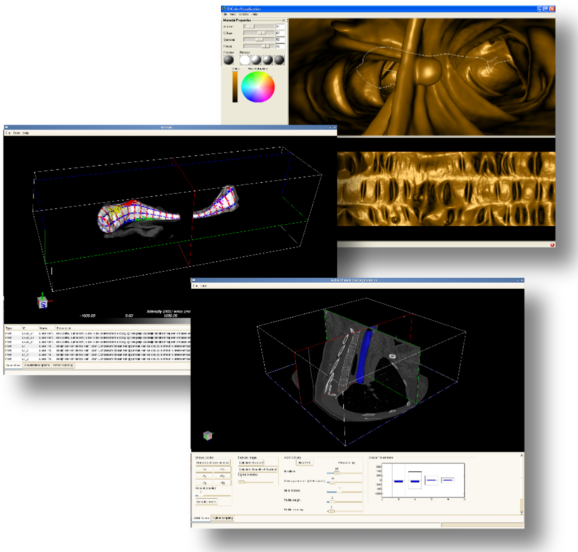

The following software has been developed during this research:

- Several surface parameterization techniques: stretch based spherical parameterization, conformal planar parameterization for disc-like surfaces, and both conformal and stretch based cylindrical parameterization.
- A cylindrical surface correspondence optimization tool set, including: segmentation, surface extraction, surface alignment, and correspondence optimization with several spatial and parameterization transforms (rigid, twist, b-spline).
- Geodesic path and distance calculation tool for triangle surfaces.
- A Tool for surface based statistical group studies, for both paired and unpaired data.

- Tools for surface approximation with spherical harmonics (spherical surfaces) and b-splines (tubular surfaces).
- A tool to generate plate sets from a surface population and a desired region of contact.
- A surface annotation tool to interactively pin-point anatomical locations on a surface. To ease the pin-pointing procedure, surface visualization is complemented with orthogonal slice volume visualization.
- An active shape model segmentation tool for general general point distribution models. Controls are provided for the user to navigate the model through the volume. Several parameters of the active shape model can be interactively modified.
- A visualization tool for virtual inspection, e.g., virtual colonoscopy. From cylindrically parameterized tubular structures, the tool provides a 3D and a flattened view with a from-the-centerline-view shading. The user can navigate through the structure by clicking on the flattened representation.

CURRICULUM VITAE

Toon Huysmans was born in Geel, Belgium on November 19, 1981. He attended high school at the Technical Institute Sint-Paulus in Mol. In 1999 he moved to Antwerp to study Computer Science and he received the Master of Science degree in Computer Science in 2003 (magna cum laude). His graduation research concerned diamond cut optimization and was carried out at the Vision Lab of the University of Antwerp in close collaboration with the companies DiamCad and DiamScan. In October 2003, he entered the world of medical image and geometry processing by joining the Vision Lab as a PhD student where he enjoyed an IWT scholarship. The research he conducted at the Vision Lab focusing on parameterization, correspondence construction, and related applications has lead to this manuscript.

PUBLICATIONS

Journal articles:

- T. Huysmans, J. Sijbers, and B. Verdonk, “Automatic Construction of Correspondences for Tubular Surfaces”, accepted for publication in IEEE Transactions on Pattern Analysis and Machine Intelligence, Special Issue on Shape Analysis and Modeling, 2009.

- Z. Mai, T. Huysmans and J. Sijbers, “Colon Visualization Using Cylindrical Parameterization”, Lecture Notes in Computer Science, Vol. 4678, p. 607-615, 2007.

- R. Pinho, J. Sijbers and T. Huysmans, “Segmentation of The Human Trachea Using Deformable Statistical Models of Tubular Shapes”, Lecture Notes in Computer Science, Vol. 4678, p. 531-542, August 2007.

- T. Huysmans, J. Sijbers, F. Vanpoucke and B. Verdonk, “Improved Shape Modeling of Tubular Objects Using Cylindrical Parameterization”, Lecture Notes in Computer Science, Vol. 4091, p. 84-91, 2006.

- T. Huysmans, J. Sijbers and B. Verdonk, “Parameterization of tubular surfaces on the cylinder”, Journal of the Winter School of Computer Graphics, Vol. 13, Nr. 3, p. 97-104, 2005.

Conference proceedings (full paper):

- R. Pinho, T. Huysmans, W. Vos and J. Sijbers, “Tracheal Stent Prediction Using Statistical Deformable Models of Tubular Shapes”, Proceedings of SPIE Medical Imaging, San Diego, CA, USA, February, 2008.

- T. Huysmans, J. Sijbers and B. Verdonk, “Statistical shape models for tubular objects”, Proceedings of IEEE BENELUX/DSP Valley Signal Processing Symposium (SPS-DARTS), p. 155-158, Antwerp, Belgium, March, 2006.

Conference proceedings (abstract only):

- A. Bernat, T. Huysmans, F. van Glabbeek, J. Sijbers, R. Pinho and J.L. Gielen, "Exploring the Clavicle: Morphometric Differences Using a 3D Model", AAOS Annual Meeting, Las Vegas,Nevada, February, (2009)

- A. Bernat, T. Huysmans, F. Van Glabbeek, J. Sijbers, H. Bortier and J. Gielen, "Morphometric Study of the Human Clavicle for the Development of an Anatomical Plate", 54th Annual Meeting of the Orthopaedic Research Society, San Francisco, Ca, United States, March, 2008.

- T. Huysmans, A. Bernat, F. van Glabbeek, J. Sijbers, J.L. Gielen and H. Bortier, "Left-Right and Gender Analysis of The Human Clavicle, A Problem in Developing an Anatomical Plate?", 21th Congress of the European Society for the Surgery of the Shoulder and the Elbow (SECEC - ESSSE) 17-20 September, p. 101, Brugge, Belgium, September, 2008.

- T. Huysmans, A. Bernat, R. Pinho, J. Sijbers, F. Van Glabbeeck, P.M. Parizel and H. Bortier, "A Framework for Morphometric Analysis of Long Bones: Application to the Human Clavicle", Liege Image Days 2008: Medical Imaging, March, 2008.

- R. Pinho, T. Huysmans, W. Vos and J. Sijbers, "Tracheal Stent Prediction Using Statistical Deformable Models of Healthy Tracheas", Liege Image Days 2008: Medical Imaging, March, 2008.

- N. Van Camp, T. Huysmans, M. Verhoye, N. Galjart, J. Sijbers and A. Van der Linden, "Statistical shape analysis on 3D MRI of the ventricular system of the Cyln2/Rsn double knock-out mice", Proceedings of the International Society for Magnetic Resonance in Medicine, p. 1869, Berlin, Germany, 2007.

- V. Van Meir, T. Huysmans, J. Sijbers and A. Van der Linden, "Statistical shape and position analysis on 3D structural MRI data of a motor region involved in vocal behavior of songbirds", Proceedings of the International Society for Magnetic Resonance in Medicine, p. 431, Berlin, Germany, 2007.

- J. Bertels, T. Huysmans, J. Sijbers, B. Verdonk and P. Parizel, "Multi-scale registration of spherical parametrizations of the human cortex", 23rd Annual Scientific Meeting of the European Society for Magnetic Resonance in Medicine and Biology, p. 89, Warsaw, Poland, 2006.

- T. Huysmans, A. Bernat, J. Sijbers, P. M. Parizel, F. Van Glabbeek and B. Verdonk, "Shape Analysis of the Human Clavicle for the Development of a Set of osteosynthesis Plates", Belgian Day on Biomedical Engineering -

IEEE/EMBS Benelux Symposium, p. 128-129, Brussels, Belgium, December, 2006.

- T. Huysmans and J. Sijbers, "Mesh smoothing through multiscale anisotropic diffusion of geometry images", 13th European Microscopy Congress (EMC), Antwerp, Belgium, August, 2004.

Articles in preparation:

- T. Huysmans and J. Sijbers, "Mapping Tubular Surfaces to the Cylinder", 2009.
- T. Huysmans, A. Bernat, R. Pinho, F. van Glabbeek, and J. Sijbers, "Shape Modeling of the Human Clavicle: Application to Anatomical Precontouring of Osteosynthesis Plates", 2009.

Submitted patents:

- T. Huysmans and J. Sijbers, "Method for Mapping Tubular Surfaces to a Cylinder", European patent application number EP09162289.4, June 9, 2009.